Molecular Hybrid Photocathodes Based on Silicon for Solar Fuel Synthesis

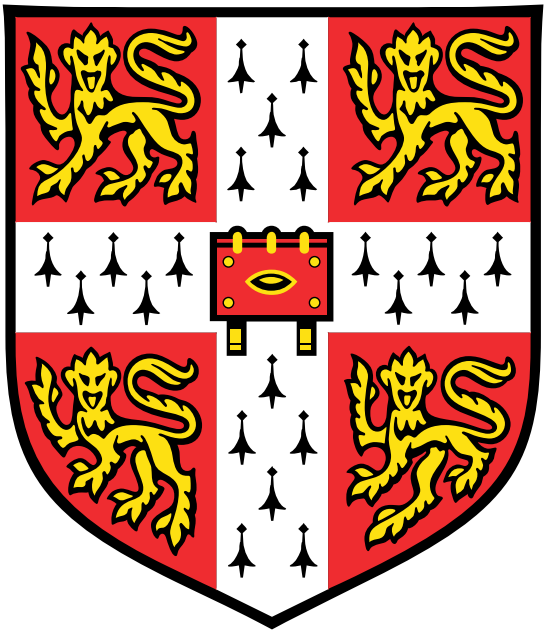

Jane Jing Leung

Department of Chemistry
University of Cambridge

A dissertation submitted for the degree of
Doctor of Philosophy

Trinity College August 2018

Abstract

Molecular Hybrid Photocathodes Based on Silicon for Solar Fuel Synthesis

Jane J. Leung

Artificial photosynthesis is broadly defined as the process of solar energy conversion into chemical fuels and represents a promising route towards alleviating the global energy crisis. In this context, the development of photocathodes for the use in photoelectrochemical cells is an attractive approach for the storage of solar energy in the form of a chemical energy carrier (*e.g.* H_2 and CO_2-reduction products from H_2O and CO_2). However, molecular catalyst-based photocathodes remain scarcely reported and typically suffer from low efficiencies and/or stabilities due to inadequate strategies for interfacing the molecular component with the light-harvesting material, with benchmark systems continuing to rely on precious metal components.

In this thesis, the straightforward preparation of a *p*-silicon|mesoporous titania|molecular catalyst photocathode assembly that is active towards proton reduction in aqueous media is first established. The mesoporous TiO_2 scaffold acts as an electron shuttle between the silicon and the catalyst, while also stabilising the silicon from passivation and enabling a high loading of molecular catalysts. When a Ni bis(diphosphine)-based catalyst is anchored on the surface of the electrode, a catalytic onset potential of $+0.4\,V$ *vs.* RHE and a high turnover number of 1×10^3 was obtained from photoelectrolysis under UV-filtered simulated solar irradiation at 1 Sun after 24 hours. Notwithstanding its aptitude for molecular catalyst immobilisation, the Si|TiO_2 photoelectrode showed great versatility towards different types of catalysts and pH conditions, highlighting the flexible platform it represents for many potential reductive catalysis transformations.

The Si|TiO_2 scaffold was extended towards solar CO_2 reduction *via* the immobilisation of a novel phosphonated cobalt bis(terpyridine) catalyst to achieve the

first precious metal-free, CO_2-reducing molecular hybrid photocathode. Reducing CO_2 in both organic-water and purely aqueous conditions, the activity of this photocathode was shown to be affected by its environment and reached record turnover numbers for CO production by a molecular photocathode under optimal conditions, maintaining stable activity for more than 24 hours. Critically, in-depth electrochemical and *in situ* resonance Raman and infrared spectroelectrochemical investigations provided key insights into the nature of the surface-bound Co complex under reducing conditions. While demonstrating the power and precision offered by such *in situ* spectroelectrochemical techniques, these studies ultimately alluded to a catalytic mechanism that contrasts with that reported for the in-solution (homogeneous) catalyst. Overall, this affords a distinct mechanistic pathway that unlocks an earlier catalytic onset and enables photoelectrochemical activity.

Finally, in the context of improving product selectivity in molecular-based CO_2 reduction, polymers based on the cobalt bis(terpyridine) motif were synthesised and immobilised on inverse opal-type electrodes designed specifically to accommodate large molecules. Rational design of the polymers' co-monomers was aimed towards the provision of an artificial environment for the active complex that would influence product selectivity, which was ultimately demonstrated by the improvement of a H_2:CO product ratio of 1:2 (molecule) to 1:6 (polymer). Further studies of this all-in-one system included modulating its degree of cross-linkage as well as a CO_2-reducing demonstration photocathode on a Si|inverse-opal TiO_2 scaffold.

Declaration

I hereby declare that this dissertation is the result of my own work and includes nothing which is the outcome of work done in collaboration except as declared in the Acknowledgements and in the text. It is not substantially the same as any that I have submitted, or, is being concurrently submitted for a degree or diploma or other qualification at the University of Cambridge or any other University or similar institution. I further state that no substantial part of my dissertation has already been submitted, or, is being concurrently submitted for any such degree, diploma or other qualification at the University of Cambridge or any other University or similar institution. This dissertation does not exceed the prescribed word limit of 60,000 words.

Jane Jing Leung
August 2018

This thesis is dedicated to my parents, Thomas and Vivian, who are great believers in education and whose unconditional love and support are the reasons I am where I am today.

Acknowledgements

I have received the support of countless individuals over the four years of my PhD. You are too many to mention and I thank you all for your contributions, big and small.

I must first thank my supervisor, Professor Erwin Reisner, for his guidance and belief in me throughout my PhD. The supportive, collaborative environment he has fostered across the years in the Reisner lab was instrumental to both the success of my research and the pleasure I had working in his group.

My biggest gratitude goes to Dr. Julien Warnan for the extended collaboration on all of our projects, from inception through to execution and publication. His depth of experience, patience and positive outlook were key to the success of my PhD and for this I will be eternally and tremendously grateful.

Dr. Khoa Ly and Dr. Nina Heidary were also key contributors to the in-depth mechanistic studies we carried out on our CO_2 reduction systems. Their enthusiasm and expertise were essential to this project and I am beholden to them for their continued support. Julian Vigil was a Masters student that Dr. Julien Warnan and myself co-supervised and with whom we collaborated heavily for the final project of my PhD. His professionalism, enthusiasm, resourcefulness and extreme aptitude were fundamental reasons for our shared achievements, and for this I both thank and congratulate him. Numerous other collaborations ensured I had the materials necessary for my research. Electrodes were fabricated in collaboration with Dr. Dong Heon Nam, Katarzyna Sokol, Esther Edwardes Moore, Andreas Wagner and Kenichi Nakanishi. Raw XPS data was provided by Dr. Chris Amey at the Cavendish Laboratory, University of Cambridge, and Dr. David Morgan at the Cardiff Catalysis Institute, Cardiff University.

I am also very grateful for the friendship and helpful discussions I had with members of the Reisner group, both past and present - you know who you are, and I will not forget the times we shared across the years in and out of the lab. In particular, the love and support from Janina, Moritz, Bertrand, Dong and Dave

P., as well as friends in the wider Cambridge community - especially Felix, Lily, Isabella and Schirin - were essential reminders of life outside the lab and made Cambridge a special place to be.

I must also thank the Woolf Fisher Trust in New Zealand and the Cambridge Trusts for the financial support I received to conduct my PhD in the form of a Woolf Fisher Scholarship. I am particularly indebted to Dr. Nigel Evans for his steadfast encouragement and concern for myself and all of the Woolf Fisher scholars throughout the years. He took it upon himself to ensure each and every one of us were achieving success in a supportive, safe environment and I am extremely grateful for him for developing an atmosphere of love reminiscent of home for all of us kiwis. Thank you, Nigel, for being the pillar that you are.

I am also extremely blessed to have had the continued encouragement from my family and friends throughout all the years of my life. Although we are spread across all corners of the globe, I felt the strength of their unwavering belief in me and unconditional understanding, which were constants I could rely on during this roller-coaster experience. I also thank my boyfriend Julien for his love, superhuman patience and endless resolve, which have sustained and carried me through all the highs and lows of my PhD. Finally, I wish to unreservedly thank my parents for everything they have done for me. I draw strength every day from the deep familial foundations that they have nurtured throughout my life in both Hong Kong and New Zealand. Their unconditional love and support are eternal gifts and I would not be where I am today without them.

List of Publications

The results of work carried out for this thesis have been included in the peer-reviewed journal articles listed below:

1. Leung, J. J.,† Warnan, J.,† Nam, D. H., Zhang, J. Z., Willkomm, J. and Reisner, E., 'Photoelectrocatalytic H_2 evolution in water with molecular catalysts immobilised on p-Si *via* a stabilising mesoporous TiO_2 interlayer', *Chem. Sci.*, **2017**, *8*, 5172–5180.

2. Leung, J. J.,† Warnan, J.,† Ly, K. H., Heidary, N., Nam, D. H., Kuehnel, M. F. and Reisner, E., 'Solar-driven reduction of aqueous CO_2 with a Co bis(terpyridine)-based photocathode', *under review.*

3. Leung, J. J.,† Vigil, J. A.,† Warnan J.,† Edwardes Moore, E. and Reisner, E., 'Rational polymer design towards tuneable molecular CO_2 reduction catalysis', *submitted.*

Contributions also made to the following peer-reviewed journal articles were not included in this thesis:

4. Li, N., Matthews, P. D., Leung, J. J., King, T. C., Wood, P. T., Luo, H.-K. and Wright, D. S., 'Synthesis, structure and properties of the manganese-doped polyoxotitanate cage $[Ti_{18}MnO_{30}(OEt)_{20}(MnPhen)_3]$ (Phen = 1,10-phenanthroline)', *Dalton Trans.*, **2015**, *44*, 19090–19096.

5. Reuillard, B.,† Warnan, J.,† Leung, J. J., Wakerley, D. W. and Reisner, E., 'A poly(cobaloxime)/carbon nanotube electrode: freestanding buckypaper with polymer-enhanced H_2 evolution performance', *Angew. Chem. Int. Ed.*, **2016**, *55*, 3952-3957.

6. Dalle K. E.,† Warnan, J.,† Leung, J. J., Reuillard, B., Karmel, I. S. and Reisner, E., 'Immobilization of first row transition metal complexes for electro- and solar-driven fuel synthesis', *Chem. Rev.*, *accepted.*

† denotes equal contribution.

Table of Contents

List of Figures

List of Tables

Glossary

η	overpotential
$E_{½}$	half-wave potential
E_{app}	applied potential
E_{cat}	catalytic onset potential
E_{g}	band gap energy
E_{onset}	photocurrent onset potential
J	photocurrent density
mesoTiO_2	mesoporous TiO_2
p-SC	p-type semiconductor
p-Si	p-type silicon
ALD	atomic layer deposition
ATR-FTIR	attenuated total reflectance Fourier-transform infrared spectroscopy
bpy	bipyridine
CB	conduction band
CE	counter electrode
CNT	carbon nanotube
CODH	carbon monoxide dehydrogenase
CPE	controlled potential electrolysis
CPPE	controlled potential photoelectrolysis
CRC	CO_2 reduction catalyst
CV	cyclic voltammogram
DMF	*N*,*N*'-dimethylformamide
DSPC	dye-sensitised photocathode
DSSC	dye-sensitised solar cell
EQE	external quantum efficiency
FDH	formate dehydrogenase
FE	Faradaic efficiency
FTO	fluorine-doped tin oxide
GC	gas chromatography

H_2ase	hydrogenase
HEC	hydrogen evolution catalyst
HER	hydrogen evolution reaction
HRMS	high-resolution mass spectrometry
ICP-OES	inductively coupled plasma optical emission spectrometry
IPCE	incident photon-to-electron efficiency
IR	infrared spectroscopy
ITO	indium tin oxide
LAPC	light-absorbing photocathode
LSV	linear sweep voltammogram
MeCN	acetonitrile
MeOH	methanol
MV	methyl viologen dichloride
NMR	nuclear magnetic resonance spectroscopy
OER	oxygen evolution reaction
PEC	photoelectrochemical
phen	phenanthroline
PV	photovoltaic
PVI	polyvinylimidazole
PVP	polyvinylpyridine
qtpy	quaterpyridine
RE	reference electrode
rpm	revolutions per minute
SEM	scanning electron microscopy
STH	solar-to-hydrogen efficiency
TAS	transient absorption spectroscopy
TOF	turnover frequency
TON	turnover number
tpy	terpyridine
UV-vis	UV-visible spectroscopy
VB	valence band
vtpy	vinylterpyridine
WE	working electrode
XPS	X-ray photoelectron spectroscopy

Chapter 1

Introduction

1.1 Solar Fuels and the Global Energy Crisis

The world faces an increasing energy crisis, both on the grounds of the environmental impact of traditional energy sources,[1,2] and in terms of the depletion of Earth's fossil fuel reserves and the socio-economic impact of non-renewable global resource distribution.[3–6] Meeting the need for scalable and cost-effective renewable energy vectors has therefore never been a greater challenge than it is in the 21st Century, especially in light of strong population and economic growth in several non-OECD countries.

Solar irradiation is geographically highly available and represents the most abundant terrestrial energy resource, with the amount of solar energy reaching the Earth's surface in one hour providing more power than the current annual global energy demand (18 TW in 2017).[7,8] It therefore follows that only a small fraction of the solar energy reaching Earth needs to be harvested to more than satisfy the burgeoning total energy demand over the coming years and centuries (predicted energy demand: 27 TW in 2040).[9]

Currently, the predominant technologies for harvesting solar energy are photovoltaic (PV) cells, which transform solar energy directly into electrical energy. Having been commercialised since the 1990s, they are today adopted in all corners of the globe, and even power human activities in outer space.[10] Silicon solar cells, the most common type of commercially available PV cells, are robust, offer high efficiencies ($> 25\,\%$) and are experiencing rapidly decreasing prices.[11] Recent statistics, however, show that only 18.5 % of global energy was supplied by electricity, with the majority of demand being met using chemical fuels for transportation

and heating.[12] Indeed, various countries with a high capacity for renewables production have issues dealing with surplus energy supplies during times of the day when demand is typically at its lowest.[13] The intermittency of solar power as a result of both the diurnal availability of sunlight and, more broadly, the annual solar cycle can be overcome by storing the electricity and dispatching it on demand to the end user, preferably with the use of inexpensive batteries – which themselves represent an extensive field of research.[14] However, perhaps a more versatile energy conversion that would address the needs of non-electricity demands is the solar-driven production of chemical fuels.[15] In this way, storage of energy within the chemical bonds of an energy-dense compound offers better gravimetric densities than electrochemical storage in batteries.[16]

Biomass, the original "solar fuel", is already used as an energy source in many places, particularly in the developing world. Contrary to common belief, the process of natural photosynthesis is not highly energy efficient, exhibiting maximum solar-to-biomass conversion efficiencies of around 4.5 %.[7] This highlights the key point that the volume of solar energy reaching Earth is such that only a small fraction of it needs to be converted to sustain all life. Nevertheless, biomass is not an ideal energy source for human activities in many ways. Crude biomass has a low energy density, does not burn cleanly and is not suitable as a transportation fuel. Besides being an energy store, it also has value in agriculture and is one of Earth's primary mechanisms for locking up both natural and anthropogenic CO_2 emissions.[17] Relying heavily on biomass would therefore spell the acceleration of dilemmas already faced by those developing countries that use biomass today; for example, a choice between having fuel or having food crops.

Hydrogen production by solar-driven water splitting, on the other hand, has been a highly desired goal for several decades ever since Fujishima and Honda's seminal report in 1972.[18] The starting material – water – is Earth-abundant, while the burning of the fuel – H_2 – produces only water as its single combustion product, therefore providing a carbon-free energy cycle. Going further towards more complex fuels, the prospect of converting anthropogenic carbon dioxide with water into carbon-based fuels, as achieved in natural photosynthesis, is also particularly appealing in view of a world with damaging, rising levels of CO_2 in the global atmosphere, especially when this can achieve liquid fuels that are better suited to current energy infrastructures than gaseous H_2 is.[19] Artificial photosynthesis, or "solar fuels", therefore aims to mimic Nature's systems and achieve highly efficient solar-driven fuel generation from sustainable sources as an economically viable contribution towards solving the global energy crisis.

1.2 Artificial Photosynthesis

1.2.1 Inspiration from Natural Photosynthesis

Natural photosynthesis, while not suitable for meeting all human energy demands, presents us with the blueprints of the process we can mimic and modify to suit our purposes (Fig. 1.1). In biochemical terms, photosynthesis begins with solar photons being absorbed by chlorophyll a pigments in the reaction centre P680 of the enzyme photosystem II (PSII), leading to the generation of electrons and holes. The holes are filled by the oxidation of H_2O, releasing O_2 and protons at the catalytic Mn_4CaO_5 cluster of the oxygen-evolving complex (OEC).[20] This yields the reducing equivalents required to produce photosynthetic fuels; namely, the electrons and protons harvested from the oxidation of water are used to build up NADPH and ATP, which are in turn consumed by the Calvin-Benson cycle for the reduction of CO_2 to sugars.[21]

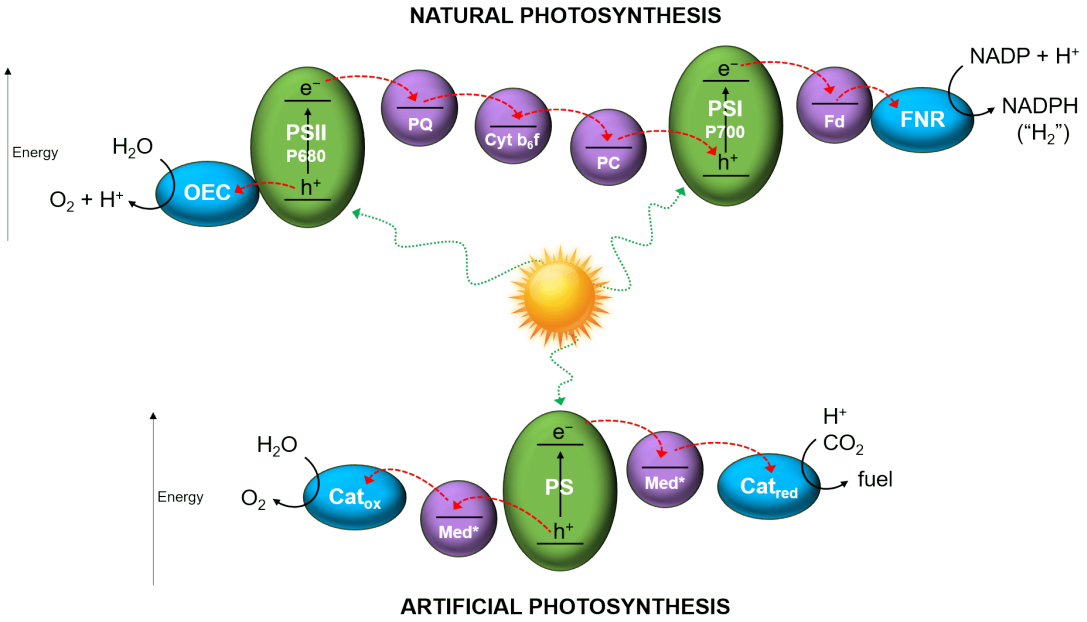

Fig. 1.1 Schematic representation of natural and artificial photosynthesis. OEC = oxygen-evolving complex, PSII = photosystem II, PQ = plastoquinone, Cyt b_6f = cytochrome b_6f complex, PC = plastocyanin, PSI = photosystem I, Fd = ferredoxin, FNR = ferredoxin-$NADP^+$ reductase, NADP = nicotinamide adenine dinucleotide phosphate, NADPH = nicotinamide adenine dinucleotide phosphate hydrogen; Cat_{ox} = oxidation catalyst, Med = mediator (*optional), PS = photosensitiser, Cat_{red} = reduction catalyst.

In fundamental terms, the key stages of natural photosynthesis can therefore be simplified into three steps: light absorption, charge separation, and catalysis,

all of which are achieved in Nature using the molecular portions of enzymes. The required components for an artificial photosynthetic system, in sum, should therefore be able to carry out these three functions. The remainder of this section of the Introduction will first consider the thermodynamics that govern H_2 evolution and CO_2 reduction as two key artificial photosynthetic conversions of interest. Then, the main approaches that can be taken to build these systems will be introduced.

1.2.2 H_2 Evolution and CO_2 Reduction

The H_2 evolution reaction (HER) is most often envisioned as half of the overall water splitting reaction, where the other half, water oxidation (or oxygen evolution reaction, OER), provides both the protons and the electrons required to evolve H_2 (equations 1.1-1.2). Water splitting is a thermodynamically uphill reaction, requiring a theoretical energy input of $237.2\,\mathrm{kJ\,mol^{-1}}$, which, in electrochemical terms, corresponds to a minimum cell voltage of 1.23 V to drive water electrolysis. It is useful to note at this stage that electrolysis never proceeds at this theoretical value, even with the best catalysts, as reaction kinetics and other factors demand for an overpotential (η) beyond this ideal threshold.

The primary challenge for the reduction of CO_2 lies in its chemically inert nature. Due to a large reorganisational energy between the linear molecule and bent radical anion, the direct one-electron reduction of CO_2 is thermodynamically extremely challenging, occurring at $-1.90\,\mathrm{V}$ *vs.* NHE (equation 1.3).[19] In contrast, the multi-electron, multi-proton reduction of CO_2 can be achieved at more moderate potentials (equations 1.4-1.8). Although examples of successful 6-electron and 8-electron conversion into methanol and methane, respectively, have been described, the most common reduction products are carbon monoxide (CO), formic acid (HCOOH) and oxalic acid. An oft-encountered challenge in such conversions is that they can be accompanied by competing proton reduction, as a result of protons being present and the H_2 evolution reaction being kinetically (and, in some cases, thermodynamically) easier. The mixture of CO and H_2 is, however, of commercial interest as it constitutes synthetic gas, or "syngas", used in Fisher-Tropsch chemistry to produce liquid fuels.[22] Nevertheless, due to the large number of possible products, solar-driven CO_2 reduction is a much more multi-faceted conversion than proton reduction as product selectivity can be difficult to achieve.

Table 1.1 Thermodynamic potentials of proton reduction, water oxidation and CO_2 reduction into a variety of products (*vs.* NHE, pH 7, 25 °C, atmospheric pressure).

$2H^+ + 2e^-$	$\longrightarrow$	H_2	$E^\circ = -0.41\,V$	(1.1)
$2H_2O$	$\longrightarrow$	$O_2 + 4H^+ + 4e^-$	$E^\circ = 0.82\,V$	(1.2)
$CO_2 + e^-$	$\longrightarrow$	$CO_2^{\cdot -}$	$E^\circ = -1.90\,V$	(1.3)
$CO_2 + 2H^+ + 2e^-$	$\longrightarrow$	$CO + H_2O$	$E^\circ = -0.53\,V$	(1.4)
$CO_2 + 2H^+ + 2e^-$	$\longrightarrow$	HCO_2H	$E^\circ = -0.61\,V$	(1.5)
$CO_2 + 4H^+ + 4e^-$	$\longrightarrow$	$HCHO$	$E^\circ = -0.48\,V$	(1.6)
$CO_2 + 6H^+ + 6e^-$	$\longrightarrow$	$CH_3OH + H_2O$	$E^\circ = -0.38\,V$	(1.7)
$CO_2 + 8H^+ + 8e^-$	$\longrightarrow$	$CH_4 + H_2O$	$E^\circ = -0.24\,V$	(1.8)

1.2.3 Approaches to Light-Driven Energy Conversion

Device Configuration

Achieving artificial photosynthesis requires consideration of the process on a device scale as well as on a molecular level. Three types of approaches (Fig. 1.2) - photocatalysis, photoelectrocatalysis and PV-electrocatalysis, each with their own advantages and disadvantages - have been disseminated below for water splitting, but similar design principles can be extended to CO_2 reduction systems. It is also noted that these approaches have been discussed in the context of immobilised catalysts, as this is the angle taken for the work described in this thesis. However, very similar considerations would also apply in the case where the catalysts have not been surface-immobilised and are instead present as solubilised species in the electrolyte solution.

(i) Photocatalytic systems. "One-pot" photocatalytic water splitting involves the combination (by dissolution or suspension) of photosensitiser(s) and catalyst(s) in a single medium.[23,24] Electron transfer occurs by close contact between the components, such as during collisions and/or by tethering of one component to the other, with a flow of electrons from donor to acceptor. If only one half-reaction

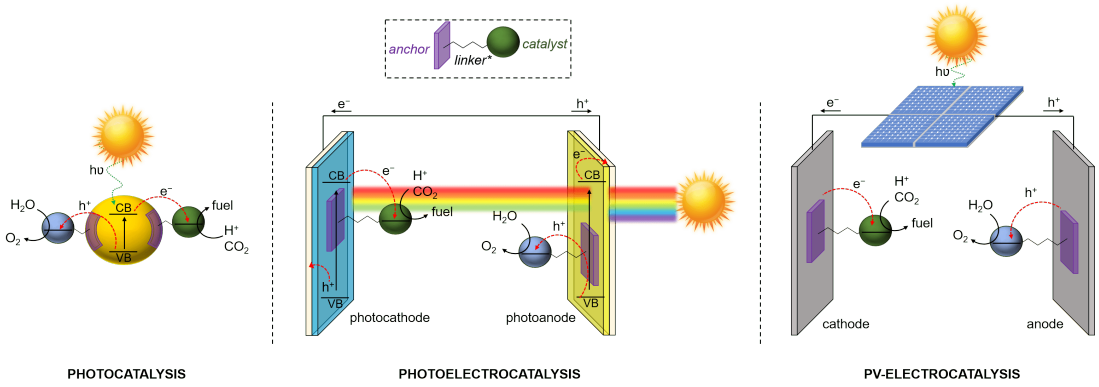

Fig. 1.2 Schematic representation of three possible device configurations towards photochemical energy conversion: photocatalysis, photoelectrocatalysis, and PV-electrocatalysis (*optional).

(*e.g.* proton reduction or water oxidation) is performed in such a system, an additional sacrificial component (electron donor or electron acceptor, respectively) must also be present in solution.[25]

Such a one-pot system benefits from a simple reactor design as all the components are in the same chamber, therefore offering the advantage of potentially low costs as no electrical wiring or expensive conducting substrates are required. However, a significant challenge lies in the fact that both the reduced and oxidised products (H_2 and O_2 in the case of water splitting) are generated in the same compartment, making product separation difficult if they are in the same phase. Further, O_2 can irreversibly damage the proton reduction catalyst, or lead to deleterious short-circuit reactions where the oxidised species is reduced, lowering the overall efficiency. Generating H_2 and O_2 together in the same compartment in significant quantities can also lead to an explosive mixture. Finally, combining all elements in a single vessel can limit the components that can be used together, as they are all required to function under the same conditions.

(ii) Photoelectrochemical systems. Photoelectrochemical (PEC) systems consist of two electrodes submerged in an electrolyte solution and often separated by a proton exchange membrane. In a complete, two-electrode system, the photoanode realises the oxidation half-reaction (*e.g.* water oxidation), generating electrons that travel through an external circuit and arrive at the photocathode, where the reduction half-reaction (*e.g.* proton reduction) takes place.[26–31] Both electrodes consist of a light harvester and a catalyst to carry out their respective reactions, although it is possible to build a system where only one electrode absorbs light and drives the dark electrode of the other half-reaction.[32,33] However, using a single light absorber to drive both half-reactions allows a theoretical limit

of only 12-18 % solar conversion efficiency to be reached, whereas employing dual photoabsorbers – one at the photoanode and one at the photocathode – allows one to use narrower band gap materials, reaching a higher theoretical solar conversion limit of 20-33 %.[34–36]

A PEC approach to artificial photosynthesis carries several advantages. Firstly, spatially separating the two half-reactions into separate compartments prevents the build-up of potentially explosive mixtures, while also facilitating eventual ease of product separation. Both half-reactions can also first be individually studied and optimised independently of one another (in a three-electrode set-up with reference and counter electrodes). Additionally, if the components in the anodic and cathodic compartments have different optimal working conditions, such as pH, then a device with different pH values in the anode and cathode compartments is a possible solution, although this pH gradient must be maintained and would therefore require an additional energy input. Finally, the fact that all components can be isolated onto an electrode surface means that, in view of scaling up such technologies to an industrial future, a shift away from one-pot systems towards PEC systems could enable easier replacement and recycling of these active components during PEC cell maintenance. The work described in this thesis takes the PEC approach towards building solar fuel devices. The components and considerations needed to build such a device are discussed in greater detail in sections 1.3-1.4.

(iii) PV-electrocatalysis systems. Photovoltaic-driven electrolysis systems are arguably the most advanced form of the three types of device configurations described here, as a direct result of both halves of this approach – PV cells and electrolysers – already being well established, commercially available technologies in their own right.[9,37] In such systems, light harvesting and catalysis are physically decoupled, with the PV cells performing the former and electrolysers performing the latter. One obvious advantage of such an approach is that the conditions required for each part to function can be optimised totally independently of the other. For instance, the light harvester is not required to be stable in aqueous conditions – a common struggle when developing PEC systems where the light harvester does need to be submerged in the electrolyte solution. Multiple PV devices can also be connected together in series to generate sufficient voltage to drive the redox reactions.[38] Arguably, the largest improvements to this technology will be made through enhancements in cell design and engineering considerations, as issues of scalability severely limit the widespread implementation of electrolyser technology in general due to large efficiency losses as the cell size is increased.

Depicted in Figure 1.2 (right) is a scenario where in place of an electrolyser is a molecular electrocatalytic system, a configuration that has been proposed and reported.[39–41]

Molecular *vs.* Heterogeneous Catalysts

In choosing a catalyst to perform the redox reactions in a solar fuel device, one has the choice between heterogeneous, material-based catalysts and molecular, metal complex-based candidates. While the former often show high stability, clear disadvantages include opaqueness – which can disallow light absorption by an underlying light-harvesting substrate, unless illumination from the backside is a viable option – as well as a lack of product selectivity, especially in the case of CO_2 conversion.[42–46] Several of the best-performing materials are also based on non-Earth-abundant elements, such as Pt and Ag. Synthetic molecular catalysts, on the other hand, can be designed such that they are based on Earth-abundant elements, and have well-defined active sites that offer an atom efficiency that is unattainable for material-based catalytic films.[47–49] They can also be deposited onto surfaces as transparent monolayers and thereby will not hinder light absorption of any underlying light-harvesting substrate. A crucial advantage of working with molecular systems – and one of the main reasons why research interest in them remains high – is that they also afford the advantage of control over their properties by way of changing key structural features, offering opportunities for one to synthetically tune a catalyst's activity, selectivity and stability. Transition metal complexes often also possess multiple accessible redox states, allowing them to facilitate multi-electron transfer processes such as those required for the reduction of CO_2 into value-added fuels. Some key H_2 evolution and CO_2 reduction catalysts (HECs and CRCs, respectively) are introduced below in section 1.3.2. The work in this thesis employs molecular catalysts to achieve H_2 evolution and CO_2 reduction in a PEC configuration.

One of the biggest drawbacks to molecular catalyst-based systems in contrast to material-based catalysts, however, is the former's lack of durability. On this note, it is important to highlight that maintaining the molecular integrity of the catalytic species is paramount. A difficult and recurring question in molecular catalysis is whether the primary compound is the true catalyst or just a precursor for the true non-molecular active species (often metals or metal oxides) produced *in situ*.[50,51] One must be particularly wary when operating under certain conditions, including strongly oxidising or reducing potentials, strongly acidic or basic media, and in the presence of water. In such cases – indeed in all cases – post-catalysis confirmation

of molecular integrity is vital. To date, experimenters still rarely report evidence of such integrity and long-term performance tests are rarely undertaken beyond a couple of hours. Ideally, the long-term integrity of the molecule must be verified in order for performance claims to be substantiated.

1.3 Molecular Photocathodes towards Solar Fuel Transformations

The desire for the reductive fuel-generating reactions of H_2 evolution and CO_2 reduction to be solar-driven can be married with the benefits of immobilising molecular catalysts onto electrode surfaces by interfacing the molecular catalysts with a light-responsive, p-type semiconducting (*p*-SC) electrode. In doing so, the thermodynamic potential required to drive the catalysts is derived from the light-harvesting electrode's own energetic levels upon light illumination. What results is a photocathode that can be paired with a corresponding photoanode to build a complete photoelectrochemical cell, whereby bias-free complete water splitting could in principle be achieved.

One such approach towards molecular catalyst-based photocathodes has been the modification of wide band gap p-type semiconducting electrodes with a photosensitiser (most often a molecular dye but occasionally a quantum dot) to photo-drive the anchored catalyst, yielding so-called dye-sensitised photocathodes (DSPC). Although the concept of dye-sensitised photoelectrochemical cells has been around for at least half a decade, the development of dye-sensitised photoanodes for molecular-based water oxidation has received much more research attention and literature examples far outnumber those of their photocathode counterparts for reductive transformations.[52–57] This number is reduced even further when one considers only those based on non-precious metal-based complexes. Nevertheless, interest in this DSPC approach for reductive fuel transformations continues to grow, with investigations ranging from devising different co-immobilisation strategies for anchoring both the photosensitiser and catalyst (*e.g.* dye-catalyst molecular dyads)[58–60] to searching for novel p-type semiconductor materials to replace nickel oxide (NiO), the currently ubiquitous but flaw-ridden p-type semiconducting material of choice.[61,62]

An alternative approach to DSPCs is to interface the molecular catalysts with narrow band gap p-type semiconducting materials that are inherently light-absorbing, thereby doing away with the need to incorporate an additional photo-

sensitiser onto the electrode.[26,28,30,31,63] Such narrow band gap *p*-SCs differ from dye-sensitised DSPCs in that photo-absorption and charge carrier generation, separation and conduction are all expected to be performed by a single material in the former, while in the latter, charge carrier conduction (and to some extent, charge carrier separation) is largely expected to be fulfilled by the non-light-absorbing wide band gap *p*-SC onto which the dye has been immobilised. The approach of using small band gap *p*-SCs to build light-absorbing photocathodes (LAPCs) therefore has the advantage over DSPC systems of reducing the number of components in the photocathode system by one.

However, despite the apparent attractiveness of such an architecture, the first example of an immobilised molecular catalyst-based LAPC in solar fuels, published in 1984,[64] was followed by decades of silence, with the remainder of existing examples to date only emerging within the last 8 years. Of these, the number that are based on precious metal-free 3d transition metal complexes and that also operate under aqueous conditions are few. For CO_2 reduction in particular, this number dwindles to zero, owing largely to the fact that the vast majority of successful molecular catalyst-based LAPCs still use precious metal-based CO_2 reduction catalysts. The challenge and scope therefore urgently remain for researchers to continue the non-trivial task of developing such photocathodes that are active and stable for reductive solar fuel transformations. The work described in this thesis is based on this approach, and the remainder of this introductory chapter will summarise its various components (sections 1.3.1-1.3.2), catalyst immobilisation strategies (section 1.4) and the current state-of-the-art systems in aqueous solutions (section 1.5).

1.3.1 Light-Absorbing Semiconductors

Just as the photosensitisers used in both solar fuel photocatalysis and photoelectrode systems have been largely based on photosensitisers inspired by and first developed for dye-sensitised solar cells, the narrow band gap *p*-SCs employed to realise LAPCs for H_2 evolution and CO_2 reduction to date have also been adopted from the solar cell field. From a thermodynamic point of view, it is crucial that the conduction band (CB) energy level of the *p*-SC is not only more negative than the thermodynamic potential for proton or CO_2 reduction for proton- or CO_2-reducing photocathodes, respectively, but must also be more negative than the potential required to drive the molecular catalyst immobilised on its surface (Fig. 1.3). Such a requirement is necessary to increase the chances of successful

electron transfer to the surface-immobilised catalyst and therefore reduce charge recombination rates with holes that reside on the semiconductor's valence band (VB).

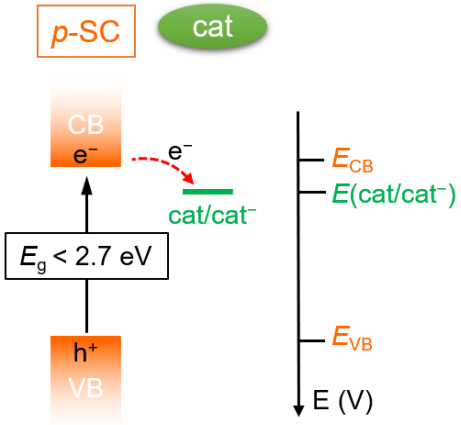

Fig. 1.3 Band diagram depicting energy level requirements for a successful light-absorbing photocathode system. cat = catalyst.

Beyond this, the band gap energy (E_g) of the *p*-SC is also important in determining the energy of wavelengths it is capable of absorbing and, therefore, the proportion of the solar spectrum that can be taken advantage of. Visible and infrared light accounts for more than 95 % of solar irradiation, but will not be absorbed by semiconductors with band gaps larger than 3.1 eV. Further considerations for the band gap must be taken if a tandem photoelectrochemical cell is the final goal. The upper limit of solar-to-hydrogen (STH) efficiency of a tandem PEC cell with a pair of semiconductors (having complementary band gaps of 1.0 and 1.6 eV) is close to 30 %, whereas only 13 % is achievable for a single light absorber PEC cell (with a band gap of 2.2 eV).[34–36]

Figure 1.4 depicts the VB and CB potentials as well as the band gaps of inorganic *p*-SC materials that have been used to date to construct LAPCs with 3d transition metal complexes. Of these, p-type silicon (*p*-Si) has the narrowest band gap (1.12 eV) and can capture photons from a significant portion of the solar spectrum, even those in the infrared (up to 1100 nm).[65,66] Semiconductors of the III-V variety – namely, indium phosphide (InP), gallium phosphide (GaP) and gallium indium phosphide ($GaInP_2$) – also have band gaps appropriate for visible light absorption (1.35 eV,[67,68] 2.26 eV[69] and 1.83 eV,[70,71] respectively).

Although the number of *p*-SC materials that have been successfully used to develop proton- or CO_2–reducing LAPCs is greater than the number of *p*-SCs

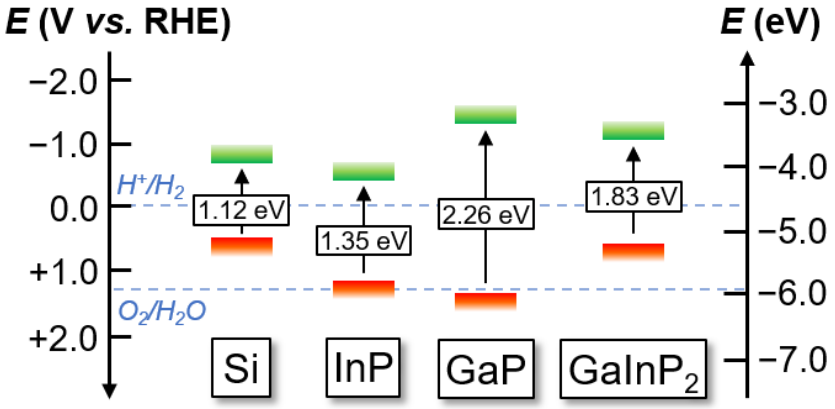

Fig. 1.4 Valence (red) and conduction (green) band potentials for inorganic *p*-type light-absorbing semiconductor materials mentioned in this chapter.

used in DSPCs (the majority of which are based on NiO), this number is still relatively low due in part to the lack of p-type light-absorbing semiconducting materials that have been found to be stable in water – an important prerequisite for operating under aqueous conditions. Specifically, it has appeared to be a challenge to develop *p*-SCs that are tolerant to acidic conditions. Needless to say, in order for the two key components of LAPCs (light harvester and catalyst) to be able to work in concert, any conditions that are found to be acceptable for maintaining semiconductor stability against corrosion must also be compatible with the conditions needed for the surface-immobilised molecular catalyst to operate. This is often why tolerance to at least slightly acidic conditions would be considered an advantage for a *p*-SC material in a proton- or CO_2-reducing context.

Si is inherently unstable in aqueous or aerobic conditions due to the formation of a silica layer, resulting in a passivating, insulating film that renders the region inactive for electrochemical reactions.[72] The most commonly used strategy to overcome this problem for H_2 evolution photocathodes has been to decorate the Si with a thin film of TiO_2 by atomic layer deposition (ALD), prior to catalyst immobilisation (note that none of these catalysts to date have been molecular catalysts).[73–76] Corrosion instability also afflicts In- and Ga-based *p*-SCs and limits their large-scale application for photoelectrochemical solar fuel devices.

In addition to Si, ALD-deposited thin films have also been applied to other unstable semiconductor materials in the context of providing protection against corrosion/passivation under photoelectrochemical hydrogen-evolving/CO_2-reducing conditions.[77–80] However, the number of such examples remains scarce, especially

when only considering molecular-based photocathodes, let alone just those based on non-precious metal-containing metal complexes. Basic prerequisites for any protective film include: (i) transparency in order to permit light to reach the semiconductor below, (ii) the ability to allow charge to pass through, (iii) stability, and (iv) possession of a compatible CB energy level such that an energetic cascade for electron transfer to the catalyst is maintained. Films that have been deposited by ALD are by definition very thin and therefore often meet conditions (i) and (ii) above, but the high cost and energy-intensive nature of this deposition method precludes its scalability to some extent.

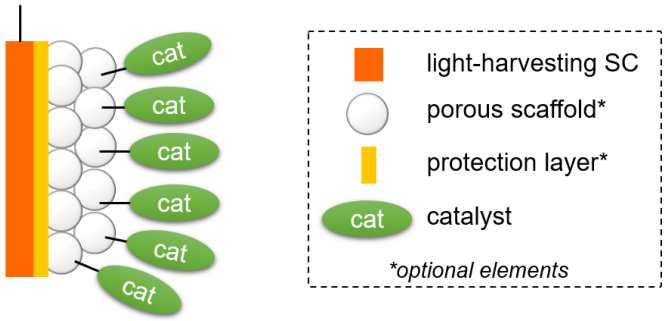

Fig. 1.5 General assembly approach taken to construct light-absorbing photocathodes, where a protection layer and additional porous scaffold are optional elements.

Finally, the *p*-SC must be able to facilitate some form of anchoring mode in order for catalyst immobilisation to be successful. Ideally, this should also allow for a significant number of molecules to be loaded onto the surface to compensate for the kinetic limitations of molecular catalysts, so some form of nanostructuring to introduce a high surface area-to-volume ratio would be beneficial. A general assembly scheme of how this may be achieved in LAPCs is presented in Figure 1.5.

1.3.2 Molecular Catalysts

H_2 Evolution Catalysts

When it comes to H_2 evolution, the noble metal platinum is the 'gold standard'. Operational under a wide range of conditions and highly active at effectively zero overpotential as a result of the optimal Pt-H adsorption energy,[81] Pt has long been used as the benchmark against which to compare the performance of other HECs.[82] However, its scarcity in the Earth's crust (5 ppb) limits any real possibility of scaling up the use of Pt in global energy solutions to the fuel crisis.

Another benchmark HEC exists in the form of naturally-occurring hydrogenase (H_2ase) enzymes, metalloproteins that reversibly catalyse H_2 evolution with near zero overpotential.[83] Various hydrogenases have been successfully incorporated into both photocatalytic and (photo)electrochemical systems,[84–90] but several factors would inhibit deployment of these enzymes in large-scale devices. These include, but are not limited to, their fragility, stringent operating conditions (pH-sensitivity), large 'per active site' size and molecular weight (> 5 nm diameter, 30-100 kDa) and high cost of extraction and purification.[83] Rather, research into the activity of H_2ase enzymes can and does serve to increase our understanding of how Nature's molecular systems can function so efficiently and, subsequently, inspire the design of synthetic catalysts. X-ray crystal structures of the active sites of three principal varieties of H_2ase ([Fe]-,[Fe-Fe]- and [Ni-Fe]-H_2ase)[91–93] reveal key common features across the board: firstly, active sites that are mono- or dinuclear metallic clusters based on 3d transition metal ions, indicating that it is possible to achieve efficient H_2 evolution catalysis with Earth-abundant metals; and secondly, ligands consisting of CO, CN^- and bridging thiolates in addition to basic protein residues.[94] Additionally, the fastest of the three varieties, [Fe-Fe]-H_2ase, also features a flexible bridgehead nitrogen atom – effectively a pendant amine group - believed to act as a proton relay to the metal centre (Fig. 1.6a).[95]

Numerous synthetic analogues of both the [Fe-Fe]- and [Ni-Fe]-H_2ase active sites have been prepared but were found to have large overpotentials and poor water solubility and stability, leading to disappointing electrocatalytic activity in a variety of configurations.[96–100] The only exceptions for better performance emerged when the enzyme mimic was incorporated into an apoprotein that had been depleted of its active site.[95,101] These results point to a key limitation in the biomimetic approach: that the entire protein structure is, more often than not, necessary in order for the active site's stability and activity to be maintained. Rather than try to precisely replicate the active site of naturally-occurring systems, an alternative approach would be to take the broader lessons learned from studying such enzymes and apply them when designing synthetic metal complexes. In this particular case of drawing inspiration from H_2ase to design HECs, what has resulted as a common motif from such efforts are metal complexes consisting of first-row transition metal ions (such as Fe, Co and Ni) with robust π-accepting ligand frameworks incorporating proton relays through the inclusion of pendant bases. The designs of two of the most widely-studied and successful classes of HECs, Co-centred cobaloximes and Ni-centred bis(diphosphine)s, follow this theme. They have been introduced in greater depth below.

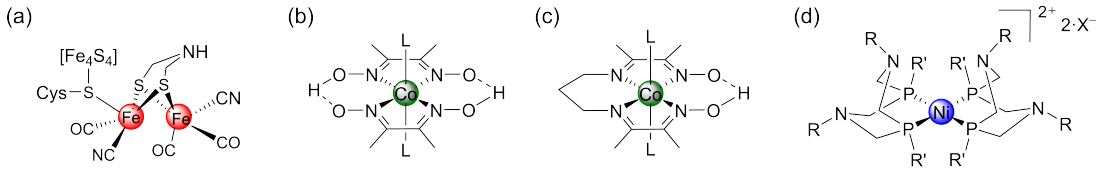

Fig. 1.6 Structures of key hydrogen evolution catalysts: (a) active site structure of [Fe-Fe]-hydrogenase, (b) cobaloxime, (c) cobalt diimine-dioxime, and (d) Ni(II) bis(diphosphine).

Although their synthesis was first reported in 1907, the catalytic activity of cobaloximes was not reported until 1964, when Schrauzer and co-workers demonstrated their use as vitamin B12 models.[102] Espenson and co-workers presented the first example of proton reduction in organic media using cobaloximes almost 30 years ago,[103] although reduction of aqueous protons only began to emerge much later in 2008.[104–106] Today, cobaloximes stand amongst the most commonly employed catalysts in electro- and photocatalytic H_2-evolution schemes.[107–109]

The general structure of a cobaloxime consists of a Co centre with two equatorial glyoxime ligands and two trans axial ligands (Fig. 1.6b). The equatorial ligands incorporate proton relays in the two hydrogen-bonded O-H-O bridges, and stabilise oxidation state changes occurring at the Co centre, enabling the complex to switch between Co(III)/Co(II)/Co(I) states. The Co(I) species is highly nucleophilic, and is the site of protonation to form the catalytically-active Co^{III}-H species.

The attraction that cobaloximes hold as proton reduction catalysts lies with a number of reasons, the most notable of which are as follows: they operate catalytically in aqueous solutions; they are synthetically facile to prepare and modify; they are among the very few synthetic catalysts that have been reported to be O_2-tolerant[110–112] – an important consideration for their use in full water splitting systems; and they possess low overpotentials for H_2 evolution.[113,114] However, their performances have been hindered by a lack of stability arising from both their equatorial diglyoxime ligand framework being subject to hydrogenation, as well as their axial ligands – which have been found to strongly influence turnover frequencies – being labile during catalysis.[115,116] Replacing one of the oxime bridges with a propanediyl bridge yields a class of related catalytic compounds, cobalt diimine-dioximes (Fig. 1.6c), that are more stable than cobaloximes against hydrolysis under acidic conditions,[117] but that possess greater overpotentials towards the HER as a result of losing one of the proton-relaying O-H-O bridges.[116] Further modifications to cobaloximes are also possible at the oximes' α-substituents and at the axial positions. For instance, pyridine ligands have been investigated as axial ligands and found to improve the basicity of the Co^{III}-hydride formed during

the catalytic cycle, thereby allowing for the final protonation step to be favoured and leading to overall improved catalytic activity.[113,116,118] Modifications at both equatorial and axial positions have also been made to introduce anchoring modes that would enable the immobilisation of cobaloximes onto a variety of surfaces towards both colloidal and electrode-based systems.[80,106,119] One example of a cobaloxime that was designed to incorporate several of the above functionalities is **CoP^3**, where the equatorial ligand contains both a phosphonic acid anchor group as well as a pyridine, the latter of which binds to the Co centre at the axial position (Fig. 1.7).[120]

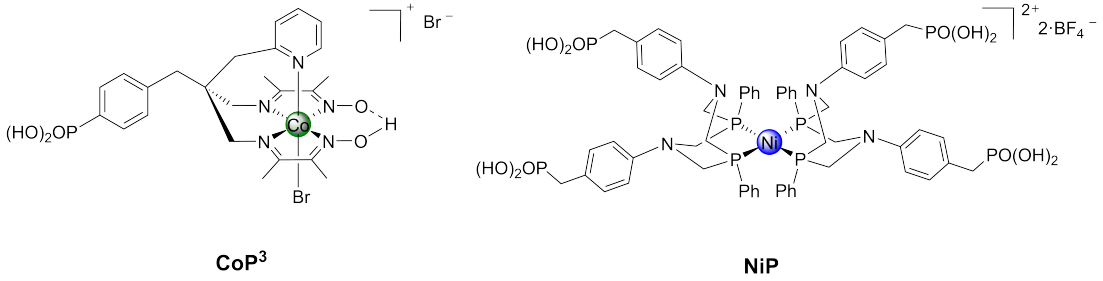

Fig. 1.7 Structures of **CoP^3** and **NiP**, two molecular hydrogen evolution catalysts used in the work described in this thesis.

Arguably the benchmark when it comes to molecular HECs, the Ni(II) bis(diphosphine) ($[Ni(P_2N_2)_2]^{2+}$) series of complexes possess a ligand framework that have long been known[121] but were only pioneered as electrocatalysts by DuBois and co-workers in the 2000s.[122] These complexes incorporate a Ni centre with two macrocyclic 1,5-diaza-3,7-diphosphacyclooctane (P_2N_2) ligands (Fig. 1.6d), and have been shown to reach a turnover frequency (TOF) of 720 h^{-1} at an overpotential of 300 mV.[122] The key to their remarkable catalytic activity lies in the combination of having pendant non-coordinating amines and flexibility in the ligand framework. The latter aspect allows the former to act as proton relays for the Ni centre and in this way facilitate inter- and intramolecular proton/hydride exchange.[123,124] The N and P functions also offer the possibility to modulate catalyst characteristics by substitution at these sites. For instance, studies of these complexes had been almost exclusively performed in organic solvents with strong acids as proton sources as a result of their insolubility in water,[125–127] but incorporation of a phosphonic acid into the ligand framework yielded the water-soluble Ni bis(diphosphine) catalyst **NiP** (Fig. 1.7), rendering studies in aqueous conditions possible.[128] Although $[Ni(P_2N_2)_2]^{2+}$-type catalysts are inhibited by O_2, they have been shown to be highly tolerant to CO, which has positive implications for their potential use in syngas generation.[111]

In addition to the above two classes of molecular catalysts discussed, other ligand frameworks that have been employed with Co and Ni centres to build HECs include polypyridines, porphyrins, cyclams and thiolates.[129,130] Although a deeper discussion of these catalysts is beyond the scope of this thesis, their existence points to a thriving community intent on achieving ever more efficient and active H_2-evolving molecular electrocatalysts.

CO_2 Reduction Catalysts

The electrochemical reduction of CO_2 on a metal was first demonstrated as early as 1870.[131] Researchers have since then evaluated a wide range of polycrystalline metals as CO_2-reducing electrode materials, including the likes of Ag, Au and Cu.[132–134] Unlike in the case of H_2 evolution where Pt is a clear benchmark, however, no single CO_2-reducing heterogeneous polycrystalline metal has been identified as a clear winner among others in terms of its energetic efficiency (overpotential requirement) and product selectivity. In Nature, two examples of enzyme classes that reduce CO_2 are carbon monoxide dehydrogenases (CODHs) and formate dehydrogenases (FDHs), which perform the reversible interconversion of CO_2 with CO and formate, respectively, extremely efficiently. For both CODHs and FDHs, classes exist where the enzymes contain transition metals in their active sites – Fe, Ni, Cu and Mo for the former,[19] and Mo and W for the latter.[135] In addition, clusters – often [Fe-S]-based – are present to both hold the transition metal active centre in place as well as serve as an electronic buffer that stabilises the charges on the active centre during the catalytic cycle.[136,137] Several groups are also within hydrogen bonding distance. Although a few attempts have been made to closely mimic the active sites of these enzymes, few have proven to exhibit notable reactivity towards the desired reaction,[138–140] further emphasising the difficulties in creating a working mimic of biological systems.

As had been discussed with the case of HECs above, metal complex CRCs have also been successfully synthesised by taking away the key learnings made through understanding naturally-occurring CO_2 reduction metalloenzymes. For example, ligand systems should be able to act as electron reservoirs and/or simply facilitate the stabilisation of electron density from the reduced metal centre during the catalytic cycle. A free coordination site for the CO_2 substrate molecule to approach the transition metal is also key, and this can be facilitated by protons in neighbouring functionalities. In all, a winning strategy for efficient CO_2 reduction must involve simultaneous multi-electron transfers and catalytic sites that direct nuclear configurations of reactants favourably for product formation.[19] After this,

themes similar to those that occurred in HEC research also arise here when aiming for better catalyst design, especially when it comes to ligand variations and how they can induce steric, electronic and other effects on the overall complex and its ensuing performance.

A wide range of ligand families together with transition metals have been employed over the years towards the synthesis of metal complex CRCs.[47,141] Core ligand types include polypyridyls, phosphines, cyclams, and aza-macrocyclic ligands, as well as porphyrins, phthalocyanines and related macrocycles, while transition metals ranging from the 1st to the 3rd row have been utilised at some stage with varying degrees of success, although the best performing molecular CRCs were for a long time - and continue to be - based on precious metals like Ru and Re. In the design of both the complexes themselves and the experimental conditions under which they are placed to carry out CO_2 reduction, one notable theme that has emerged regardless of the metal and the ligand type has been the inclusion of weak Brønsted or Lewis acids. These acids are thought to serve two possible purposes: to stabilise the primary CO_2 adduct, and to help the cleavage of the C-O bond leading to formation of, say, CO.[141] This effect can be achieved by either adding a weak Brønsted acid directly into the operating electrolyte solution,[142–144] or by installing acid functionalities on the ligand framework itself such that they are within sufficient vicinity of the metal centre and can act as an internal proton source.[145–147] In a similar manner, it has been shown that incorporating pendant, "protonable" NH base groups on the ligand framework can introduce a proton responsivity and hence increased stability of the metal-CO adduct *via* these protonated amines.[148,149] In fact, a Fe-porphyrin complex with four charged trimethylanilinium groups along with a large concentration of phenol added into the electrolyte solution was recently reported to have unprecedented catalytic efficiency towards CO_2 reduction, and stands today as one of the benchmark molecular catalysts to beat in homogeneous conditions (Fig. 1.8a).[150]

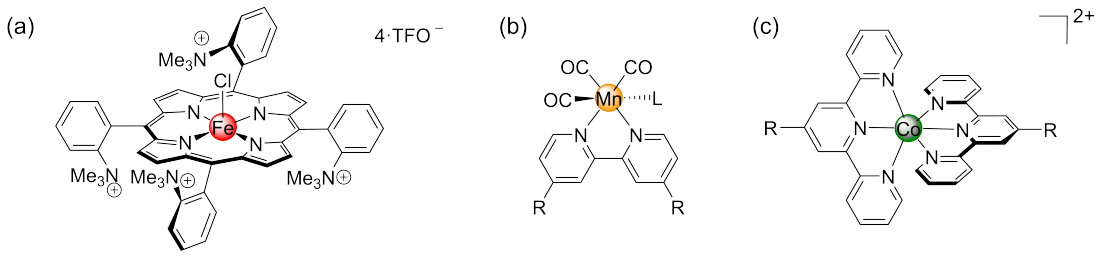

Fig. 1.8 Structures of key CO_2 reduction catalysts: (a) recently described benchmark Fe-porphyrin catalyst,[150] (b) Mn-bipyridine tricarbonyl, and (c) Co bis(terpyridine).

In addition to the above ligand modifications, other desirable alterations are those that lead to increased solubility and functionality in aqueous solutions. At present, the vast majority of molecular CRCs work only in aprotic solvents,[151] while any foreseeable application for such catalysts in devices that carry out artificial photosynthesis on commercially relevant scales would need water-compatibility as a prerequisite. This is especially true if the cathodic CO_2 reduction half-reaction is to be paired with an anodic half-reaction such as water oxidation. To this end, the introduction of charged functionalities (acids and bases) onto the ligand framework have been shown to achieve increased catalyst functionality in water.[152,153] Ni(II) cyclams are also a rare example of a class of molecular catalysts that operate in aqueous conditions for selective CO_2 reduction.[47]

One of the broadest and most diverse class of ligands – and the one under which the catalysts used in thesis fall under – is that of polypyridyls.[154] To mediate the multi-electron, proton-involving transformations necessary for catalytic CO_2 reduction, molecular catalysts must have the ability to store multiple reducing equivalents. This can be achieved either by reducing the metal centre, which then necessitates a ligand field capable of stabilising the reduced metal ions, or by reducing the ligand scaffold itself, with the metal serving as a mediator for electron relay. In this context, polypyridine ligands have been proven appropriate to support catalysts for CO_2 reduction as they offer the ability to not only stabilise the reduced metal centres but also to accept reducing equivalents within the ligand π system, allowing for the storage of multiple reducing equivalents across the entire molecule.[155–157]

Parent polypyridine ligands include bipyridine (bpy), terpyridine (tpy), quaterpyridine (qtpy) and phenanthroline (phen). The seminal work of Sauvage/Lehn using $Re(X)(bpy)(CO)_3$ for photocatalytic and photo-assisted CO_2 reduction to CO is among some of the earliest developments of molecular CRCs in general.[158] Many more followed in the 1980s and 1990s but the field was revitalised in the 2010s with a particular focus on 1st row transition metals. For instance, the CO_2 reduction catalytic activity of Mn analogues of the aforementioned Re "Lehn-type" catalysts were reported in 2011 by Deronzier and collaborators (Fig. 1.8b), and followed up by mechanistic investigations of these complexes.[143,146,159–161] Fe, Ni, Cr and Cu polypyridyls have also all been studied for their CO_2-reducing capabilities to varying degrees.[154]

Of most relevance to the context of this thesis are Co polypyridyls, in particular Co terpyridines (Fig. 1.8c). The first Co polypyridyl complex catalysing CO_2 reduction was reported by Lehn and Ziessel in 1982.[162] Rather than synthesise

discrete molecular species, variable concentrations of $CoCl_2$ and bpy were added in a mixture and assumed to form Co-bpy complexes *in situ*. Upon varying the ratios of $CoCl_2$:bpy, the general trend was observed wherein larger amounts of additional bpy ligand significantly decreased the amount of CO produced but increased production of H_2. This report was the first indication that Co polypyridyls could be potentially used in catalytic systems for CO_2 reduction and, further, possibly generated in straightforward *in situ* processes. This was followed by reports on pre-synthesised Co polpyridyl complexes of varying denticities and their electrochemistries, indicating a strikingly high degree of versatility of Co polpyridyl sytsems as CRCs.[163–165]

Renewed interest in the $[Co(tpy)_2]^{2+}$ platform prompted further mechanistic studies by Fontecave and co-workers. Using *N,N'*-dimethylformamide (DMF):H_2O mixtures as the solvent, the observation of reversible one-electron waves at half-wave potentials ($E_{½}$) of -0.17 and $-1.17\,V$ *vs.* Fc^+/Fc corresponding to the $Co^{III/II}$ and $Co^{II/I}$ redox couples, respectively, as well as two ligand-based reductions at -2.03 and $-2.46\,V$ *vs.* Fc^+/Fc was confirmed.[166] Cathodic current enhancements at the $-2.03\,V$ *vs.* Fc^+/Fc wave in CO_2-saturated solutions were observed, alongside CO_2 reduction products after performing controlled potential electrolysis (CPE), suggesting that the complex required ligand reduction before entering its catalytic cycle. Notably, the only carbon-containing product reported was CO, alongside varying ratios of H_2. No CH_4, formaldehyde or even formate were detected above background levels. The ratios of CO and H_2 produced could be tuned by varying the applied potential during CPE. Mixing varying ratios of $CoCl_2$ and the tpy ligand – in a manner reminiscent of the previous study described by Lehn and Ziessel – also resulted in varying product selectivities, presumably due to the formation of increasing amounts of mono(tpy) species as the $CoCl_2$:tpy ratio decreases from 1:2 to 1:1.[166] Ligand modifications at the positions para to the nitrogen with withdrawing and donating groups also allowed for tailoring of the electronic structure of these complexes and, consequently, product selectivity once again.[167]

1.4 Immobilising Molecular Catalysts

1.4.1 General Considerations

The term 'immobilise' is defined here as the use of physical or chemical means to prevent a molecule (the catalyst) from freely diffusing away from a surface

(the electrode). The immobilisation of molecular catalysts onto surfaces towards (photo)electrodes active for solar fuel transformations has been achieved in a variety of manners. In many cases – perhaps with the exception of incorporating the molecular catalysts into an external matrix like a Nafion® membrane – this requires the chemical modification of the catalyst's ligand framework with appropriate moieties that would facilitate surface immobilisation in either a non-covalent or a covalent mode. The choice of these anchoring moieties depends first and foremost on the surface on which catalyst immobilisation is envisioned. In the context of photocathodes, the vast majority of these surfaces have been inorganic semiconductors, including metal oxides and non-oxide group III-V/group IV type semiconductors, as mentioned in section 1.3.1. The method by which catalysts can be immobilised on these surfaces have therefore had to take into account the characteristics and surface chemistries of these semiconductors.

An important prerequisite is the catalyst's ability to anchor onto the semiconductor surface in such a way that the construct remains stable for long periods of time under catalytic operating conditions. The act of catalyst immobilisation should in effect be innocent in that it should not hinder the complex's ability to catalyse the desired reactions. In this context, one notable difference between narrow band gap semiconductor-based LAPCs and, say, wide band gap semiconductor-based DSPCs is that the anchoring mode must allow for efficient charge transfer to occur between the semiconductor surface and the molecular complex in the former, whereas charge transfer between the co-adsorbed photosensitiser and the catalyst is most important in the latter. In fact, charge transfer between the semiconductor surface and the molecular catalyst should be avoided in DSPCs as it could lead to undesired charge recombination between the reduced catalyst and holes in the *p*-SC VB. With this in mind, and knowing that electron transfer is affected by distance, a long linker on the molecular catalyst could be beneficial in DSPCs, while the opposite – a shorter linker – might be desired in LAPCs. The effect of linker length on the kinetics of charge separation and recombination in semiconductor-molecular catalyst hybrid photoelectrodes is important, as has been demonstrated by an extensive case study on the interfacial electron transfer dynamics of a series of immobilised TiO_2|cobaloxime systems.[168] Here, it was revealed that the electron transfer rate from the semiconductor to the attached cobalt catalyst was exponentially dependent on the distance between the TiO_2 and the metal centre.

The most widely-adopted approaches – and their respective advantages and disadvantages – for molecular catalyst surface immobilisation specifically onto

inorganic semiconductors for reductive solar fuel transformations will be considered below. Then, taking a broader view beyond photoelectrodes, this will be followed by a brief highlight on some benefits that could potentially (and have been reported to) arise from the surface immobilisation of catalysts in general.

1.4.2 Strategies for Immobilising Catalysts on Semiconductors

A large number of examples where molecular catalysts were immobilised on inorganic semiconductors have seen the metal complexes interfaced with a metal oxide surface, whether the latter is the light-absorbing semiconductor itself or simply a conduit for electron transfer from the underlying light absorber (*e.g.* a protection layer). The majority of the anchoring groups utilised for anchoring both molecular catalysts and photosensitisers onto metal oxides to build LAPCs and/or DSPCs were originally developed and studied for dye immobilisation in dye-sensitised solar cells (DSSCs), and later adopted to build photoanodes and photocathodes towards solar fuel synthesis. To this end, a large number of chemical functions have been described to allow the grafting of photosensitisers and/or catalysts onto metal oxides, including carboxylic acids, phosphonic acids, organosilanes/silatranes, hydroxamic acids and acetylacetone.[169–175] Each present their own set of pros and cons in terms of stability, surface coverage, electronic properties, and the synthetic effort required to introduce them onto the dye/catalyst, but all share a common reliance on the formation of metal-oxygen bonds between the surface's metal atoms and the anchoring group's oxygen atoms.

Among these different anchoring moieties, carboxylic acids and phosphonic acids stand out both in terms of being the most widely applied for solar fuel photoelectrodes, but also in terms of being the only ones to be adopted for specifically catalyst anchorage onto metal oxides towards reductive fuel transformations. Although studies on the binding modes and stability characteristics of carboxylates and phosphonates have been conducted mostly in the context of dye immobilisation, some general lessons can nevertheless be applied to the context of reductive catalysis.[171,176]

For both carboxylates and phosphonates, anchoring onto metal oxides is believed to occur *via* condensation reactions involving the incoming acid moiety and hydroxyl groups that exist on the surface of the metal oxide, resulting in a covalent interaction between the metal oxide surface and the bound molecule.[174] Hydrogen bonding between the acid groups and surface oxides is also possible, but would not

be expected to impart as strong a bondage as a covalent interaction would. Studies have suggested that carboxylates can form monodentate, chelating or bidentate bridging binding modes to a metal oxide surface, with the bidentate mode being most preferred (Fig. 1.9a).[177–179] Experimental evidence for this understanding exists in the form of Fourier-transform infrared spectroscopy studies, where loss of the discrete C=O stretching mode in the spectra upon surface binding indicates bidentate binding.[180] Phosphonic acid anchoring groups have also been shown to be capable of a variety of binding modes (Fig. 1.9b).[181] Mono-, bi- and tridentate modes are thought to be possible,[178] with bidentate being the one most often proposed, especially when the metal oxide is classified as a poor Lewis acid.[171] However, contradictions exist in reports, suggesting that there is disagreement on the exact nature of this bidentate mode. For instance, the disappearance of the P=O stretch in the IR spectrum of TiO_2-bound bipyridine- and porphyrin-based dye complexes has been observed and would suggest binding of the phosphoryl group to the metal surface,[174,178] while other reports have observed the retention of this P=O stretching mode and diminishments of only the P-O-H absorptions.[182] The relevant conclusion in both cases is most likely that surface modification conditions can affect the binding modes that result on the oxide surfaces.[183,184]

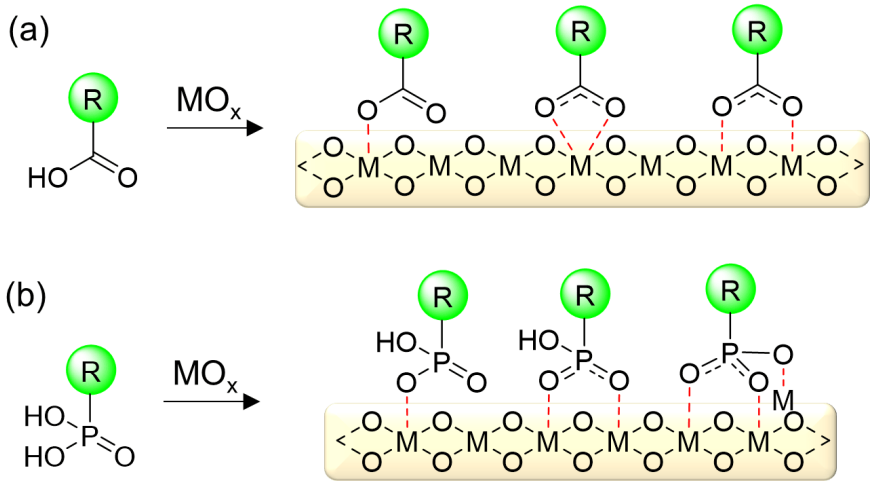

Fig. 1.9 Surface binding motifs for molecules onto metal oxides (MO_x) using (a) carboxylate anchoring moieties, through monodentate, chelating or bidentate binding modes, or (b) phosphonate anchoring moieties, through mono-, bi- or tridentate modes.

The widespread adoption of carboxylic acids to anchor dyes for DSSCs has been ensured by this moiety's facile synthesis and ability to facilitate fast electron transfer. The latter is made possible by the enhanced electronic coupling from the carboxylate anchor to a metal oxide like TiO_2, where sp^2 hybridisation of the acid favours electron delocalisation.[171] While such attributes are important in

the context of DSSCs, photoelectrochemical cells operated in aqueous conditions require robust anchoring of the catalyst molecules, something that carboxylates are widely known to be able to achieve only under low pH conditions (< 4).[178,185] One key attraction of using phosphonates over carboxylates, therefore, is the former's increased resistance to hydrolysis at higher pH values (up to 7), opening a wider window in which these devices can be operated in aqueous conditions.[186–188] The strength of these covalent bonds means that removal of phosphonates from the surface would typically require either harsh basic conditions that dissolve the metal oxide or plasma etching.[189,190]

Besides the covalent binding interactions afforded by the acidic moieties described above, the only other approach that has been employed for catalyst immobilisation on semiconductor electrodes has been the deposition of polymeric films that incorporate the electrocatalysts. This approach has been widely adopted for the grafting of molecular catalysts onto conductive substrates, most notably carbon-based electrodes, for a wide variety of redox transformations even beyond the realm of solar fuels.[191–199] In most of these cases, *in situ* polymerisation onto the electrode surface – as opposed to pre-forming the polymers prior to immobilisation – was most common. Such conducting substrates are particularly amenable to electropolymerisation techniques because they are not limited in the electrochemical potential that they need to deliver to induce such processes. In contrast, the requirement for an electrochemical polymerisation process could preclude use of light-absorbing semiconducting electrodes that may either prevent the application of the required potential if it lies within the semiconductor's band gap, or lead to competitive degradation of the photoelectrode material itself.

Nevertheless, there exist a few cases where a polymerised electrocatalyst has been immobilised on an inorganic semiconducting electrode. In many cases, the interaction between the polymeric film and the underlying substrate has been non-covalent in nature, whereby catalyst immobilisation is assumed to be achieved primarily by the polymer film's robustness and insolubility into the surrounding electrolyte solution. On metal oxide surfaces, this method has been employed only for dye-sensitised water oxidation photoanodes, but these reports serve as elegant depictions of how a polymeric overlayer can achieve both catalyst and substrate stabilisation.[200–203] In these recent examples, vinyl groups on both the dyes' and catalysts' ligand frameworks were polymerised through oxidative and reductive electrochemical processes. Polymerised electrocatalysts forming non-covalent interactions with the underlying substrate have also been employed in the context of CO_2 reduction, where the ligands of Ru bipyridine catalysts formed

part of polypyrrole backbones.[204] This methodology was extended onto non-oxide semiconductor surfaces, including GaP and InP (see section 1.5.2 below).

In addition to non-covalently interacting polymers, covalently-attached polymers of electrocatalysts have also been prepared on non-oxide semiconductors in a limited number of examples. Making use of a wide body of work in which molecules were covalently grafted directly onto surfaces such as Si, GaAs and GaP for the purposes of preventing oxide formation,[205–209] polyvinylpyridine and polyimidazole polymers were covalently grafted onto GaP surfaces *via* UV-induced polymerisation. These polymers bore pyridine-containing functionalities that served as attachment points for cobaloxime and Co/Fe porphyrin catalysts, yielding photocathodes that were active for H_2 evolution. This body of work is described in greater detail below in section 1.5.1.

1.4.3 Benefits of Catalyst Immobilisation

The general advantages of taking a photoelectrochemical approach over a homogeneous, one-pot solution set-up were briefly discussed above in section 1.2.3. Beyond these, another practical consideration to make when immobilising molecular catalysts is that attaching them to an electrode surface ensures they are constantly under catalytic turnover during an experiment, and therefore enables *in operando* and post-catalysis characterisation by electrochemical means. If in a homogeneous configuration, dynamic electrochemical techniques such as cyclic voltammetry only sample molecular species within a thin film in the vicinity of the electrode surface, thereby limiting the amount of sample under consideration to that which can diffuse into this small volume on the timescale of the experiment.[210] Therefore, performing exhaustive electrocatalysis to understand the stability of the catalyst under such circumstances would be challenging, since most catalyst molecules will spend most of the experiment away from the electrode, not undergoing turnover, and possibly experiencing competing degradation processes. Further, *in situ* or *ex situ* spectroscopic characterisation of the bulk solution therefore would not give representative information about the molecules subjected to electrochemical potential. Benchmarking and mechanistic investigations can therefore be greatly facilitated by catalyst immobilisation. From a performance point of view, diffusional limitations are also removed and the efficiency of electron transfer is increased, allowing the catalyst to collect the multiple electrons required in time to perform the desired reaction.

Another general benefit to catalyst immobilisation is that the catalyst no longer needs to be soluble in the reaction medium. This is especially pertinent towards operating molecular catalysts in favoured aqueous conditions when they are not themselves soluble in water. Reports have emerged where the catalyst was not operable in homogeneous aqueous conditions but could take advantage of being immobilised on an electrode surface to access such aqueous working environments.[63,211–213]

In addition to the above, a number of key benefits have arisen from the literature that illustrate how the catalytic performance of molecular systems towards both proton and CO_2 reduction can be enhanced *via* surface immobilisation means, without modifying the catalytic core itself. Using select examples as demonstrations, these benefits specifically from the perspective of the catalysts will now be briefly highlighted, with the aim of illustrating how immobilisation can provide opportunities for their enhanced performance compared to when they remain in homogeneous configurations.

One key thematic that has emerged among some works has been the realisation that immobilisation can open possibilities to mimic the active site of enzymes by providing an environment for the molecular complex that is conducive towards efficient catalysis. As discussed above in section 1.3.2, the active sites of enzymes have served as inspirations for the design of proton- and CO_2-reducing molecular catalysts, but these small molecular catalytic cores – especially when in solution – often do not perform anywhere near the levels observed for Nature's enzymes. An understanding of this discrepancy can be found when we consider the fact that during their catalytic cycles, enzymes rely upon chemical structures extraneous to their active site. Often, substrates and electrons need to be efficiently conveyed to and from the active site using gas channels and electron relays. Synthetic catalysts that have been rationally designed to mimic the active core of enzymes might contain useful appendages in their primary, immediate coordination sphere but thereafter lack helpful units at further vicinities. Immobilising them onto surfaces can remediate this by achieving certain beneficial environments for the metal complexes and therefore be a step towards mimicking the pocket in which the active site of enzymes reside.

In several cases, this environment has been achieved by means of incorporating the catalyst into a polymer framework which is in turn immobilised onto an electrode surface. For instance, Pickett and co-workers immobilised a di-nuclear Fe complex that mimics the active site of [Fe-Fe]-hydrogenases onto an electropolymerised polypyrrole film on glassy carbon, where the intention was for the

conductive polymer to aid electron transfer to the catalyst much like Fe-S clusters do in hydrogenases.[214] McCrory and co-workers deposited a CO_2-reducing catalyst onto a polymeric film – cobalt phthalocyanine (**CoPc**) in polyvinylpyridine (PVP) on a graphite electrode (Fig. 1.10) – and found markedly improved catalytic performance when compared to polymer-free **CoPc**, which, by itself, is an unremarkable catalyst that displays poor selectivity and relatively low activity for CO_2 reduction over competing proton reduction.[215] In this work, elegant and extensive studies were carried out to deconvolute two possible effects of incorporating **CoPc** into the PVP film and both were eventually found to act in synergy to give rise to the enhanced performances observed. Namely, (i) individual pyridine residues of PVP can coordinate to the square planar cobalt centre of **CoPc**, which helps because axial coordination of pyridine has been implicated in enhanced CO_2 reduction activity for **CoPc** and cobalt porphyrin catalysts;[193,216,217] and (ii) the high concentration of uncoordinated pyridine residues throughout the PVP film that, when protonated in acidic solution, may enable secondary coordination sphere effects, such as hydrogen bonding interactions that stabilise activated intermediates, as well as outer sphere effects like making protons available around the catalyst's active site (Fig. 1.10).

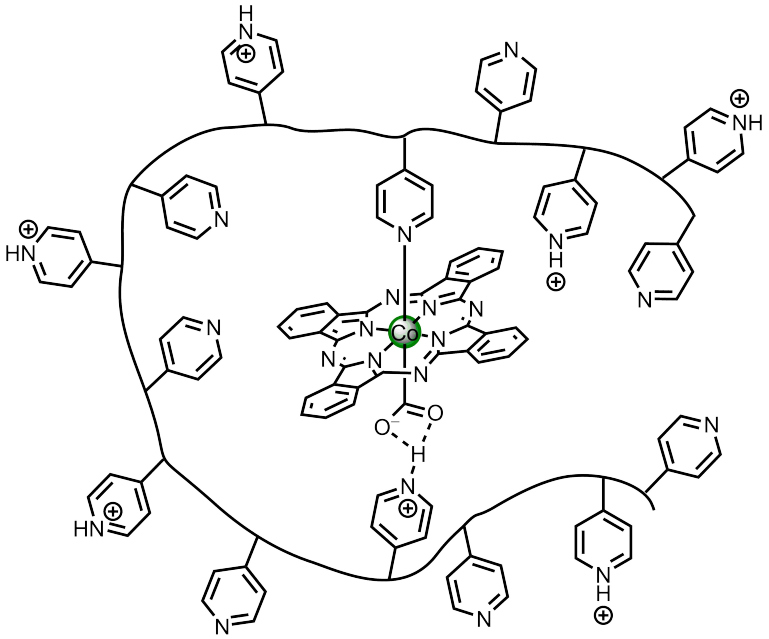

Fig. 1.10 Schematic representation of a molecular cobalt phthalocyanine CO_2 reduction catalyst immobilised in polyvinylpyridine, as described by McCrory and colleagues.[215]

Koper and colleagues investigated the effect of encapsulating a CO_2-reducing indium protoporphyrin catalyst into different types of polymer membranes on

a carbon substrate, and came to similar conclusions to those of the previously mentioned work by McCrory.[218] Namely, in comparison to the polymer-free catalyst, the catalyst's encapsulation in a variety of polymer membranes enhanced selectivity and activity. For instance, the presence of aromatic building blocks in PVP and poly(3,4-ethylenedioxythiophene) polystyrenesulphonate (PEDOT:PSS) polymers was believed to facilitate axial coordination to the indium metal centre by electron donation. The only exception was when the catalyst was embedded into a Nafion® membrane, where the high concentration of protons was presumed to negatively affect product selectivity. In addition to underscoring the importance of the chemical structures of the polymers, different conducting substrates and pre-treatments of these substrates were also found to heavily influence selectivity and stability outcomes, independent of polymers immobilised on them. This further demonstrates that immobilisation is often not an inert act in itself, and that the surface chemistry and environment can play definitive roles in a catalyst's subsequent performance. This all adds to the toolbox at our disposal for fine-tuning the performance of immobilised molecular catalysts.

In addition to flat surfaces, polymers have also been used to immobilise molecular catalysts into porous structures. In our group, we demonstrated that immobilising a cobaloxime as part of a polymer framework (**pPyCo**) onto a carbon nanotube (CNT) scaffold yielded enhanced proton-reducing performances as compared to when a non-polymeric, analogous molecular cobaloxime (**PyCo**) was deposited onto CNTs (Fig. 1.11).[107] This was achieved by the rational selection of co-monomers on the polymer that accompanied the catalytic core: a pyrene-containing co-monomer to ensure robust anchoring onto the CNT *via* π-π stacking, and an ethylene glycol-containing co-monomer to both improve polymer solubility and provide a hydrophilic environment beneficial towards H_2 evolution in the vicinity of the cobaloxime core. As a result of this, the polymeric hybrid electrode displayed a catalytic activity four times higher and twice as stable as compared to its monomeric counterpart. This demonstrated the proof-of-concept that tuning the catalyst's environment (outer coordination sphere) instead of the active catalytic centre (first coordination sphere) is a viable strategy to improve catalytic performances. In addition, both the monomeric and the polymeric cobaloxime maintained reasonable performances under the presence of air. This stability under such demanding atmospheres was thought to be attributed to the CNT matrix itself effectively acting as a protective shield and reducing O_2 before it reached the cobaloxime centres within, testifying once again that the substrate on which a catalyst is immobilised need not be an inert surface and can play an active role in improving electrode performances.

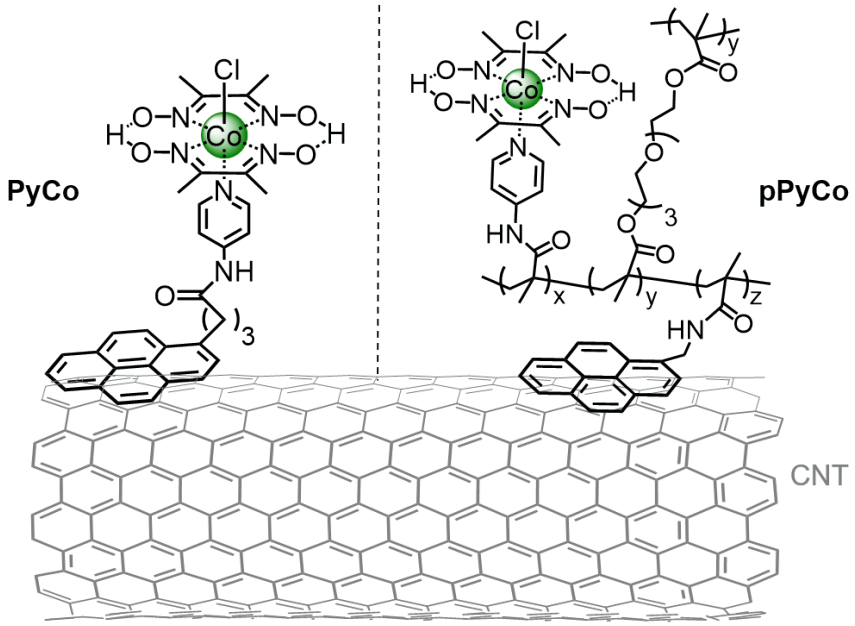

Fig. 1.11 Schematic representation of a molecular cobaloxime **PyCo** and a polymeric analogue **pPyCo** immobilised on carbon nanotubes, as described by our group.[107]

Indeed, another way in which CNT scaffolds have been postulated to protect molecular catalysts has been the former's ability to prevent a build-up of reduced intermediate species of the latter that could lead to degradative side reactions. Artero and co-workers covalently anchored a proton reduction cobalt diimine dioxime complex onto CNTs and found that the steady supply of electrons from the CNTs to the surface-bound catalyst prevented the aforementioned build-up of reduced intermediate species, leading to a significant improvement in the lifetime of the catalyst (turnover number, TON $\approx$ 33000 in this configuration compared to TON $\approx$ 50 when the catalyst is operated in solution).[211] Another important factor that was speculated to determine improved stability was the fact that once grafted onto the CNT material, the molecular complexes were less able to undergo reductive homocoupling to yield dimer complexes not suitable for catalysis.

This leads us to another common proposition found in the literature regarding improved performances of molecular complexes once immobilised: their ability to couple bimolecularly and form dimers can be affected, leading to either improved or reduced performance depending on whether dimerisation leads to active or inactive species, respectively. The effect of catalyst immobilisation on catalyst dimerisation in the context of solar fuels has been documented since as early as the 1980s. In 1984, Lieber and Lewis reported that a cobalt phthalocyanine catalysed CO_2 reduction to CO much more selectively and at turnover frequencies three orders of

magnitude greater when adsorbed on a carbon cloth than when in a homogeneous solution.[219] The suppression of site-site interactions that could cause dimerisation and deactivation was postulated as the explanation for the observed improvement. In 1991, Enyo and co-workers came to a similar conclusion when they immobilised a CO_2-reducing cobalt porphyrin catalyst onto glassy carbon *via* axial coordination of a surface-bound pyridine to the cobalt centre: intermolecular interaction was prohibited as a result of molecular immobilisation, thereby avoiding deactivation pathways that were observed in homogeneous solutions of this catalyst.[220] Although not directly proven, having a pyridine bound as an axial ligand was also speculated to benefit the catalytic reactivity of the bound molecule through the so-called trans-effect as a result of the pyridine being trans to the vacant coordination site of the five-coordinate complex.[221] Overall, what resulted is a stark difference between the catalyst immobilised on an electrode (TON $\approx$ 107, stable for over three days) *vs.* in solution (TON $\approx$ 50).

The suppression of dimerisation has also been observed for rhenium bipyridine (Re-bpy) catalysts. Meyer electropolymerised Re-bpy catalysts onto a Pt disc electrode and observed TONs that were an order of magnitude greater than an analogous molecular catalyst in solution, citing a stabilisation of the catalyst against deactivation pathways by way of this polymerisation.[222] In our group, the immobilisation of a phosphonic acid-modified Re-bpy catalyst onto TiO_2 nanoparticles reduced the concentration of inactive Re dimer species, as shown by transient absorption spectroscopy (TAS) measurements.[223] TAS also revealed a significantly longer lifetime of the reduced, catalytic Re species on TiO_2 than when in solution, which would have further contributed to the 26-fold increase in the CO_2 reduction yield of the immobilised *vs.* homogeneous catalyst.

In some cases, instead of being a degradative pathway, dimerisation can form the active catalytic species. A well-documented example of this is the Mn analogue of "Lehn-type" Re-bpy catalysts, first reported by Deronzier *et al.* and as mentioned above in section 1.3.[159] Although we have just discussed how immobilisation has been reported to suppress dimerisation, the dimerisation of Mn-bpy catalysts when immobilised on surfaces in sufficiently high concentrations (especially in porous matrices that confine the molecules) – such that the molecules are in fact predisposed to dimerise – has been recently shown in our group (Fig. 1.12).[212,224] On a transparent, mesoporous TiO_2 (mesoTiO_2) electrode, the dimerisation of a Mn-bpy catalyst modified with a phosphonic acid anchoring moiety, **MnP**, could be tracked by UV-vis spectroelectrochemistry and demonstrated for the first time on a surface.[224] On a CNT scaffold, a pyrene-anchored Mn-bpy catalyst, **MnPyr**,

was immobilised in varying concentrations and, in doing so, its predisposition towards dimerisation could be effectively tuned.[212] At low surface concentrations, the catalyst remained mostly in its monomeric form and favoured the catalysis of CO_2 reduction to formate. On the other hand, when immobilised at high concentrations, the catalyst was found mostly in its dimeric form and favoured formation of CO. This is an elegant demonstration of how catalyst behaviour – more specifically, its product selectivity – can be fine-tuned simply by controlling its loading concentration on a surface, without the need to carry out other, more complicated modifications to the electrode or catalyst structure itself.

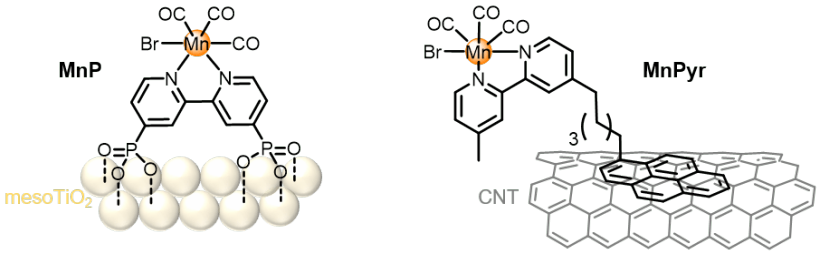

Fig. 1.12 Schematic representation of **MnP** and **MnPyr** immobilised on mesoporous TiO_2 and CNTs, respectively, as described in our group.[212,224]

Although the reasons are not always explained, another consequence of catalyst immobilisation that has been frequently reported is an earlier catalytic onset potential when compared to the catalyst in solution. Abruña and co-workers reported a series of 3d transition metal complexes with vinyl-substituted terpyridine (vtpy) ligands that had been polymerised onto glassy carbon electrodes.[225,226] Catalytic current enhancement in CO_2-saturated DMF solutions was observed for the poly[Co-$(vtpy)_2$] films at $-1.29\,V$ *vs.* Fc^+/Fc, which is $0.80\,V$ more positive than that required for the homogeneous, monomeric counterpart $[Co(tpy)_2]^{2+}$.[226] It was speculated that steric constraints caused by polymerisation forces one or both of the terpyridines on the cobalt centre to become bidentate instead of tridentate, thus opening up a coordination site at which catalysis can begin. Significantly earlier onset potentials compared to their homogeneous counterparts were also seen for Ni- and Fe-vtpy polymer films.[225] Here, "cooperativity effects" were supposedly at play, where the higher concentration of immobilised catalysts presumably allowed for two reduced molecules to cooperate in the CO_2 reduction catalytic cycle. Cowan and co-workers were also able to demonstrate an earlier catalytic onset potential for a CO_2 reduction molecular catalyst – this time, a Mn-bpy – as a direct result of its immobilisation into a Nafion® membrane, the latter of which provides a proton-rich environment to aid the proton-dependent catalytic mechanism.[227] Earlier onset potentials have also been observed for surface-

immobilised H_2-evolving catalysts. For example, Rose *et al.* covalently attached a Ni-centred DuBois-type catalyst onto a *p*-Si electrode and observed a catalytic onset that occurs 0.20 V more positive than if the catalyst was in solution in contact with the *p*-Si electrode.[228] In this case, the enhanced performance of the semiconductor-catalyst construct was thought to be due to expedited electron transfer to the catalytic core by the conjugated phenyl linker *via* which it is anchored to the electrode surface.

1.5 State of the Art

In the following section, reports of photocathodes based on molecular catalysts immobilised on narrow band gap, light-absorbing semiconductors that are active for proton reduction and CO_2 reduction in aqueous solutions at the time of writing is summarised. An emphasis is placed on those utilising Earth-abundant 3d transition metal catalysts; those based on precious metals are discussed for CO_2 reduction photocathodes only in the context of belonging to the current state of the art. For H_2-evolving photoelectrodes, the discussion has been organised according to the type of semiconductor substrate used; this has not been done for CO_2-reducing photoelectrodes due to the small number of examples of the latter.

1.5.1 H_2 Evolution Photoelectrodes

Indium Phosphide

The first example of a molecular catalyst-modified LAPC active for H_2 evolution (other than one other example from the 1980s – see below) emerged in 2010. Pickett and co-workers built a cross-linked InP nanoarray to serve as the light-absorbing component and upon this incorporated an iron-sulphur electrocatalyst, **MC1** (Fig. 1.13), that somewhat resembles the subsite of [Fe-Fe]-hydrogenases.[229] **MC1** was immobilised on the InP surface by exposure of the electrode to a solution of the iron catalyst, and adsorption of the molecule onto the semiconductor surface was presumed to occur *via* direct binding of the sulfide bridges to the indium. When tested in pH 7 aqueous solution (0.1 M $NaBF_4$) under illumination from a 395 nm LED array, the InP|**MC1** photocathode displayed an onset potential of 0.51 V *vs.* RHE but produced only tiny photocurrents of $< 1\,\mu A\,cm^{-2}$. Nevertheless, when held at a bias of 0.21 V *vs.* RHE under photoelectrocatalysis conditions for 1 h, H_2 production was detected at a decent Faradaic efficiency (FE) of 60 %. This

early work paved the way for what remains a relatively young and unpopulated field of molecular electrocatalyst incorporation onto solid-state light-absorbing semiconductors for solar fuel photocathodes.

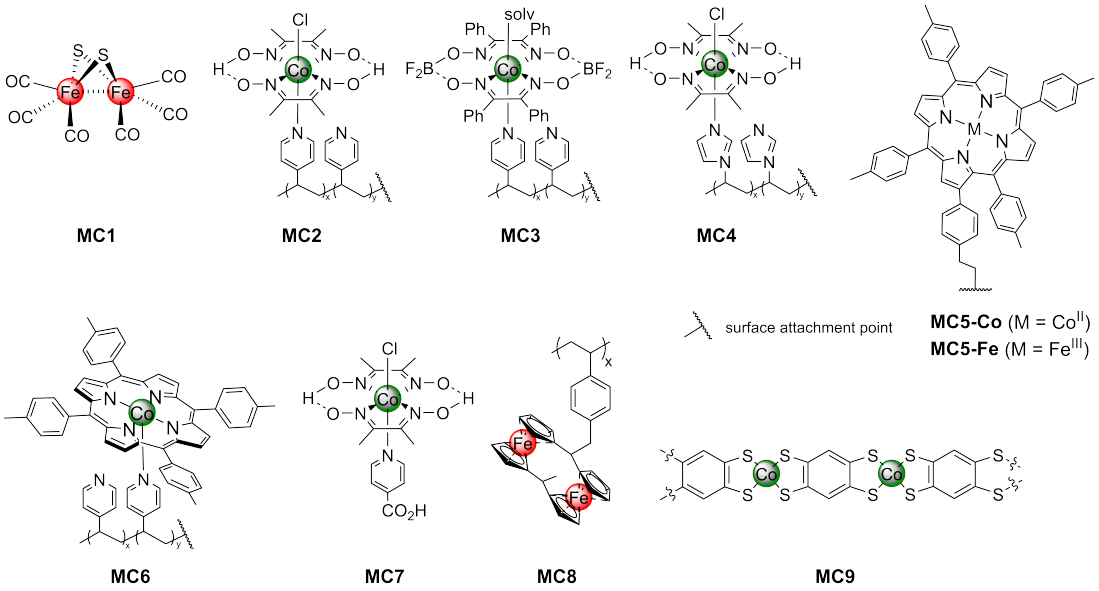

Fig. 1.13 Structures of molecular catalysts **MC1**-**MC9** used in previously-published light-absorbing photocathodes with immobilised 3d metal complex electrocatalysts active for proton reduction in aqueous systems.

Gallium Phosphide

What followed thereafter in the field of LAPCs for molecular catalyst-driven proton reduction was a series of work based also on another visible light-absorbing III-V type semiconductor, GaP, by the Moore group at Arizona State University. In all cases, this was achieved by exploiting UV-induced immobilisation chemistry of terminal alkenes[230] to GaP to drive single step surface-initiated photopolymerisation and yield a polymer on the surface with pendent groups that provide attachments points for cobaloxime catalysts. Although H_2 evolution was not demonstrated in those cases, a very similar approach had been previously used on GaP and Si surfaces to immobilise a proton reduction Ni bis(diphosphine) catalyst *via* formation of an amide bond between the catalyst and molecules that had first been surface-grafted by UV-light induced formation of Ga-O-C or Si-C linkages, respectively.[209] This work inspired the methodology undertaken to construct the series of GaP|polymer-cobaloxime photocathodes for proton reduction.

The first example saw vinylpyridine molecules being photochemically grafted and polymerised onto a (100) GaP surface, followed by base-promoted chloride

replacement of $[CoCl_2(dmgH)(dmgH_2)]$ by pyridyl groups on the surface-attached PVP polymer brushes to yield the final GaP|**MC2** photocathodes (Fig. 1.13).[231,232] Performing the surface catalyst immobilisation in two steps in this way means that saturation of the pyridine units with cobaloxime units is unlikely; indeed, evidence of these remnant pyridines free from Co was observed in XPS measurements. Nevertheless, it was expected that using a polymer bearing multiple pyridine binding sites would significantly increase the per geometric area loading capacity of the catalysts onto the semiconductor, as compared to approaches using self-assembled monolayers of molecules.

Under $100\,mW\,cm^{-2}$ illumination and in pH 7 phosphate buffer solution, the GaP|**MC2** photocathode displayed an onset potential of 0.76 V *vs.* RHE, as compared to 0.69 V *vs.* RHE for a catalyst-free GaP|PVP electrode. The fill factor for the *J*-*V* response of the open circuit voltage also improved dramatically upon incorporation of the Co catalyst ($>200\,\%$ increase), confirming that the presence of the cobaloxime promotes charge transfer across the surface. Under AM1.5G illumination in photoelectrocatalysis conditions, a photocurrent density of $-1.2\,mA\,cm^{-2}$ and a FE for H_2 evolution of 88 % was achieved at an applied bias of 0.17 V *vs.* RHE. Gradual loss of activity was attributed to loss of cobaloxime species from the surface and is consistent with many previous works that indicate the axial pyridine of similar cobaloxime complexes becomes labile during redox cycling.[233,234] The photocurrent density of GaP|**MC2** was also found to have a linear dependence on the illumination intensity, which indicates that photocarrier transport to the interface was a likely limiting factor for the performance of this photocathode.[231]

As is the case with catalysts operating in solution, the activity of surface-immobilised catalysts can also be influenced by the ligands on the metal centre. This was demonstrated when the oxime-linking hydrogen atoms of the cobaloxime in the previous work were replaced with bridging BF_2 groups instead (**MC3**, Fig. 1.13).[235] This synthetic manipulation has been previously shown to impart stability during solution operation of cobaloxime catalysts against acid hydrolysis and to tune the catalytic redox features such that the overpotential is lower.[103,236] A similar consequence was observed in the case of the GaP|polymer-bound constructs. At pH 7, GaP|**MC2** outperformed GaP|**MC3** in terms of photocurrent density reached ($-1.2\,mA\,cm^{-2}$ for the former *vs.* $-0.56\,mA\,cm^{-2}$ for the latter, at 0.0 V *vs.* RHE). However, the photoactivities of both electrodes become comparable when the pH is lowered to 4.5 ($-1.1\,mA\,cm^{-2}$ at 0.0 V *vs.* RHE). These results indicate that proton activity at neutral pH is not high enough to boost H_2

production of GaP|**MC3** to the levels observed with GaP|**MC2**, and that there is a requirement of acidic conditions to induce catalysis; this is most likely due to a correlation between the Co^{II}/Co^{I} reduction potential and the basicity of Co^{I} to form Co^{III}-hydride during the catalytic cycle.

The versatility of using a polymer graft to interface molecular catalysts with a semiconductor substrate was further demonstrated when the polyvinylpyridine polymer was replaced with a polyvinylimidazole (PVI) instead; the imidazole units of the latter bind to the cobaloxime in the axial position in much the same way that the pyridine units of the former do (**MC4**, Fig. 1.13).[237] The polymer grafting approach was further extended to different GaP(111) faces with **MC4** polymers, and the GaP(111)|**MC4** photocathodes were found to exhibit very similar performance parameters to their GaP(100) counterparts as well as to one another (111A *vs.* 111B faces).[238] XPS measurements in these works provided an estimate of 28-35 % for the loading of cobalt centres to all available ligand binding units in the polymer film, thereby illustrating the aforementioned point that saturation of all ligand sites on the polymer with cobaloxime catalysts is unlikely when this layer-by-layer electrode fabrication method (polymer deposition first, followed by catalyst modification) is employed.

UV-induced polymerisation of olefins can be exploited in much the same way for attaching individual molecules to a GaP surface as for inducing surface-initiated polymerisation. This approach was employed to immobilise Co- and Fe-centred porphyrins bearing a pendent 4-vinylphenyl surface attachment group at the β-position of the porphyrin ring structure (**MC5-Co** and **MC5-Fe**, respectively, Fig. 1.13).[239] Notable differences between this work and the previous reports on GaP are the fact that the surface-immobilised molecular units remain discrete and each possess their own attachment point in the absence of any polymer, and also the fact that the complexes' metal centres are already present within the catalysts' ligand framework prior to surface grafting. The latter point means that surface attachment of the complete catalytic complexes is a one-step process; synthetic work undertaken to modify the porphyrin with a pendent vinylphenyl moiety has allowed for this.

Finally, metalloporphyrins were also attached to GaP by using the same procedure previously reported for UV-induced polymerisation of PVP onto the semiconductor, followed by Co-porphyrin attachment to the pyridine units (**MC6**, Fig. 1.13).[240] This approach involves two steps to achieve **MC6** surface attachment, but does not involve synthetic steps to modify the porphyrin macrocycle with a surface attachment functionality. Performance parameters under pho-

toelectrocatalysis conditions were near-identical to those of the GaP|**MC5**-Co photocathodes, suggesting that the PVP surface coating does not diminish the performance gains afforded by Co-porphyrin surface modification.

In summary, a series of reports where UV-induced attachment of olefin groups to a Ga surface was leveraged in all cases have been published for surface attachment of proton-reducing cobaloximes and metalloporphyrins onto GaP semiconductor substrates. Although iterations between these reports were small, they demonstrated that slight modifications at the catalyst level (ligand functionalities of cobaloxime, cobaloxime *vs.* metalloporphyin), polymer level (PVP *vs.* PVI) and GaP level (100 faces *vs.* 111 faces) can all be undertaken using this reasonably versatile motif. The CB of GaP is poised almost a volt more negative than the thermodynamic potential for proton reduction, which, though energy wasteful in some cases, makes it an attractive material choice for proton-reducing photocathodes where the catalysts require a significant overpotential.[241–243] However, its optical band gap ($E_g = 2.26\,\text{eV}$) is significant enough to preclude its ability to absorb photons with wavelengths longer than 549 nm and therefore would significantly limit the overall external quantum efficiency (EQE) of the system. Gains could therefore be made if GaP were to be replaced by a semiconductor with a narrower band gap, provided of course that overpotential requirements of any surface-bound catalyst were still met.

Gallium Indium Phosphide

To date, the majority of LAPCs reported to be active for proton reduction are operated in neutral or acidic conditions, most often because the pH values at which both the semiconductor is stable and the catalyst can operate lie within this window. The only exception to this is a $GaInP_2|TiO_2|$cobaloxime$|TiO_2$ construct reported by Turner and colleagues that is operated at pH 13 conditions.[80] This is a significant advantage for tandem applications with the water-splitting oxygen evolution reaction, for which basic conditions is preferred.[244] However, such strongly alkaline conditions can also make molecular catalysts susceptible to transformations.[51]

In this photocathode, both TiO_2 layers were deposited by ALD and their functions were reported to be multi-fold. The 35 nm-thick ALD-TiO_2 layer directly interfaced with $GaInP_2$ provides a conformal layer to protect the III-V semiconductor from corrosion in aqueous solutions,[245] while also providing oxide sites for surface attachment of the isonictonic acid-functionalised (*i.e.* carboxylic

acid-containing) cobaloxime molecules (**MC7**, Fig. 1.13). On the other hand, the 10 nm-thick TiO_2 overlayer deposited on top of the cobaloxime was thought to provide stabilisation of the carboxylate linkage under such harsh conditions, although direct comparison of the PEC performances of $GaInP_2|TiO_2|$**MC7**$|TiO_2$ electrode with an overlayer-free $GaInP_2|TiO_2|$**MC7** photocathode was not discussed.

Under illumination in pH 13 (0.1 M NaOH) aqueous solution, the $GaInP_2|TiO_2|$-**MC7**$|TiO_2$ photocathode exhibited an onset potential at ≈ 0.70 V *vs.* RHE, and reached a current density of $-11\,\mathrm{mA\,cm^{-2}}$ at 0.0 V *vs.* RHE in linear sweep voltammetry experiments. Under photoelectrolysis conditions, the photocurrent dropped by only 5 % within the first 20 min and near-unity FE was reported. However, the photocurrent density continued to drop sharply for the first 2.5 h but plateaued at $-$4-5 $\mathrm{mA\,cm^{-2}}$, where it remained for the remainder of the 20 h electrolysis. It is noted that the molecular integrity of the photocathode was not directly verified post-catalysis, although some evidence of loss of the TiO_2 protective overlayer was given from XPS and SEM measurements.

Silicon

Besides III-V semiconductors, the only other inorganic *p*-SC that has been adopted for building molecular catalyst-based photocathodes is *p*-Si. Already widely adopted in both academic and commercial realms of the solar cell field, the Earth-abundance and small band gap of this material withholds it as an attractive light-harvesting material for solar fuel generation. However, the inherent instability of Si in aqueous and aerobic conditions in terms of formation of a passivating silica layer has complicated its widespread adoption to date. Several reports describe the deposition of protection layers to limit this instability, but often require severe precautions and expensive techniques, most commonly ALD.[78] Further, most of these reports subsequently deposited non-molecular, precious metal heterogeneous catalysts atop the protection layer to complete construction of the H_2-evolving photocathodes. As such, the majority of molecular catalyst-based LAPCs for proton reduction based on Si have been operated under either organic solvents or extremely acidic aqueous solutions, where the Si is more stable.

The very first example of a molecular catalyst interfaced with a *p*-SC to yield a proton-reducing photocathode is in fact based on p-type silicon and operates under acidic conditions. In 1984, Mueller-Westerhoff incorporated a bimetallic metallocene ("ferrocenophane")-type molecular complex with a polystyrene polymer (**MC8**, Fig. 1.13) in a bid to provide a mode by which the former could be

attached with the latter as a film to an electrode surface.[64] Although most of the photoelectrochemistry was undertaken in neat HBF_3OH electrolyte, the Si|**MC8** photocathode was also reported to operate under acidic aqueous conditions, such as 1 M $HClO_4$ (*n.b.* pH not given), in which it exhibited a photocurrent onset potential of $\approx 0.241\,\mathrm{V}$ *vs.* SHE.

The next report of a 3d transition metal complex-modified Si photocathode came much later in 2015 and was operated under extremely acidic conditions in the absence of a protection layer between the Si and the catalyst. Building on their recent work where they demonstrated the incorporation of cobalt dithiolene units into two-dimensional (2D) metal-organic surfaces,[246] Marinescu and colleagues extended this methodology to construct one-dimensional (1D) cobalt diothiolene MOS based on benzene-1,2,4,5-tetrathiolate (BTT) frameworks (**MC9**, Fig. 1.13) and deposited these as thin films on Si electrodes.[247] The surface concentration of **MC9** atop the Si can be easily modified by varying the amount of catalyst dropcast on the electrode, and was found to possess a maximum of $6.3\,\mu\mathrm{mol\,cm^{-2}}$, which is 2-3 orders of magnitude higher than the loading reported for typical mesoporous structures. However, due to the opaque black nature of the catalyst and its subsequent ability to absorb incident photons, the optimum surface concentration found to give the best photoelectrochemical performance was $4.0\,\mu\mathrm{mol\,cm^{-2}}$. With this loading, the Si|**MC9** photocathode exhibited a photocurrent onset potential of $\approx 0.2\,\mathrm{V}$ *vs.* RHE and reached a photocurrent density of $-3.8\,\mathrm{mA\,cm^{-2}}$ at 0.0 V *vs.* RHE when operated in a pH 1.3 aqueous H_2SO_4 solution. When held at a potential of $-0.12\,\mathrm{V}$ *vs.* RHE, the Si|**MC9** photocathode appeared to be stable for only 20 min, during which a FE for H_2 evolution of 80 % was measured. The main reason for the photocathode's instability was delamination of the catalyst from the Si surface; this instability is perhaps unsurprising given the lack of a direct binding mode between the 1D MOS and the Si surface. Nevertheless, the impressive photocurrents and the straightforward catalyst synthesis are notable.

1.5.2 CO_2 Reduction Photoelectrodes

Perhaps unsurprisingly, the progress made in CO_2 reduction photocathodes based on Earth-abundant transition metal complexes immobilised on light-absorbing semiconductors lags far behind that of proton-reducing photocathodes. To date, reported molecule-based photocathodes performing CO_2 reduction remain scarce, whether in organic or water-containing media, and continue to rely heavily on precious metal-containing components. In fact, when considering only systems

where there is water present in the operating conditions, only the series of work published by Sato, Morikawa, Arai and co-workers since 2010 fit the bill, and all utilised precious metal Ru-centred metal complexes as the molecular catalysts. Nevertheless, this body of work demonstrates the versatility of certain immobilisation methods through the wide range of narrow band gap semiconductors on which these catalysts were deposited.

Taking inspiration from the catalysts employed by Deronzier and Chardon-Noblat,[204] a range of closely-related Ru bipyridine-based catalysts were polymerised (chemically or electrochemically) onto a number of different narrow band gap semiconductors, including Zn-doped InP,[248] Cu_2ZnSnS_4,[249] GaP and N-doped Ta_2O_5 (**MC10**, Fig. 1.14).[250] Their studies were further extended to a non-polymeric, discrete Ru bipyridine catalyst immobilised on *p*-type Fe_2O_3 photocathodes, which were assembled as a multiheterojunction structure with additional TiO_2 and Cr_2O_3 layers to enhance band-bending effects and to prevent photochemical dissolution of the Fe_2O_3 into the surrounding solution under reductive conditions.[251]

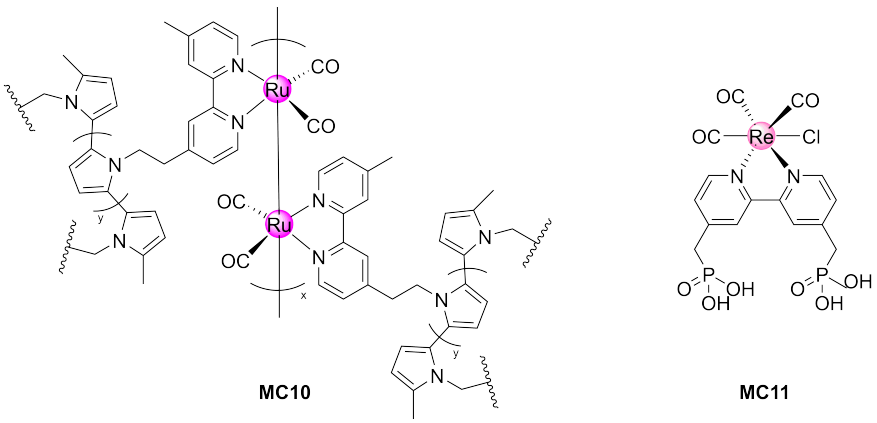

Fig. 1.14 Structures of molecular catalysts **MC10**-**MC11** used in previously-published light-absorbing photocathodes with immobilised metal complex electrocatalysts active for CO_2 reduction in both organic and aqueous systems.

In almost all of the above studies, the method by which the catalyst – polymeric or not – was immobilised onto the semiconductor was found to play a role in the robustness and subsequent CO_2-reducing performance of the photocathode. For instance, supplementing the initial cathodic photoelectropolymerisation step with an additional anodic electropolymerisation step was found to improve performances, presumably because the cathodic step forms Ru-Ru bonds in the polymeric film while the anodic step accelerates formation of the catalyst's polypyrrole backbone.[248] In the case of the discrete Ru molecular catalysts on Fe_2O_3, comparing two catalysts with similar overpotential requirements side-by-side always found

the one with an anchor such as carboxylic acid to yield the better-performing photocathode than one without an appropriate anchor.[251] A similar conclusion was reached when comparing polymerised Ru catalysts with phosphate anchor functionalities to analogous polymers without such anchors.[250] Therefore, despite their employment of only Ru-based catalysts and the production of mostly formate in the vast majority of these examples (the exception being the Fe_2O_3 photocathode, which also produced CO), this body of work is still important in paving the way for aqueous CO_2 reduction with molecular LAPCs and highlighting the important conclusion that the mode and method of catalyst immobilisation can play a large role in determining the end result, irregardless of the catalyst's performance when in solution.

Even if we were to consider anhydrous conditions where enhanced photocathode and/or catalyst stability may be expected, only a few reports exist, and all depend on Re-based catalysts.[77,252] For instance, a Re bipyridine catalyst (**MC11**, Fig. 1.14) immobilised on a Cu_2O photoelectrode protected by multiple atomic-layer-deposited coatings was still only operated in anhydrous acetonitrile (MeCN), achieving a TON for CO of 70.[77] When we extend our scope even further to include photosensitiser-modified, large band gap semiconductor-based photocathodes, the majority of these DSPC systems still consist of precious metal-based catalysts, some alongside dyes that are precious metal-based as well.[77,252–256] For example, a benchmark report of such systems consists of a Ru-Re dye-catalyst dyad immobilised on NiO that evolves CO in dry DMF solution.[256]

The desire to move away from precious metal-based CO_2 reduction catalysts is evident when considering the small body of work that has emerged in recent years where Earth-abundant metal complexes have been employed in organic solvents with a narrow band gap, light-absorbing semiconductor, either dissolved in solution or immobilised on the semiconductor surface. In 2013, Pickett *et al.* reported CO_2 reduction to CO by Fe porphyrin catalysts in solution, photodriven by a H-terminated, *p*-Si photoelectrode.[257] This system was operated in dry organic solvents with CF_3CH_2OH as the added proton source. Chardon-Noblat and Fabre later reported the pairing of Si nanowire electrodes (SiNWs) with the Mn-bpy catalysts that Deronzier and Chardon-Noblat had previously pioneered as alternatives to Lehn-type Re analogues.[258] In this work, three such catalysts were operated as homogeneous catalysts in MeCN solution and demonstrated the superior properties of nanostructured SiNWs as compared to flat Si electrodes in terms of their higher electrochemically active surface area and higher capacity to decouple minority carrier generation and collection. A pyrrole-based derivative of

this class of Mn catalysts was also electropolymerised directly onto the SiNWs and was shown *via* cyclic voltammetry to give enhanced photocurrents under CO_2 and 5 % H_2O, although sustained CO_2 reduction catalysis was not reported in this case. Finally, in a similar manner, Li and co-workers recently found that CO_2 reduction in MeCN solutions with 1-2 % of added H_2O by Co tris(2-pyridylmethyl)amine catalysts in solution was better at nanostructured SiNW electrodes than planar Si surfaces.[259]

1.5.3 Summary and Outlook

In summary, the number of examples of metal complex catalysts – especially those based on Earth-abundant elements – immobilised on light-absorbing semiconductors to construct LAPCs for solar fuel generation under aqueous conditions remains sparse. One of the biggest hurdles facing development in this field is the search for light-absorbing p-type semiconductors that are stable in water. Indeed, none of the LASCs utilised to date are inherently stable and have therefore either been operated under extreme pH conditions where corrosion is less likely and/or have been decorated with some sort of protection layer. For example, the "state of the art" of such H_2-evolving photocathodes is a $GaInP_2$-based photocathode decorated with two ALD-deposited TiO_2 layers and operated under extremely basic pH 13 conditions.[80]

In examples where a metal oxide interlayer has not been employed to protect the underlying semiconductor, a polymer has most often been touted to perform the same function of stabilising the corrosion-susceptible semiconductor in the absence of any other protection. For instance, the majority of GaP-based photocathodes discussed above for H_2 evolution were operated under pH-neutral conditions but possessed an organic polymer film atop the semiconductor, which supposedly protected it as well as provided attachment sites for molecular Co catalysts. Another work also sought to protect Si by depositing metal-organic surfaces with incorporated catalysts directly on top of the light-harvesting semiconductor.[247] However, the majority of reports do not discuss the stability of their photocathodes beyond 1 h, rendering a fair assessment of the true stability of the semiconductor and any overlying so-called protection layer extremely difficult.

In contrast to DSPCs where the majority of molecular species (photosensitisers and catalysts alike) have been immobilised on the semiconducting substrate by acidic moieties (phosphonic or carboxylic), polymeric architectures have been more commonly exploited to immobilise catalysts in constructing LAPCs. The

concept of UV-induced surface polymerisation of olefin-containing catalyst ligands was adopted to produce a range of GaP|polymer-cobaloxime and GaP|polymer-porphyrin H_2-evolving photocathodes. In these works, the polymer was bound to the underlying semiconductor by a direct covalent linkage, whereas in other works on Si, the experimenters relied on non-covalent interactions to result in polymer immobilisation onto the surface,[64,247] although the nature of these interactions were never discussed.

Once again, when it comes to H_2 evolution, the ease of working with cobaloximes is made apparent by the fact that the majority of LAPCs discussed above are based on this class of catalysts. It is imperative that the focus shifts towards finding ways to immobilise other classes of molecular catalysts that are more active and stable than cobaloximes. Indeed, there is a dire need to do so with CO_2 reduction catalysts in particular, where the vast majority of works employ either Ru- or Re-based metal complexes and no precious metal-free systems currently exist to date. The lack of progress made for CO_2-reducing photocathodes illustrates the difficulties in doing so as a result of issues like product selectivity, especially in aqueous conditions, and the fact that the most well-studied and efficient molecular catalysts to date still rely on precious metals. Although CO_2 reduction is more challenging of a feat to achieve – thermodynamically and kinetically – than proton reduction, there is little reason why the lessons learned to date in different immobilisation approaches with, say, cobaloximes cannot be carried through and applied to other molecules. Alongside this, there still remains an urgent need, once again, to report photocathode performances with more rigour and standardisation, especially in terms of long-term capabilities and the explicit acknowledgment of whether molecular integrity has been maintained during such long photoelectrocatalysis timeframes; the latter should be backed up with hard experimental evidence.

1.6 Thesis Outline

As discussed in depth in this chapter, there is a strong desire in the field of solar fuel synthesis to marry the benefits of molecular electrocatalysts with those of surface immobilisation for molecule-driven photoelectrocatalysis. The non-triviality of this task is made evident by the limited number of reported molecular photocathodes in the literature, their poor stabilities and efficiencies, and the employment of intricate techniques such as atomic layer deposition during electrode fabrication. Moreover, the vast majority of (and in the case of CO_2 reduction, all) reports to

date utilise precious metal-based components, be it in the light harvester (small band gap, light-absorbing inorganic semiconductors or molecular dyes) or the metal complex catalyst. The above are challenges that the work in this thesis aims to address. Namely, the molecular photoelectrodes designed and studied in this thesis had to meet three criteria: (i) the usage of only Earth-abundant materials, (ii) simple, low-cost fabrication techniques, and (iii) the ability to perform robust proton reduction and CO_2 reduction in aqueous environments.

To this end, the fabrication of a *p*-silicon|mesoporous titania (Si|*meso*TiO_2) photoelectrode is established in Chapter 2. Multiple H_2 evolution catalysts of different varieties – molecular, enzymatic and metallic – were deposited on the surface of this photoelectrode to demonstrate the versatility of this architecture. Importantly, in the case of the synthetic molecular catalysts, it is clear that this strategy allows the transferral of performances achieved in solution-based systems onto the photoelectrodes, attesting to the effective electronic communication between the photoelectrode's various components. This was aided by the molecular catalysts' possession of phosphonic acid moieties that provide a robust anchoring onto the metal oxide surface of Si|*meso*TiO_2. In particular, the photocathode utilising an anchor-bearing $[Ni(P_2N_2)_2]^{2+}$ (DuBois-type) catalyst was stable for over a day and achieved performances in aqueous solutions that exceeded those of all previously published systems with immobilised catalysts of the same class. The ability for the catalyst-free photoelectrode to store long-lived photogenerated charges in the conduction band of TiO_2 was also studied by (photo)electrochemical methods.

Having demonstrated the wider applicability and stability of the Si|*meso*TiO_2 architecture for reductive transformations under aqueous conditions, this platform was extended towards molecular CO_2 reduction catalysis in Chapter 3. A phosphonate-bearing cobalt(II) bis(terpyridine)-type catalyst was synthesised and immobilised on the scaffold to yield the first precious metal-free CO_2-reducing molecular photocathode. The photoelectrocatalytic ability of Si|*meso*TiO_2|**CotpyP** to reduce CO_2 was studied in both organic-water mixtures and purely aqueous conditions. Optimum operating conditions were determined, where record turnover numbers were achieved.

A deeper consideration of the photoelectrocatalysis achieved with this CO_2-reducing photocathode led to findings that point towards a lower catalytic onset potential and structural preservation of the immobilised catalyst – both observations of which contrast with literature precedence for analogous solution-based catalysts. In response to this, Chapter 4 presents an in-depth study conducted by

cyclic voltammetry, spectroelectrochemical resonance Raman spectroscopy and spectroelectrochemical infrared spectroscopy to elucidate a possible mechanistic pathway for this surface-immobilised catalyst. Critically, these studies did indeed allude to a distinctly different mechanistic pathway to that of previously reported, in-solution metal bis(terpyridine) catalysts. This was apparently possible as a consequence of immobilisation, which unlocks an earlier catalytic onset and better electrocatalytic performance while enabling aqueous CO_2 reduction with our hybrid photocathode.

In Chapter 5, an approach comprising of embedding the cobalt bis(terpyridine) motif into a polymer matrix was employed to demonstrate the scope of tuning catalyst performance by changing its outer coordination sphere instead of its primary ligand structure. The rational design of these polymers allowed for both modulation of the degree of cross-linking and an artificially-engineered hydrophobicity in the catalyst environment, leading to improved product selectivity for CO_2 reduction products. The synergy between the polymers' size and the large pores of inverse-opal metal oxide electrodes used in this work was also an important design principle.

Finally, Chapter 6 disseminates the key conclusions of this body of work and offers future directions for its continuation. In particular, the need to extend this methodology to different materials – for both light harvester and catalyst – and issues of interfacial optimisation are highlighted.

1.7 References

(1) Hansen, J.; Johnson, D.; Lacis, A.; Lebedeff, S.; Lee, P.; Rind, D.; Russell, G. *Science* **1981**, *213*, 957–966.

(2) Ciais, P.; Sabine, C.; Bala, G.; Bopp, L.; Brovkin, V.; Canadell, J.; Chhabra, A.; DeFries, R.; Galloway, J.; Heimann, M.; Jones, C.; Le Quéré, C.; Myneni, R. B.; Piao, S.; Thornton, P. *Carbon and Other Biogeochemical Cycles. In Climate Change 2013: The Physical Science Basis. Contribution of Working Group I to the Fifth Assessment Report of the Intergovernmental Panel on Climate Change*; tech. rep.; Cambridge, United Kingdom and New York, NY, USA, 2013.

(3) Wilkinson, P.; Smith, K. R.; Joffe, M.; Haines, A. *Lancet* **2007**, *370*, 965–978.

(4) Armaroli, N.; Balzani, V. *Angew. Chem. Int. Ed.* **2007**, *46*, 52–66.

(5) Hoekstra, A. Y.; Wiedmann, T. O. *Science* **2014**, *344*, 1114–1118.

(6) Hoffert, M. I. *Science* **2010**, *329*, 1292–1294.

(7) Barber, J. *Chem. Soc. Rev.* **2009**, *38*, 185–196.

(8) US Energy Information Administration *International Energy Outlook 2017*; tech. rep.; 2017.

(9) Green, M. A.; Hishikawa, Y.; Dunlop, E. D.; Levi, D. H.; Hohl-Ebinger, J.; Ho-Baillie, A. W. *Prog. Photovoltaics Res. Appl.* **2018**, *26*, 3–12.

(10) International Energy Agency *Renewables 2017*; tech. rep.; 2017.

(11) Feldman, D.; Barbose, G.; Margolis, R.; Bolinger, M.; Chung, D.; Fu, R.; Seel, J.; Davidson, C.; Naïm Darghouth; Wiser, R. *Photovoltaic System Pricing Trends: Historical, Recent and Near-Term Projections*; tech. rep.; NREL Laboratory, 2015, pp 1–32.

(12) International Energy Agency *Key World Energy Statistics*; tech. rep.; 2017.

(13) Lund, H.; Münster, E. *Appl. Energy* **2003**, *76*, 65–74.

(14) Armand, M.; Tarascon, J. M. *Nature* **2008**, *451*, 652–657.

(15) Lewis, N. S.; Nocera, D. G. *Proc. Natl. Acad. Sci.* **2006**, *103*, 15729–15735.

(16) Cook, T. R.; Dogutan, D. K.; Reece, S. Y.; Surendranath, Y.; Teets, T. S.; Nocera, D. G. *Chem. Rev.* **2010**, *110*, 6474–6502.

(17) Berndes, G.; Hoogwijk, M.; Van Den Broek, R. *Biomass and Bioenergy* **2003**, *25*, 1–28.

(18) Fujishima, A.; Honda, K. *Nature* **1972**, *238*, 37–38.

(19) Benson, E. E.; Kubiak, C. P.; Sathrum, A. J.; Smieja, J. M. *Chem. Soc. Rev.* **2009**, *38*, 89–99.

(20) Umena, Y.; Kawakami, K.; Shen, J. R.; Kamiya, N. *Nature* **2011**, *473*, 55–60.

(21) Nelson, N.; Ben-Shem, A. *Nat. Rev. Mol. Cell Biol.* **2004**, *5*, 971–982.

(22) Fischer, F.; Tropsch, H. *Brennstoff-Chemie* **1926**, *7*, 97–104.

(23) Maeda, K.; Domen, K. *J. Phys. Chem. Lett.* **2010**, *1*, 2655–2661.

(24) Kudo, A.; Miseki, Y. *Chem. Soc. Rev.* **2009**, *38*, 253–278.

(25) Willkomm, J.; Orchard, K. L.; Reynal, A.; Pastor, E.; Durrant, J. R.; Reisner, E. *Chem. Soc. Rev.* **2016**, *45*, 9–23.

(26) Wen, F.; Li, C. *Acc. Chem. Res.* **2013**, *46*, 2355–2364.

(27) Andreiadis, E. S.; Chavarot-Kerlidou, M.; Fontecave, M.; Artero, V. *Photochem. Photobiol.* **2011**, *87*, 946–964.

(28) Queyriaux, N.; Kaeffer, N.; Morozan, A.; Chavarot-Kerlidou, M.; Artero, V. *J. Photochem. Photobiol. C Photochem. Rev.* **2015**, *25*, 90–105.

(29) Liu, X.; Inagaki, S.; Gong, J. *Angew. Chem. Int. Ed.* **2016**, *55*, 14924–14950.

(30) Tian, H. *ChemSusChem* **2015**, *8*, 3746–3759.

(31) Wang, M.; Yang, Y.; Shen, J.; Jiang, J.; Sun, L. *Sustain. Energy Fuels* **2017**, *1*, 1641–1663.

(32) Aoi, S.; Mase, K.; Ohkubo, K.; Suenobu, T.; Fukuzumi, S. *ACS Energy Lett.* **2017**, *2*, 532–536.

(33) Rosser, T. E.; Gross, M. A.; Lai, Y.-H.; Reisner, E. *Chem. Sci.* **2016**, *7*, 4024–4035.

(34) Bolton, J. R.; Strickler, S. J.; Connolly, J. S. *Nature* **1985**, *316*, 495–500.

(35) Hu, S.; Xiang, C.; Haussener, S.; Berger, A. D.; Lewis, N. S. *Energy Environ. Sci.* **2013**, *6*, 2984.

(36) Prévot, M. S.; Sivula, K. *J. Phys. Chem. C* **2013**, *117*, 17879–17893.

(37) Carmo, M.; Fritz, D. L.; Mergel, J.; Stolten, D. *Int. J. Hydrogen Energy* **2013**, *38*, 4901–4934.

(38) Jacobsson, T. J.; Fjällström, V.; Sahlberg, M.; Edoff, M.; Edvinsson, T. *Energy Environ. Sci.* **2013**, *6*, 3676–3683.

(39) Schreier, M.; Héroguel, F.; Steier, L.; Ahmad, S.; Luterbacher, J. S.; Mayer, M. T.; Luo, J.; Grätzel, M. *Nat. Energy* **2017**, *2*, 17087.

(40) Luo, J.; Im, J.-H.; Mayer, M. T.; Schreier, M.; Nazeeruddin, M. K.; Park, N.-G.; Tilley, S. D.; Fan, H. J.; Grätzel, M. *Science* **2014**, *345*, 1593–1596.

(41) Schreier, M.; Curvat, L.; Giordano, F.; Steier, L.; Abate, A.; Zakeeruddin, S. M.; Luo, J.; Mayer, M. T.; Grätzel, M. *Nat. Commun.* **2015**, *6*, 7326.

(42) Sivula, K.; Van De Krol, R. *Nat. Rev. Mater.* **2016**, *1*, 15010.

(43) Roy, S. C.; Varghese, O. K.; Paulose, M.; Grimes, C. A. *ACS Nano* **2010**, *4*, 1259–1278.

(44) Dhakshinamoorthy, A.; Navalon, S.; Corma, A.; Garcia, H. *Energy Environ. Sci.* **2012**, *5*, 9217–9233.

(45) Zhang, P.; Zhang, J.; Gong, J. *Chem. Soc. Rev.* **2014**, *43*, 4395–4422.

(46) Ran, J.; Zhang, J.; Yu, J.; Jaroniec, M.; Qiao, S. Z. *Chem. Soc. Rev.* **2014**, *43*, 7787–7812.

(47) Takeda, H.; Cometto, C.; Ishitani, O.; Robert, M. *ACS Catal.* **2017**, *7*, 70–88.

(48) Wang, M.; Chen, L.; Sun, L. *Energy Environ. Sci.* **2012**, *5*, 6763–6778.

(49) Losse, S.; Vos, J. G.; Rau, S. *Coord. Chem. Rev.* **2010**, *254*, 2492–2504.

(50) Hong, D.; Mandal, S.; Yamada, Y.; Lee, Y.-M.; Nam, W.; Llobet, A.; Fukuzumi, S. *Inorg. Chem.* **2013**, *52*, 9522–9531.

(51) Artero, V.; Fontecave, M. *Chem. Soc. Rev.* **2013**, *42*, 2338–2356.

(52) Xu, P.; McCool, N. S.; Mallouk, T. E. *Nano Today* **2017**, *14*, 42–58.

(53) Youngblood, W. J.; Lee, S.-h. A.; Maeda, K.; Mallouk, T. E. *Acc. Chem. Res.* **2009**, *42*, 1966–1973.

(54) Gust, D.; Moore, T. A.; Moore, A. N. A. L. *Acc. Chem. Res.* **2009**, *42*, 1890–1898.

(55) Concepcion, J. J.; Jurss, J. W.; Brennaman, M. K.; Hoertz, P. G.; Patrocinio, A. O. T.; Murakami Iha, N. Y.; Templeton, J. L.; Meyer, T. J. *Acc. Chem. Res.* **2009**, *42*, 1954–1965.

(56) Brennaman, M. K.; Dillon, R. J.; Alibabaei, L.; Gish, M. K.; Dares, C. J.; Ashford, D. L.; House, R. L.; Meyer, G. J.; Papanikolas, J. M.; Meyer, T. J. *J. Am. Chem. Soc.* **2016**, *138*, 13085–13102.

(57) Gibson, E. A. *Chem. Soc. Rev.* **2017**, *46*, 6194–6209.

(58) Gross, M. A.; Creissen, C. E.; Orchard, K. L.; Reisner, E. *Chem. Sci.* **2016**, *7*, 5537–5546.

(59) Kaeffer, N.; Massin, J.; Lebrun, C.; Renault, O.; Chavarot-Kerlidou, M.; Artero, V. *J. Am. Chem. Soc.* **2016**, *138*, 12308–12311.

(60) Shan, B.; Das, A. K.; Marquard, S.; Farnum, B. H.; Wang, D.; Bullock, R. M.; Meyer, T. J. *Energy Environ. Sci.* **2016**, *9*, 3693–3697.

(61) Creissen, C. E.; Warnan, J.; Reisner, E. *Chem. Sci.* **2018**, *9*, 1439–1447.

(62) D'Amario, L.; Föhlinger, J.; Boschloo, G.; Hammarström, L. *Chem. Sci.* **2018**, *9*, 223–230.

(63) Bullock, R. M.; Das, A. K.; Appel, A. M. *Chem. - A Eur. J.* **2017**, *23*, 7626–7641.

(64) Mueller-Westerhoff, U. T.; Nazzal, A. *J. Am. Chem. Soc.* **1984**, *106*, 5381–5382.

(65) Nikolaychuk, P. A. *Silicon* **2014**, *6*, 109–116.

(66) Sun, K.; Shen, S.; Liang, Y.; Burrows, P. E.; Mao, S. S.; Wang, D. *Chem. Rev.* **2014**, *114*, 8662–8719.

(67) Lee, M. H.; Takei, K.; Zhang, J.; Kapadia, R.; Zheng, M.; Chen, Y. Z.; Nah, J.; Matthews, T. S.; Chueh, Y. L.; Ager, J. W.; Javey, A. *Angew. Chem. Int. Ed.* **2012**, *51*, 10760–10764.

(68) Hettick, M.; Zheng, M.; Lin, Y.; Sutter-Fella, C. M.; Ager, J. W.; Javey, A. *J. Phys. Chem. Lett.* **2015**, *6*, 2177–2182.

(69) Cedeno, D.; Krawicz, A.; Moore, G. F. *Interface Focus* **2015**, *5*, 20140085.

(70) Bansal, A.; Turner, J. A. *J. Phys. Chem. B* **2000**, *104*, 6591–6598.

(71) MacLeod, B. A.; Steirer, K. X.; Young, J. L.; Koldemir, U.; Sellinger, A.; Turner, J. A.; Deutsch, T. G.; Olson, D. C. *ACS Appl. Mater. Interfaces* **2015**, *7*, 11346–11350.

(72) Madani, M. R.; Ajmera, P. K. *Electron. Lett.* **1988**, *24*, 856–857.

(73) Lin, Y.; Battaglia, C.; Boccard, M.; Hettick, M.; Yu, Z.; Ballif, C.; Ager, J. W.; Javey, A. *Nano Lett.* **2013**, *13*, 5615–5618.

(74) Seger, B.; Pedersen, T.; Laursen, A.; Vesborg, P.; Hansen, O.; Chorkendorff, I. *J. Am. Chem. Soc.* **2013**, *135*, 1057–1064.

(75) Morales-Guio, C. G.; Thorwarth, K.; Niesen, B.; Liardet, L.; Patscheider, J.; Ballif, C.; Hu, X. *J. Am. Chem. Soc.* **2015**, *137*, 7035–7038.

(76) Seger, B.; Laursen, A. B.; Vesborg, P. C. K.; Pedersen, T.; Hansen, O.; Dahl, S.; Chorkendorff, I. *Angew. Chem. Int. Ed.* **2012**, *51*, 9128–9131.

(77) Schreier, M.; Luo, J.; Gao, P.; Moehl, T.; Mayer, M. T.; Grätzel, M. *J. Am. Chem. Soc.* **2016**, *138*, 1938–1946.

(78) Hu, S.; Lewis, N. S.; Ager, J. W.; Yang, J.; McKone, J. R.; Strandwitz, N. C. *J. Phys. Chem. C* **2015**, *119*, 24201–24228.

(79) Bae, D.; Seger, B.; Vesborg, P. C. K.; Hansen, O.; Chorkendorff, I. *Chem. Soc. Rev.* **2017**, *46*, 1933–1954.

(80) Gu, J.; Yan, Y.; Young, J. L.; Steirer, K. X.; Neale, N. R.; Turner, J. A. *Nat. Mater.* **2016**, *15*, 456–460.

(81) Conway, B. E.; Jerkiewicz, G. *Electrochim. Acta* **2000**, *45*, 4075–4083.

(82) McCrory, C. C. L.; Jung, S.; Ferrer, I. M.; Chatman, S. M.; Peters, J. C.; Jaramillo, T. F. *J. Am. Chem. Soc.* **2015**, *137*, 4347–4357.

(83) Lubitz, W.; Ogata, H.; Rüdiger, O.; Reijerse, E. *Chem. Rev.* **2014**, *114*, 4081–4148.

(84) Vincent, K. A.; Parkin, A.; Armstrong, F. A. *Chem. Rev.* **2007**, *107*, 4366–4413.

(85) Mersch, D.; Lee, C. Y.; Zhang, J. Z.; Brinkert, K.; Fontecilla-Camps, J. C.; Rutherford, A. W.; Reisner, E. *J. Am. Chem. Soc.* **2015**, *137*, 8541–8549.

(86) Lee, C. Y.; Park, H. S.; Fontecilla-Camps, J. C.; Reisner, E. *Angew. Chem. Int. Ed.* **2016**, *55*, 5971–5974.

(87) Reisner, E.; Powell, D. J.; Cavazza, C.; Fontecilla-Camps, J. C.; Armstrong, F. A. *J. Am. Chem. Soc.* **2009**, *131*, 18457–18466.

(88) Caputo, C. A.; Gross, M. A.; Lau, V. W.; Cavazza, C.; Lotsch, B. V.; Reisner, E. *Angew. Chem. Int. Ed.* **2014**, *53*, 11538–11542.

(89) Caputo, C. A.; Wang, L.; Beranek, R.; Reisner, E. *Chem. Sci.* **2015**, *6*, 5690–5694.

(90) Brown, K. A.; Wilker, M. B.; Boehm, M.; Dukovic, G.; King, P. W. *J. Am. Chem. Soc.* **2012**, *134*, 5627–5636.

(91) Peters, J. W.; Lanzilotta, W. N.; Lemon, B. J.; Seefeldt, L. C. *Science* **1998**, *282*, 1853–1858.

(92) Nicolet, Y.; Piras, C.; Legrand, P.; Hatchikian, C. E.; Fontecilla-Camps, J. C. *Structure* **1999**, *7*, 13–23.

(93) Ogata, H.; Hirota, S.; Nakahara, A.; Komori, H.; Shibata, N.; Kato, T.; Kano, K.; Higuchi, Y. *Structure* **2005**, *13*, 1635–1642.

(94) Evans, R. M.; Brooke, E. J.; Wehlin, S. A.; Nomerotskaia, E.; Sargent, F.; Carr, S. B.; Phillips, S. E.; Armstrong, F. A. *Nat. Chem. Biol.* **2016**, *12*, 46–50.

(95) Berggren, G.; Adamska, A.; Lambertz, C.; Simmons, T. R.; Esselborn, J.; Atta, M.; Gambarelli, S.; Mouesca, J. M.; Reijerse, E.; Lubitz, W.; Happe, T.; Artero, V.; Fontecave, M. *Nature* **2013**, *499*, 66–69.

(96) Felton, G. A.; Mebi, C. A.; Petro, B. J.; Vannucci, A. K.; Evans, D. H.; Glass, R. S.; Lichtenberger, D. L. *J. Organomet. Chem.* **2009**, *694*, 2681–2699.

(97) Pullen, S.; Fei, H.; Orthaber, A.; Cohen, S. M.; Ott, S. *J. Am. Chem. Soc.* **2013**, *135*, 16997–17003.

(98) Wang, H. Y.; Wang, W. G.; Si, G.; Wang, F.; Tung, C. H.; Wu, L. Z. *Langmuir* **2010**, *26*, 9766–9771.

(99) Li, X.; Wang, M.; Zheng, D.; Han, K.; Dong, J.; Sun, L. *Energy Environ. Sci.* **2012**, *5*, 8220–8224.

(100) Wombwell, C.; Reisner, E. *Chem. - A Eur. J.* **2015**, *21*, 8096–8104.

(101) Simmons, T. R.; Berggren, G.; Bacchi, M.; Fontecave, M.; Artero, V. *Coord. Chem. Rev.* **2014**, *270-271*, 127–150.

(102) Schrauzer, G. N.; Kohnle, J. *Chem. Ber.* **1964**, *97*, 3056–3064.

(103) Connolly, P.; Espenson, J. H. *Inorg. Chem.* **1986**, *25*, 2684–2688.

(104) Du, P.; Schneider, J.; Luo, G.; Brennessel, W. W.; Eisenberg, R. *Inorg. Chem.* **2009**, *48*, 4952–4962.

(105) Du, P.; Knowles, K.; Eisenberg, R. *J. Am. Chem. Soc* **2008**, *130*, 12576–12577.

(106) Lakadamyali, F.; Reisner, E. *Chem. Commun.* **2011**, *47*, 1695–1697.

(107) Reuillard, B.; Warnan, J.; Leung, J. J.; Wakerley, D. W.; Reisner, E. *Angew. Chem. Int. Ed.* **2016**, *55*, 3952–3957.

(108) Fihri, A.; Artero, V.; Pereira, A.; Fontecave, M. *Dalton Trans.* **2008**, 5567–5569.

(109) Fihri, A.; Artero, V.; Razavet, M.; Baffert, C.; Leibl, W.; Fontecave, M. *Angew. Chem. Int. Ed.* **2008**, *47*, 564–567.

(110) Wakerley, D. W.; Reisner, E. *Energy Environ. Sci.* **2015**, *8*, 2283–2295.

(111) Wakerley, D. W.; Gross, M. A.; Reisner, E. *Chem. Commun.* **2014**, *50*, 15995–15998.

(112) Lakadamyali, F.; Kato, M.; Muresan, N. M.; Reisner, E. *Angew. Chem. Int. Ed.* **2012**, *51*, 9381–9384.

(113) Razavet, M.; Artero, V.; Fontecave, M. *Inorg. Chem.* **2005**, *44*, 4786–4795.

(114) McCrory, C. C. L.; Uyeda, C.; Peters, J. C. *J. Am. Chem. Soc.* **2012**, *134*, 3164–3170.

(115) Simándi, L. I.; Szeverényi, Z.; Budó-Záhonyi, É. *Inorg. Nucl. Chem. Lett.* **1975**, *11*, 773–777.

(116) Wakerley, D. W.; Reisner, E. *Phys. Chem. Chem. Phys.* **2014**, *16*, 5739–5746.

(117) Jacques, P.-A.; Artero, V.; Pécaut, J.; Fontecave, M. *Proc. Natl. Acad. Sci. U. S. A.* **2009**, *106*, 20627–20632.

(118) Panagiotopoulos, A.; Ladomenou, K.; Sun, D.; Artero, V.; Coutsolelos, A. G. *Dalton Trans.* **2016**, *45*, 6732–6738.

(119) Muresan, N. M.; Willkomm, J.; Mersch, D.; Vaynzof, Y.; Reisner, E. *Angew. Chem. Int. Ed.* **2012**, *51*, 12749–12753.

(120) Willkomm, J.; Muresan, N. M.; Reisner, E. *Chem. Sci.* **2015**, *6*, 2727–2736.

(121) G. Märkl, V.; Jin, G.; Schoerner, C. *Tetrahedron Lett.* **1980**, *21*, 1409–1412.

(122) Wilson, A. D.; Newell, R. H.; McNevin, M. J.; Muckerman, J. T.; Rakowski DuBois, M.; DuBois, D. L. *J. Am. Chem. Soc.* **2006**, *128*, 358–366.

(123) Horvath, S.; Fernandez, L. E.; Soudackov, A. V.; Hammes-Schiffer, S. *Proc. Natl. Acad. Sci.* **2012**, *109*, 15663–15668.

(124) Rountree, E. S.; Dempsey, J. L. *J. Am. Chem. Soc.* **2015**, *137*, 13371–13380.

(125) Tran, P. D.; Le Goff, A.; Heidkamp, J.; Jousselme, B.; Guillet, N.; Palacin, S.; Dau, H.; Fontecave, M.; Artero, V. *Angew. Chem. Int. Ed.* **2011**, *50*, 1371–1374.

(126) Kilgore, U. J.; Roberts, J. A. S.; Pool, D. H.; Appel, A. M.; Stewart, M. P.; Rakowski DuBois, M.; Dougherty, W. G.; Kassel, W. S.; Bullock, R. M.; DuBois, D. L. *J. Am. Chem. Soc.* **2011**, *133*, 5861–5872.

(127) Kilgore, U. J.; Stewart, M. P.; Helm, M. L.; Dougherty, W. G.; Kassel, W. S.; Rakowski DuBois, M.; DuBois, D. L.; Bullock, R. M. *Inorg. Chem.* **2011**, *50*, 10908–10918.

(128) Gross, M. A.; Reynal, A.; Durrant, J. R.; Reisner, E. *J. Am. Chem. Soc.* **2014**, *136*, 356–366.

(129) Eckenhoff, W. T.; Eisenberg, R. *Dalton Trans.* **2012**, *41*, 13004–13021.

(130) Berardi, S.; Drouet, S.; Francàs, L.; Gimbert-Suriñach, C.; Guttentag, M.; Richmond, C.; Stoll, T.; Llobet, A. *Chem. Soc. Rev.* **2014**, *43*, 7501–7519.

(131) Royer, M. E. *C. R. Acad. Sci. Paris* **1870**, *70*, 73.

(132) Hori, Y. In *Mod. Asp. Electrochem.* Springer, New York, NY: 2008, pp 89–189.

(133) Whipple, D. T.; Kenis, P. J. *J. Phys. Chem. Lett.* **2010**, *1*, 3451–3458.

(134) Ran, J.; Jaroniec, M.; Qiao, S.-Z. *Adv. Mater.* **2018**, *30*, 1704649.

(135) Maia, L. B.; Moura, J. J.; Moura, I. *J. Biol. Inorg. Chem.* **2015**, *20*, 287–309.

(136) Jeoung, J.-H.; Dobbek, H. *Science* **2007**, *318*, 1461–1464.

(137) Boyington, J. C.; Gladyshev, V. N.; Khangulov, S. V.; Stadtman, T. C.; Sun, P. D. *Science* **1997**, *275*, 1305–1308.

(138) Tezuka, M.; Yajima, T.; Tsuchiya, A.; Matsumoto, Y.; Uchida, Y.; Hidai, M. *J. Am. Chem. Soc.* **1982**, *104*, 6834–6836.

(139) Takuma, M.; Ohki, Y.; Tatsumi, K. *Inorg. Chem.* **2005**, *44*, 6034–6043.

(140) Porcher, J. P.; Fogeron, T.; Gomez-Mingot, M.; Derat, E.; Chamoreau, L. M.; Li, Y.; Fontecave, M. *Angew. Chem. Int. Ed.* **2015**, *54*, 14090–14093.

(141) Savéant, J.-M. *Chem. Rev.* **2008**, *108*, 2348–2378.

(142) Sampson, M. D.; Nguyen, A. D.; Grice, K. A.; Moore, C. E.; Rheingold, A. L.; Kubiak, C. P. *J. Am. Chem. Soc.* **2014**, *136*, 5460–5471.

(143) Sampson, M. D.; Kubiak, C. P. *J. Am. Chem. Soc.* **2016**, *138*, 1386–1393.

(144) Smieja, J. M.; Sampson, M. D.; Grice, K. A.; Benson, E. E.; Froehlich, J. D.; Kubiak, C. P. *Inorg. Chem.* **2013**, *52*, 2484–2491.

(145) Agarwal, J.; Shaw, T. W.; Schaefer, H. F.; Bocarsly, A. B. *Inorg. Chem.* **2015**, *54*, 5285–5294.

(146) Franco, F.; Cometto, C.; Ferrero Vallana, F.; Sordello, F.; Priola, E.; Minero, C.; Nervi, C.; Gobetto, R. *Chem. Commun.* **2014**, *50*, 14670–14673.

(147) Costentin, C.; Robert, M.; Savéant, J. M. *Acc. Chem. Res.* **2015**, *48*, 2996–3006.

(148) Chapovetsky, A.; Do, T. H.; Haiges, R.; Takase, M. K.; Marinescu, S. C. *J. Am. Chem. Soc.* **2016**, *138*, 5765–5768.

(149) Duan, L.; Manbeck, G. F.; Kowalczyk, M.; Szalda, D. J.; Muckerman, J. T.; Himeda, Y.; Fujita, E. *Inorg. Chem.* **2016**, *55*, 4582–4594.

(150) Azcarate, I.; Costentin, C.; Robert, M.; Savéant, J. M. *J. Am. Chem. Soc.* **2016**, *138*, 16639–16644.

(151) Qiao, J.; Liu, Y.; Hong, F.; Zhang, J. *Chem. Soc. Rev.* **2014**, *43*, 631–675.

(152) Neri, G.; Aldous, I. M.; Walsh, J. J.; Hardwick, L. J.; Cowan, A. J. *Chem. Sci.* **2016**, *7*, 1521–1526.

(153) Costentin, C.; Robert, M.; Savéant, J.-M.; Tatin, A. *Proc. Natl. Acad. Sci.* **2015**, *112*, 6882–6886.

(154) Elgrishi, N.; Chambers, M. B.; Wang, X.; Fontecave, M. *Chem. Soc. Rev.* **2017**, *46*, 761–796.

(155) England, J.; Bill, E.; Weyhermüller, T.; Neese, F.; Atanasov, M.; Wieghardt, K. *Inorg. Chem.* **2015**, *54*, 12002–12018.

(156) Wang, M.; Weyhermüller, T.; Bill, E.; Ye, S.; Wieghardt, K. *Inorg. Chem.* **2016**, *55*, 5019–5036.

(157) Wang, M.; England, J.; Weyhermüller, T.; Wieghardt, K. *Inorg. Chem.* **2014**, *53*, 2276–2287.

(158) Hawecker, J.; Lehn, J.-M.; Ziessel, R. *J. Chem. Soc., Chem. Commun.* **1983**, 536–538.

(159) Bourrez, M.; Molton, F.; Chardon-Noblat, S.; Deronzier, A. *Angew. Chem. Int. Ed.* **2011**, *50*, 9903–9906.

(160) Machan, C. W.; Stanton, C. J.; Vandezande, J. E.; Majetich, G. F.; Schaefer, H. F.; Kubiak, C. P.; Agarwal, J. *Inorg. Chem.* **2015**, *54*, 8849–8856.

(161) Bourrez, M.; Orio, M.; Molton, F.; Vezin, H.; Duboc, C.; Deronzier, A.; Chardon-Noblat, S. *Angew. Chem. Int. Ed.* **2014**, *53*, 240–243.

(162) Lehn, J. M.; Ziessel, R. *Proc. Natl. Acad. Sci. U. S. A.* **1982**, *79*, 701–704.

(163) Simpson, T. C.; Durand, R. R. *Electrochim. Acta* **1988**, *33*, 581–583.

(164) Arana, C.; Yan, S.; Keshavarz-K., M.; Potts, K. T.; Abruña, H. D. *Inorg. Chem.* **1992**, *31*, 3680–3682.

(165) Keene, F. R.; Creutz, C.; Sutin, N. *Coord. Chem. Rev.* **1985**, *64*, 247–260.

(166) Elgrishi, N.; Chambers, M. B.; Artero, V.; Fontecave, M. *Phys. Chem. Chem. Phys.* **2014**, *16*, 13635–13644.

(167) Elgrishi, N.; Chambers, M. B.; Fontecave, M. *Chem. Sci.* **2015**, *6*, 2522–2531.

(168) Reynal, A.; Willkomm, J.; Muresan, N. M.; Lakadamyali, F.; Planells, M.; Reisner, E.; Durrant, J. R. *Chem. Commun.* **2014**, *50*, 12768–12771.

(169) Pujari, S. P.; Scheres, L.; Marcelis, A. T.; Zuilhof, H. *Angew. Chem. Int. Ed.* **2014**, *53*, 6322–6356.

(170) Mutin, P. H.; Guerrero, G.; Vioux, A. *J. Mater. Chem.* **2005**, *15*, 3761–3768.

(171) Materna, K. L.; Crabtree, R. H.; Brudvig, G. W. *Chem. Soc. Rev.* **2017**, *46*, 6099–6110.

(172) Martini, L. A.; Moore, G. F.; Milot, R. L.; Cai, L. Z.; Sheehan, S. W.; Schmuttenmaer, C. A.; Brudvig, G. W.; Crabtree, R. H. *J. Phys. Chem. C* **2013**, *117*, 14526–14533.

(173) Brewster, T. P.; Konezny, S. J.; Sheehan, S. W.; Martini, L. A.; Schmuttenmaer, C. A.; Batista, V. S.; Crabtree, R. H. *Inorg. Chem.* **2013**, *52*, 6752–6764.

(174) Brennan, B. J.; Llansola Portolés, M. J.; Liddell, P. A.; Moore, T. A.; Moore, A. L.; Gust, D. *Phys. Chem. Chem. Phys.* **2013**, *15*, 16605–16614.

(175) Boissezon, R.; Muller, J.; Beaugeard, V.; Monge, S.; Robin, J.-J. *RSC Adv.* **2014**, *4*, 35690–35707.

(176) Paniagua, S. A.; Giordano, A. J.; Smith, O. L.; Barlow, S.; Li, H.; Armstrong, N. R.; Pemberton, J. E.; Brédas, J. L.; Ginger, D.; Marder, S. R. *Chem. Rev.* **2016**, *116*, 7117–7158.

(177) Ernstorfer, R.; Gundlach, L.; Felber, S.; Storck, W.; Eichberger, R.; Willig, F. *J. Phys. Chem. B* **2006**, *110*, 25383–25391.

(178) Bae, E.; Choi, W.; Park, J.; Shin, H. S.; Kim, S. B.; Lee, J. S. *J. Phys. Chem. B* **2004**, *108*, 14093–14101.

(179) Finnie, K. S.; Bartlett, J. R.; Woolfrey, J. L. *Langmuir* **1998**, *14*, 2744–2749.

(180) Yu, Z.; Li, F.; Sun, L. *Energy Environ. Sci.* **2015**, *8*, 760–775.

(181) Brodard-Severac, F.; Guerrero, G.; Maquet, J.; Florian, P.; Gervais, C.; Mutin, P. H. *Chem. Mater.* **2008**, *20*, 5191–5196.

(182) Paniagua, S. A.; Hotchkiss, P. J.; Jones, S. C.; Marder, S. R.; Mudalige, A.; Marrikar, F. S.; Pemberton, J. E.; Armstrong, N. R. *J. Phys. Chem. C* **2008**, *112*, 7809–7817.

(183) Gawalt, E. S.; Avaltroni, M. J.; Koch, N.; Schwartz, J. *Langmuir* **2001**, *17*, 5736–5738.

(184) Hanson, E. L.; Schwartz, J.; Nickel, B.; Koch, N.; Danisman, M. F. *J. Am. Chem. Soc.* **2003**, *125*, 16074–16080.

(185) Lim, M. S.; Feng, K.; Chen, X.; Wu, N.; Raman, A.; Nightingale, J.; Gawalt, E. S.; Korakakis, D.; Hornak, L. A.; Timperman, A. T. *Langmuir* **2007**, *23*, 2444–2452.

(186) Gillaizeau-Gauthier, I.; Odobel, F.; Alebbi, M.; Argazzi, R.; Costa, E.; Bignozzi, C. A.; Qu, P.; Meyer, G. J. *Inorg. Chem.* **2001**, *40*, 6073–6079.

(187) Hanson, K.; Brennaman, M. K.; Luo, H.; Glasson, C. R. K.; Concepcion, J. J.; Song, W.; Meyer, T. J. *ACS Appl. Mater. Interfaces* **2012**, *4*, 1462–1469.

(188) Norris, M. R.; Concepcion, J. J.; Glasson, C. R.; Fang, Z.; Lapides, A. M.; Ashford, D. L.; Templeton, J. L.; Meyer, T. J. *Inorg. Chem.* **2013**, *52*, 12492–12501.

(189) Queffélec, C.; Petit, M.; Janvier, P.; Knight, D. A.; Bujoli, B. *Chem. Rev.* **2012**, *112*, 3777–3807.

(190) Zhang, L.; Cole, J. M. *ACS Appl. Mater. Interfaces* **2015**, *7*, 3427–3455.

(191) Mao, F.; Mano, N.; Heller, A. *J. Am. Chem. Soc.* **2003**, *125*, 4951–4957.

(192) Zhou, Q.; Shi, G. *J. Am. Chem. Soc.* **2016**, *138*, 2868–2876.

(193) Abe, T.; Yoshida, T.; Tokita, S.; Taguchi, F.; Imaya, H.; Kaneko, M. *J. Electroanal. Chem.* **1996**, *412*, 125–132.

(194) Plumeré, N.; Rüdiger, O.; Oughli, A. A.; Williams, R.; Vivekananthan, J.; Pöller, S.; Schuhmann, W.; Lubitz, W. *Nat. Chem.* **2014**, *6*, 822–827.

(195) MacAodha, D.; Ferrer, M. L.; Conghaile, P. Ó.; Kavanagh, P.; Leech, D. *Phys. Chem. Chem. Phys.* **2012**, *14*, 14667–14672.

(196) Hickey, D. P.; Milton, R. D.; Chen, D.; Sigman, M. S.; Minteer, S. D. *ACS Catal.* **2015**, *5*, 5519–5524.

(197) Reuillard, B.; Le Goff, A.; Cosnier, S. *Anal. Chem.* **2014**, *86*, 4409–4415.

(198) Pander, J. E.; Fogg, A.; Bocarsly, A. B. *ChemCatChem* **2016**, *8*, 3536–3545.

(199) Cosnier, S.; Holzinger, M. *Chem. Soc. Rev.* **2011**, *40*, 2146–2156.

(200) Cecchet, F.; Alebbi, M.; Bignozzi, C. A.; Paolucci, F. *Inorganica Chim. Acta* **2006**, *359*, 3871–3874.

(201) Lapides, A. M.; Ashford, D. L.; Hanson, K.; Torelli, D. A.; Templeton, J. L.; Meyer, T. J. *J. Am. Chem. Soc.* **2013**, *135*, 15450–15458.

(202) Ashford, D. L.; Lapides, A. M.; Vannucci, A. K.; Hanson, K.; Torelli, D. A.; Harrison, D. P.; Templeton, J. L.; Meyer, T. J. *J. Am. Chem. Soc.* **2014**, *136*, 6578–6581.

(203) Moss, J. A.; Yang, J. C.; Stipkala, J. M.; Wen, X.; Bignozzi, C. A.; Meyer, G. J.; Meyer, T. J. *Inorg. Chem.* **2004**, *43*, 1784–1792.

(204) Chardon-Noblat, S.; Deronzier, A.; Ziessel, R.; Zsoldos, D. *J. Electroanal. Chem.* **1998**, *444*, 253–260.

(205) Peczonczyk, S. L.; Mukherjee, J.; Carim, A. I.; Maldonado, S. *Langmuir* **2012**, *28*, 4672–4682.

(206) Stewart, M. P.; Maya, F.; Kosynkin, D. V.; Dirk, S. M.; Stapleton, J. J.; McGuiness, C. L.; Allara, D. L.; Tour, J. M. *J. Am. Chem. Soc.* **2004**, *126*, 370–378.

(207) Wang, X.; Ruther, R. E.; Streifer, J. A.; Hamers, R. J. *J. Am. Chem. Soc.* **2010**, *132*, 4048–4049.

(208) Richards, D.; Zemlyanov, D.; Ivanisevic, A. *Langmuir* **2010**, *26*, 8141–8146.

(209) Moore, G. F.; Sharp, I. D. *J. Phys. Chem. Lett.* **2013**, *4*, 568–572.

(210) Costentin, C.; Drouet, S.; Robert, M.; Savéant, J.-M. *J. Am. Chem. Soc.* **2012**, *134*, 11235–11242.

(211) Andreiadis, E. S.; Jacques, P. A.; Tran, P. D.; Leyris, A.; Chavarot-Kerlidou, M.; Jousselme, B.; Matheron, M.; Pécaut, J.; Palacin, S.; Fontecave, M.; Artero, V. *Nat. Chem.* **2013**, *5*, 48–53.

(212) Reuillard, B.; Ly, K. H.; Rosser, T. E.; Kuehnel, M. F.; Zebger, I.; Reisner, E. *J. Am. Chem. Soc.* **2017**, *139*, 14425–14435.

(213) Kuehnel, M. F.; Orchard, K. L.; Dalle, K. E.; Reisner, E. *J. Am. Chem. Soc.* **2017**, *139*, 7217–7223.

(214) Ibrahim, S. K.; Liu, X.; Tard, C.; Pickett, C. J. *Chem. Commun.* **2007**, 1535–1537.

(215) Kramer, W. W.; McCrory, C. C. L. *Chem. Sci.* **2016**, *7*, 2506–2515.

(216) Aga, H.; Aramata, A.; Hisaeda, Y. *J. Electroanal. Chem.* **1997**, *437*, 111–118.

(217) Yoshida, T.; Kamato, K.; Tsukamoto, M.; Iida, T.; Schlettwein, D.; Wöhrle, D.; Kaneko, M. *J. Electroanal. Chem.* **1995**, *385*, 209–225.

(218) Birdja, Y. Y.; Vos, R. E.; Wezendonk, T. A.; Jiang, L.; Kapteijn, F.; Koper, M. T. *ACS Catal.* **2018**, *8*, 4420–4428.

(219) Lieber, C. M.; Lewis, N. S. *J. Am. Chem. Soc.* **1984**, *106*, 5033–5034.

(220) Atoguchi, T.; Aramata, A.; Kazusaka, A.; Enyo, M. *J. Electroanal. Chem.* **1991**, *318*, 309–320.

(221) Huheey, J. E. In *Inorg. Chem. Princ. Struct. React.* 3rd ed.; Harper & Row: New York, 1983, p 539.

(222) O'Toole, T. R.; Margerum, L. D.; Westmoreland, T. D.; Vining, W. J.; Murray, R. W.; Meyer, T. J. *J. Chem. Soc. Chem. Commun.* **1985**, 1416–1417.

(223) Windle, C. D.; Pastor, E.; Reynal, A.; Whitwood, A. C.; Vaynzof, Y.; Durrant, J. R.; Perutz, R. N.; Reisner, E. *Chem. - A Eur. J.* **2015**, *21*, 3746–3754.

(224) Rosser, T. E.; Windle, C. D.; Reisner, E. *Angew. Chem. Int. Ed.* **2016**, *55*, 7388–7392.

(225) Arana, C.; Keshavarz, M.; Potts, K.; Abruña, H. *Inorganica Chim. Acta* **1994**, *225*, 285–295.

(226) Hurrell, H. C.; Mogstad, A. L.; Usifer, D. A.; Potts, K. T.; Abruña, H. D. *Inorg. Chem.* **1989**, *28*, 1080–1084.

(227) Walsh, J. J.; Neri, G.; Smith, C. L.; Cowan, A. J. *Chem. Commun.* **2014**, *50*, 12698–12701.

(228) Seo, J.; Pekarek, R. T.; Rose, M. J. *Chem. Commun.* **2015**, *51*, 13264–13267.

(229) Nann, T.; Ibrahim, S. K.; Woi, P. M.; Xu, S.; Ziegler, J.; Pickett, C. J. *Angew. Chem. Int. Ed.* **2010**, *49*, 1574–1577.

(230) Buriak, J. M. *Chem. Rev.* **2002**, *102*, 1271–1308.

(231) Krawicz, A.; Cedeno, D.; Moore, G. F. *Phys. Chem. Chem. Phys.* **2014**, *16*, 15719–16314.

(232) Krawicz, A.; Yang, J.; Anzenberg, E.; Yano, J.; Sharp, I. D.; Moore, G. F. *J. Am. Chem. Soc.* **2013**, *135*, 11861–11868.

(233) Muckerman, J. T.; Fujita, E. *Chem. Commun.* **2011**, *47*, 12456–12458.

(234) Solis, B. H.; Hammes-Schiffer, S. *Inorg. Chem.* **2011**, *50*, 11252–11262.

(235) Cedeno, D.; Krawicz, A.; Doak, P.; Yu, M.; Neaton, J. B.; Moore, G. F. *J. Phys. Chem. Lett.* **2014**, *5*, 3222–3226.

(236) Bakac, A.; Espenson, J. H. *J. Am. Chem. Soc.* **1984**, *106*, 5197–5202.

(237) Beiler, A. M.; Khusnutdinova, D.; Jacob, S. I.; Moore, G. F. *Ind. Eng. Chem. Res.* **2016**, *55*, 5306–5314.

(238) Beiler, A. M.; Khusnutdinova, D.; Jacob, S. I.; Moore, G. F. *ACS Appl. Mater. Interfaces* **2016**, *8*, 10038–10047.

(239) Khusnutdinova, D.; Beiler, A. M.; Wadsworth, B. L.; Jacob, S. I.; Moore, G. F. *Chem. Sci.* **2017**, *8*, 253–259.

(240) Beiler, A. M.; Khusnutdinova, D.; Wadsworth, B. L.; Moore, G. F. *Inorg. Chem.* **2017**, *56*, 12178–12185.

(241) Price, M. J.; Maldonado, S. *J. Phys. Chem. C* **2009**, *113*, 11988–11994.

(242) Sun, J.; Liu, C.; Yang, P. *J. Am. Chem. Soc.* **2011**, *133*, 19306–19309.

(243) Kaiser, B.; Fertig, D.; Ziegler, J.; Klett, J.; Hoch, S.; Jaegermann, W. *ChemPhysChem* **2012**, *13*, 3053–3060.

(244) Walter, M. G.; Warren, E. L.; McKone, J. R.; Boettcher, S. W.; Mi, Q.; Santori, E. A.; Lewis, N. S. *Chem. Rev.* **2010**, *110*, 6446–6473.

(245) Khaselev, O.; Turner, J. A. *J. Electrochem. Soc.* **1998**, *145*, 3335–3339.

(246) Clough, A. J.; Yoo, J. W.; Mecklenburg, M. H.; Marinescu, S. C. *J. Am. Chem. Soc.* **2015**, *137*, 118–121.

(247) Downes, C. A.; Marinescu, S. C. *J. Am. Chem. Soc.* **2015**, *137*, 13740–13743.

(248) Arai, T.; Sato, S.; Uemura, K.; Morikawa, T.; Kajino, T.; Motohiro, T. *Chem. Commun.* **2010**, *46*, 6944–6946.

(249) Arai, T.; Tajima, S.; Sato, S.; Uemura, K.; Morikawa, T.; Kajino, T. *Chem. Commun.* **2011**, *47*, 12664–12666.

(250) Sato, S.; Arai, T.; Morikawa, T.; Uemura, K.; Suzuki, T. M.; Tanaka, H.; Kajino, T. *J. Am. Chem. Soc.* **2011**, *133*, 15240–15243.

(251) Sekizawa, K.; Sato, S.; Arai, T.; Morikawa, T. *ACS Catal.* **2018**, *8*, 1405–1416.

(252) Apaydin, D. H.; Tordin, E.; Portenkirchner, E.; Aufischer, G.; Schlager, S.; Weichselbaumer, M.; Oppelt, K.; Sariciftci, N. S. *ChemistrySelect* **2016**, *6*, 1156–1162.

(253) Kou, Y.; Nakatani, S.; Sunagawa, G.; Tachikawa, Y.; Masui, D.; Shimada, T.; Takagi, S.; Tryk, D. A.; Nabetani, Y.; Tachibana, H.; Inoue, H. *J. Catal.* **2014**, *310*, 57–66.

(254) Kumagai, H.; Sahara, G.; Maeda, K.; Higashi, M.; Abe, R.; Ishitani, O. *Chem. Sci.* **2017**, *8*, 4242–4249.

(255) Sahara, G.; Kumagai, H.; Maeda, K.; Kaeffer, N.; Artero, V.; Higashi, M.; Abe, R.; Ishitani, O. *J. Am. Chem. Soc.* **2016**, *138*, 14152–14158.

(256) Sahara, G.; Abe, R.; Higashi, M.; Morikawa, T.; Maeda, K.; Ueda, K.; Ishitani, O. *Chem. Commun.* **2015**, *51*, 10722–10725.

(257) Alenezi, K.; Ibrahim, S. K.; Li, P.; Pickett, C. J. *Chem. - A Eur. J.* **2013**, *19*, 13522–13527.

(258) Torralba-Penalver, E.; Luo, Y.; Compain, J. D.; Chardon-Noblat, S.; Fabre, B. *ACS Catal.* **2015**, *5*, 6138–6147.

(259) He, D.; Jin, T.; Li, W.; Pantovich, S.; Wang, D.; Li, G. *Chem. Eur. J.* **2016**, *22*, 13064–13067.

Chapter 2

Interfacing Catalysts with *p*-type Silicon *via* a Mesoporous TiO_2 Interlayer towards Photoelectrocatalytic H_2 Reduction

The contents of this chapter have been published in a peer-reviewed article: Chem. Sci., **2017**, *8,* 5172-5180. *Results presented were obtained solely by the author of this thesis, with contributions from others as outlined here: Julien Warnan is acknowledged for characterising the photoelectrodes by IR, UV-vis and ICP-OES. Julien Warnan and Dong Heon Nam shared photoelectrode fabrication with the author. Jenny Zhang is acknowledged for sharing photoelectrocatalysis experiments on the hydrogenase-based photocathodes with the author. Benjamin Martindale and Janina Willkomm are both acknowledged for synthesising* ***NiP*** *and* ***CoP***[3]*, respectively. Raw XPS data was provided by the Cavendish Laboratory at the University of Cambridge.*

2.1 Introduction

Due to their numerous advantages as discussed previously in Chapter 1 (*e.g.* selective and atom-efficient catalysis, transparency and synthetic tuneability), the use of molecular catalysts represents an interesting strategy in developing

integrated systems for solar water splitting.[1] Several approaches have been pursued to electrically wire a molecular catalyst to a light harvester, both homogeneously and heterogeneously.[2–4] By addressing problems such as slow kinetics and the need for a high catalyst concentration, the immobilisation of molecules has gained more interest in recent years, resulting in the development of molecular catalyst-based photoelectrochemical cells.[5–14]

Despite significant progress being made in the assembly of molecular photoelectrodes, light-driven, H_2-evolving, molecular-based photocathodes that operate in aqueous media remain scarcely reported.[11,15–18] Those reported frequently suffer from low photocurrents, tedious optimisations, complex electrode architectures, modest photo-stabilities and limited versatility towards different molecular catalysts.[6,14] In this context, the straightforward and robust combination of molecular catalysts with a light-harvesting surface remains a major challenge, due in part to the need for water-stable light harvesters and molecular catalysts. Furthermore, a functional and efficient electrode requires the two components to be paired in a way to allow for effective electronic communication, whilst maintaining their intrinsic physicochemical properties, and providing a high loading of the catalyst.

Silicon is the second-most Earth-abundant element in the Earth's crust and its widespread utilisation in the photovoltaic industry has resulted in a substantial price drop for crystalline Si in recent years.[19] In addition, it possesses a conduction band energy level of around $-0.5\,\mathrm{V}$ *vs.* NHE (pH 7) and a band gap energy of 1.12 eV. This categorises Si as a potentially promising material for the assembly of a photoelectrode with significant driving force for proton reduction and the ability to harvest photons across a wide range of wavelengths, even those in the infrared.[20,21] Impressive photocurrents for proton reduction have been previously observed when *p*-Si was paired with a non-molecular catalyst.[22–26] Unfortunately, owing to the material's instability in aqueous or aerobic conditions due to the formation of an insulating silica (SiO_x) layer, these currents were not always maintained. Perhaps for this reason, proton reduction by immobilised molecular catalysts on *p*-Si has so far only been achieved in organic solvents.[7,12] Different protection layers have been reported to limit this instability, but often require severe precautions and expensive techniques during fabrication, such as ALD or other vacuum-driven deposition methods.[25]

Another potential limitation to the implementation of commercial crystalline *p*-Si as a light-harvesting substrate in photocathodes is its inherent flatness. This is especially problematic for molecular catalysts as they typically turn over more slowly and have a larger footprint than the benchmark noble metal platinum, which

requires an increased loading capacity to compensate for the reduced per effective surface area activity on the photocathode. A similar problem was addressed in dye-sensitised solar cells, where a high surface area architecture, commonly a mesoporous TiO_2 layer, is employed to boost the loading capacity of molecular dyes.[27,28] Incidentally, owing to its metal oxide nature and hydrophilicity, TiO_2 has been extensively reported as a tolerant, functionalisable platform for the immobilisation of a wide range of chemical species.[28–30] Due to its conduction and valence band energy levels being both lower than those of *p*-Si, TiO_2 is also expected to be able to act as an electron-selective layer that shuttles electrons to a surface-immobilised catalyst. Finally, TiO_2 has been shown to be able to protect Si as a flat ALD-deposited layer.[12,22]

The work described in this chapter therefore aims to demonstrate that a molecular catalyst can be efficiently and straightforwardly interfaced with *p*-Si to photoelectrochemically reduce protons to molecular hydrogen in aqueous conditions. Concurrently, we sought to engineer versatility into the choice of catalyst for which such a scaffold would be appropriate by employing a functionalisable mesoporous titanium dioxide (*meso*TiO_2) interlayer (Fig. 2.1). To this end, two phosphonated molecular proton reduction catalysts developed previously in our laboratory, DuBois-type **NiP** and cobalt diimine-dioxime **CoP^3**, were anchored at the surface of a mesoporous TiO_2 scaffold slot-coated onto Si (Fig. 2.1). **NiP** belongs to a family of hydrogenase-inspired Ni(II) bis(diphosphine) H_2 evolution catalysts that display high activity and operate in both aqueous and non-aqueous conditions (see Chapter 1 section 1.3.2).[31–33] The presence of phosphonic acid groups allows for its robust binding to metal oxides, making **NiP** a promising candidate for single-site heterogeneous proton reduction on electrodes. In addition, the Co diimine–dioxime catalyst **CoP^3** also bears a phosphonic acid anchoring group covalently bonded to the equatorial ligand of the catalyst core for robust attachment on metal oxides, and a pendant axial pyridine ligand to improve the performance for H_2 catalysis.[34] Although high loadings of these molecules on metal oxides have been previously demonstrated, their successful incorporation as functional catalysts in a photocathodic device remains elusive.[13,34,35]

Metallic platinum and a [NiFeSe]-hydrogenase (H_2ase) were also employed as proton reduction catalysts on this Si|*meso*TiO_2 scaffold, with the former acting as a benchmark precious metal and the latter determining the photocathode's biocompatibility. In addition to characterising the activity and stability of these electrodes, photoelectrochemical studies were also conducted to explore the presence of long-lived charges in the CB of TiO_2.

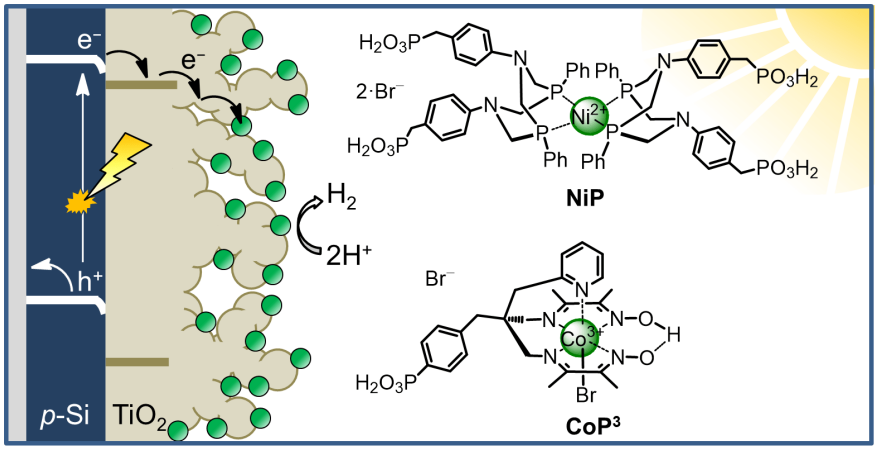

Fig. 2.1 Schematic diagram of PEC H_2 evolution with the Si|*meso*TiO_2|catalyst photocathode and chemical structures of the immobilised molecular catalysts **NiP** and **CoP³**.

2.2 Results and Discussion

2.2.1 Assembly of Molecular Photocathodes

The first step towards realising the final functional molecular photocathode required the development of a method for the preparation of the mesoporous TiO_2 interlayer on *p*-Si that would require only facile and low-cost laboratory techniques, while still presenting a photoelectrode platform that would prove to be robust in aqueous operating conditions. This was achieved in a relatively straightforward manner, as follows. Immediately after etching *p*-Si with hydrofluoric acid to remove native oxide that would have formed upon the wafer's exposure to air, a TiO_2 paste (15–20 nm particles, 100 % anatase) was slot-coated over a defined area of *p*-Si and the assembly annealed under atmospheric conditions following a controlled step-wise sintering procedure up to 450 °C (see Section 2.4.2 for full experimental details).

The approximately 6 µm-thick TiO_2 layer of the resulting electrode (Si|-*meso*TiO_2) was homogeneous and crack-free, as is evident in images taken by scanning electron microscopy (SEM; Fig. 2.2a-b). The uniformity of the *meso*TiO_2 film maintains semi-transparency (Fig. 2.3), which limits light scattering and bestows anti-reflective properties, allowing *p*-Si to collect more of the incident photons during front illumination in photoelectrochemical conditions and photogenerate more charges.

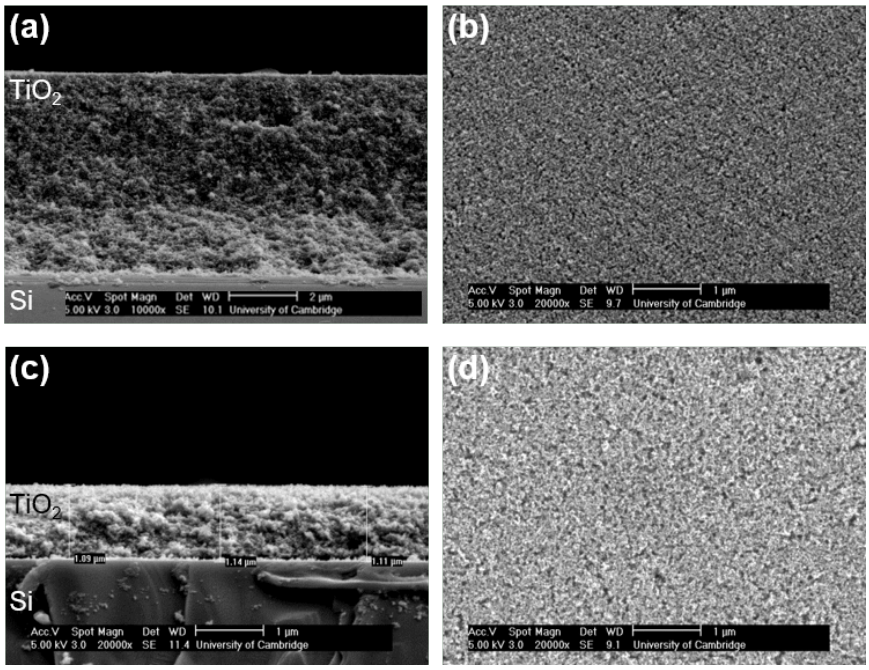

Fig. 2.2 SEM images of Si|*meso*TiO_2 electrodes with *meso*TiO_2 thickness of (a-b) 6.0 µm and (c-d) 1.1 µm, as viewed in cross-section and from the top, respectively.

Immobilisation of the molecular catalysts **NiP** or **CoP³** was accomplished *via* overnight immersion of Si|*meso*TiO_2 electrodes in a methanol (MeOH) solution of the desired catalyst (0.25 mM) to yield the final Si|*meso*TiO_2|**NiP** and Si|*meso*TiO_2|**CoP³** photocathodes, respectively. At this point, clear colour changes of the *meso*TiO_2 scaffold that correspond to the original colours of the molecular catalysts (yellow in the case of Si|*meso*TiO_2|**CoP³** and purple for Si|*meso*TiO_2|**NiP**; see Fig. 2.3 bottom right for illustration of **NiP**'s case) serve as the first testaments to their successful immobilisation. In order to prepare an analogous photoelectrode with a benchmark precious metal H_2 evolution catalyst for comparison of performances, Pt was thermodeposited on Si|*meso*TiO_2 from a solution of hexachloroplatinic acid, resulting in a Si|*meso*TiO_2|Pt electrode.

The final necessary steps towards completion of the photocathodes involved fabricating a conductive back contact and insulating the entire assembly with an epoxy adhesive to prevent short circuits occurring with the surrounding operating electrolyte solution, leaving uncovered only the area to be exposed to light illumination ($S \approx 0.2\,cm^2$). Full experimental details of all above steps are given in Experimental Section 2.4.2 and are represented photographically in Fig. 2.3.

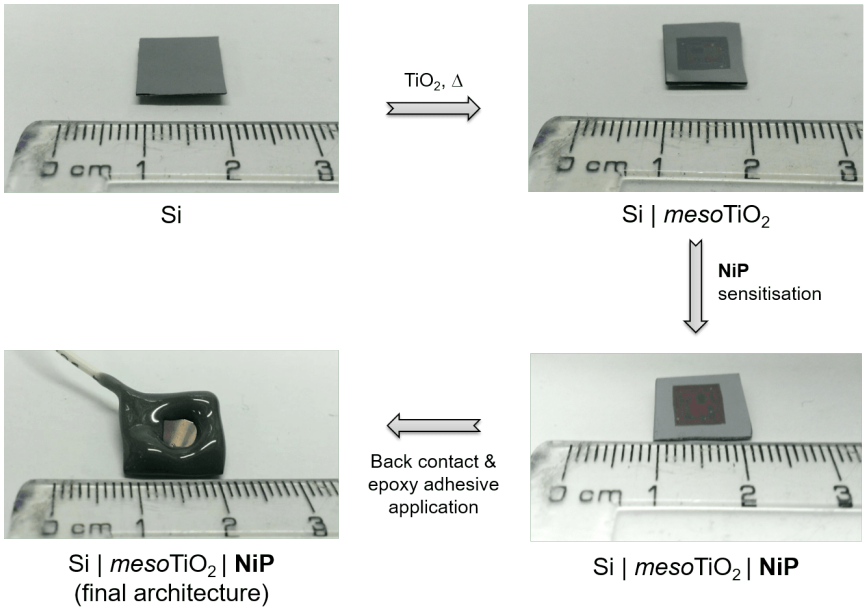

Fig. 2.3 Photographs of typical electrodes at various stages of preparation towards the final Si|*meso*TiO_2|**NiP** photocathode.

2.2.2 Physical Characterisation of Molecular Photocathodes

A number of spectroscopic techniques were employed to confirm the immobilisation and quantities of **NiP** and **CoP³** on the photoelectrodes. Firstly, comparison of the attenuated total reflectance Fourier-transform infrared (ATR-FTIR) spectra of the unbound catalysts to those of their corresponding catalyst-loaded electrodes confirmed the catalysts' successful attachment to the TiO_2 scaffold. Vibrational bands at 1610, 1509 and 1434 cm^{-1} observed in the spectrum of Si|*meso*TiO_2|**NiP** are consistent with the ATR-FTIR spectrum obtained of the **NiP** powder and were attributed to the aromatic rings' ν(C=C) and the δ(C–H) of the methylene bridges (Fig. 2.4, black and blue traces). In the case of **CoP³**-functionalised Si|*meso*TiO_2 electrodes, the aromatic rings' ν(C=C) and ν(C=N) vibrations were recorded at 1617 and 1538 cm^{-1}, concomitantly with the disappearance of the phosphonic acid-related vibrational bands at 1245 and 1131 cm^{-1} upon surface binding (Fig. 2.5, black and blue traces). The latter observation contrasts with that of the spectrum of the Si|*meso*TiO_2|**NiP** photoelectrode, where phosphonic acid features at 1251 and 1185 cm^{-1} still remain partially visible, most likely as a consequence of at least two out of four PO_3H_2 functions in **NiP** remaining unbound.

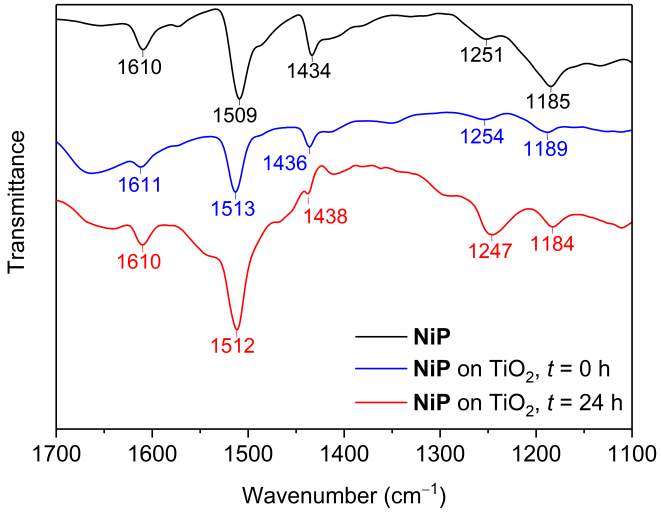

Fig. 2.4 ATR-FTIR spectra of **NiP** powder (black), and of Si|*meso*TiO_2|**NiP** before (blue) and after (red) 24 h CPPE.

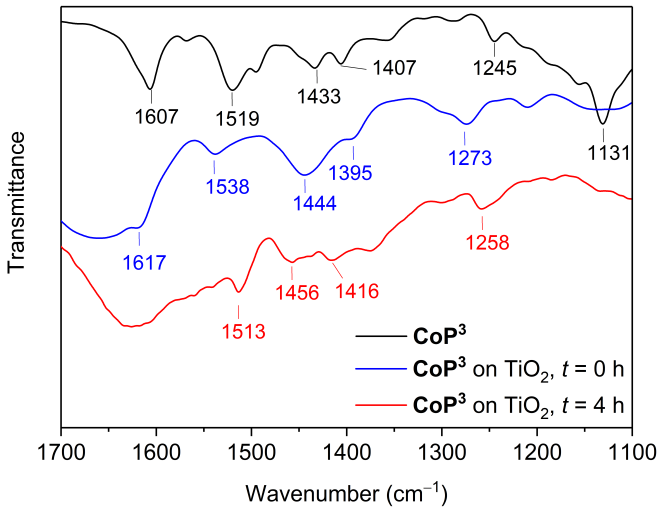

Fig. 2.5 ATR-FTIR spectra of **CoP^3** powder (black), and of Si|*meso*TiO_2|**CoP^3** before (blue) and after (red) 4 h CPPE.

X-ray photoelectron spectroscopy (XPS) spectra show characteristic binding energy peaks in the Co_{2p} or Ni_{2p}, N_{1s} and P_{2p} regions for fresh Si|*meso*TiO_2|**CoP³** and Si|*meso*TiO_2|**NiP** electrodes, respectively, at energies close to those previously reported for similar catalysts (Fig. 2.6 and 2.7, blue traces).[13,36,37] In the Co_{2p} region of the former, two broad signals corresponding to $2p_{1/2}$ and $2p_{3/2}$ core levels were observed at 795.4 and 780.4 eV respectively, whereas the Ni_{2p} region of the latter shows the same respective core levels at 872.0 and 854.8 eV. Peaks in the N_{1s} and P_{2p} core level regions of both photocathodes arose from their ligands and anchoring groups.

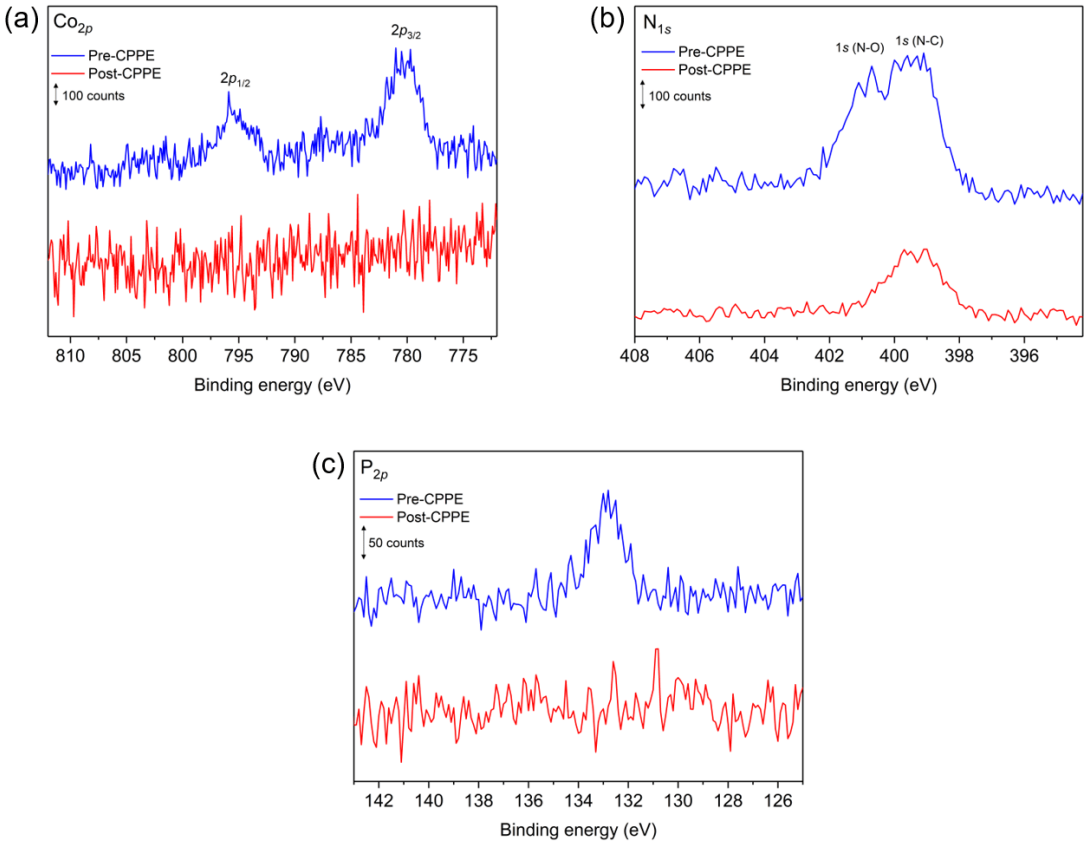

Fig. 2.6 XPS analysis of Si|*meso*TiO_2|**CoP³** electrodes in the (a) Co_{2p}, (b) N_{1s} and (c) P_{2p} regions, before (blue traces) and after (red traces) 30 min of CPPE.

The amounts of **CoP³** and **NiP** loaded onto the Si|*meso*TiO_2 electrodes were quantified by spectrophotometry following desorption of the catalyst from the corresponding electrode with tetrabutylammonium hydroxide in MeOH (0.1 M, Fig. B.1). The loadings of **CoP³** and **NiP** on Si|*meso*TiO_2 were determined to be $93.9 \pm 8.9\,\mathrm{mol\,cm^{-2}}$ and $38.3 \pm 4.2\,\mathrm{nmol\,cm^{-2}}$ (geometric surface area), respectively (Table 2.1). The higher loading of **CoP³** is in line with a smaller steric footprint as compared to the **NiP** molecule. Reducing the thickness of

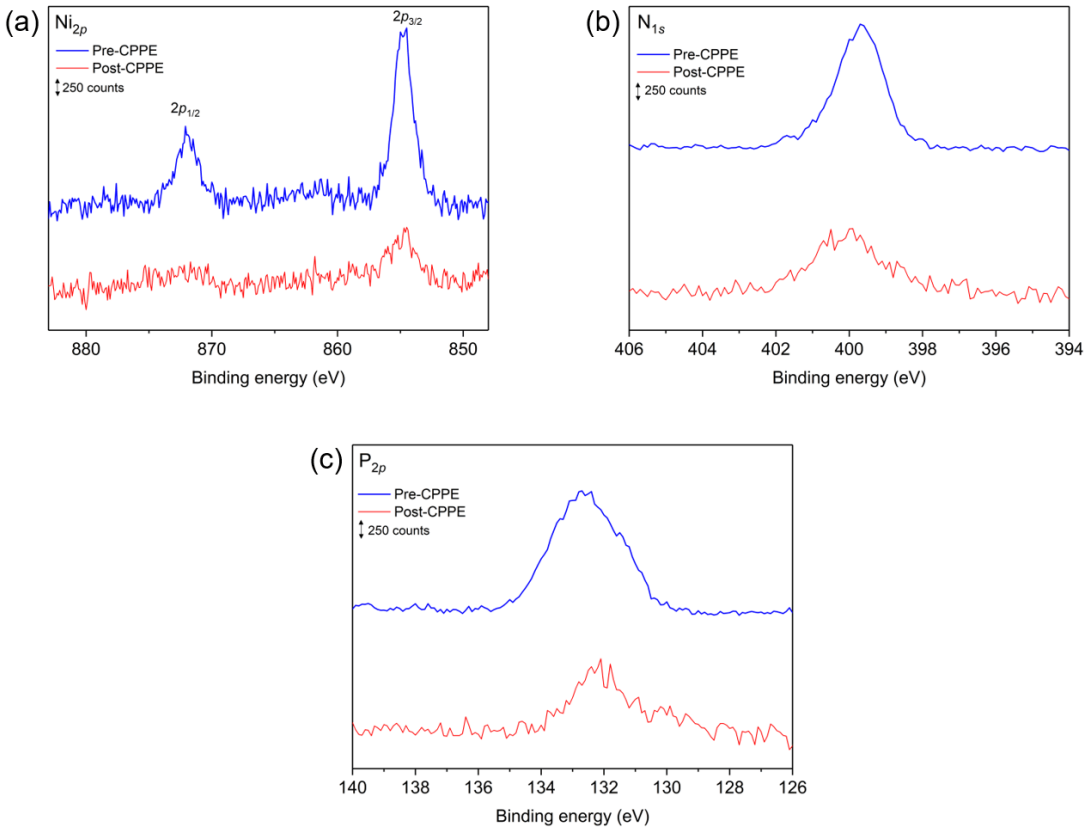

Fig. 2.7 XPS analysis of Si|*meso*TiO_2|**NiP** electrodes in the (a) Ni_{2p}, (b) N_{1s} and (c) P_{2p} regions, before (blue traces) and after (red traces) 24 h of CPPE.

the mesoporous scaffold resulted in a lower molecular loading, as demonstrated with **NiP** ($5.6 \pm 1.4\,\mathrm{nmol\,cm^{-2}}$ on *meso*TiO_2 thickness of 1.1 µm). The fact that loading scales more or less linearly with thickness suggests that full penetration of the molecular catalyst throughout the thicker mesoporous *meso*TiO_2 film is occurring. Overall, these values are consistent with previously reported loadings onto mesoporous metal oxide-based electrodes for phosphonic acid-bearing catalysts.[10,13,34]

Table 2.1 Quantification of molecular catalysts loaded on the surface of different photoelectrodes as estimated by UV-vis spectroscopy measurements. Loadings are given per geometrical surface area.

Photocathode	*meso*TiO_2 layer thickness (µm)	Molecular catalyst loadings ($\mathrm{nmol\,cm^{-2}}$)
Si|*meso*TiO_2|**CoP³**	6.0	93.9 ± 8.9
Si|*meso*TiO_2|**NiP**	6.0	38.3 ± 4.2
Si|*meso*TiO_2|**NiP**	1.1	5.6 ± 1.4

2.2.3 Photoelectrocatalytic H_2 Evolution

The photoelectrocatalytic performances of the molecular H_2 evolution photoelectrodes Si|*meso*TiO_2|**NiP** and Si|*meso*TiO_2|**CoP³** were determined by a series of photoelectrochemical experiments, namely: linear sweep voltammetry, controlled potential photoelectrolysis (CPPE) and a determination of incident photon-to-electron efficiency (IPCE) under applied bias. In some cases, the results were compared to those obtained with the benchmark Si|*meso*TiO_2|Pt photoelectrode.

Linear sweep voltammograms (LSVs) under chopped UV-filtered simulated solar illumination (AM1.5G, 100 mW cm^{-2}, $\lambda > 400\,\mathrm{nm}$) were recorded of the Si|*meso*TiO_2|**NiP** and Si|*meso*TiO_2|**CoP³** photocathodes and compared to those of Si|*meso*TiO_2|Pt, Si|*meso*TiO_2 and bare Si (submitted to the same sintering steps as all other electrodes; Fig. 2.8). In pH 4.5 aqueous electrolyte solution (0.1 M acetic acid), a photocurrent onset potential (E_{onset}) of approximately 0.4 V *vs.* RHE is observed for all Si|*meso*TiO_2 electrodes (with and without catalysts), and the *meso*TiO_2-free (bare) *p*-Si counterpart remains inactive even at more cathodic potentials. The passivity of the bare *p*-Si electrode is attributed to the fast, heat-accelerated formation of an insulating layer of silica *via* a thermal oxidation reaction, as is consistent with previous reports.[38] This inactivity of the bare electrode demonstrates that, remarkably, simple slot-coating with a porous *meso*TiO_2

scaffold (the preparation method previously described) can limit complete Si insulation and enable a productive electron transfer pathway from photoexcited *p*-Si to the CB of *meso*TiO_2 in the case of the *meso*TiO_2-coated electrodes, despite the high temperature annealing process under atmospheric conditions. It is noted that a large proportion of the photocurrent observed from the catalyst-free Si|*meso*TiO_2 electrode originates from a "charging" current (filling of the metal oxide's CB) as opposed to productive catalysis; this mechanism is discussed in more detail below in section 2.2.7.

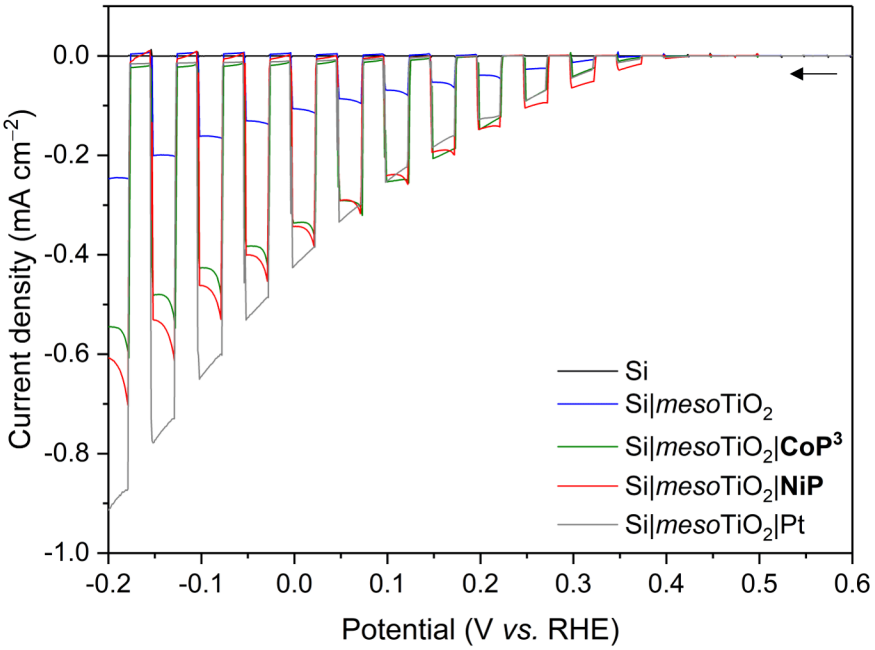

Fig. 2.8 LSVs of Si (black), Si|*meso*TiO_2 (blue), Si|*meso*TiO_2|**CoP^3** (green), Si|*meso*TiO_2|**NiP** (red) and Si|*meso*TiO_2|Pt (grey) electrodes under chopped illumination. Arrow indicates scan start and direction. Conditions: aqueous acetic acid solution (0.1 M, pH 4.5), UV-filtered simulated solar light irradiation (AM1.5G, 100 mW cm^{-2}, $\lambda > 400$ nm), N_2 atmosphere, room temperature, $\nu = 5$ mV s^{-1}.

Upon loading of Si|*meso*TiO_2 with proton reduction catalysts, the photocurrent is clearly enhanced: at 0.0 V *vs.* RHE, a photocurrent density ($|J|$) of 430 µA cm^{-2} is obtained with Si|*meso*TiO_2|Pt, whereas Si|*meso*TiO_2|**NiP** and Si|*meso*TiO_2|**CoP^3** achieve approximately 340 µA cm^{-2}. The broad cathodic recombination peaks observed in the LSVs of the molecular catalyst-loaded electrodes might originate from the slow kinetic rate of **NiP** and **CoP^3** to generate H_2. All catalyst-modified electrodes exhibit slightly earlier onset potentials than the unmodified Si|*meso*TiO_2 electrode (as can be seen more clearly in the LSV conducted under continuous light illumination in Fig. B.2). Nevertheless, the proximity of these values across all

electrodes suggests that E_{onset} is predominantly controlled by the *p*–*n* Si–*meso*TiO_2 interface, irrespective of modifications at the *meso*TiO_2–electrolyte interface.[12]

Although E_{onset} compares well with previously-reported crystalline *p*-Si-based photocathodes,[23,39] we observed a relatively small photocurrent with Si|*meso*TiO_2|-Pt,[25] which may be attributed to the formation of some insulating SiO_x layer during the aerobic sintering process. Nonetheless, our results with Si|*meso*TiO_2|Pt confirm that electron transfer from *p*-Si to a *meso*TiO_2-bound proton reduction catalyst is possible, and simultaneously allow us to elucidate the maximum photocurrent that is likely to be obtainable with our photocathode preparation if kinetic barriers were minimal at the catalyst–electrolyte interface. In fact, the photocurrent densities obtained compare well with those of the molecular catalyst-based electrodes, indicating that the molecular-based electrodes perform at maximum performance that can be expected under these conditions.

The effects of different *meso*TiO_2 thicknesses and pH conditions were also studied for the Si|*meso*TiO_2|**NiP** photocathodes (Fig. 2.9). As mentioned above, reducing the thickness of the mesoporous scaffold resulted in a proportionately lower loading of **NiP** ($5.6 \pm 1.4\,nmol\,cm^{-2}$ on *meso*TiO_2 with a thickness of 1.1 µm, Table 2.1) and consequently gave rise to a lower performing photocathode with smaller photocurrents (Fig. 2.9a). A pH optimum was observed at 4.5, which agrees with previous catalytic studies with **NiP** (Fig. 2.9b).[31]

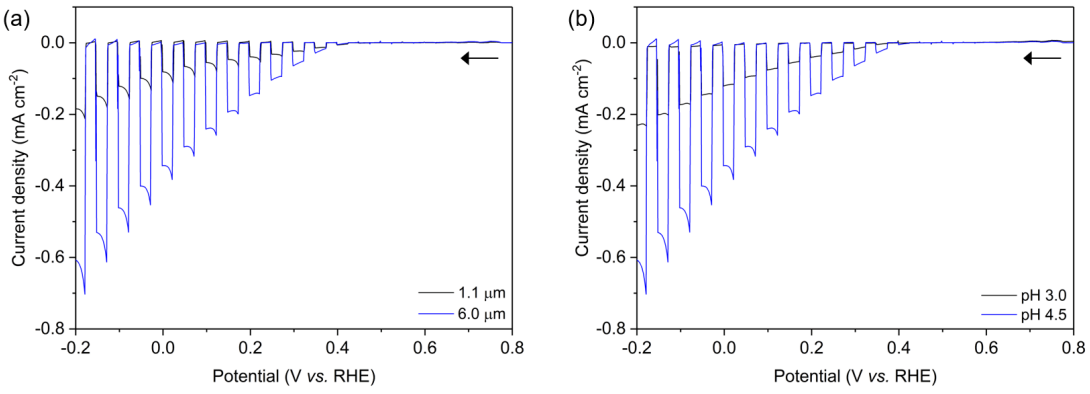

Fig. 2.9 LSVs under chopped illumination of Si|*meso*TiO_2|**NiP** electrodes, (a) prepared with two different thicknesses of the *meso*TiO_2 layer and tested under pH 4.5 conditions, and (b) prepared with a *meso*TiO_2 thickness of 6.0 µm and tested under two different pH conditions. Arrows indicate scan start and direction. Conditions: aqueous acetic acid solution (0.1 M), UV-filtered simulated solar light irradiation (AM1.5G, $100\,mW\,cm^{-2}$, $\lambda > 400\,nm$), N_2 atmosphere, room temperature, $\nu = 5\,mV\,s^{-1}$.

Having established the photocathode architecture as a viable platform on which to interface molecular catalysts, their prolonged H_2 evolution performance and stability were studied. This was carried out by way of controlled potential photoelectrolysis under UV-filtered simulated solar light illumination (AM1.5G, 100 mW cm^{-2}, $\lambda > 400$ nm) at an applied potential (E_{app}) of 0.0 V *vs.* RHE (Fig. 2.10) for up to 24 h, during which the headspace H_2 was analysed at regular intervals by gas chromatography (Fig. 2.11; see Experimental Section 2.4.4).

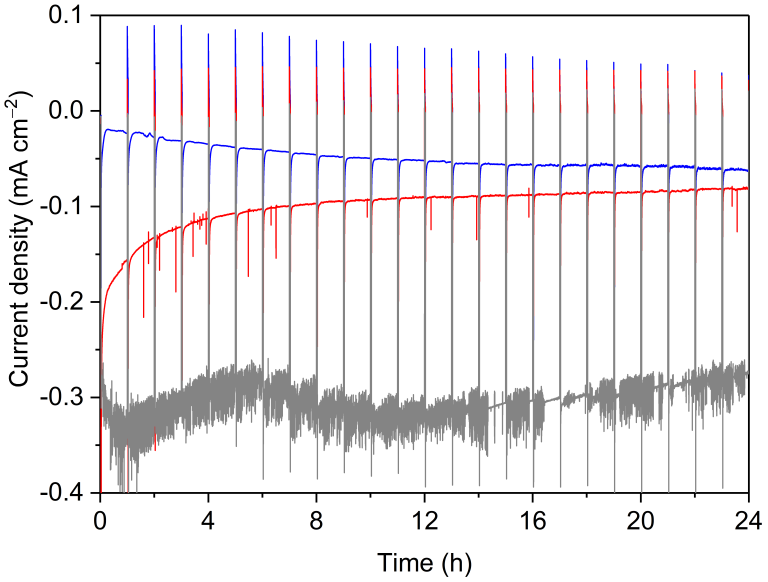

Fig. 2.10 CPPE traces for Si|*meso*TiO_2 (blue trace), Si|*meso*TiO_2|**NiP** (red trace) and Si|*meso*TiO_2|Pt (grey trace) electrodes at $E_{app} = 0.0$ V *vs.* RHE under continuous illumination with an hourly dark chop lasting for two min each. Conditions: aqueous acetic acid solution (0.1 M, pH 4.5), UV-filtered simulated solar light irradiation (AM1.5G, 100 mW cm^{-2}, $\lambda > 400$ nm), N_2 atmosphere, room temperature.

The bare *p*-Si electrode produced only a miniscule photocurrent density and detectable amounts of H_2 were not observed (Fig. B.3); this is unsurprising given the inactivity of this TiO_2-free photoelectrode as determined previously by linear sweep voltammetry. On the other hand, the Si|*meso*TiO_2 electrode is not innocent in proton reduction and produces a small amount of H_2. However, its low Faradaic efficiency of 28–30 % implies that the majority of the photocurrent must be generated from processes other than catalytic proton reduction (Fig. 2.11a). A likely source for this photocurrent - charging the CB of TiO_2 - is discussed below in section 2.2.7. Si|*meso*TiO_2|**NiP** displays a FE up to 87 % in the early stages of CPPE that remains at 76 ± 2 % even after 24 h. An increasing FE was observed during the first few hours, which is likely due to initial filling of trap states in TiO_2 and the reduction of residual O_2 in the pores of the mesoporous

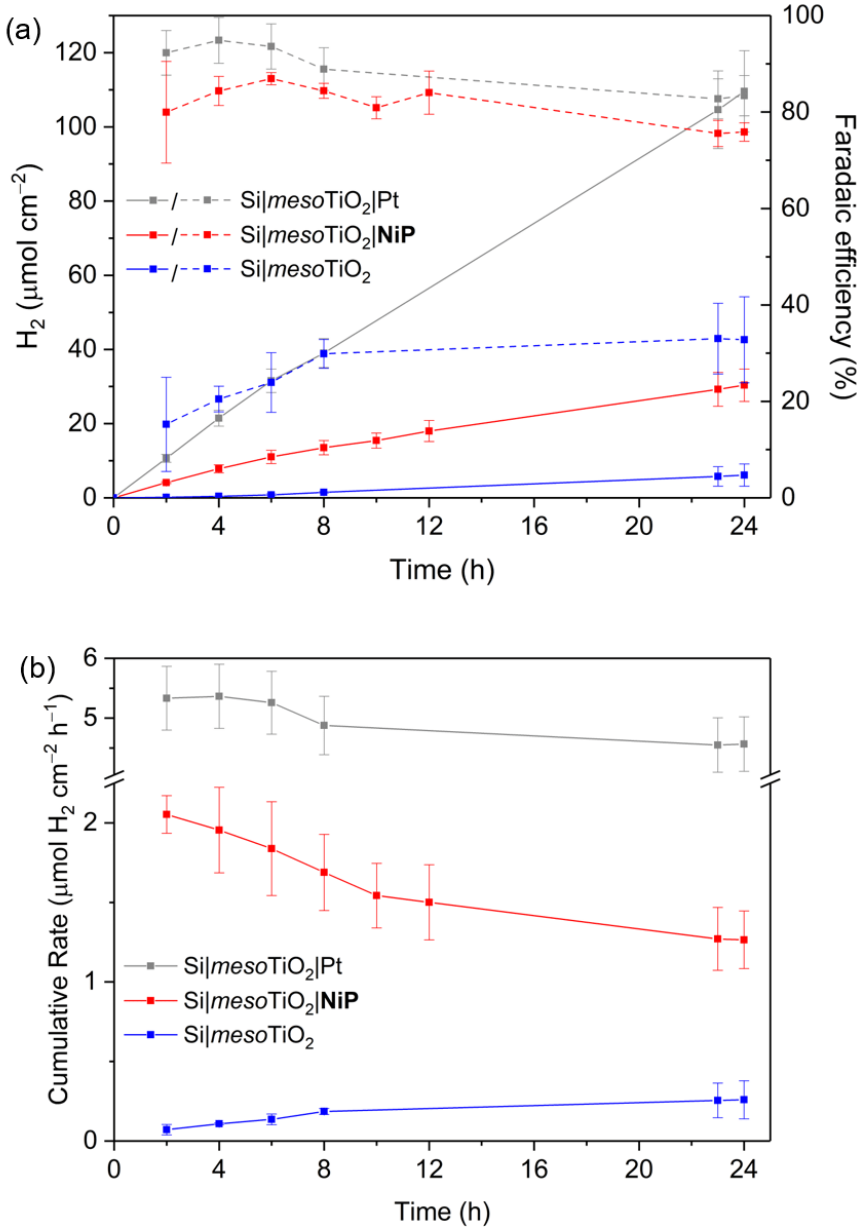

Fig. 2.11 CPPE data for Si|*meso*TiO_2 (blue traces), Si|*meso*TiO_2|**NiP** (red traces) and Si|*meso*TiO_2|Pt (grey traces) electrodes at $E_{app} = 0.0$ V *vs.* RHE during continuous UV-filtered simulated solar light irradiation. (a) H_2 evolution (solid lines) and Faradaic efficiency (cumulative over time; dashed lines); (b) cumulative rate of H_2 production per geometrical surface area of the electrodes. Conditions: aqueous acetic acid solution (0.1 M, pH 4.5), UV-filtered simulated solar light irradiation (AM1.5G, 100 mW cm^{-2}, $\lambda > 400$ nm), N_2 atmosphere, room temperature.

scaffold.[29] Generally, the slightly lower FE compared to the Pt-based electrode could be attributed to the progressive degradation/desorption of some reduced **NiP**, leading to unproductive electron transfer pathways. Nevertheless, these values are consistent with the FE reported previously for dark electrolysis of **NiP** on a *meso*TiO_2 electrode.[13] Tracking the cumulative rate of H_2 production per surface area also showed that the **NiP**-modified photocathode continues to exhibit greater H_2 evolution activity compared to an unmodied Si|*meso*TiO_2 electrode even after a day (Fig. 2.11b; note that the more conventional rate metric, turnover frequency, has not been used to compare the photoelectrodes in this case as it cannot be applied to the catalyst-free electrode).

A **NiP**-based turnover number ($TON_{\mathbf{NiP}}$) of 646 ± 141 was obtained after 24 h CPPE with the Si|*meso*TiO_2|**NiP** electrodes, and is close to being the highest TON reported for this catalyst in both homogeneous and heterogeneous configurations (Fig. 2.12).[8,13,31] Note, however, that this value was corrected for H_2 evolution from Si|*meso*TiO_2 and is therefore a lower estimate of its activity. If we assume a clear kinetic advantage of **NiP** over any solution-exposed *meso*TiO_2 and the catalyst's highly efficient communication with the metal oxide, then all electrons reaching the solution *via* the catalyst and not directly from *meso*TiO_2 would give an upper bound of $TON_{\mathbf{NiP}} = 1082 \pm 244$ at 24 h, representing a record value. Overall, these values are in agreement with the best previously reported $TON_{\mathbf{NiP}}$, where **NiP** was used in electrocatalytic and photocatalytic H_2 generation with sacrificial electron donors.[13,31,40] Importantly, this therefore demonstrates that the intrinsic activity of **NiP** can be exploited upon immobilisation onto photoelectrodes - something that remains a struggle in the attempt to immobilise all manner of molecular catalysts onto electrode systems in this field. It also supports the conclusion that the catalyst's molecular integrity is maintained throughout CPPE, as opposed to the previously reported transformation of some immobilised molecular catalysts under catalysis conditions.[41–43] The integrity of the molecular photoelectrodes post-CPPE was examined in greater detail with spectroscopic techniques as described in section 2.2.4 below.

Although the photocurrent density, FE and rate of H_2 production of Si|*meso*TiO_2-|**NiP** (blue traces in Figs. 2.10, 2.11 and 2.12) dropped gradually after several hours, most likely as a result of slow catalyst desorption/degradation, Si|*meso*TiO_2|Pt (grey traces), on the other hand, continued to evolve H_2 at near unity FE even after 24 h of CPPE, maintaining a steady photocurrent density throughout. The precious metal catalyst thereby demonstrates the enduring stability of the Si|*meso*TiO_2

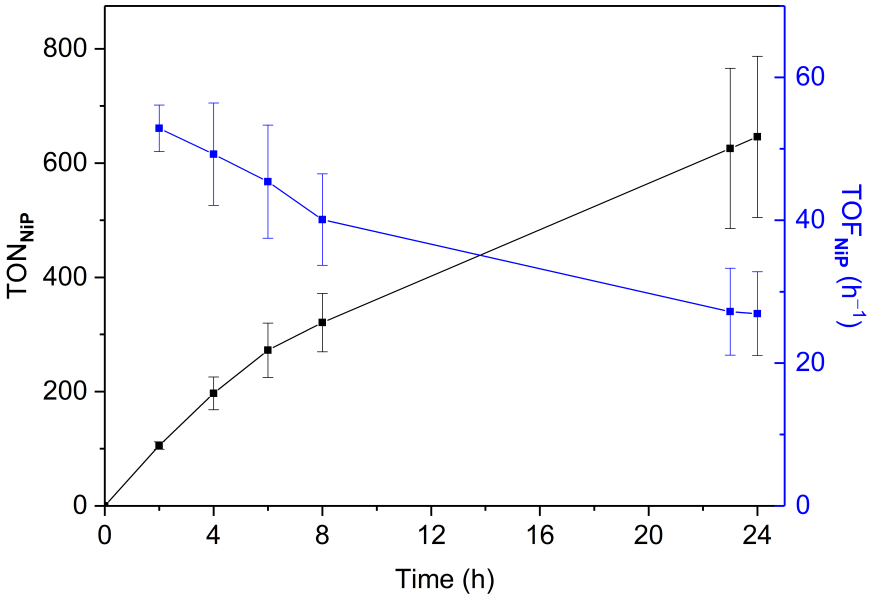

Fig. 2.12 Turnover number and turnover frequency (cumulative over duration of CPPE) of **NiP** over 24 h CPPE of Si|*meso*TiO_2|**NiP** (background H_2 production by a Si|*meso*TiO_2 control electrode has been subtracted). Conditions: $E_{app} = 0.0$ V *vs.* RHE, aqueous acetic acid solution (0.1 M, pH 4.5), UV-filtered simulated solar light irradiation (AM1.5G, 100 mW cm^{-2}, $\lambda > 400$ nm), N_2 atmosphere, room temperature.

architecture in aqueous conditions, and highlights its appeal as a scaffold for different proton reduction catalysts that could possess a range of stabilities.

CPPE of Si|*meso*TiO_2|**CoP³** revealed a photocathode that also possesses proton reduction capabilities superior to that of the unmodified Si|*meso*TiO_2 electrode for up to 1 h (Fig. 2.13). A progressive decline in the photocathode's performance is, however, apparent in both its slowing H_2 production rate and decreasing photocurrent density, the latter of which diminished significantly within the first 0.5 h of CPPE. This trend is in agreement with previous reports of the limited stability of **CoP³**, where degradation may be attributed to ligand hydrogenation and/or the formation of a ligand radical species.[34,44–46] In homogeneous solution systems, **NiP** is also generally a superior catalyst to the cobalt diimine–dioxime **CoP³**, and so it is also therefore unsurprising that their corresponding photoelectrodes possess the same relative performances. A final $TON_{\mathbf{CoP^3}}$ of 10.5 ± 0.5 (for which background H_2 evolution from Si|*meso*TiO_2 was once again subtracted to give the lower bound) was achieved after 4 h. As was the case with **NiP** and its respective photoelectrode, this TON value matches well with those reported for **CoP³** in homogeneous configurations,[34] once again demonstrating that in adopting this Si|*meso*TiO_2 scaffold, it is possible to directly transfer these molecular catalysts

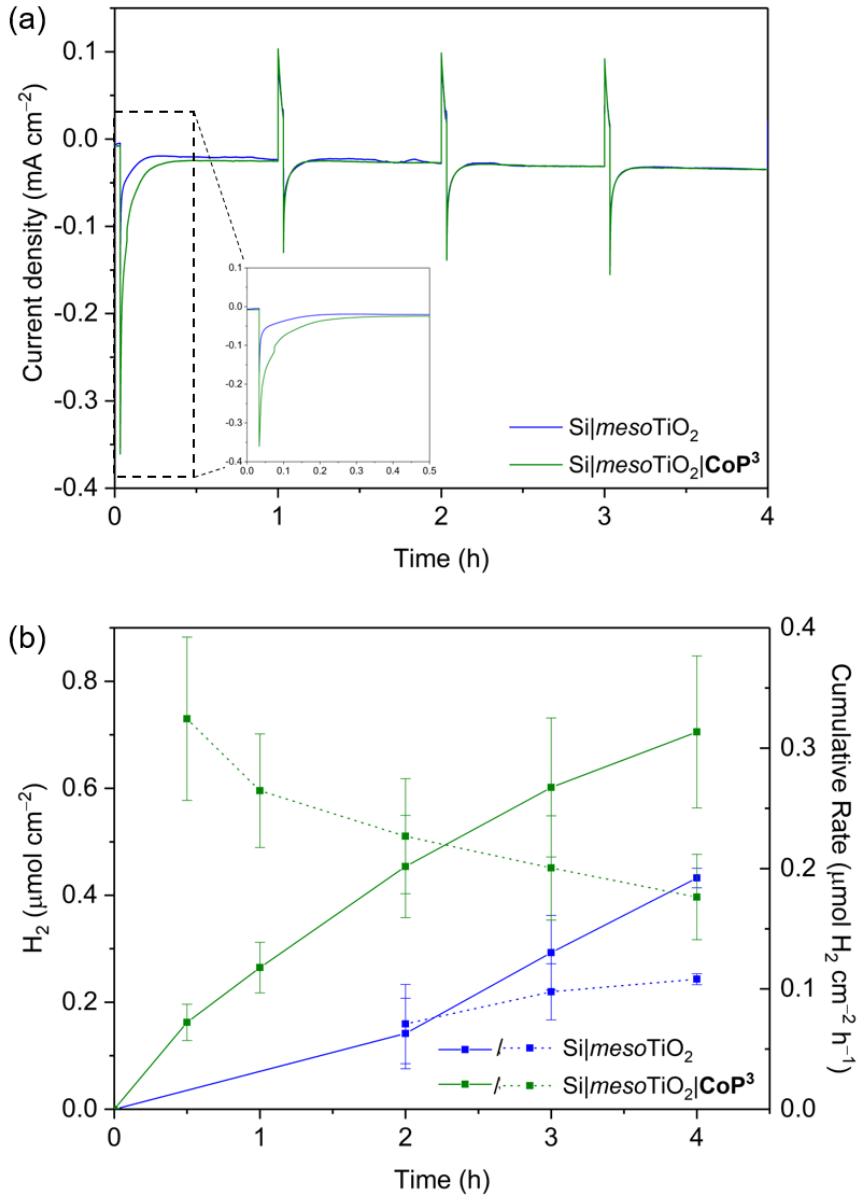

Fig. 2.13 CPPE data for Si|*meso*TiO$_2$|**CoP^3** as compared to Si|*meso*TiO$_2$: (a) chronoamperometry trace (inset: close-up of first 0.5 h); (b) H_2 evolution (solid lines) and cumulative rate of H_2 production per geometrical surface area of the electrodes (dashed lines). Conditions: $E_{app} = 0.0$ V *vs.* RHE, aqueous acetic acid solution (0.1 M, pH 4.5), UV-filtered simulated solar light irradiation (AM1.5G, 100 mW cm^{-2}, $\lambda > 400$ nm), N_2 atmosphere, room temperature.

from their optimised solution-based conditions onto a photoelectrode surface without losing any H_2 evolution performance.

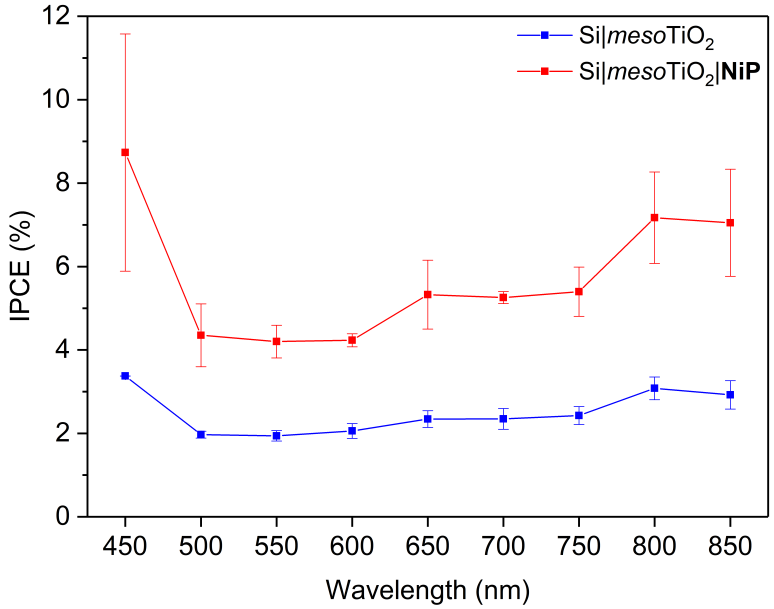

Fig. 2.14 IPCE spectra of Si|*meso*TiO_2 and Si|*meso*TiO_2|**NiP**, measured at $E_{app} = 0.0\,V$ *vs.* RHE. Conditions: aqueous acetic acid solution (0.1 M, pH 4.5), N_2 atmosphere, room temperature.

Finally, the incident photon-to-current efficiency (IPCE) spectrum of the best-performing molecular photoelectrode, Si|*meso*TiO_2|**NiP**, was measured under $E_{app} = 0.0\,V$ *vs.* RHE across 450-850 nm wavelengths to gain a better understanding of how its photoresponse varies with the energy of absorbed wavelengths. The spectrum of the catalyst-modified photoelectrode showed an IPCE of approximately 6 % across all measured wavelengths and an approximately two-fold enhancement compared to that of catalyst-free Si|*meso*TiO_2 (Fig. 2.14). The photoresponse covers the visible and extends into the IR region, maintaining relative homogeneity across the wavelengths, and highlights the clear advantage brought about by *p*-Si as it allows the conversion of low-energy photons into free charge carriers for the reduction of protons to H_2. In fact, *p*-Si is expected to be able to absorb photons with wavelengths up to 1000 nm, although this could not be explicitly demonstrated with our photoelectrodes as the laboratory set-up at our disposal unfortunately only permitted measurements up to a maximum wavelength of 850 nm.

2.2.4 Post-Catalysis Molecular Integrity

As discussed in Chapter 1 section 1.2.3, post-catalysis characterisation of molecular catalyst-based photocathodes is important in order to allow for assessment of their molecular integrity in a field where the transformation of molecular catalysts into non-molecular active species is a constant yet still rarely-verified possibility.[41,43,47,48]

The gradual decrease in catalytic activity over time as well as features in the ATR-FTIR and XPS spectra support the lasting integrity of the molecular **NiP** catalyst on Si|*meso*TiO_2|**NiP**, greatly limiting the possibility that the enduring activity from this photocathode arises from the formation of some other non-molecular Ni-based catalytic species. All characteristic bands cross the ATR-FTIR spectrum of the photocathode prior to electrolysis reappear in the spectrum of the photocathode that has undergone a full day of CPPE (Fig. 2.4, red trace). In addition, all binding energy peaks arising from core levels in the Ni_{2p}, N_{1s} and P_{2p} regions are present in the XPS spectra of both fresh and electrolysed photocathodes, while metallic Ni (expected at a binding energy of 852.6 eV) that might have been suspected to contribute to catalysis was not detected (Fig. 2.7, red traces). The reduced intensity of these XPS peaks after electrolysis is likely attributable to the initial loss of catalyst molecules chemisorbed on the top of the *meso*TiO_2, whereas molecules trapped deeper within the porous matrix give rise to catalytic activity over a longer period of time but are not readily accessible by XPS (a surface-sensitive technique). Finally, comparing LSVs of the Si|*meso*TiO_2|**NiP** photocathode both before and after 24 h of photoelectrolysis shows the retention of broad cathodic recombination peaks characteristic of molecular catalysts' slow kinetics, along with a decrease in photocurrent intensity by roughly half (Fig. 2.15). This is in agreement with some loss/degradation of the molecular catalyst from the photocathode, as previously deduced from the chronoamperogram.

In contrast to the case of Si|*meso*TiO_2|**NiP**, both ATR-FTIR and XPS analysis attest the instability of **CoP^3** on the Si|*meso*TiO_2|**CoP^3** photocathode (red traces in Figs. 2.5 and 2.6). Characteristic IR bands and Co_{2p} and P_{2p} signals in the XPS spectra have mostly disappeared or are altered after CPPE, leaving behind only a weak N_{1s} XPS signal, probably as a result of small traces of ligand species still attached to the surface. These results are in line with the short lifetime of catalytic activity observed from Si|*meso*TiO_2|**CoP^3** above, and further highlight the impressive durability of **NiP** in a field where stable, highly active immobilised molecular catalysts for the hydrogen evolution reaction remain hard to identify, especially on photocathodes.

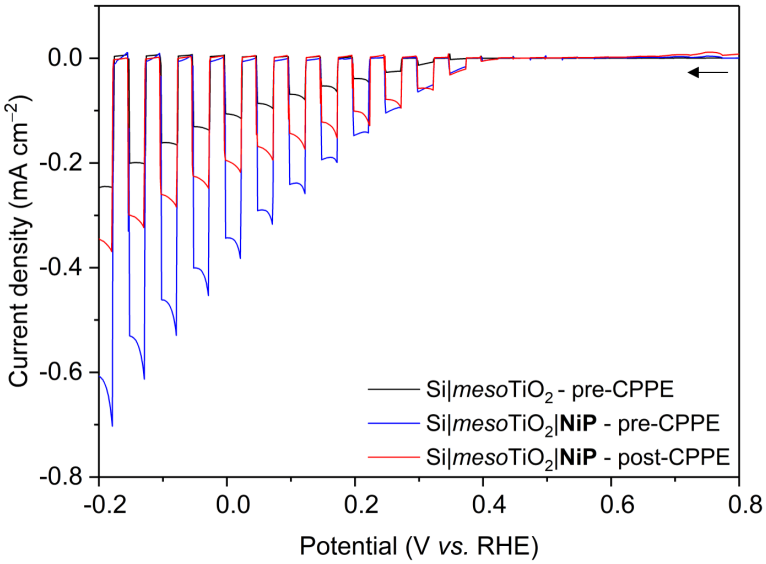

Fig. 2.15 LSVs under chopped illumination of Si|*meso*TiO_2, and Si|*meso*TiO_2|**NiP** before and after 24 h CPPE. Arrow indicates scan start and direction. Conditions: aqueous acetic acid solution (0.1 M, pH 4.5), UV-filtered simulated solar light irradiation (AM1.5G, 100 mW cm^{-2}, $\lambda > 400$ nm), N_2 atmosphere, room temperature, $\nu = 5$ mV s^{-1}.

2.2.5 Biocompatibility of Si|*meso*TiO_2 Photoelectrode

With the desire to further demonstrate the versatility of our Si|*meso*TiO_2 cathodes beyond their suitability for synthetic catalysts, the photoelectrode scaffold was also interfaced with a [NiFeSe]-hydrogenase enzyme isolated from *Desulfomicrobium baculatum* as the proton reduction catalyst.[49] Hydrogenases display exceptionally high catalytic rates for H_2 production at marginal overpotentials that are currently only matched by the precious metal platinum. [NiFeSe]-H_2ases in particular are suitable catalysts for applications in water splitting as they display a bias towards H_2 evolution in the presence of O_2, with marginal inhibition by H_2 itself.[50] The immobilisation of the H_2ase onto our electrodes was achieved by drop-coating a diluted stock solution of the enzyme on Si|*meso*TiO_2 under an inert atmosphere, affording the Si|*meso*TiO_2|H_2ase electrode. The interaction between TiO_2 and H_2ase is thought to occur at the enzyme's surface-exposed glutamate and aspartate residues in close proximity to the distal Fe–S cluster relay, the latter of which is expected to deliver photo-excited electrons to the embedded active site for H_2 generation.[51,52] The biocompatibility of TiO_2 towards H_2ase had already been previously recognised by reports where the enzyme has been immobilised on either TiO_2 nanoparticles[52] or on flat TiO_2 electrodes[53] towards H_2-evolving systems. As expected, however, the flatness of the electrode in the latter did not lend itself

to high loadings of the enzyme (which possesses a steric footprint much larger than that of synthetic metal complex catalysts), and a photocurrent density of only $\approx -2\,\mu A\,cm^{-2}$ was obtained in that case.

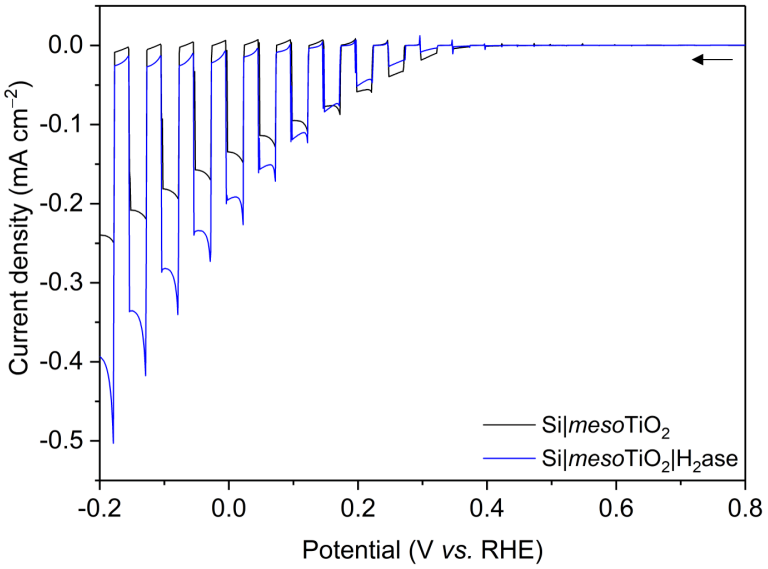

Fig. 2.16 LSVs under chopped illumination of Si|*meso*TiO_2 and Si|*meso*TiO_2|H_2ase. Arrow indicates scan start and direction. Conditions: aqueous MES solution (50 mM, pH 6.0), UV-filtered simulated solar light irradiation (AM1.5G, 100 mW cm^{-2}, $\lambda > 400$ nm), N_2 atmosphere, room temperature, $\nu = 5\,mV\,s^{-1}$.

Unlike for the molecular catalyst-modified photoelectrodes discussed above, photoelectrochemical measurements of Si|*meso*TiO_2|H_2ase were conducted in a pH 6.0 buffer solution in accordance with previously-determined optimal conditions for the enzyme.[52–54] LSVs revealed a clear enhancement of the unmodified Si|*meso*TiO_2's photocurrent upon introduction of the enzyme, with $|J| = 195\,\mu A\,cm^{-2}$ achieved at 0.0 V *vs.* RHE for Si|*meso*TiO_2|H_2ase (Fig. 2.16). During sustained CPPE at $E_{app} = 0.0$ V *vs.* RHE, Si|*meso*TiO_2|H_2ase displays a significantly higher initial photocurrent density (89.7 µA cm^{-2}, Fig. 2.17a) and rate of H_2 production (Fig. 2.17b) than the catalyst-free Si|*meso*TiO_2 electrode under identical conditions. These observed photocurrents exceed those previously reported for a Si|*flat*–TiO_2|H_2ase by a factor of 30,[53] highlighting the advantages of a homogeneous and well-connected mesoporous-structured TiO_2 scaffold in its ability to offer much higher enzyme loadings than an analogous flat surface. Direct determination of the true loading of H_2ase on Si|*meso*TiO_2 following drop-casting of the enzyme stock solution and rinsing with water could not be carried out, as none of the techniques available to us would have permitted detection of such small quantities. Nevertheless, if the total drop-casted amount (32 pmol cm^{-2})

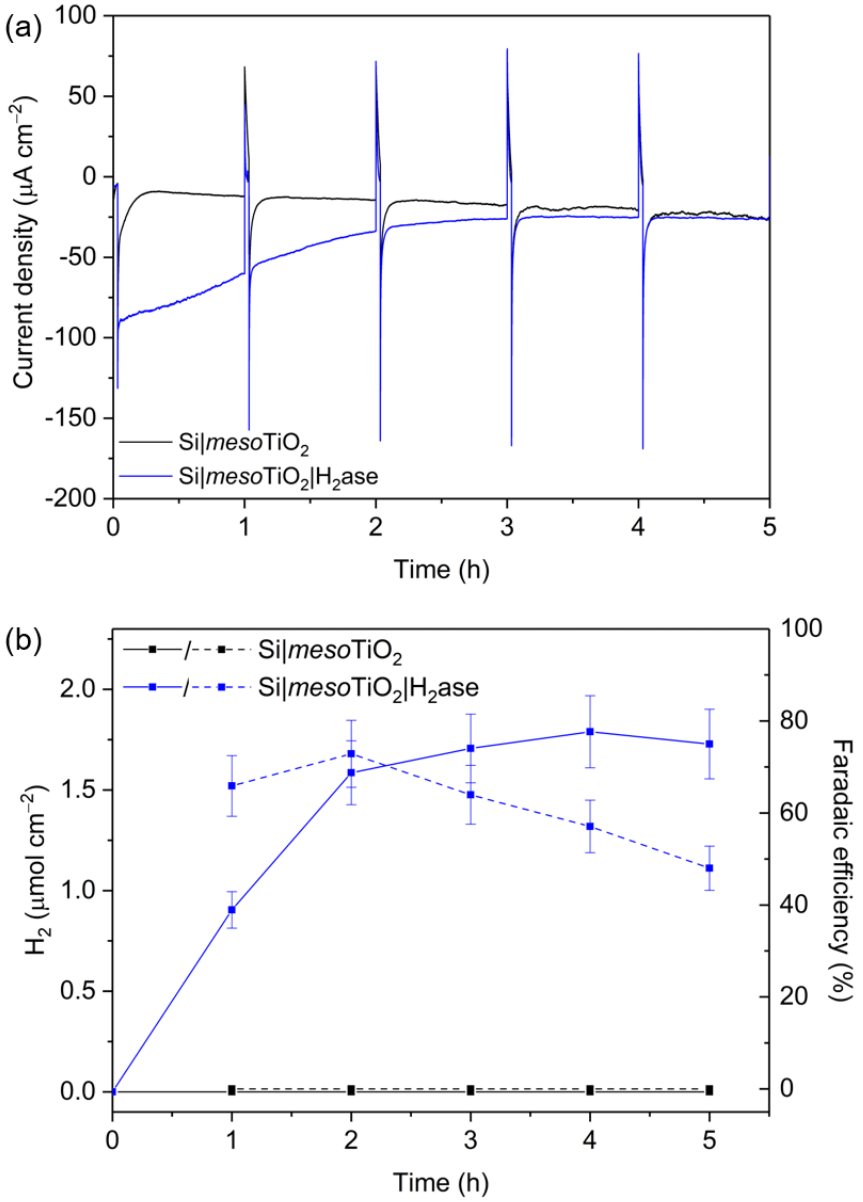

Fig. 2.17 CPPE data for Si|*meso*TiO_2|H_2ase as compared to Si|*meso*TiO_2: (a) chronoamperometry trace; (b) H_2 evolution (solid lines) and Faradaic efficiency (cumulative over duration of CPPE, dashed lines). Conditions: $E_{app} = 0.0$ V *vs.* RHE, aqueous MES solution (50 mM, pH 6.0), UV-filtered simulated solar light irradiation (AM1.5G, 100 mW cm^{-2}, $\lambda > 400$ nm), N_2 atmosphere, room temperature.

is taken as an upper bound of the possible loading, this yields a lower bound estimate of the electrode's TON_{H_2ase} in the order of $\approx 5.5 \times 10^4$ after 5 h of CPPE.

Despite the above evidence that wiring of the enzyme to the semiconductor TiO_2 has been successful in the realisation of a functional H_2-evolving photocathode, the highest FE achieved for Si|*meso*TiO_2|H_2ase is a good but modest 75.7 ± 4.0 % and the photocathode is active for at most 4 h. In trying to understand this, one must recognise that the large footprint of the H_2ase (8–10 nm)[55] makes full penetration of the enzyme *throughout* the mesoporous *meso*TiO_2 film (pore size $\approx$ 15–20 nm) difficult and it is likely that the enzyme adsorbed mostly on top of the mesoporous scaffold, leaving a significant proportion of TiO_2 beneath unmodified. Unoptimal coverage due to an insufficient penetration depth of the enzyme is therefore a likely explanation for the less-than-unity FE and limited lifetime of Si|*meso*TiO_2|H_2ase during CPPE, after which 'film loss' (degradation, re-orientation or desorption) has removed the electroactive enzyme film. Nevertheless, the biocompatibility of TiO_2 withholds this metal oxide as an attractive interfacing material on which to achieve effective adsorption of enzymes, and the improvements on photocurrent achieved in this study compared to those previously reported validate that addressing enzyme loading with porous structures can be a significant pathway to improved enzyme-based devices.[54,56–58] Follow-up work to rationally design a photocathode that maintains the merits of the Si|*meso*TiO_2 interface whilst optimising the scaffold's dimensions to better accommodate large biomolecules like hydrogenase has been recently reported.[59]

2.2.6 Comparison with State of the Art

A challenge in the preparation of molecular catalyst-based photocathodes is the transferral of the catalyst's solution performance onto a robust photoelectrode. This difficulty is illustrated by the low turnover numbers (< 3) in recent attempts to integrate **NiP** onto photocathodic architectures.[8,9] With a $TON_{\mathbf{NiP}}$ value > 600, our system achieves catalytic cycles that are among the highest reported for a molecular catalyst on a photocathode and in the same order of magnitude as previously reported solution systems at the time of writing.[31,40,60] In addition, we achieved a TON of > 10 with $\mathbf{CoP^3}$, which is also consistent with the previously-reported performance of this catalyst during solar H_2 production on dye-sensitised TiO_2 nanoparticles in the presence of a sacrificial hole scavenger.[34] These results, together with the demonstrated biocompatibility of the Si|*meso*TiO_2 electrode, show a chemical benignancy of the photocathode assembly towards a variety of

catalysts and thus highlight its potential adaptability. In addition, the assessed stability and molecular nature of the Si|*meso*TiO_2|**NiP** electrode and **NiP** catalyst, respectively, reflect the congruity of the system in a field where TONs are scarcely reported and sometimes remain subject to fundamental questions regarding molecular integrity.[43,61]

Another peculiar problem lies in designing an efficient and simple interface to integrate the molecular catalyst with the light-harvesting material. Unlike previously reported systems where the catalyst has been immobilised alongside a dye on a porous metal oxide (*e.g.* NiO),[8,9,17,18,62–65] or deposited at the surface of a flat photoactive material,[11,15,16,66–70] our system separates the light harvester from the catalyst *via* a mesoporous *n*-type semiconductor layer, which presents several benefits. As demonstrated by major advances realised in its preparation over the past years, such a mesoporous TiO_2-based interlayer could deliver a straightforward, generalisable and high surface area catalyst immobilisation platform *via* popular anchoring groups.[10,27] Concomitantly, it affords a direct electron transfer to the bound catalyst as a result of the existence of a chemical bond, as well as low probabilities of charge recombination between the catalyst and the light harvester by acting as a hole-blocking layer. Despite all of its above advantages, a mesoporous TiO_2 scaffold had not yet been employed in a molecular photocathode for PEC H_2 evolution; under aqueous conditions; nor without the need for an additional ALD-deposited interlayer. The presence of a *meso*TiO_2 interlayer in our system does not strongly affect the potential photovoltage of the silicon electrode, as the measured underpotential for proton reduction ($\approx 0.4\,V$ *vs.* RHE) compares well with those of previously reported *p*-Si-based photocathodes.[22] Finally, in contrast to NiO-based photocathodes, the system does not require any other co-immobilised molecules due to its light harvester|*meso*TiO_2|catalyst architecture, thereby avoiding the need to carry out ratio optimisations, as well as potential kinetic and stability limitations resulting from using an added dye. Thus, the photocathode displayed a photocurrent density of $340\,\mu A\,cm^{-2}$ at $0.0\,V$ *vs.* RHE when loaded with **NiP**, representing a 3- to 150-fold improvement as compared to the results reported with dye-sensitised NiO-based architectures.

Although the photocurrents achieved with our molecular-based photocathodes are relatively modest compared to the best state-of-the-art photocathodes, similar values are attained with the platinised equivalent. This shows that our system's bottleneck probably originates from the limited number of available charge carriers and that it could therefore be improved by optimising the electrode preparation procedure. On the other hand, the modest photovoltage displayed

by the Si|*meso*TiO_2|catalyst architecture has its main origin in *p*-Si's small band gap and charge recombination. Nevertheless, as confirmed by the IPCE measurements under applied bias, *p*-Si allows for the broadest conversion of wavelengths, including low-energy IR photons (7 % at 850 nm), among molecular catalyst-based electrodes. Consequently, such an architecture could benefit the preparation of a molecular-based tandem PEC device towards full water splitting when utilised as the proton-reducing electrode.

2.2.7 Charging Currents in TiO_2

In the process of evaluating the photoelectrochemical performance of our various proton-reducing Si|*meso*TiO_2-based photoelectrodes, multiple observations were noted that eventually led us to study the charging and discharging of the CB of TiO_2 in our electrode architecture.

A charging behaviour was first evidenced when performing consecutive LSVs in both reducing and oxidising scanning directions on the photocathodes (Fig. 2.18). In the case of LSVs conducted from anodic to cathodic potentials for the catalyst-free Si|*meso*TiO_2 electrode, the second scan always displays an anodic dark current at the scan start (0.8 V *vs.* RHE, Fig. 2.18a blue trace). When subsequently scanning in the anodic direction upon scan reversal from the cathodic scan, an anodic dark current once again manifests from approximately 0.0 to 0.4 V *vs.* RHE (red trace). This can be attributed to the CB being subsequently "discharged" at more positive applied potentials following the two previous cathodic scans that charged it, hence giving rise to an anodic dark current.

Revealingly, when either **NiP**, Pt or H_2ase is surface-bound on Si|*meso*TiO_2, no such discharging features were observed when scanning in either cathodic or anodic directions (Fig. 2.18b-d). This observation signifies a lack of discharging and therefore a corresponding lack of any preceding charging events in the catalyst-modified electrodes, suggesting efficient charge transfer from the CB of *meso*TiO_2 to the proton reduction catalyst. In other words, these catalysts, even molecular **NiP**, are effective at lowering the kinetic barrier and therefore providing high activity for proton reduction. Even after 24 h of CPPE, no evidence of substantial charge accumulation from charging is observed in the case of Si|*meso*TiO_2|**NiP**, which is made apparent by the lack of an anodic dark current in the reverse LSV scan of an electrode that has undergone photoelectrocatalysis (Fig. 2.18f, red trace). This indicates that the amount of molecular catalyst remaining on the cathode at this time is still sufficient to ensure efficient extraction of charges

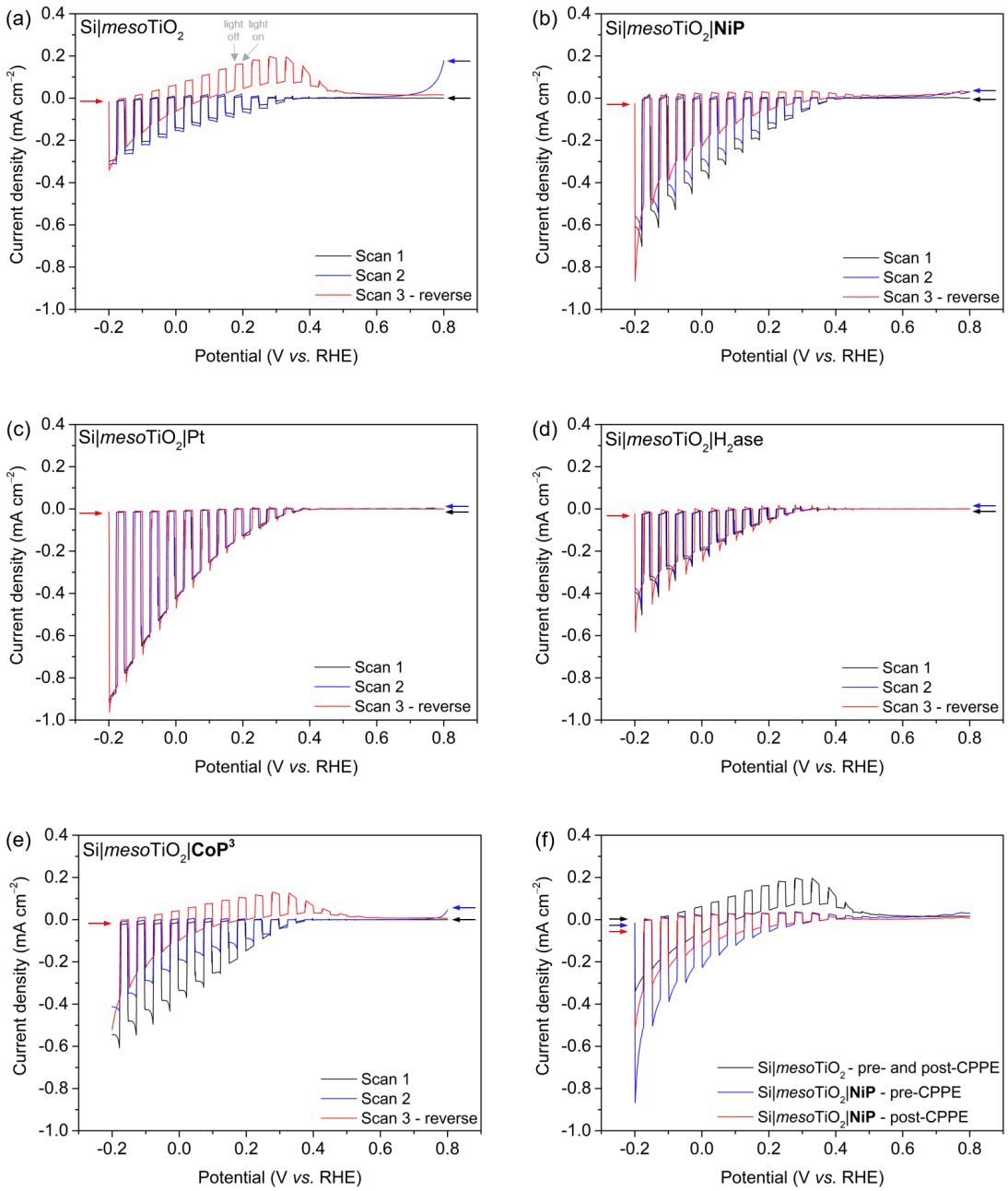

Fig. 2.18 LSVs under chopped illumination of fresh (a) Si|*meso*TiO_2, (b) Si|*meso*TiO_2|**NiP**, (c) Si|*meso*TiO_2|Pt, (d) Si|*meso*TiO_2|H_2ase and (e) Si|*meso*TiO_2|**CoP**$^{\mathbf{3}}$, with the first two scans in cathodic direction (black and blue traces) and the third scan in anodic direction following scan reversal (red traces). (f) Reverse scans only for Si|*meso*TiO_2 and Si|*meso*TiO_2|**NiP** photoelectrodes before and after CPPE. Arrows indicate scan start and directions for all LSVs. Conditions: aqueous acetic acid solution (0.1 M, pH 4.5) for all electrodes apart from Si|*meso*TiO_2|H_2ase (50 mM MES buffer, pH 6.0), UV-filtered simulated solar light irradiation (AM1.5G, 100 mW cm^{-2}, $\lambda > 400$ nm), N_2 atmosphere, room temperature, $\nu = 5$ mV s^{-1}.

from the CB of TiO_2, and hence provide a good FE. Taking this into account and considering the clear kinetic advantage of **NiP** compared to catalyst-free *meso*TiO_2 demonstrated here, the upper estimate of $TON_{\mathbf{NiP}}$ given above (without background substraction) gains credibility.[71] As an aside, with these observations in consecutive LSVs conducted on Si|*meso*TiO_2|H_2ase, successful electronic wiring of the semiconductor *meso*TiO_2 to the H_2ase enzyme can be confirmed when we see that features in Si|*meso*TiO_2's LSVs that indicate charging up of *meso*TiO_2's CB are completely erased by the presence of the enzyme (Fig. 2.18d).

In contrast, fresh **CoP^3**-loaded electrodes already feature electrochemical discharging of the CB in the second cathodic LSV alongside a significant drop in cathodic photocurrent intensity (Fig. 2.18e). In addition, the subsequent reverse scan also displays anodic dark currents similar to those recorded in the case of the bare Si|*meso*TiO_2 electrode. Both observations confirm the previously reported instability of this catalyst and/or its inefficient charge extraction from the CB of *meso*TiO_2, as we have already seen from this photoelectrode's performance above.[34]

Another telling observation that pointed towards charging up of *meso*TiO_2's CB when there are no efficient catalysts immobilised on the surface were anodic dark currents observed when dark chopping for a brief two minutes every hour during CPPE of Si|*meso*TiO_2, as indicated in an enlarged view of the CPPE trace in Fig. 2.19. Similar to the anodic dark currents observed in linear sweep voltammetry experiments, the dark currents seen here during CPPE confirm the temporary storage of electrons in the CB of *meso*TiO_2 and their subsequent discharging in the dark. On the other hand, the anodic dark current is almost absent in the case of, for instance, Si|*meso*TiO_2|**NiP**, as the catalyst efficiently collects electrons from the *meso*TiO_2 CB.

The discharging of TiO_2's CB was monitored in a separate experiment by recording the slow decay of the anodic current during a dark chronoamperometry after having first charged the Si|*meso*TiO_2 electrode under light (Fig. 2.20a). In short, a potential of 0.0 V *vs.* RHE was applied under UV-filtered solar light illumination for a short period of time in the first phase, corresponding to the charging of the CB. In the subsequent second phase, corresponding to the discharging step, 0.0 V *vs.* RHE was applied once again but this time in the dark, and the dark current that resulted was measured. The observed slow decay (15 min) of the anodic current indicates that our system allows for the existence of long-lived electrons trapped in *meso*TiO_2. Electron trapping in *meso*TiO_2 has been extensively studied and is believed to be localised in the *meso*TiO_2 lattice as Ti^{3+} sites, but

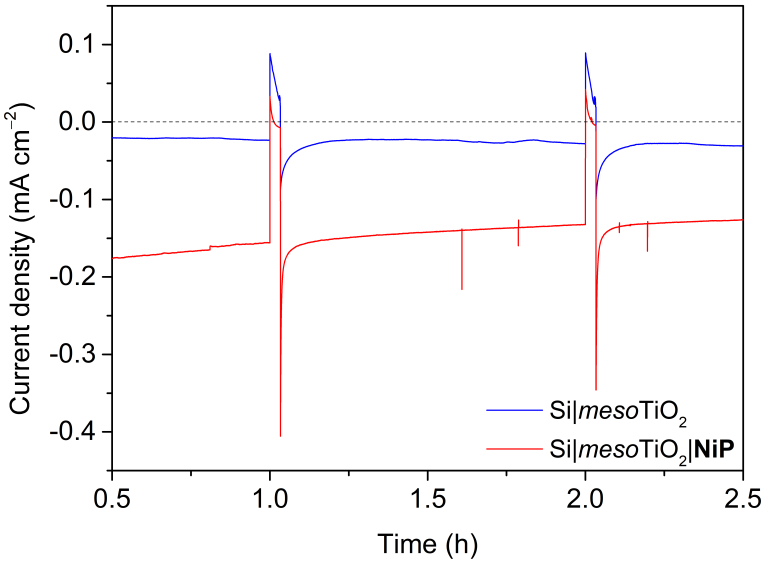

Fig. 2.19 Enlarged view of the first two dark chops during CPPE of Si|*meso*TiO_2 (blue trace) and Si|*meso*TiO_2|**NiP** (red trace), showing anodic dark current for the former and the lack of any dark current for the latter. Conditions: $E_{app} = 0.0\,V$ *vs.* RHE, aqueous acetic acid solution (0.1 M, pH 4.5), UV-filtered simulated solar light irradiation (AM1.5G, 100 mW cm^{-2}, $\lambda > 400\,nm$), N_2 atmosphere, room temperature.

the storage of such trapped states lasting for timescales beyond microseconds has been scarcely reported.[72,73] In contrast, the current decays almost instantly to the baseline with the introduction of an electron acceptor (*i.e.* methyl viologen dichloride, MV; $E_{(MV/MV^-)} \approx -0.45\,V$ *vs.* SHE) to the electrolyte solution (Fig. 2.20a, blue trace), concurrent with the appearance of a blue colour from the reduced methyl viologen radical at the surface of the electrode. Both observations indicate the reduction of MV species by electrons located in the *meso*TiO_2 CB. Performing another discharge-monitoring experiment in the presence of an anchored catalyst such as **NiP** (and with no MV) resulted in the absence of any anodic dark current during dark chronoamperometry following CB charging by light, as the electrons are efficiently transferred to the catalyst (Fig. 2.20b).

With all of the above, it is thereby demonstrated that the well-known ability of *meso*TiO_2 to trap electrons can be exploited in our Si|*meso*TiO_2 architecture. This represents the first application of this phenomenon *via* the fabrication of a device capable of storing visible light-generated electrons on an electrode. The realisation of these long-lived electrons following photoexcitation of the Si|*meso*TiO_2 electrode could allow one to envision devices that are capable of temporal decoupling between the photo-production of the electric charge and its utilisation in the form of electricity or chemical synthesis, and may therefore be an

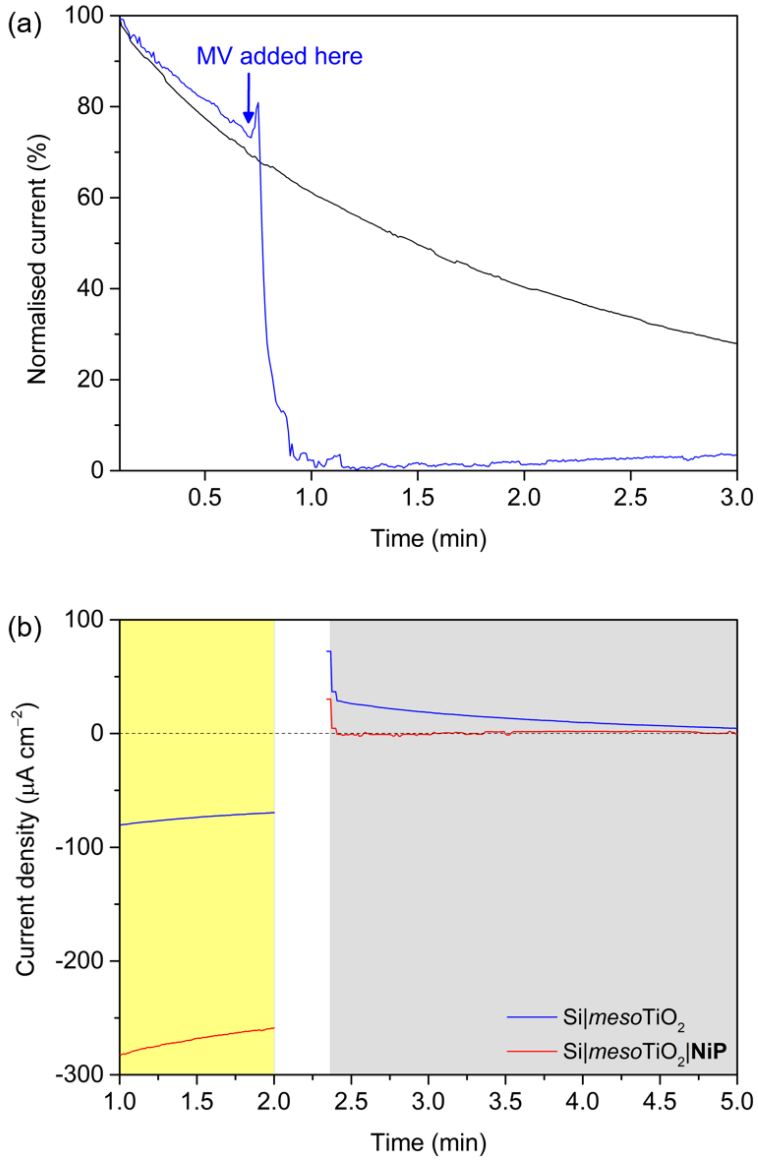

Fig. 2.20 (a) Chronoamperograms of Si|*meso*TiO_2 in the dark (normalised and given as a percentage) after being exposed to light (to charge the CB), without MV (black trace) and with MV added partway (blue trace). (b) Chronoamperograms of Si|*meso*TiO_2 (blue traces) and Si|*meso*TiO_2|**NiP** (red traces) in the light (yellow region) and subsequently in the dark (grey region), separated by a brief period in the dark without applied bias (white region). Conditions: E_{app} during both light and dark phases = 0.0 V *vs.* RHE, aqueous acetic acid solution (0.1 M, pH 4.5), UV-filtered simulated solar light irradiation (AM1.5G, 100 mW cm^{-2}, $\lambda > 400$ nm), N_2 atmosphere, room temperature.

attractive means of short (solar-charged capacitors)- and long (solar fuels)-term storage of solar energy.[74–77]

2.3 Conclusion

In conclusion, the first example of the solar-driven reduction of aqueous protons to hydrogen by molecular catalysts immobilised on light-harvesting *p*-Si is demonstrated. This was achieved by the straightforward deposition of an interfacing mesoporous TiO_2 scaffold, which not only afforded a high loading of molecular catalyst, but also represents a low-cost method of integrating a catalyst with *p*-Si. The Si–*meso*TiO_2 interface consistently offers an underpotential of 400 mV for the H_2 evolution reaction and, in the absence of a catalyst, represents an architecture that allows for the storage of solar energy in the form of trapped electrons lasting for several minutes. The charging of the CB of *meso*TiO_2 in this way allows us to envision the use of this electrode as a short- and long-term electron-storing, light-rechargeable device.

The molecular catalyst-modified Si|*meso*TiO_2|**NiP** reached the highest photocurrent and TON known for a molecular catalyst belonging to the popular DuBois-type family on a photocathode in aqueous media, and continues to evolve hydrogen at high Faradaic efficiencies even after 24 h of operation under UV-filtered simulated solar light illumination, highlighting the stability of both the Si–*meso*TiO_2 assembly and the molecular catalyst itself. The fact that no loss of performance was experienced when immobilising the molecular catalyst onto the photoelectrode scaffold demonstrates something that is a continued struggle in the field: the ability to transfer catalyst performances in solution systems onto an electrode surface towards more scalable PEC configurations. IPCE studies under bias showed the photoelectrode's ability to utilise low-energy photons and, therefore, its suitability for coupling with large band gap-based photoanodes in a potential tandem PEC device. Finally, the diversity of other catalysts used in this work (metallic Pt, molecular cobaloxime **CoP^3** and hydrogenase) are a strong testament to the versatility offered by this approach and the opportunities it presents for evaluating a wide array of existing and future catalysts immobilised on a stable photocathode towards solar-driven hydrogen evolution and other redox transformations.

2.4 Experimental Section

2.4.1 Materials

Reagents and materials used throughout this work were obtained in high purity from commercial suppliers and used as received. Laboratory grade reagents were used in all synthetic procedures and chemicals used for electrochemical experiments were of the highest available purity. Commercial *p*-type boron-doped silicon wafers (resistivity of 1-10 ohm cm; <100>; 500 µm thickness; single-side polished) were purchased from University Wafer. Milli-Q® water (18.2 MΩ cm at 25 °C) was used throughout this work in synthetic and electrochemical procedures. Buffer solutions were made using analytical grade reagents and titrated to the desired pH, as determined by a pH electrode (Mettler Toledo; SevenEasy) using NaOH. **NiP** and **CoP³** were synthesised and characterised according to previous reports.[31,34] The [NiFeSe]-hydrogenase used in this study was isolated from *Desulfomicrobium baculatum*, and was provided by Dr Juan C. Fontecilla-Camps and Dr Christine Cavazza (Institut de Biologie Structurale, Grenoble, France).

2.4.2 Assembly of Photocathodes

Si and Si|*meso*TiO_2 Fabrication

The Si wafers (1.2 cm × 2.5 cm) were sequentially cleaned with acetone, isopropanol, ethanol, and piranha solutions for 10 min each. The bare *p*-Si electrodes were obtained after removing the native oxide layers from the surface by immersing the electrodes in hydrofluoric acid (65 %, Merck Millipore) for 1 min and then rinsing with Milli-Q® water. The mesoporous TiO_2 scaffold was deposited on *p*-Si by slot-coating commercial Ti-Nanoxide pastes (15-20 nm particles, 100 % anatase, Solaronix) over a defined area (0.7 cm × 0.7 cm).

The electrodes both with (towards Si|*meso*TiO_2) and without (towards bare Si control) the mesoporous TiO_2 paste were then immediately transferred into a Carbolite furnace pre-heated at 135 °C and annealed under atmospheric conditions using the following heating ramp. The temperature was increased to 325 °C and held at this temperature for 5 min, after which the temperature was further augmented to 375 °C and maintained for 5 min at this temperature. The temperature was finally allowed to reach 450 °C, where it remained for 30 min. The electrodes were removed from the furnace after a slow cooling period to 80 °C. The thickness of the resulting TiO_2 layers was measured by scanning electron

microscopy. Layers of 6 µm or 1.1 µm were obtained when using T/SP or T600 TiO_2 pastes, respectively.

Catalyst Immobilisation and Back Contact Assembly

Immobilisation of the molecular catalysts on Si|*meso*TiO_2 electrodes to yield Si|*meso*TiO_2|**NiP** and Si|*meso*TiO_2|**CoP³** was carried out by soaking the electrodes in a 0.25 mM solution of the corresponding catalyst in dry MeOH for 16 h, after which they were rinsed with MeOH. Platinisation of Si|*meso*TiO_2 to yield Si|*meso*TiO_2|Pt electrodes was achieved by brushing a solution of hexachloroplatinic acid hydrate in isopropanol ($2\,mg\,ml^{-1}$) across the top of the electrode. This operation was repeated three times, allowing the solvent to dry between each deposition. The cells were then transferred into a Carbolite furnace at 350 °C for 20 min, followed by slow cooling to room temperature.

The H_2ase was purified using a previously published method.[78] The stock solution (specific activity $2115\,\mu mol\,H_2\,min^{-1}\,mg^{-1}$, stored at −30 °C) was thawed immediately before use and diluted with 20 mM Tris/HCl buffer (pH 7) in an anaerobic glovebox to give 8 µM H_2ase aliquots. Prior to enzyme immobilisation, the Si|*meso*TiO_2 electrodes were UV-ozone treated for 10 min in a UV/Ozone ProCleanerTM (BioForce Nanosciences). One aliquot of H_2ase solution (1 µL, 8 pmol) was drop-cast onto each electrode ($0.25\,cm^2$) and allowed to fully dry, yielding the final Si|*meso*TiO_2|H_2ase electrode.

All photocathodes were subsequently back-contacted and insulated by an epoxy adhesive prior to further use. Sand paper was used to abrade the surface of the Si electrode's unpolished side before application of a conductive silver paint (RS® Components 186-3593), after which an electrical wire was connected to the dry silver using the same conductive silver paint. Upon drying, a dark grey epoxy adhesive (Loctite® Hysol® 3423) was applied on both sides of the electrodes, leaving only the surface to be analysed ($S \approx 0.2\,cm^2$) exposed. The cells were then allowed to dry thoroughly for 18 h at room temperature in air before use.

2.4.3 Physical Characterisation of Molecular Photocathodes

SEM images were recorded on a FEI Philips XL30 FEG ESEM instrument at 5 kV acceleration voltage. ATR-FTIR spectra of the compounds as powders or the functionalised TiO_2 were recorded on a Nicolet iS50 spectrometer. XPS was

performed on an ESCALAB 250Xi spectrometer (Thermo Fisher Scientific, East Grindstead, UK) utilising a monochromatic Al-Kα source (50-300 W, 0.2-1 mm spot size). The quantification of the amount of immobilised **NiP** or **CoP^3** (mole per geometrical area) on the Si|*meso*TiO_2|catalyst electrodes was evaluated by UV-visible spectroscopy after desorption of the catalyst from the corresponding electrode. Typically, the Si|*meso*TiO_2|catalyst electrode ($S \approx 0.5\,cm^2$) was immersed for 1.5 h in a MeOH bath containing tetrabutylammonium hydroxide (0.1 M). The **NiP** and **CoP^3** solutions' absorptions were then measured ($l = 1$ cm) at 350 and 400 nm, respectively, and the concentrations were estimated using the molar absorption curves in Figure B.1. UV-vis spectra were collected using a Varian Cary 50 Bio UV-vis spectrometer.

2.4.4 Photoelectrochemical Methods

Photoelectrocatalysis Set-Up

LSVs and CPPEs were performed with an Ivium CompactStat potentiostat. A Newport Oriel Xenon 150 W solar light simulator (100 mW cm^{-2}, AM1.5G with IR water and UV ($\lambda > 400$ nm) filters) was used as the light source. A three-electrode configuration was employed in a custom-made airtight two-compartment PEC cell with a Nafion membrane separating the compartments. A platinum mesh was used as counter electrode (CE) and an $Ag/AgCl_{(sat.\ KCl)}$ electrode as reference electrode (RE). All electrochemical measurements were performed at room temperature in aqueous acetic acid solutions (0.1 M, pH 3.0 or 4.5), except for Si|*meso*TiO_2|H_2ase and related control experiments, where a MES buffer (2-(*N*-morpholino)ethanesulphonic acid, 50 mM, pH 6.0) was used. LSVs were conducted at a scan rate of 5 mV s^{-1} with chopped light alternating between dark and light every 5 s. The onset potential was defined as the potential at which a photocurrent density of $|J| = 10\,\mu A\,cm^{-2}$ was achieved by the respective electrode. The applied potential during CPPE was 0.0 V *vs.* RHE, and continuous illumination was maintained, apart from hourly dark chops lasting for 2 min each. CPPE of **CoP^3** and H_2ase was ceased after 4 h and 5 h, respectively; all others were continued for 24 h.

Product Quantification

For all CPPE experiments, the electrolyte solution in both compartments of the PEC cell was purged prior with N_2 containing 2 % CH_4 as an internal standard

for gas chromatography (GC) measurements. The amount of gaseous H_2 was analysed by headspace gas analysis using an Agilent 7890A Series GC equipped with a 5 Å molecular sieve column (N_2 carrier gas at a flow rate of approximately $3\,mL\,min^{-1}$). The GC oven holding the columns was kept isothermal at 45 °C, and a thermal conductivity detector was employed. Aliquots (75 µL) of the headspace gas were removed from the PEC cell for GC analysis at regular time intervals using a gas-tight syringe (Hamilton, GASTIGHT) and injected into the GC. The amount of H_2 produced was quantified as described in Appendix A. The FE of the photocathodes was calculated by comparing the expected amount of H_2 produced as indicated by the total charge passed through the electrode and the actual amount produced (see Appendix A). Analytical measurements were performed in triplicate and the standard deviation of each data point is denoted by error bars (calculations described in Appendix A).

Incident Photon-to-Current Efficiency Measurement Under Applied Bias

IPCE measurements under applied bias were conducted in the same electrochemical cell set-up as used for PEC performance experiments (above), with the solar light simulator coupled to a monochromator (MSH300, LOT Quantum design). The sequence carried out at each wavelength was 1 min of illumination, followed by 5 min in the dark. The current was collected at two points per second, with the initial 10 and final 10 points of each light cycle averaged; the electrode's dark current was subtracted from this average to give the final photocurrent. Sample photocurrent data were normalised to the output of a power meter (Thorlabs PM100D Compact Power and Energy Meter Console). Measurements were performed in triplicate and the standard deviation at each wavelength is denoted by error bars. IPCE was calculated according to the following equation:

$$IPCE = \frac{electrons/cm^2/s}{photons/cm^2/s} = \frac{|J| \times h \times c}{P_{\text{mono}} \times \lambda} \tag{2.1}$$

where J and P_{mono} are the photocurrent density and calibrated, monochromated illumination power intensity, respectively, at wavelength λ, h is Planck's constant and c is the speed of light.

2.4.5 Analysis of TiO_2 Charging Currents

The charging and discharging of TiO_2's CB were studied by two successive chronoamperometric experiments, conducted on Si|*meso*TiO_2 and Si|*meso*TiO_2|-**NiP** electrodes each. These were conducted at room temperature in a one-compartment PEC cell in a three-electrode configuration with an acetic acid solution (0.1 M, pH 4.5). In the first chronoamperometry phase, a potential of 0.0 V *vs.* RHE was applied for 2 min under solar light illumination (AM1.5G, 100 mW cm^{-2}, $\lambda > 400$ nm), corresponding to the charging of the CB of TiO_2. After this first phase, 20 sec were allowed to pass where the electrode was left in the dark with no applied potential. In the following second chronoamperometry phase, corresponding to the discharging step, 0.0 V *vs.* RHE was applied in the dark. In some cases, a solution of MV in the electrolyte solution was injected partway through the second chronoamperometry (final concentration in PEC cell = 10 mM). The recorded current was normalised and is given as a percentage. A similar experiment was also conducted on Si|*meso*TiO_2|**NiP** (without the addition of MV).

2.5 References

(1) Andreiadis, E. S.; Chavarot-Kerlidou, M.; Fontecave, M.; Artero, V. *Photochem. Photobiol.* **2011**, *87*, 946–964.

(2) Tran, P. D.; Wong, L. H.; Barber, J.; Loo, J. S. *Energy Environ. Sci.* **2012**, *5*, 5902–5918.

(3) Willkomm, J.; Orchard, K. L.; Reynal, A.; Pastor, E.; Durrant, J. R.; Reisner, E. *Chem. Soc. Rev.* **2016**, *45*, 9–23.

(4) Zhang, X.; Peng, T.; Song, S. *J. Mater. Chem. A* **2016**, *4*, 2365–2402.

(5) Queyriaux, N.; Kaeffer, N.; Morozan, A.; Chavarot-Kerlidou, M.; Artero, V. *J. Photochem. Photobiol. C Photochem. Rev.* **2015**, *25*, 90–105.

(6) Tian, H. *ChemSusChem* **2015**, *8*, 3746–3759.

(7) Seo, J.; Pekarek, R. T.; Rose, M. J. *Chem. Commun.* **2015**, *51*, 13264–13267.

(8) Gross, M. A.; Creissen, C. E.; Orchard, K. L.; Reisner, E. *Chem. Sci.* **2016**, *7*, 5537–5546.

(9) Shan, B.; Das, A.; Marquard, S. L.; Farnum, B. H.; Wang, D.; Bullock, R. M. M.; Meyer, T. J. *Energy Environ. Sci.* **2016**, *9*, 3693–3697.

(10) Schreier, M.; Luo, J.; Gao, P.; Moehl, T.; Mayer, M. T.; Grätzel, M. *J. Am. Chem. Soc.* **2016**, *138*, 1938–1946.

(11) Gu, J.; Yan, Y.; Young, J. L.; Steirer, K. X.; Neale, N. R.; Turner, J. A. *Nat. Mater.* **2016**, *15*, 456–460.

(12) Kim, H. J.; Seo, J.; Rose, M. J. *ACS Appl. Mater. Interfaces* **2016**, *8*, 1061–1066.

(13) Rosser, T. E.; Gross, M. A.; Lai, Y.-H.; Reisner, E. *Chem. Sci.* **2016**, *7*, 4024–4035.

(14) Brennaman, M. K.; Dillon, R. J.; Alibabaei, L.; Gish, M. K.; Dares, C. J.; Ashford, D. L.; House, R. L.; Meyer, G. J.; Papanikolas, J. M.; Meyer, T. J. *J. Am. Chem. Soc.* **2016**, *138*, 13085–13102.

(15) Krawicz, A.; Yang, J.; Anzenberg, E.; Yano, J.; Sharp, I. D.; Moore, G. F. *J. Am. Chem. Soc.* **2013**, *135*, 11861–11868.

(16) Khusnutdinova, D.; Beiler, A. M.; Wadsworth, B. L.; Jacob, S. I.; Moore, G. F. *Chem. Sci.* **2017**, *8*, 253–259.

(17) Li, F.; Fan, K.; Xu, B.; Gabrielsson, E.; Daniel, Q.; Li, L.; Sun, L. *J. Am. Chem. Soc.* **2015**, *137*, 9153–9159.

(18) Antila, L. J.; Ghamgosar, P.; Maji, S.; Tian, H.; Ott, S.; Hammarström, L. *ACS Energy Lett.* **2016**, *1*, 1106–1111.

(19) Feldman, D.; Barbose, G.; James, T.; Weaver, S.; Fu, R.; Davidson, C. *US Dep. Energy* **2014**, 1–32.

(20) Nikolaychuk, P. A. *Silicon* **2014**, *6*, 109–116.

(21) Sun, K.; Shen, S.; Liang, Y.; Burrows, P. E.; Mao, S. S.; Wang, D. *Chem. Rev.* **2014**, *114*, 8662–8719.

(22) Seger, B.; Pedersen, T.; Laursen, A.; Vesborg, P.; Hansen, O.; Chorkendorff, I. *J. Am. Chem. Soc.* **2013**, *135*, 1057–1064.

(23) Esposito, D. V.; Levin, I.; Moffat, T. P.; Talin, A. A. *Nat. Mater.* **2013**, *12*, 562–568.

(24) Downes, C. A.; Marinescu, S. C. *J. Am. Chem. Soc.* **2015**, *137*, 13740–13743.

(25) Hu, S.; Lewis, N. S.; Ager, J. W.; Yang, J.; McKone, J. R.; Strandwitz, N. C. *J. Phys. Chem. C* **2015**, *119*, 24201–24228.

(26) Hou, Y.; Abrams, B. L.; Vesborg, P. C.; Björketun, M. E.; Herbst, K.; Bech, L.; Setti, A. M.; Damsgaard, C. D.; Pedersen, T.; Hansen, O.; Rossmeisl, J.; Dahl, S.; Nørskov, J. K.; Chorkendorff, I. *Nat. Mater.* **2011**, *10*, 434–438.

(27) O'Regan, B.; Grätzel, M. *Nature* **1991**, *353*, 737–740.

(28) Ma, Y.; Wang, X. L.; Jia, Y. S.; Chen, X. B.; Han, H. X.; Li, C. *Chem. Rev.* **2014**, *114*, 9987–10043.

(29) Thompson, T. L.; Yates, J. T. *Chem. Rev* **2006**, *106*, 4428–4453.

(30) Chen, X.; Mao, S. S. *Chem. Rev.* **2007**, *107*, 2891–2959.

(31) Gross, M. A.; Reynal, A.; Durrant, J. R.; Reisner, E. *J. Am. Chem. Soc.* **2014**, *136*, 356–366.

(32) Helm, M. L.; Stewart, M. P.; Bullock, R. M.; Dubois, M. R.; Dubois, D. L. *Science* **2011**, *333*, 863–866.

(33) Kilgore, U. J.; Roberts, J. A. S.; Pool, D. H.; Appel, A. M.; Stewart, M. P.; DuBois, M. R.; Dougherty, W. G.; Kassel, W. S.; Bullock, R. M.; DuBois, D. L. *J. Am. Chem. Soc.* **2011**, *133*, 5861–5872.

(34) Willkomm, J.; Muresan, N. M.; Reisner, E. *Chem. Sci.* **2015**, *6*, 2727–2736.

(35) Creissen, C. E.; Warnan, J.; Reisner, E. *Chem. Sci.* **2018**, *9*, 1439–1447.

(36) Muresan, N. M.; Willkomm, J.; Mersch, D.; Vaynzof, Y.; Reisner, E. *Angew. Chem. Int. Ed.* **2012**, *51*, 12749–12753.

(37) Reuillard, B.; Warnan, J.; Leung, J. J.; Wakerley, D. W.; Reisner, E. *Angew. Chem. Int. Ed.* **2016**, *55*, 3952–3957.

(38) Madani, M. R.; Ajmera, P. K. *Electron. Lett.* **1988**, *24*, 856–857.

(39) Ji, L.; Mcdaniel, M. D.; Wang, S.; Posadas, A. B.; Li, X.; Huang, H.; Lee, J. C.; Demkov, A. A.; Bard, A. J.; Ekerdt, J. G.; Yu, E. T. *Nat. Nanotechnol.* **2015**, *10*, 84–90.

(40) Martindale, B. C.; Joliat, E.; Bachmann, C.; Alberto, R.; Reisner, E. *Angew. Chem. Int. Ed.* **2016**, *55*, 9402–9406.

(41) Widegren, J. A.; Finke, R. G. *J. Mol. Catal. A Chem.* **2003**, *198*, 317–341.

(42) Cobo, S.; Heidkamp, J.; Jacques, P. A.; Fize, J.; Fourmond, V.; Guetaz, L.; Jousselme, B.; Ivanova, V.; Dau, H.; Palacin, S.; Fontecave, M.; Artero, V. *Nat. Mater.* **2012**, *11*, 802–807.

(43) Artero, V.; Fontecave, M. *Chem. Soc. Rev.* **2013**, *42*, 2338–2356.

(44) Simándi, L. I.; Szeverényi, Z.; Budó-Záhonyi, É. *Inorg. Nucl. Chem. Lett.* **1975**, *11*, 773–777.

(45) Zhang, P.; Jacques, P.-A.; Chavarot-Kerlidou, M.; Wang, M.; Fontecave, M.; Artero, V.; Sun, L.; Fontecave, M.; Artero, V. *Inorg. Chem.* **2012**, *51*, 2115–2120.

(46) Lacy, D. C.; Roberts, G. M.; Peters, J. C. *J. Am. Chem. Soc.* **2015**, *137*, 4860–4864.

(47) Kaeffer, N.; Morozan, A.; Fize, J.; Martinez, E.; Guetaz, L.; Artero, V. *ACS Catal.* **2016**, *6*, 3727–3737.

(48) Li, W.; He, D.; Sheehan, S. W.; He, Y.; Thorne, J. E.; Yao, X.; Brudvig, G. W.; Wang, D. *Energy Environ. Sci.* **2016**, *9*, 1794–1802.

(49) Wombwell, C.; Caputo, C. A.; Reisner, E. *Acc. Chem. Res.* **2015**, *48*, 2858–2865.

(50) Parkin, A.; Goldet, G.; Cavazza, C.; Fontecilla-Camps, J. C.; Armstrong, F. A. *J. Am. Chem. Soc.* **2008**, *130*, 13410–13416.

(51) Reisner, E. *Eur. J. Inorg. Chem.* **2011**, 1005–1016.

(52) Caputo, C. A.; Wang, L.; Beranek, R.; Reisner, E. *Chem. Sci.* **2015**, *6*, 5690–5694.

(53) Lee, C. Y.; Park, H. S.; Fontecilla-Camps, J. C.; Reisner, E. *Angew. Chem. Int. Ed.* **2016**, *55*, 5971–5974.

(54) Mersch, D.; Lee, C. Y.; Zhang, J. Z.; Brinkert, K.; Fontecilla-Camps, J. C.; Rutherford, A. W.; Reisner, E. *J. Am. Chem. Soc.* **2015**, *137*, 8541–8549.

(55) Garcin, E.; Vernede, X.; Hatchikian, E. C.; Volbeda, A.; Frey, M.; Fontecilla-Camps, J. C. *Structure* **1999**, *7*, 557–566.

(56) Sokol, K. P.; Mersch, D.; Hartmann, V.; Zhang, J. Z.; Nowaczyk, M. M.; Rögner, M.; Ruff, A.; Schuhmann, W.; Plumeré, N.; Reisner, E. *Energy Environ. Sci.* **2016**, *9*, 3698–3709.

(57) Kato, M.; Cardona, T.; Rutherford, A. W.; Reisner, E. *J. Am. Chem. Soc.* **2012**, *134*, 8332–8335.

(58) Kato, M.; Cardona, T.; Rutherford, A. W.; Reisner, E. *J. Am. Chem. Soc.* **2013**, *135*, 10610–10613.

(59) Nam, D. H.; Zhang, J. Z.; Andrei, V.; Kornienko, N.; Heidary, N.; Wagner, A.; Nakanishi, K.; Sokol, K. P.; Slater, B.; Zebger, I.; Hofmann, S.; Fontecilla-Camps, J. C.; Park, C. B.; Reisner, E. *Angew. Chem. Int. Ed.* **2018**, *57*, 10595–10599.

(60) McLaughlin, M. P.; McCormick, T. M.; Eisenberg, R.; Holland, P. L. *Chem. Commun.* **2011**, *47*, 7989–7991.

(61) Donck, S.; Fize, J.; Gravel, E.; Doris, E.; Artero, V. *Chem. Commun.* **2016**, *52*, 11783–11786.

(62) Tong, L.; Iwase, A.; Nattestad, A.; Bach, U.; Weidelener, M.; Götz, G.; Mishra, A.; Bäuerle, P.; Amal, R.; Wallace, G. G.; Mozer, A. J. *Energy Environ. Sci.* **2012**, *5*, 9472.

(63) Ji, Z.; He, M.; Huang, Z.; Ozkan, U.; Wu, Y. *J. Am. Chem. Soc.* **2013**, *135*, 11696–11699.

(64) Fan, K.; Li, F.; Wang, L.; Daniel, Q.; Gabrielsson, E.; Sun, L. *Phys. Chem. Chem. Phys.* **2014**, *16*, 25234–25240.

(65) Meng, P.; Wang, M.; Yang, Y.; Zhang, S.; Sun, L. *J. Mater. Chem. A* **2015**, *3*, 18852–18859.

(66) Nann, T.; Ibrahim, S. K.; Woi, P. M.; Xu, S.; Ziegler, J.; Pickett, C. J. *Angew. Chem. Int. Ed.* **2010**, *49*, 1574–1577.

(67) Cedeno, D.; Krawicz, A.; Doak, P.; Yu, M.; Neaton, J. B.; Moore, G. F. *J. Phys. Chem. Lett.* **2014**, *5*, 3222–3226.

(68) Chen, Y.; Chen, H.; Tian, H. *Chem. Commun.* **2015**, *51*, 11508–11511.

(69) Beiler, A. M.; Khusnutdinova, D.; Jacob, S. I.; Moore, G. F. *ACS Appl. Mater. Interfaces* **2016**, *8*, 10038–10047.

(70) Krawicz, A.; Cedeno, D.; Moore, G. F. *Phys. Chem. Chem. Phys.* **2014**, *16*, 15719–16314.

(71) Heller, A. *Science* **1984**, *223*, 1141–1148.

(72) Xiong, L.; Ouyang, M.; Yan, L.; Li, J.; Qiu, M.; Yu, Y. *Chem. Lett.* **2009**, *38*, 1154–1155.

(73) Henderson, M. A. *Surf. Sci. Rep.* **2011**, *66*, 185–297.

(74) Mohamed, H. H.; Mendive, C. B.; Dillert, R.; Bahnemann, D. W. *J. Phys. Chem. A* **2011**, *115*, 2139–2147.

(75) Symes, M. D.; Cronin, L. *Nat. Chem.* **2013**, *5*, 403–409.

(76) Kasap, H.; Caputo, C. A.; Martindale, B. C. M.; Godin, R.; Lau, V. W.-H.; Lotsch, B. V.; Durrant, J. R.; Reisner, E. *J. Am. Chem. Soc.* **2016**, *138*, 9183–9192.

(77) Lau, V. W.-H.; Klose, D.; Kasap, H.; Podjaski, F.; Pignié, M.-C.; Reisner, E.; Jeschke, G.; Lotsch, B. V. *Angew. Chem. Int. Ed.* **2017**, *56*, 510–514.

(78) Hatchikian, E. C.; Bruschi, M.; Le Gall, J. *Biochem. Biophys. Res. Commun.* **1978**, *82*, 451–461.

Chapter 3

Reduction of Aqueous CO_2 with a Cobalt Bis(terpyridine)-Based Photocathode

The contents of this chapter have been submitted for publication as a peer-reviewed article. Results presented were obtained solely by the author of this thesis, with contributions from others as outlined here: Julien Warnan is acknowledged for synthesising the catalyst ***CotpyP*** *and characterising it by IR and UV-vis spectroscopies. Julien Warnan and Dong Heon Nam shared photoelectrode fabrication with the author. Raw XPS data was provided by the Cardiff Catalysis Institute at Cardiff University.*

3.1 Introduction

The solar-driven conversion of CO_2 and water into renewable fuels and chemicals offers a promising route to storing the Sun's intermittent and diffuse energy.[1,2] However, achieving scalable and selective photoelectrodes for aqueous CO_2 conversion without generating hydrogen from competing proton reduction has yet to be accomplished, as was previously discussed in Chapter 1 section 1.5.2.[3] CO_2-reducing molecular catalysts offer a distinct advantage over non-molecular heterogeneous materials as they often combine high product selectivity with high efficiency, and their transparency ensures light penetration to allow for absorption by the semiconductor.[4] On the other hand, photoelectrodes published to date based on precious metal-free heterogeneous catalysts for CO_2 reduction suffer from low selectivity, low Faradaic efficiencies, and the inability to avoid compet-

ing hydrogen evolution in aqueous solution.[5] Therefore, as was the case for H_2 evolution photocathodes, the immobilisation of molecular catalysts onto light-harvesting semiconductor photoelectrodes is an emerging approach to overcome these obstacles for CO_2 reduction.[6,7] As previously discussed in Chapter 1, in contrast to most homogeneous photocatalytic systems, molecular photocathodes require no sacrificial electron source and only a minimal amount of catalyst, while transferring photoexcited electrons without the kinetic limitations of catalyst diffusion. However, only precious metal-containing molecular photocathodes have been reported for aqueous CO_2 reduction to date,[8–12] the majority with formate ($HCOO^-$) over carbon monoxide (CO) as the predominant product.

The work described in this chapter represents the first report of a precious metal-free molecular catalyst-based photocathode for CO_2 reduction. The photoelectrochemical hybrid system consists of the same scaffold developed previously in Chapter 2: a p-silicon (Si) photoelectrode modified with a mesoporous titania (*meso*TiO_2) layer. In much the same way as it first appealed to us in the work described in Chapter 2, silicon's ubiquity in the Earth's crust and price drop as a result of its utilisation in the photovoltaic industry make it an attractive material in economic terms. Its conduction band energy delivers approximately 0.4 V for the reduction of CO_2 to CO and the small energy band gap of 1.12 eV enables panchromatic light harvesting in the ultraviolet, visible and near-infrared regions. The *meso*TiO_2 interlayer provides a high surface area scaffold for binding of a phosphonated cobalt(II) bis(terpyridine) catalyst, **CotpyP** (Fig. 3.1). Upon solar light irradiation, Si is able to inject electrons into TiO_2, which then shuttles them to the anchored Co catalyst.

3.2 Results and Discussion

3.2.1 Synthesis of CotpyP and Photocathode Assembly

The CO_2 reduction catalyst **CotpyP** (Fig. 3.1) was synthesised by self-assembly of $Co(BF_4)_2{\cdot}6H_2O$ with two equivalents of phosphonated terpyridine, 2,2':6',2"-terpyridine-4'-phosphonic acid (**tpyP**). Full synthetic details and characterisation (^1H and ^{31}P nuclear magnetic resonance (NMR) spectroscopy, high-resolution mass spectrometry (HRMS), IR and elemental analysis) are available in the Experimental Section 3.4.3). Unshielded chemical shifts in the range of 9 to 100 ppm characteristic of a paramagnetic cobalt(II) bis(terpyridine) complex were

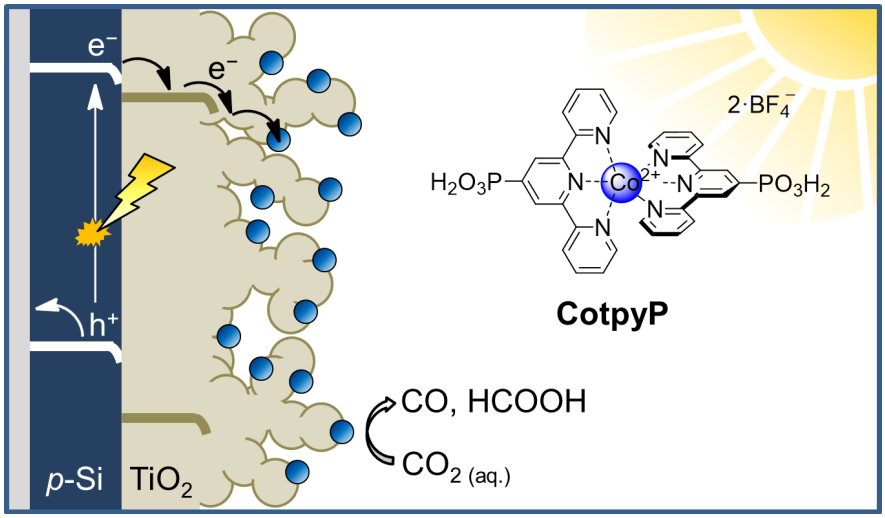

Fig. 3.1 Schematic diagram of CO_2 reduction with Si|*meso*TiO_2|**CotpyP** photocathode.

observed in the ^{1}H NMR (MeOD-d^4) spectrum.[13] It is worth noting that no additional peaks indicative of the mono(terpyridine) complex were observed, implying an equilibrium in favour of the bis(terpyridine) complex in MeOH.[14,15]

ATR-FTIR of the isolated **CotpyP** displayed bands at 1604, 1475, 1413 cm^{-1} (Fig. 3.2), which are assigned to stretching vibrations of aromatic rings.[16] The UV-vis spectrum of **CotpyP** in solution displays three absorption maxima ($\lambda_{max} = 448$, 510 and 555 nm in methanol), which have been previously attributed to metal-to-ligand charge transfer transitions for low-spin cobalt(II) bis(terpyridine) species (Fig. 3.3a).[17]

The Si|*meso*TiO_2|**CotpyP** photocathode was assembled by first depositing a stabilising mesoporous, anatase TiO_2 scaffold (TiO_2 particle size ~15–20 nm, film thickness ~6 µm) on Si as previously described in Chapter 2 Experimental Section 2.4.2 (Fig. C.1).[18] The Si|*meso*TiO_2 electrodes were subsequently modified with the catalyst by immersion in a methanol solution of **CotpyP**. UV-visible spectroscopic features for the adsorbed **CotpyP** were comparable to the isolated catalyst (Fig. 3.3b), suggesting that its structure is preserved upon immobilisation. Similarly, ATR-FTIR revealed the same fingerprint upon immobilisation of the catalyst (Fig. 3.2, blue trace), whereas XPS showed binding signals in the Co_{2p}, P_{2p} and N_{1s} regions with elemental atomic concentration ratios in general agreement with the catalyst structure (Fig. 3.4, Table 3.1). The loading of the chemisorbed **CotpyP** on the *meso*TiO_2 scaffold was estimated by inductively coupled plasma optical emission spectrometry (ICP-OES) after desorption as 45.0 ± 7.4 nmol cm^{-2},

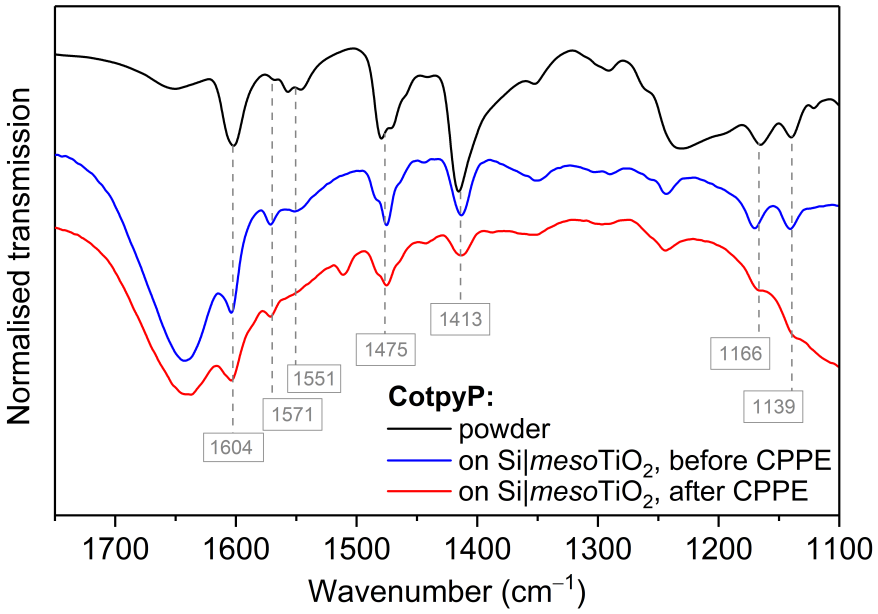

Fig. 3.2 ATR-FTIR spectra of **CotpyP** as a powder (black trace), and after immobilisation on *meso*TiO_2 before (blue trace) and after (red trace) 1 h of CPPE. CPPE conditions: $E_{app} = -1.0$ V *vs.* Fc^+/Fc, 1 Sun (AM1.5G, 100 mW cm^{-2}, $\lambda > 400$ nm), CO_2-saturated conditions in 6:4 MeCN:H_2O with 0.1 M $TBABF_4$ at room temperature.

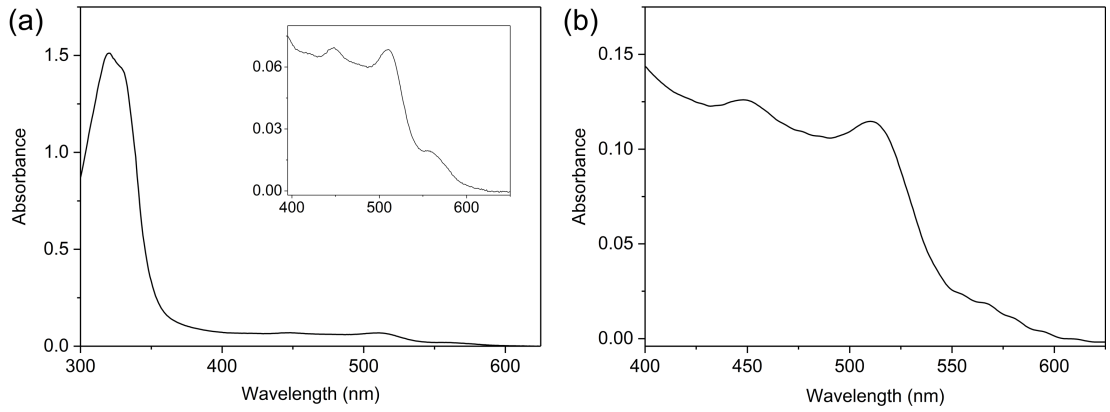

Fig. 3.3 UV-visible spectra of self-assembled **CotpyP** (a) in MeOH (0.25 mM, room temperature; inset: close-up of 400-650 nm range) and (b) immobilised on a transparent mesoporous TiO_2 electrode (thickness: 6 µm).

which is in agreement with previously-reported molecular loadings on mesoporous films, including those on the same Si|*meso*TiO_2 scaffold in Chapter 2.

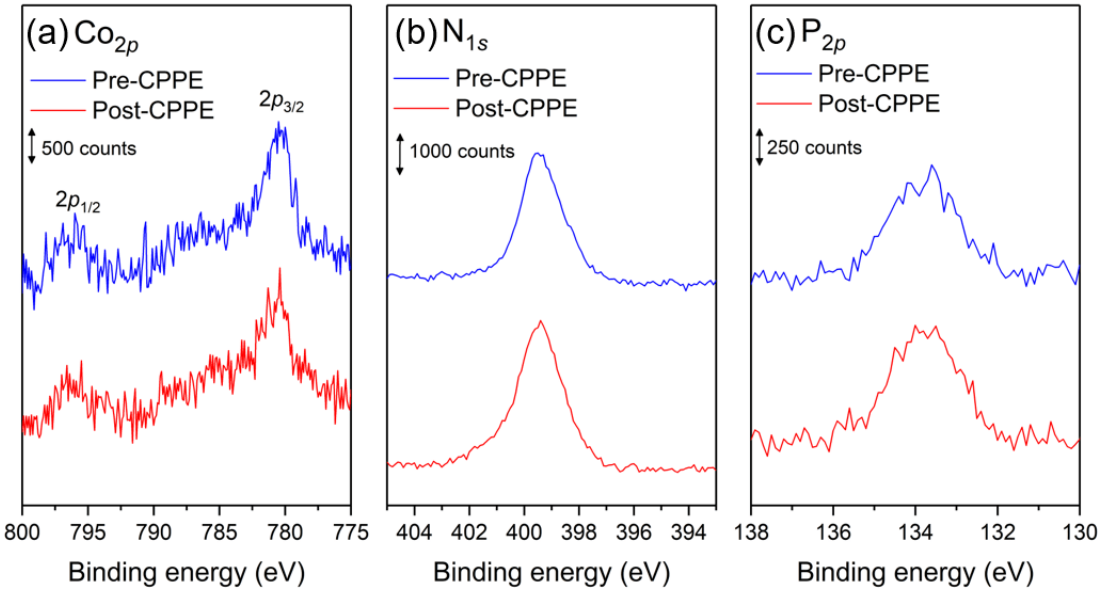

Fig. 3.4 XPS spectra of Si|*meso*TiO_2|**CotpyP** electrodes in the (a) Co_{2p}, (b) N_{1s} and (c) P_{2p} regions showing peaks attributed to Co^{II}-N, pyridine N and phosphonic acid groups, respectively, before (blue traces) and after (red traces) 8 h of CPPE.[19–21] CPPE conditions: $E_{app} = -1.0$ V *vs.* Fc^+/Fc, 1 Sun (AM1.5G, 100 mW cm^{-2}, $\lambda > 400$ nm), CO_2-saturated conditions in 6:4 MeCN:H_2O with 0.1 M $TBABF_4$ at room temperature.

Table 3.1 Atomic concentrations and resulting Co:X (X = P, N) ratios as given by binding signals in the Co_{2p}, N_{1s} and P_{2p} regions of XPS spectra of Si|*meso*TiO_2|**CotpyP** before and after 8 h of CPPE. CPPE conditions: $E_{app} = -1.0$ V *vs.* Fc^+/Fc, 1 Sun (AM1.5G, 100 mW cm^{-2}, $\lambda > 400$ nm), CO_2-saturated conditions in 6:4 MeCN:H_2O with 0.1 M $TBABF_4$ at room temperature.

Binding signal	% Atomic concentration		Co : X ratio	
	Before CPPE	*After CPPE*	*Before CPPE*	*After CPPE*
$Co_{2p_{3/2}}$	0.37	0.27	-	-
N_{1s}	2.17	2.3	1 : 5.9	1 : 8.5
P_{2p}	0.92	0.84	1 : 2.5	1 : 3.1

3.2.2 Photoelectrocatalytic CO_2 Reduction

Controlled potential photoelectrolysis of Si|*meso*TiO_2|**CotpyP** was conducted under a CO_2 atmosphere at $E_{app} = -1.0$ V *vs.* Fc^+/Fc under continuous UV-filtered

simulated solar irradiation (AM1.5G, 100 mW cm^{-2}, $\lambda > 400$ nm) at room temperature. CO and H_2 were quantified by gas chromatography, whereas $HCOO^-$ was quantified by ion chromatography. Different electrolyte solution compositions were studied to identify optimal conditions for the system.

No CO_2 reduction products were detected with Si|*meso*TiO_2|**CotpyP** in anhydrous acetonitrile (MeCN) containing 0.1 M tetrabutylammonium tetrafluoroborate ($TBABF_4$) after several hours of CPPE. Addition of water into the electrolyte solution resulted in catalytic CO_2 reduction with the turnover number for CO_2 reduction (TON_{CO_2} = TON_{CO} + TON_{HCOO^-}) rising from 13 (9:1 v:v MeCN:H_2O) to 108 (7:3 MeCN:H_2O) after 8 h CPPE upon increasing the H_2O content. The selectivity for CO was favoured in all cases and the overall FE (FE_{H_2} + FE_{CO} + FE_{HCOO^-}) increased from 12 % (9:1 MeCN:H_2O) to 53 % (7:3 MeCN:H_2O) (Fig. 3.5 and Table 3.2, the latter of which disseminates all CPPE results in full). We note that H_2 production is not discussed in terms of TON as the catalyst-free Si|*meso*TiO_2 electrode also produces a minimal amount of H_2 and this may contribute to overall H_2 produced by Si|*meso*TiO_2|**CotpyP** (Fig. C.2). The modest FE under these conditions can be partially attributed to initial reduction of trapped O_2 in the *meso*TiO_2 architecture, ineffective catalyst reduction or progressive desorption leading to unproductive electron transfer pathways.[22] The latter is implied by the steadily decreasing turnover frequency for CO production (TOF_{CO}) over time (Fig. 3.6).

Further increase in water content resulted in the activity increasing up to an optimal point at 40 % water. In 6:4 MeCN:H_2O, a remarkably stable photocurrent as well as an overall FE of 77 % (with FE_{CO} = 48 %) and a TON_{CO_2} of 159 were achieved after 8 h CPPE (Fig. 3.5 and 3.7a). The photocathode maintained activity during 24 h of operation and achieved a TON_{CO_2} of 381 (TON_{CO} = 334, TON_{HCOO^-} = 47, Fig. C.3). Bringing the water content to 50 % also allowed for robust CPPE with a constant TOF_{CO} over time (Fig. 3.6), but a slightly reduced TON_{CO_2} and FE. Thus, increasing the water content in the electrolyte solution from 10-30 % to 40-50 % has an apparently beneficial effect on the stability and activity of the catalyst and/or the performance of the full photocathode assembly.

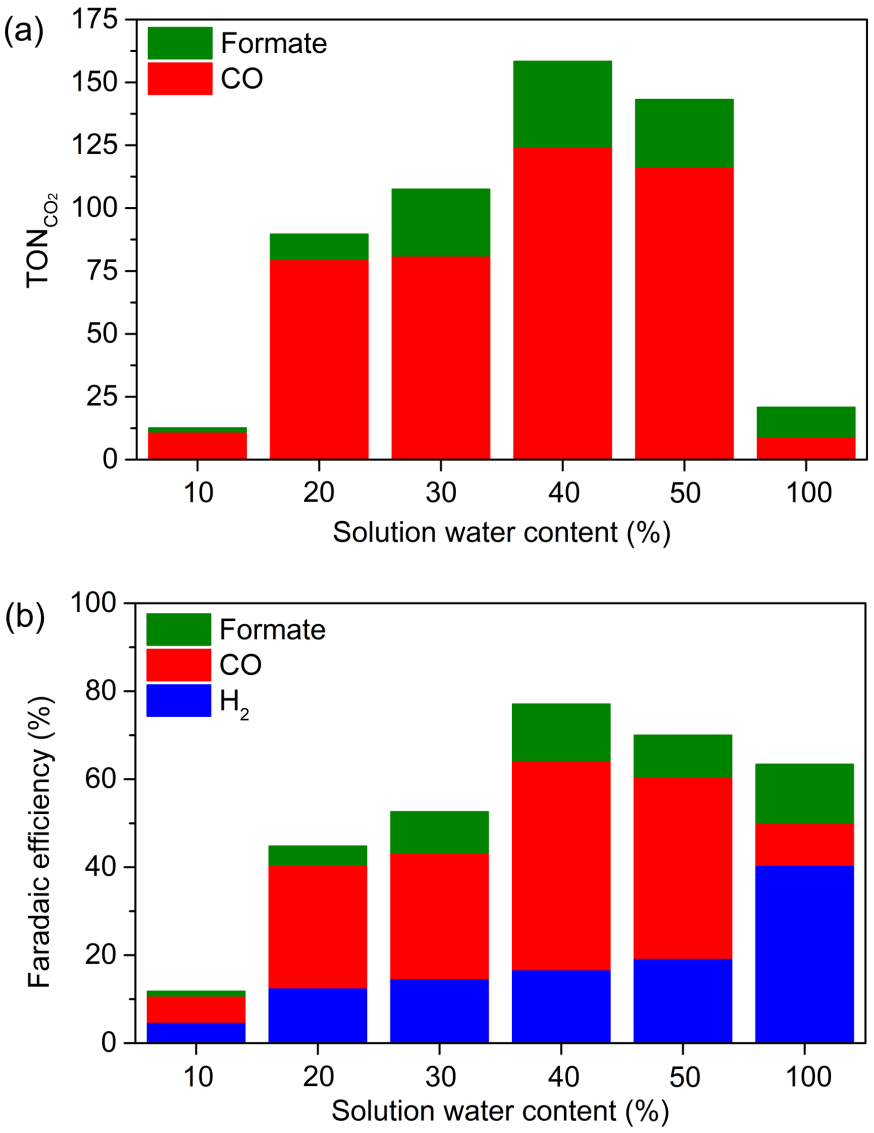

Fig. 3.5 Performance of Si|*meso*TiO_2|**CotpyP** photocathodes in different electrolyte solutions after 8 h of CPPE: (a) TON for CO_2 reduction products, and (b) FEs (cumulative over the duration of the CPPE) for all products. Conditions: $E_{app} = -1.0$ V *vs.* Fc^+/Fc for MeCN:H_2O mixtures, $E_{app} = 0.0$ V *vs.* RHE for H_2O; simulated solar light (AM1.5G, 100 mW cm^{-2}, $\lambda > 400$ nm); CO_2-saturated solutions of $TBABF_4$ (0.1 M) in MeCN:H_2O mixtures (solution water content 10-50 %) or $KHCO_3$ (0.1 M, pH 6.7) in pure water; room temperature.

Table 3.2 Summary of results obtained from 8 h of CPPE with Si|*meso*TiO_2|**CotpyP** in different operating electrolyte solutions: product quantities, TON for CO_2 reduction products and Faradaic efficiency cumulative over the 8 h period. Note that TON for H_2 has not been included as the catalyst-free Si|*meso*TiO_2 photoelectrode also produces some H_2 (see Fig. C.2) and this background production cannot be excluded from the results here. Results from optimum conditions are highlighted in red. CPPE conditions: $E_{app} = -1.0\,V$ *vs.* Fc^+/Fc for MeCN:H_2O mixtures, $E_{app} = 0.0\,V$ *vs.* RHE for H_2O; simulated solar light (AM1.5G, $100\,mW\,cm^{-2}$, $\lambda > 400\,nm$); CO_2-saturated conditions; room temperature.

Electrolyte solution	**Product** ($\mu mol\,cm^{-2}$)				**Turnover number**			**Faradaic efficiency** (%)			
	CO	$HCOO^-$	H_2	**Total**	CO	$HCOO^-$	**Total**	CO	$HCOO^-$	H_2	**Total**
9:1 MeCN:H_2O (0.1 M $TBABF_4$)	0.50 ± 0.04	0.069 ± 0.003	0.40 ± 0.03	**1.0 ± 0.05**	11.1 ± 2.0	1.5 ± 0.3	**12.6 ± 2.0**	6.0 ± 0.5	1.0 ± 0.05	4.8 ± 0.3	**11.8 ± 0.6**
8:2 MeCN:H_2O (0.1 M $TBABF_4$)	3.6 ± 0.3	0.45 ± 0.02	2.0 ± 0.1	**6.1 ± 0.3**	79.6 ± 14.6	10.1 ± 1.7	**89.7 ± 14.7**	27.9 ± 2.2	4.3 ± 0.2	12.6 ± 0.9	**44.8 ± 2.4**
7:3 MeCN:H_2O (0.1 M $TBABF_4$)	3.6 ± 0.3	1.2 ± 0.06	2.1 ± 0.1	**6.9 ± 0.3**	81.0 ± 14.8	26.5 ± 4.6	**107.5 ± 15.5**	28.6 ± 2.3	9.3 ± 0.5	14.7 ± 1.0	**52.6 ± 2.6**
6:4 MeCN:H_2O (0.1 M $TBABF_4$)	5.6 ± 0.6	1.5 ± 0.08	2.0 ± 0.2	**9.1 ± 0.6**	124.5 ± 24.0	33.9 ± 5.8	**158.4 ± 24.7**	47.6 ± 4.7	12.8 ± 0.6	16.7 ± 1.6	**77.1 ± 5.0**
5:5 MeCN:H_2O (0.1 M $TBABF_4$)	5.2 ± 0.4	1.2 ± 0.06	2.5 ± 0.2	**8.9 ± 0.4**	116.5 ± 20.8	26.6 ± 4.6	**143.2 ± 21.3**	41.2 ± 2.9	9.4 ± 0.5	19.3 ± 1.5	**70.0 ± 3.3**
H_2O (0.1 M $KHCO_3$)	0.40 ± 0.03	0.53 ± 0.03	1.6 ± 0.1	**2.5 ± 0.1**	9.0 ± 1.6	11.8 ± 2.0	**20.8 ± 2.6**	9.5 ± 0.7	13.4 ± 0.7	40.5 ± 3.2	**63.4 ± 3.4**

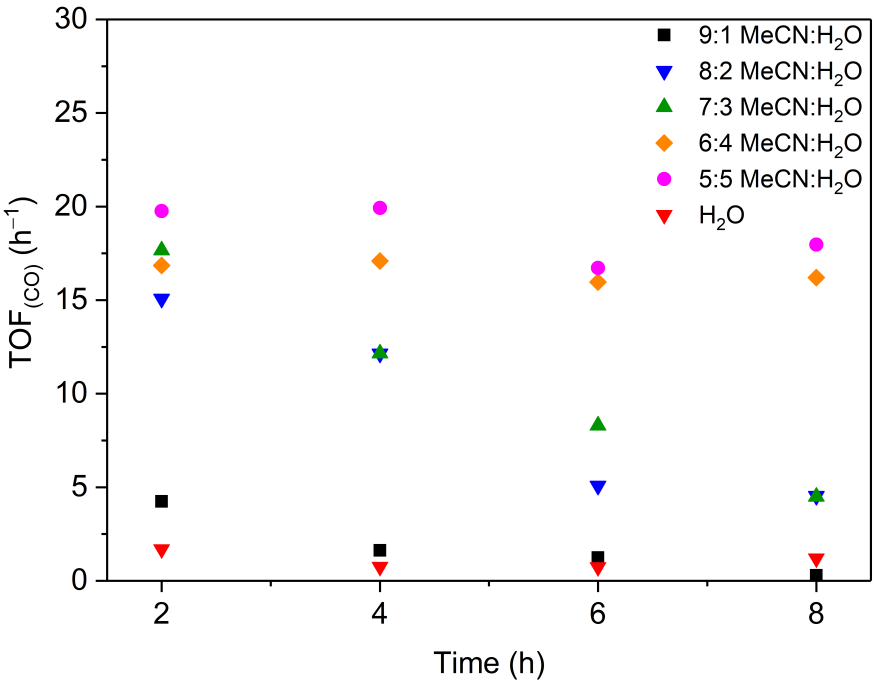

Fig. 3.6 Catalytic turnover frequencies for CO production (cumulative over duration of CPPE) by Si|*meso*TiO_2|**CotpyP** photocathodes in a variety of electrolyte solution systems during 8 h of CPPE. Conditions: $E_{app} = -1.0$ V *vs.* Fc^+/Fc for MeCN:H_2O mixtures, $E_{app} = 0.0$ V *vs.* RHE for H_2O; simulated solar light (AM1.5G, 100 mW cm^{-2}, $\lambda > 400$ nm); CO_2-saturated solutions of $TBABF_4$ (0.1 M) in MeCN:H_2O mixtures (solution water content 10-50 %) or $KHCO_3$ (0.1 M, pH 6.7) in pure water; room temperature.

The Si|*meso*TiO_2|**CotpyP** photocathode was also found to display catalytic CO_2 reduction activity in pure CO_2-saturated water (0.1 M $KHCO_3$) at pH 6.7, reaching a TON_{CO_2} of 21 with a Faradaic efficiency for CO and $HCOO^-$ at 9.5 % and 13 %, respectively, after 8 h CPPE (Fig. 3.5). Interestingly, the catalytic selectivity changed from CO as the main product in hydro-organic media to formate and H_2 in purely aqueous electrolyte solution, highlighting a shift towards proton-containing products. Despite the TOF_{CO} being low from the outset, it remains constant during CPPE in water (Fig. 3.6), again implying good catalyst stability with an increasing presence of water. The latter is also supported by observations of stability made from cyclic voltammograms (CVs) conducted on a mesoporous indium tin oxide (ITO) film on a fluorine-doped tin oxide-coated glass electrode (*meso*ITO|**CotpyP**). *Meso*ITO was employed as it provides conductivity over a wide potential range. Repetitive CV scans of this electrode in a three-electrode configuration in N_2-purged aqueous electrolyte solution (0.1 M Na_2SO_4) displayed reversible redox waves for the formal Co^{III}/Co^{II} and Co^{II}/Co^{I} couples that remain unaltered during repetitive cycling, as well as a practically zero

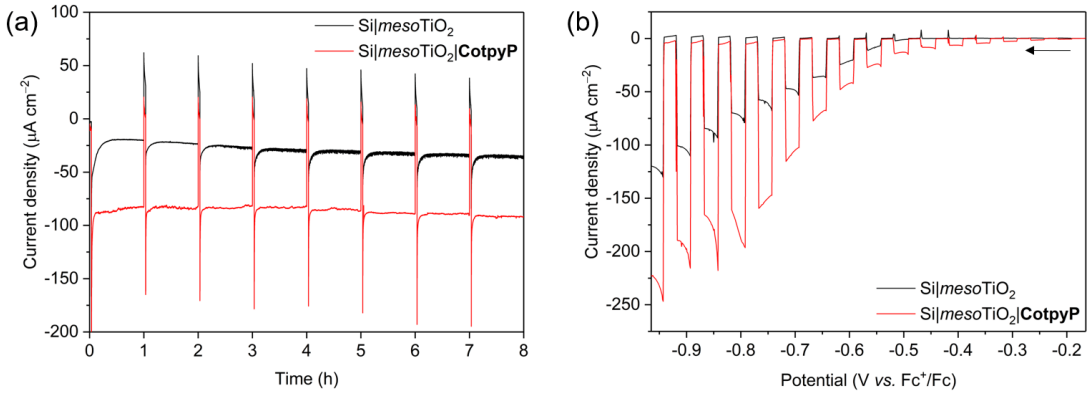

Fig. 3.7 (a) CPPE (*J*-*t*) traces ($E_{app} = -1.0\,V$ *vs.* Fc^+/Fc) with Si|*meso*TiO_2 (black trace) and Si|*meso*TiO_2|**CotpyP** (red trace) photocathodes under continuous illumination and an hourly 2 min dark chop (for close-up see Fig. C.4). (b) LSVs of Si|*meso*TiO_2 and Si|*meso*TiO_2|**CotpyP** with chopped illumination ($\nu = 5\,mV\,s^{-1}$); the arrow indicates scan start. Conditions: 6:4 MeCN:H_2O (0.1 M $TBABF_4$); 1 Sun (AM1.5G, $100\,mW\,cm^{-2}$, $\lambda > 400\,nm$); CO_2-saturated conditions; room temperature.

peak-to-peak separation at slow scan rates and a linear dependence of current density to scan rate, which both indicate robust catalyst immobilisation in the first instance (Fig. 3.8).

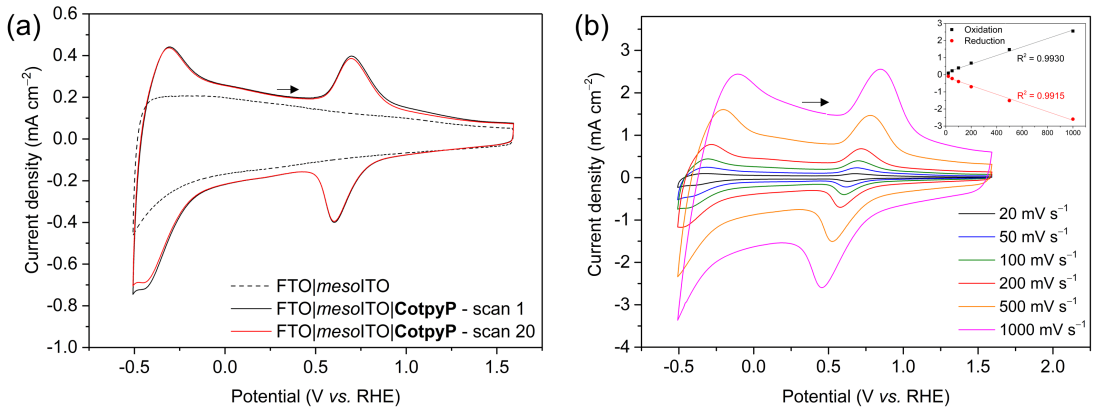

Fig. 3.8 CVs of *meso*ITO|**CotpyP** in aqueous solution (0.1 M Na_2SO_4, pH 6.8, N_2-purged, room temperature). Arrows indicate the scan start and no **CotpyP** was present in solution. (a) CVs recorded at $\nu = 50\,mV\,s^{-1}$; the first scan is shown as black trace, the 20th as red trace and a control scan without **CotpyP** as dashed trace. (b) CVs recorded at different scan rates (inset: immobilisation of **CotpyP** on ITO is confirmed by linear dependency of current on scan rate).

Linear sweep voltammograms with chopped illumination in the optimal electrolyte solution (6:4 MeCN:H_2O) revealed a photocurrent onset potential at $-0.44\,V$ *vs.* Fc^+/Fc for Si|*meso*TiO_2|**CotpyP**, compared to $-0.56\,V$ *vs.* Fc^+/Fc for

the bare Si|*meso*TiO_2 electrode (Fig. 3.7b). **CotpyP**-functionalised photoelectrodes showing approximately double the photocurrent and an onset that occurs 120 mV earlier than its catalyst-free counterpart is probably a manifestation of fast electron transfer in the presence of the catalyst. Note that the majority of charges in the **CotpyP**-free photoelectrode are likely charging of TiO_2 without promoting catalysis in the short timescale of LSVs, as was the case with the H_2-evolving photocathodes in Chapter 2 (Fig. C.4).[18]

Several control experiments were conducted in 6:4 MeCN:H_2O solution to ascertain that CO_2 reduction catalysis originated from **CotpyP** (Fig. 3.9). Product analysis following CPPE with both bare Si|*meso*TiO_2 under CO_2 and Si|*meso*TiO_2|-**CotpyP** under N_2 revealed only traces of H_2 and no CO_2 reduction products (Fig. C.2 and C.5). Isotopic labelling experiments conducted with Si|*meso*TiO_2|-**CotpyP** in a $^{13}CO_2$-saturated solution confirmed that CO originated from CO_2 and not another carbon source (determined by gas-phase IR analysis; Fig. 3.10). CPPE was also conducted on a photoelectrode modified with the catalyst metal salt precursor, $Co(BF_4)_2{\cdot}6H_2O$ (Si|*meso*TiO_2|$Co(BF_4)_2$; Fig. C.6) to determine that CO_2 reduction was not being performed by Co salt released from the degrading molecular catalyst. In this case, mostly H_2 at a FE of 84 % and minimal CO and formate were produced, and can be ascribed to catalysis carried out by a heterogeneous deposit. This is also suggested by the initial period of growth in the current density trace indicative of metal deposition (Fig. C.6a),[23] which was never observed in chronoamperograms obtained from Si|*meso*TiO_2|**CotpyP**.

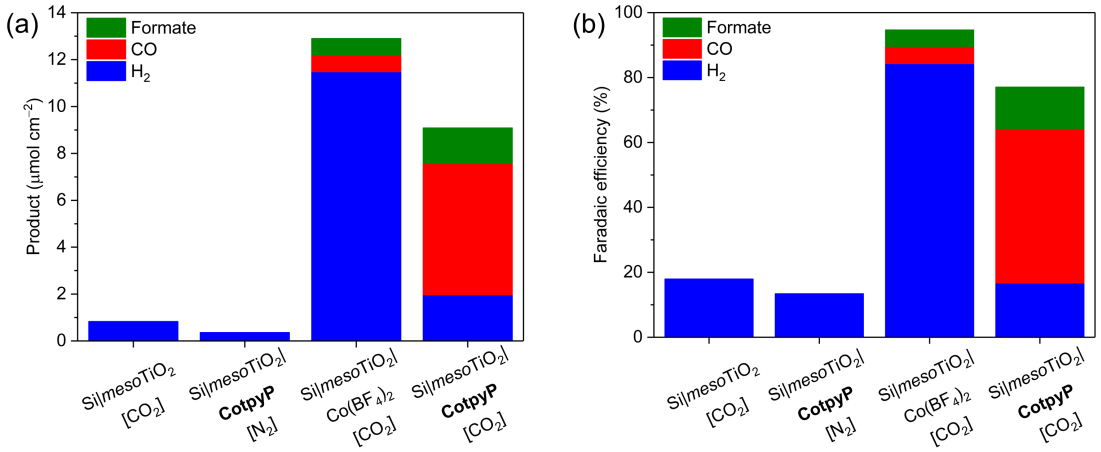

Fig. 3.9 (a) Product analyses and (b) Faradaic efficiencies of Si|*meso*TiO_2|**CotpyP** and control experiments after 8 h of CPPE. Conditions: $E_{app} = -1.0$ V *vs.* Fc^+/Fc; 6:4 MeCN:H_2O (0.1 M $TBABF_4$); 1 Sun (AM1.5G, 100 mW cm^{-2}, $\lambda > 400$ nm); room temperature; atmosphere indicated in square brackets.

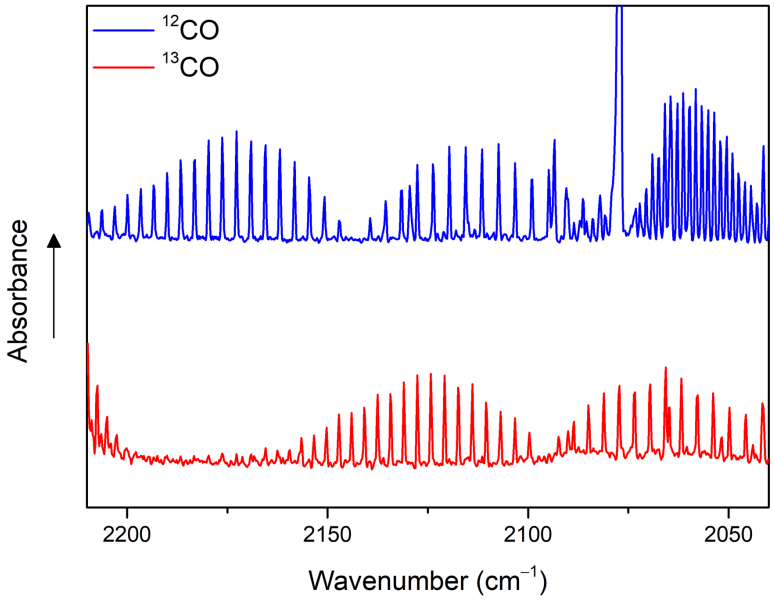

Fig. 3.10 Isotopic labelling control experiment: IR spectra of samples of the gaseous products taken after 4 h of CPPE of Si|*meso*TiO_2|**CotpyP** under a $^{12}CO_2$ and a $^{13}CO_2$ environment. Conditions: $E_{app} = -1.0$ V *vs.* Fc^+/Fc; 6:4 MeCN:H_2O (0.1 M $TBABF_4$); 1 Sun (AM1.5G, 100 mW cm^{-2}, $\lambda > 400$ nm); room temperature.

Analyses by ATR-FTIR and XPS were further employed to confirm the post-CPPE molecular integrity of **CotpyP**. The FTIR fingerprint spectrum remained largely unchanged (Fig. 3.2, red trace), whereas the XPS spectra showed clear signals at pre-CPPE binding energies and the absence of one at 778.2 eV in the Co_{2p} region that would indicate metallic Co (Fig. 3.4 and Table 3.1).[24] Only a small change in the atomic concentration ratios was observed, suggesting a small loss of the metal centre.

The inability of the immobilised **CotpyP** catalyst to turn over under anhydrous conditions implies a proton-dependent mechanism, but the substantial rate enhancements for CO_2 reduction up to 40 % water content suggest an additional role of H_2O to explain the strong solvent-dependent performance of Si|*meso*TiO_2|**CotpyP**. Firstly, the enhanced catalytic rate with increasing H_2O content (TOF_{CO}, Fig. 3.6) is due to a changing thermodynamic landscape as $E°'(CO_2/CO)$ becomes less negative, resulting in a more exergonic reaction upon addition of water to MeCN. This change in $E°'(CO_2/CO)$ was only recently first reported by Matsubara for mixtures of MeCN and H_2O,[25] and was found to be most pronounced when the volume percentage of water (x) is $0 < x < 16$, plateauing at $16 < x < 45$. Our optimal conditions ($x = 40$) lies within this latter region, thus ratifying our optimum conditions. Secondly, (photo)electrocatalytic CO_2 reduction is commonly limited by its low solubility in solutions with high

water content, which would partially explain a performance maximum at median water concentrations.[26,27] This limited availability of CO_2 and the correspondingly higher concentration of protons would also favour H_2 evolution.

Finally, another phenomenon that could be at play is the impact on the TiO_2 electrode's interface. As the water concentration increases in aprotic solvents, the proton adsorption-desorption equilibrium at the metal oxide electrode-solution interface would favour proton adsorption.[28,29] This results in two consequences: (i) a shift of the CB of TiO_2 to more positive potentials, and (ii) changes in the surface hydrophilicity and local pH.[29–31] Consequently, the further addition of water in our system causes less thermodynamic driving force for both proton and CO_2 reduction and a more protic environment with a lower CO_2 concentration, resulting in lower activity and selectivity.

3.2.3 Comparison with State of the Art

To date, reported molecule-based photocathodes performing CO_2 reduction remain scarce, whether in organic or water-containing media, and continue to rely on precious metal-containing components.[8–12,32–34] Moreover, even in anhydrous conditions where enhanced photocathode and/or catalyst stability may be expected, only a few reports exist, and all depend on Re-based catalysts.[32–34] For instance, a Re-bipyridine catalyst on a Cu_2O photoelectrode protected by multiple atomic-layer-deposited coatings has been reported to achieve a TON_{CO} of 70 in anhydrous MeCN.[34] Another benchmark system consists of a Ru-Re dye-catalyst dyad immobilised on NiO that evolves CO in dry DMF solution.[32] Systems reported in water continue to face activity issues and favour H_2 and $HCOO^-$ over CO production. Apart from one that produces CO,[12] the few reports on narrow band gap semiconductors in water produce only formate with a TON_{HCOO^-} that does not exceed 20,[8,10] and are all based on Ru-centred metal complex catalysts.

When it comes to purely aqueous solutions, photoelectrochemical production of CO was achieved with Re- and Ru-centred catalysts, in dye-catalyst dyads on wide band gap semiconductors[9,11] or immobilised on a hematite photoelectrode,[12] respectively, with the maximum TON_{CO} in these systems reaching 125. In these CO-producing systems, H_2 and $HCOO^-$ also occurred as co-products – the former in quantities above half the amount of CO,[9] and the latter at similar proportions of CO[12] – demonstrating a continued struggle with product selectivity even with molecule-catalysed systems.

Despite not containing precious metals, the performance of our **CotpyP**-functionalised silicon photocathode exceeds all previous reports in both TONs towards CO_2-reduction products and stability.[8–12,32–34] Although the potential of Si as an Earth-abundant light harvester has been previously recognised to drive homogeneous molecular catalysts (in solution) for solar CO_2 reduction,[35,36] this work represents the first successful immobilisation of such a molecular catalyst onto Si to yield a discrete, functional photocathode. This also allowed us to demonstrate CO production in pure water, which is unprecedented for a precious metal-free synthetic molecular catalyst on a photocathode. Demonstrating aqueous CO_2 conversion for more than one day with the Co-centred molecular catalyst photo-driven by Si is therefore an extremely strong basis for further improvement towards scalable, high-performance systems.

3.3 Conclusion

In conclusion, this work represents the first precious metal-free molecular photocathode towards solar-driven CO_2 reduction, in any kind of media (aqueous or not). This Si|*meso*TiO_2|**CotpyP** electrode is active towards CO and formate production in both hydro-organic and purely aqueous solution, achieving a TON for CO_2-reduction products as high as 381 after 24 h – a record value that exceeds previously reported benchmarks for molecular photocathodes (including those containing precious metal complexes). Furthermore, with a selectivity towards CO of ∼75 % across all gaseous products, our photocathode compares favourably with most reported precious metal-free photocathodes based on heterogeneous material catalysts that deliver state-of-the-art performances. The results further highlight that altering the water content of the photoelectrocatalysis media has a pronounced effect on the stability, activity, and product selectivity of the photocathode.

3.4 Experimental Section

3.4.1 Materials

Chemicals purchased for analytical measurements were of the highest available purity. Commercial *p*-type boron-doped silicon wafers (resistivity of 1-10 ohm cm; <100>; 500 µm thickness; single-side polished) were purchased from University

Wafer. The TiO_2 paste was purchased from Solaronix (15-20 nm, Ti-Nanoxide T/SP, 100 % anatase). Fluorine-doped tin oxide (FTO)-coated glass sheets were purchased from Sigma Aldrich (SnO_2/F, 7 Ω sq^{-1} sheet resistance, 300 × 300 × 2 mm). ITO nanopowder (< 50 nm particle size; BET = 27 m^2 $g^{˘1}$; 90 % In_2O_3, 10 % SnO_2) was obtained from Sigma Aldrich. $KHCO_3$ and $Co(BF_4)_2{\cdot}6H_2O$ (96 %) were purchased from Alfa Aesar and 2,2':6',2"-terpyridine-4'phosphonic acid was purchased from HetCat, Switzerland (98 %). $TBABF_4$ was purchased from Sigma Aldrich (≥ 99.0 %, electrochemical grade). Methanol and acetonitrile were both distilled over calcium hydride before use. All aqueous experimental solutions were prepared with ultrapure Milli-Q® water (18.2 MΩ cm at 25 °C). $^{13}CO_2$ (> 99 atom % ^{13}C) was purchased from Sigma Aldrich.

3.4.2 Physical Characterisation

^1H and ^{31}P NMR spectra were recorded on a Bruker 500 Hz DCH cryoprobe spectrometer at room temperature. Chemical shifts are given in ppm and coupling constants in Hz. Chemical shifts for ^1H NMR spectra are referenced relative to residual protium in the deuterated methanol (Euriso-top). High-resolution mass spectra were recorded using a ThermoScientific Orbitrap Classic mass spectrometer. UV-vis spectra were collected using a Varian Cary 50 Bio UV-vis spectrometer. For solution spectra, a quartz cuvette (Hellma, 1 cm path length) was used. ATR-FTIR spectra were recorded on a Nicolet iS50 spectrometer. Elemental analysis was carried out by the Microanalysis Service of the Department of Chemistry, University of Cambridge, using a Perkin-Elmer 240 Elemental Analyser. ICP-OES measurements were conducted by the Microanalysis Service of the Department of Chemistry, University of Cambridge, on a Thermo Scientific iCAP 7400 ICP-OES DUO spectrometer. XPS was performed by Surface Analysis services at the Cardiff Catalysis Institute, School of Chemistry, Cardiff University, on a Thermo Fisher Scientific Kα^+ spectrometer using a micro-focused monochromatic Al X-ray source (72 W) over an area of approximately 400 microns, with argon sputtering performed using a Thermo Scientific MAGCIS source operating in the monatomic mode at 4 kV over a raster area of approximately 2 mm^2. Data analysis was performed in CasaXPS using a Shirley type background and Scofield cross sections, with an energy dependence of −0.6.

3.4.3 Synthesis and Characterisation of CotpyP

2,2':6',2"-terpyridine-4'phosphonic acid (**tpyP**; 30.0 mg, 9.6×10^{-5} mol) and $Co(BF_4)_2{\cdot}6H_2O$ (14.3 mg, 4.2×10^{-5} mol) were placed in a round bottom flask under N_2 atmosphere and solubilised with 6 mL of MeOH (a few drops of water can be added to improve the solubility). The solution was stirred for 24 h at room temperature during which the colour gradually turned from colourless to red-brown, attesting to the formation of the cobalt bis(terpyridine) complex. Ethanol (4 mL) was then added, followed by ethyl acetate to precipitate the complex. The solid was filtered off on Millipore and washed with ethyl acetate. The solid was dried under vacuum to afford 21 mg of **CotpyP** complex as a fine brown powder (58 % yield). ^{1}H NMR (MeOD, 500 MHz): δ_H (ppm) = 91.00 (bs), 52.39 (s), 38.82 (s), 32.86 (s), 9.74 (s); ^{31}P NMR (MeOD, 202 MHz): δ_P (ppm) = 34.25; FT-IR (ATR): σ (cm^{-1}): 1604, 1558, 1480, 1416, 1166, 1140. HRMS (+ESI, m/z): calcd. for $C_{30}H_{23}O_6N_6{}^{56}Co_1P_2$ $[M\text{-}H^+\text{-}2{\cdot}BF_4{}^{-1}]^+$: 684.0481; found, 684.0472. Anal. calcd. for $C_{30}H_{24}B_2Co_1F_8N_6O_6P_2$: C, 41.95; H, 2.82; N, 9.78; P, 7.21; found: C, 41.76; H, 3.22; N, 9.57; P, 7.32. UV-vis (MeOH): λ_{max} (nm) = 320, 448, 510, 555.

3.4.4 Assembly of Molecular Electrodes

Fabrication of *meso*ITO and Si|*meso*TiO_2 Electrodes

FTO-coated glass sheets were cut into 1 cm × 3 cm pieces and cleaned by immersing them in a solution of water, ammonia (35 %, Fisher Scientific) and hydrogen peroxide (30 % w/v, Breckland Scientific Supplies) in a 5:1:1 v:v ratio at 70 °C for 30 min. The glass slides were subsequently sonicated in water and dried at room temperature. An ITO suspension consisting of 20 wt % of ITO nanopowder in 5 M acetic acid in ethanol was prepared and sonicated well. This was spin-coated onto the cleaned FTO glass slides over a 1 cm × 0.8 cm area defined using Scotch® tape (3M) as spacers, using a volume of 200 µL per slide and a spin speed of 1000 rpm over 1 min. The solution was left to dry completely in air before removing the tape and annealing in a Carbolite furnace under atmospheric conditions using the following temperature program: heating from 25 °C to 400 °C (5 °C min^{-1}), holding at 400 °C for 30 min before slowly cooling down to room temperature in the furnace chamber, to yield the resulting *meso*ITO electrodes. The preparation of the Si|*meso*TiO_2 electrodes was conducted following the procedure outlined in Chapter 2 section 2.4.2.

Assembly of *meso*ITO|CotpyP and Si|*meso*TiO_2|CotpyP

Immobilisation of **CotpyP** on *meso*ITO and Si|*meso*TiO_2 was carried out by soaking the electrodes in a methanolic solution of **CotpyP** (prepared by the dropwise addition of a MeOH solution of **tpyP** to a MeOH solution of $Co(BF_4)_2{\cdot}6H_2O$ to give a final concentration of 0.25 mM) for 16 h. The *meso*ITO|**CotpyP** and Si|*meso*TiO_2|**CotpyP** electrodes were rinsed with MeOH and dried prior to use. In the case of Si|*meso*TiO_2|**CotpyP**, the photocathodes were subsequently back-contacted and insulated by an epoxy adhesive prior to further use. Sand paper was used to abrade the surface of the electrode's unpolished side before application of a conductive silver paint (RS® Components 186-3593), after which an electrical wire was connected to the dry silver using the same conductive silver paint. Upon drying, an off-white opaque epoxy adhesive (Loctite® EA 9466) was applied on both sides of the electrodes, leaving only the photoactive surface ($S \approx 0.2\,cm^2$) exposed. The electrodes were allowed to dry thoroughly for 40 h in air before use. In the case of the control experiment using a Si|*meso*TiO_2|$Co(BF_4)_2$ electrode, a solution of the $Co(BF_4)_2{\cdot}6H_2O$ salt (0.25 mM) was used to sensitise the Si|*meso*TiO_2 electrode instead of **CotpyP**.

Quantification of Catalyst Loading

The quantification of the amount of immobilised **CotpyP** (mole per geometrical area) on the Si|*meso*TiO_2|**CotpyP** electrodes was evaluated in triplicate by ICP-OES after digestion of Si|*meso*TiO_2|**CotpyP** electrodes ($S \approx 1\,cm^2$ film area) in aqueous HNO_3 (70 %) overnight and dilution to 2 % v/v with Milli-Q® water.

3.4.5 Photoelectrochemical Methods

Photoelectrocatalysis Set-Up

All electrochemical experiments were performed with an Ivium CompactStat potentiostat. A three-electrode configuration was employed in airtight compartments, with a Pt mesh as the counter electrode and a Ag/AgCl electrode in either saturated $KCl_{(aq.)}$ for aqueous experiments or in a solution with the same composition as the electrolyte for organic-water mixture experiments as the reference electrode. In organic-water mixtures, the RE was regularly referenced against the ferrocene couple (Fc^+/Fc). Variations in the potential of the Fc^+/Fc couple in different solvent mixtures were taken into account.[37] The electrolyte was $TBABF_4$ (0.1 M)

in organic-water mixtures and $KHCO_3$ (0.1 M, pH 6.7) in aqueous solutions. All electrochemical measurements were performed at room temperature.

CVs were recorded with *meso*ITO-based working electrodes (WEs) in the dark in one-compartment cells. The electrolyte solution was purged with N_2 to remove atmospheric O_2. Linear sweep voltammograms and controlled potential photoelectrolysis were performed on Si|*meso*TiO_2-based electrodes as the WEs. A Newport Oriel Xenon 150 W solar light simulator (100 mW cm^{-2}, AM1.5G with IR water and UV ($\lambda > 400$ nm) filters) was used as the light source. Custom-made airtight two-compartment photoelectrochemical cells were employed for all photoelectrochemical measurements, where a glass frit or Nafion membrane was used to separate the compartments for organic-water mixtures or aqueous solutions, respectively. LSVs were conducted at a scan rate of 5 mV s^{-1} with chopped light alternating between dark and light every 5 s. The photocurrent onset potential, E_{onset} was defined as the potential at which a photocurrent density of $|J| = 10\,\mu\text{A cm}^{-2}$ was achieved by the respective electrode. The applied potential during CPPE was -1.0 V *vs.* Fc^+/Fc or 0.0 V *vs.* RHE in organic-water or pure water solutions, respectively. Continuous illumination was maintained, apart from hourly dark chops lasting for 2 min each.

Product Quantification

Prior to all photoelectrochemical experiments, the electrolyte solution in both compartments of the photoelectrochemical cell was purged with CO_2 containing 2 % CH_4 as an internal standard for gas chromatography measurements; the only exception was in the case of N_2 atmosphere control experiments, where the solution was purged with N_2 containing 2 % CH_4. The amounts of gaseous CO and H_2 produced were analysed by headspace gas analysis using a Shimadzu Tracera GC-2010 Plus with a barrier discharge ionisation detector (BID). The GC was equipped with a ShinCarbon micro ST column (0.53 mm diameter) kept at 40 °C using helium carrier gas. Aliquots (50 µL) of the headspace gas were removed for GC analysis at regular time intervals using a gas-tight syringe (Hamilton, GASTIGHT). The amount of gas produced was quantified as described in Appendix A. Formic acid was analysed by ion chromatography using a Metrohm 882 compact IC plus ion chromatography system, with a solution of carbonate (4 mM) containing acetone (50 mL L^{-1}) as the eluent after calibration with solutions of different known formate concentrations. The Faradaic efficiency of the photocathodes was calculated by comparing the expected amount of total product as indicated by the total charge passed through the electrode and the actual amount produced

(see Appendix A). Analytical measurements were performed in triplicate and the standard deviation of each data point is given in Table 3.2 (calculations described in Appendix A).

Isotopic Labelling Experiment

CPPE of Si|*meso*TiO_2|**CotpyP** was performed under 6:4 MeCN:H_2O conditions with $^{13}CO_2$ as the headspace gas. After 4 h, the photoelectrochemical cell headspace was transferred to an evacuated gas IR cell (SpecAc, 10 cm path length, equipped with KBr windows) and a high-resolution transmission spectrum was collected on a Thermo Scientific Nicolet iS50 FT-IR spectrometer.

3.5 References

(1) Benson, E. E.; Kubiak, C. P.; Sathrum, A. J.; Smieja, J. M. *Chem. Soc. Rev.* **2009**, *38*, 89–99.

(2) Detz, R.; Reek, J. N. H.; van der Zwaan, B. *Energy Environ. Sci.* **2018**, *11*, 1653–1669.

(3) Appel, A. M. et al. *Chem. Rev.* **2013**, *113*, 6621–6658.

(4) Takeda, H.; Cometto, C.; Ishitani, O.; Robert, M. *ACS Catal.* **2017**, *7*, 70–88.

(5) Zhang, L.; Zhao, Z.-J.; Wang, T.; Gong, J. *Chem. Soc. Rev.* **2018**, *47*, 5423–5443.

(6) Tian, H. *ChemSusChem* **2015**, *8*, 3746–3759.

(7) Wang, M.; Yang, Y.; Shen, J.; Jiang, J.; Sun, L. *Sustain. Energy Fuels* **2017**, *1*, 1641–1663.

(8) Arai, T.; Sato, S.; Uemura, K.; Morikawa, T.; Kajino, T.; Motohiro, T. *Chem. Commun.* **2010**, *46*, 6944–6946.

(9) Kumagai, H.; Sahara, G.; Maeda, K.; Higashi, M.; Abe, R.; Ishitani, O. *Chem. Sci.* **2017**, *8*, 4242–4249.

(10) Sato, S.; Arai, T.; Morikawa, T.; Uemura, K.; Suzuki, T. M.; Tanaka, H.; Kajino, T. *J. Am. Chem. Soc.* **2011**, *133*, 15240–15243.

(11) Sahara, G.; Kumagai, H.; Maeda, K.; Kaeffer, N.; Artero, V.; Higashi, M.; Abe, R.; Ishitani, O. *J. Am. Chem. Soc.* **2016**, *138*, 14152–14158.

(12) Sekizawa, K.; Sato, S.; Arai, T.; Morikawa, T. *ACS Catal.* **2018**, *8*, 1405–1416.

(13) Chow, H. S.; Constable, E. C.; Housecroft, C. E.; Kulicke, K. J.; Tao, Y. *Dalton Trans.* **2005**, 236–237.

(14) Constable, E. C.; Harris, K.; Housecroft, C. E.; Neuburger, M.; Zampese, J. A. *Dalton Trans.* **2011**, *40*, 11441–11450.

(15) Henderson, I. M.; Hayward, R. C. *J. Mater. Chem.* **2012**, *22*, 21366–21369.

(16) Potts, K. T.; Usifer, D. A.; Guadalupe, A.; Abruña, H. D. *J. Am. Chem. Soc.* **1987**, *109*, 3961–3967.

(17) Enachescu, C.; Krivokapic, I.; Zerara, M.; Real, J. A.; Amstutz, N.; Hauser, A. *Inorganica Chim. Acta* **2007**, *360*, 3945–3950.

(18) Leung, J. J.; Warnan, J.; Nam, D. H.; Zhang, J. Z.; Willkomm, J.; Reisner, E. *Chem. Sci.* **2017**, *8*, 5172–5180.

(19) Liu, W.; Zhang, L.; Yan, W.; Liu, X.; Yang, X.; Miao, S.; Wang, W.; Wang, A.; Zhang, T. *Chem. Sci.* **2016**, *7*, 5758–5764.

(20) Seip, C. T.; Talham, D. R. *Mater. Res. Bull.* **1999**, *34*, 437–445.

(21) Muresan, N. M.; Willkomm, J.; Mersch, D.; Vaynzof, Y.; Reisner, E. *Angew. Chem. Int. Ed. Engl.* **2012**, *51*, 12749–12753.

(22) Fuchs, P.; Hess, U.; Holst, H. H.; Lund, H. *Acta Chem. Scand. B* **1981**, *35*, 185–192.

(23) Cobo, S.; Heidkamp, J.; Jacques, P.-A.; Fize, J.; Fourmond, V.; Guetaz, L.; Jousselme, B.; Ivanova, V.; Dau, H.; Palacin, S.; Fontecave, M.; Artero, V. *Nat. Mater.* **2012**, *11*, 802–807.

(24) Chuang, T.; Brundle, C.; Rice, D. *Surf. Sci.* **1976**, *59*, 413–429.

(25) Matsubara, Y. *ACS Energy Lett.* **2017**, 1886–1891.

(26) Perry, R. H., *Perry's Chemical Engineers' Handbook*, 8th ed.; Perry, R. H., Green, D. W., Eds.; New York ; London : McGraw-Hill, c2008.: New York; London, 2008.

(27) Gennaro, A.; Isse, A. A.; Vianello, E. *J. Electroanal. Chem. Interfacial Electrochem.* **1990**, *289*, 203–215.

(28) Sumita, M.; Sodeyama, K.; Han, L.; Tateyama, Y. *J. Phys. Chem. C* **2011**, *115*, 19849–19855.

(29) Heinzel, A. B.; Teschner, D. M.; Schumacher, R. *Ber. Bunsenges. Phys. Chem.* **1981**, *85*, 1117–1119.

(30) Enright, B.; Redmond, G.; Fitzmaurice, D. *J. Phys. Chem.* **1994**, *98*, 6195–6200.

(31) Won, D. I.; Lee, J. S.; Ji, J. M.; Jung, W. J.; Son, H. J.; Pac, C.; Kang, S. O. *J. Am. Chem. Soc.* **2015**, *137*, 13679–13690.

(32) Sahara, G.; Abe, R.; Higashi, M.; Morikawa, T.; Maeda, K.; Ueda, K.; Ishitani, O. *Chem. Commun.* **2015**, *51*, 10722–10725.

(33) Apaydin, D. H.; Tordin, E.; Portenkirchner, E.; Aufischer, G.; Schlager, S.; Weichselbaumer, M.; Oppelt, K.; Sariciftci, N. S. *ChemistrySelect* **2016**, *6*, 1156–1162.

(34) Schreier, M.; Luo, J.; Gao, P.; Moehl, T.; Mayer, M. T.; Grätzel, M. *J. Am. Chem. Soc.* **2016**, *138*, 1938–1946.

(35) Kumar, B.; Smieja, J. M.; Kubiak, C. P. *J. Phys. Chem. C* **2010**, *114*, 14220–14223.

(36) Alenezi, K.; Ibrahim, S. K.; Li, P.; Pickett, C. J. *Chem. Eur. J.* **2013**, *19*, 13522–13527.

(37) Lanning, J. A.; Chambers, J. Q. *Anal. Chem.* **1973**, *45*, 1010–1016.

Chapter 4

Mechanistic Studies on Surface-Immobilised Cobalt Bis(terpyridine) Catalyst

The contents of this chapter have been submitted for publication as a peer-reviewed article. Results presented were obtained solely by the author of this thesis, with contributions from others as outlined here: Julien Warnan is acknowledged for synthesising the mono(terpyridine) catalyst $CoCl_2$(tpy). Khoa H. Ly conducted resonance Raman spectroelectrochemical measurements at the Technical University of Berlin. Nina Heidary carried out infrared spectroelectrochemical measurements with the author.

4.1 Introduction

In the previous chapter, the importance of the photocathode environment on the photoelectrocatalytic performance of Si|*meso*TiO_2|**CotpyP** was already noted. Further, it is important to realise that the performance of **CotpyP** in this photocathode far exceeded that of any previously reported Co bis(terpyridine) catalyst – whether in solution or immobilised on dark electrodes – in terms of stability and activity.[1] This is even more remarkable when one recognises that the thermodynamic potential offered by the Si|*meso*TiO_2 electrode ($E_{CB}(TiO_2)$ $\sim -0.1\,V$ *vs.* NHE, pH 0) is rather small, especially when considering the significant overpotential previously reported for cobalt bis(terpyridine) complexes in solution ($\sim -2.0\,V$ *vs.* $Fc^+/Fc \approx -1.4\,V$ *vs.* NHE, pH 0).[1,2] In order to gain a deeper understanding of the unexpected activity of our hybrid photocathode (*i.e.* apparent

mismatch of driving force provided by the photoelectrode and literature reports of the catalytic onset of cobalt bis(terpyridines)) and perhaps to provide further explanation for the strong solvent-dependent behaviour we observed in Chapter 3, detailed mechanistic investigations were executed by (spectro)electrochemical experiments, the results and implications of which are discussed in this chapter.

More specifically, CVs as well as potential-controlled ATR-IR and confocal resonance Raman (RR) studies were conducted on **CotpyP**-modified mesoporous ITO (*meso*ITO; particle size $< 50\,\text{nm}$, film thickness $3\,\mu\text{m}$) electrodes. The complementarity of the two spectroscopic techniques delivered a global (ATR-IR) and specific (RR) monitoring approach to elucidate structural changes of the symmetrical **CotpyP** catalyst under an applied potential. Notably, the spectroelectrochemical Raman studies conducted here are the first example of such techniques applied to molecular catalysts immobilised on non-plasmonic surfaces, while the spectroelectrochemical IR studies are the first instance of such techniques applied to molecular catalysts immobilised on metal oxide surfaces, in any context. Observations made from all of these experiments will be described first, followed by a collective discussion of their implications as a whole, culminating as a mechanistic interpretation of the surface-immobilised **CotpyP** catalyst.

4.2 Results and Discussion

4.2.1 Cyclic Voltammetry Studies

CVs of *meso*ITO|**CotpyP** electrodes were recorded in 9:1 MeCN:H_2O (0.1 M $TBABF_4$) electrolyte solution under N_2 (Fig. 4.1a and D.1). An anodic sweep displayed a reversible redox wave at $E_{½} = -0.12\,\text{V}$ *vs.* Fc^+/Fc ($\boldsymbol{E_1}$) that can be assigned to the Co^{III}/Co^{II} redox couple in accordance with similar values previously observed.[2] Upon scan reversal towards negative potentials, a quasi-reversible wave emerges at $E_{½} = -1.36\,\text{V}$ *vs.* Fc^+/Fc ($\boldsymbol{E_2}$). The current density of this wave at $\boldsymbol{E_2}$ decreased upon consecutive scan cycles with the concomitant appearance of a new reversible redox wave at $E_{½} = -1.0\,\text{V}$ *vs.* Fc^+/Fc ($\boldsymbol{E_3}$). In agreement with previous reports,[2] waves at $\boldsymbol{E_2}$ can be assigned to the Co^{II}/Co^{I} redox couple and the emerging wave at $\boldsymbol{E_3}$ is therefore attributed to the formation of a Co^{II}/Co^{I} couple belonging to a new species that is more easily reduced than the original complex. Notably, although the anodic wave at $\boldsymbol{E_3}$ can already be observed in the first scan, the corresponding cathodic wave only appears in the second scan (Fig. D.1). In contrast, the Co^{III}/Co^{II} couple at $\boldsymbol{E_1}$ remained largely unchanged

throughout cycling. When the electrolyte solution is switched to 9:1 DMF:H_2O from MeCN:H_2O, a comparable voltammetric behaviour was observed (Fig. D.2), indicating that the organic solvent - or at least its specific identity - does not seem to be responsible for the couple at $\boldsymbol{E_3}$.

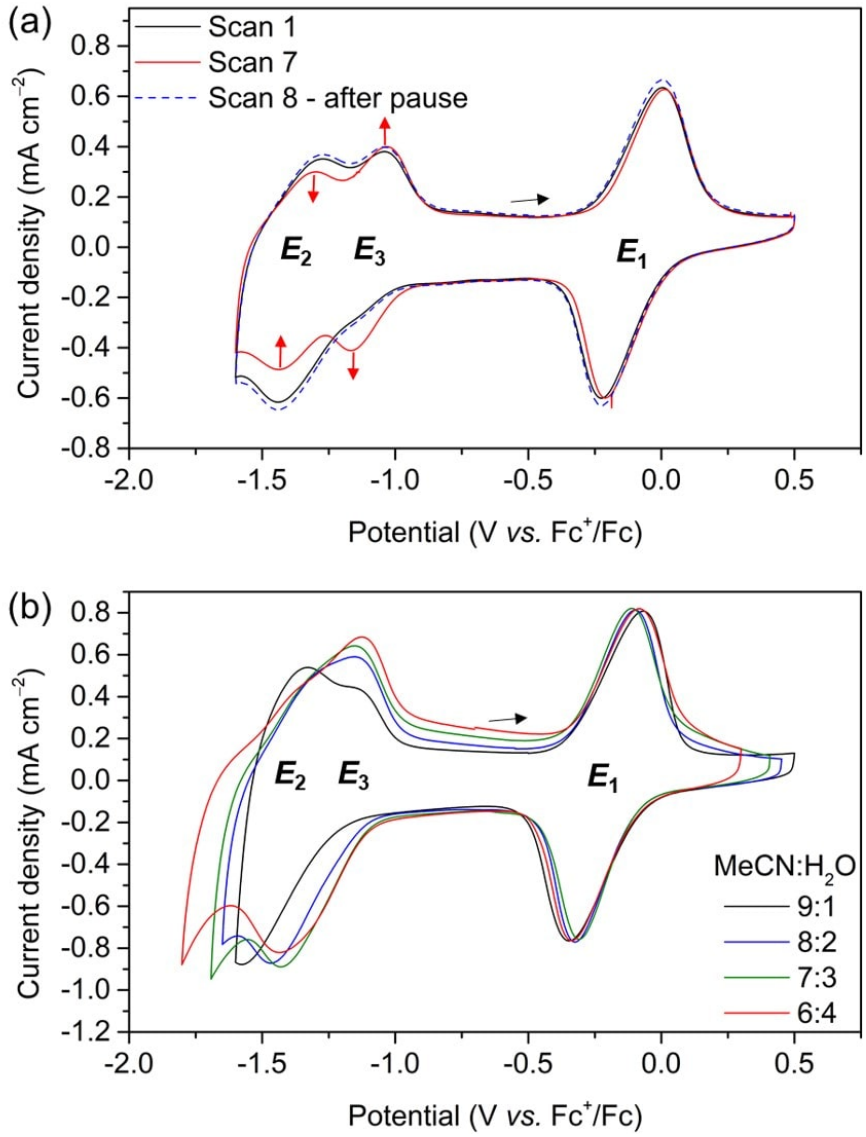

Fig. 4.1 (a) Consecutive CVs of *meso*ITO|**CotpyP** in 9:1 MeCN:H_2O (0.1 M $TBABF_4$) with scans 1 and 7 being shown (red arrows indicate change in wave intensities); scan 8 was recorded after a pause at open circuit potential. (b) CVs of *meso*ITO|**CotpyP** in MeCN:H_2O ratios of 9:1, 8:2, 7:3 and 6:4 (0.1 M $TBABF_4$), with scan 1 shown. Black arrows indicate scan start. Conditions: $\nu = 50\,\mathrm{mV\,s^{-1}}$; N_2 atmosphere; room temperature.

Increasing the water content of the electrolyte solution sequentially from 9:1 to 6:4 (MeCN:H_2O mixtures) resulted in faster growth of the $\boldsymbol{E_3}$ redox

couple (Fig. 4.1b), which points towards a water/proton-involving process for the formation of the new species. Notably, running CVs after removing the applied potential (at an open circuit potential of $-0.5\,\mathrm{V}$ *vs.* Fc^+/Fc) following an initial set of consecutive scans in water-poor 9:1 MeCN:H_2O showed the same voltammetric response as the original 1st scan (Fig. 4.1a, compare scans 7 and 8). The latter behaviour suggests that the process is more laboured in 9:1 MeCN:H_2O and apparently only accessible if certain conditions induced by electrode polarisation are met; these are discussed further below.

CVs of *meso*ITO|**CotpyP** under a CO_2 atmosphere show a catalytic onset reduction wave ($E_{cat} \sim -1.03\,\mathrm{V}$ *vs.* Fc^+/Fc) that is more pronounced in 6:4 MeCN:H_2O compared to 9:1 MeCN:H_2O (Fig. 4.2 and D.3), which is consistent with its better activity in a more water-rich solution composition as previously discussed for CPPE results in Chapter 3. Notably, the catalytic onset potential occurs ~1 V earlier than those generally reported for Co bis(terpyridine) catalysts in solution.[2] Waves observed for the oxidation of Co^I at $-0.96\,\mathrm{V}$ *vs.* Fc^+/Fc under these conditions may suggest residual [Co^I] species, and/or the formation of a Co-CO adduct as previously suggested.[3]

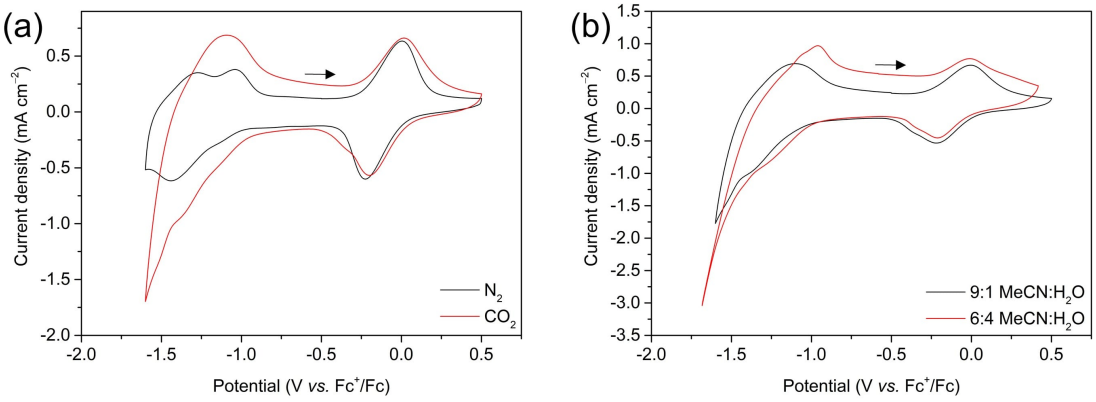

Fig. 4.2 CVs of *meso*ITO|**CotpyP** in (a) 9:1 MeCN:H_2O in N_2- and CO_2-saturated conditions, and (b) in 9:1 MeCN:H_2O and 6:4 MeCN:H_2O in CO_2-saturated conditions. Arrows indicate scan start. Conditions: 0.1 M $TBABF_4$; $\nu = 50\,\mathrm{mV\,s^{-1}}$; room temperature.

4.2.2 *In-Situ* Spectroelectrochemical Resonance Raman Spectroscopy Studies

Confocal RR spectroelectrochemistry was employed to investigate the potential-dependent features of the adsorbed catalyst at a molecular level *in situ*. The RR spectra of dry *meso*ITO|**CotpyP** (in absence of solution) recorded at 413, 458,

and 514 nm excitation wavelengths (λ_{ex}) were dominated by bands located at 1355, 1483 and 1613 cm^{-1} with altered relative intensities depending on the employed excitation wavelength (Fig. D.4; characteristic frequencies given in Table D.1) and are consistent with previous reports for terpyridine-based complexes.[4–6] High RR intensities were obtained as a result of the high effective surface area resulting from the mesoporous electrode architecture,[5,7,8] and the strong electronic absorption of the complex in the visible spectrum.[9,10] Once again, structural preservation of the complex upon surface immobilisation was confirmed by the spectrum of the dry *meso*ITO|**CotpyP** electrode matching that of the **CotpyP** powder and not a cobalt mono(terpyridine) (Fig. 4.3a and Table D.1). Continued conservation of the structural bis-ligation upon placing the electrode in 9:1 MeCN:H_2O solution (0.1 M $TBABF_4$) was further indicated by an unchanged RR band pattern (Fig. 4.3b).

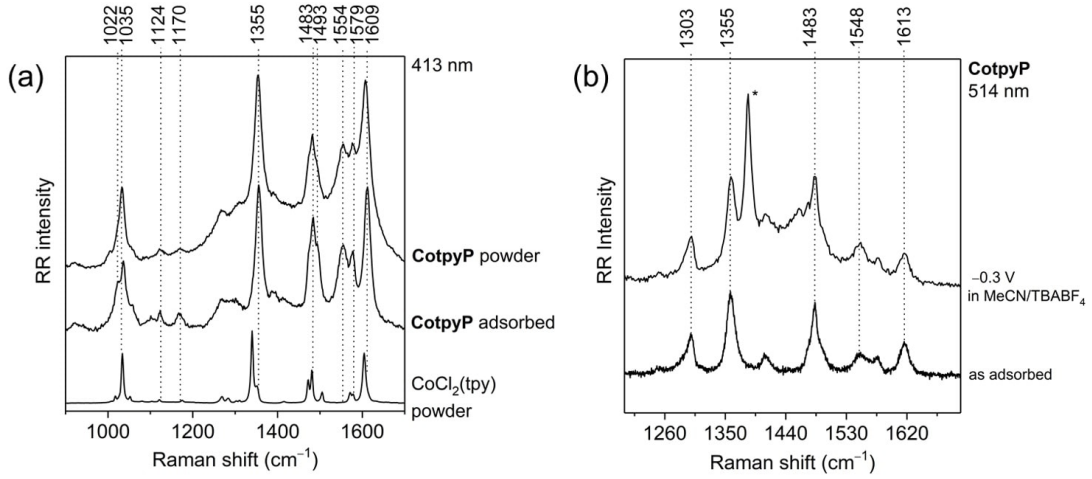

Fig. 4.3 (a) RR spectra ($\lambda_{ex} = 413$ nm) of dry *meso*ITO|**CotpyP** (in absence of solution) compared to bis(terpyridine) **CotpyP** and mono(terpyridine) $CoCl_2$(tpy) powders. Good spectral agreement between the adsorbed **CotpyP** and the neat **CotpyP** is observed. (b) Comparison between RR spectra ($\lambda_{ex} = 514$ nm) of dry *meso*ITO|**CotpyP** and *meso*ITO|**CotpyP** in 9:1 MeCN:H_2O (0.1 M $TBABF_4$) at $E_{app} = -0.3$ V *vs.* Fc^+/Fc. An excellent match between both spectra is observed, indicating that the bis(**tpyP**) ligation is maintained when the complex is immersed in the electrolyte solution. The band at 1385 cm^{-1} (denoted with *) is assigned to the CH_3 rocking mode of MeCN,[11] and does not overlap with any relevant signals arising from **CotpyP**.

Potential-dependent confocal RR spectra were subsequently recorded with *meso*ITO|**CotpyP** at E_{app} between 0.5 V and −1.6 V *vs.* Fc^+/Fc (Fig. 4.4a). At positive potentials, a weakly pronounced spectral pattern with major bands located at 1571 (not specifically labelled) and 1621 cm^{-1} was observed (Table D.2). Lowering E_{app} below 0.0 V *vs.* Fc^+/Fc caused the disappearance of these bands with

a concomitant rise of intense bands at 1358, 1485, 1552 and 1610 (not specifically labelled) cm^{-1}, which are in good agreement to those for the native [Co^{II}] state in the **CotpyP** powder (Fig. 4.3a). Further lowering E_{app} below $-1.0\,V$ and $-1.6\,V$ *vs.* Fc^+/Fc resulted in bands rising at 1476, 1566 and 1603 cm^{-1} attributed to the [Co^{I}] state, with the simultaneous disappearance of the aforementioned **Co^{II}tpyP** bands. As these changes are minimal and were all fully reversible upon changing the potential-step direction, they do not suggest irreversible alteration of the complex's symmetry and its metal's first coordination sphere.

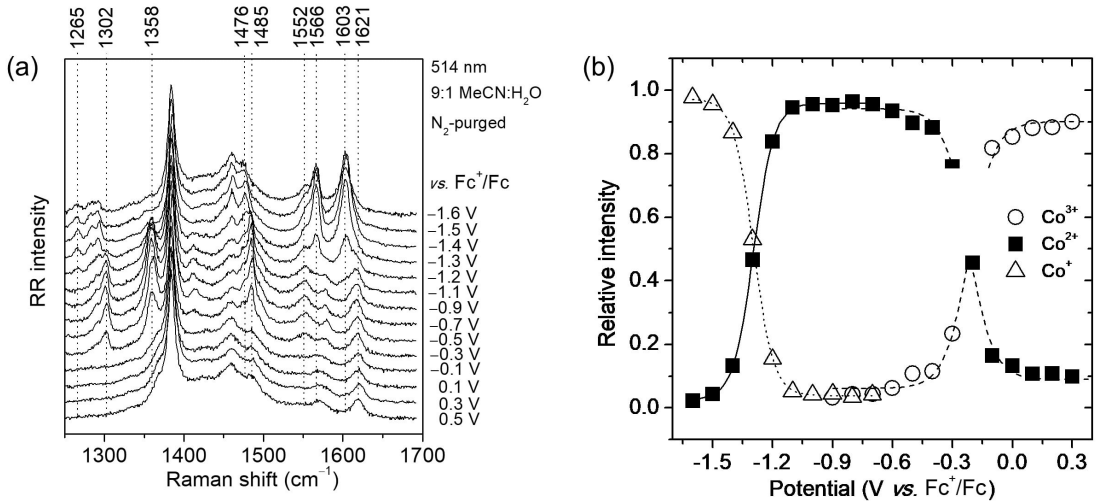

Fig. 4.4 Confocal RR spectroelectrochemistry of *meso*ITO|**CotpyP** ($\lambda_{ex} = 514\,nm$). (a) RR spectra at different E_{app}. (b) Relative intensities of the Co^{3+} (circle), Co^{2+} (square) and Co^{+} (triangle) redox species as a function of E_{app}, with inflection points at -0.18 and $-1.32\,V$ *vs.* Fc^+/Fc. The relative intensities were derived using component fit analysis of the RR spectra (Fig. 4.5). Note that due to the intrinsically lower RR activity of Co^{3+} and Co^{2+} species causing an inaccuracy in the calculation procedure of about 10 %, the relative intensities of Co^{2+} and Co^{3+} at positive potentials do not reach full redox conversion conditions, *i.e.* 0 and 1, respectively. Conditions: 9:1 MeCN:H_2O (0.1 M $TBABF_4$, N_2) at room temperature.

Component spectra analysis was subsequently performed to assign the observed spectral patterns to the complex in different redox states. The potential-dependent RR spectra of *meso*ITO|**CotpyP** over the full potential window could be fitted to a high degree of accuracy using three component spectra (Fig. 4.5; see Experimental Section 4.4.3 for a detailed description). One of the component spectra fully resembled the RR spectrum obtained for the dry *meso*ITO|**CotpyP** electrode (in absence of solution; Fig. D.4 and 4.3b). To confirm that the spectral components can indeed be assigned to three Co oxidation states, relative intensities of the components were plotted against E_{app}. This approach resulted in matching

sigmoidal curves that indicate complete interconversion from one oxidation state to another (Fig. 4.4b). The apparent redox potentials can be estimated from the inflection points of these sigmoidal curves (−0.18 and −1.32 V *vs.* Fc^+/Fc), and were found to match those determined for Co^{III}/Co^{II} ($\boldsymbol{E_1}$) and Co^{II}/Co^{I} ($\boldsymbol{E_2}$) from voltammetric experiments (Fig. 4.1).

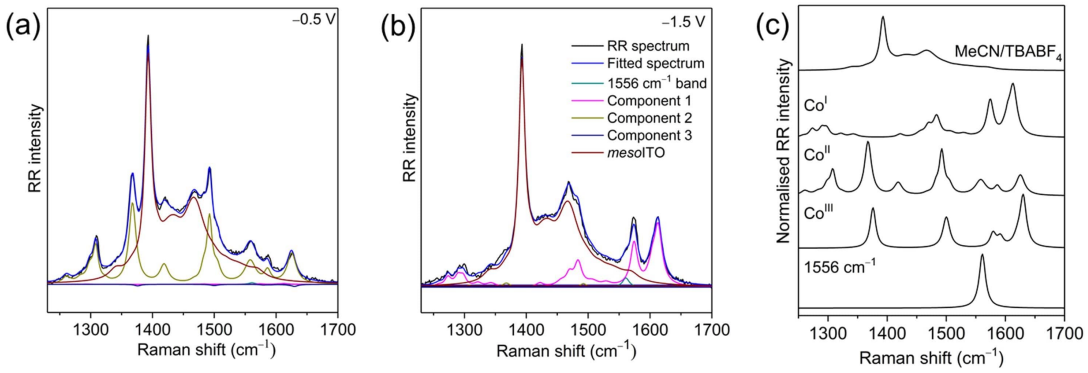

Fig. 4.5 Component fit analyses performed for RR spectra of *meso*ITO|**CotpyP** ($\lambda_{ex} = 514$ nm). Component fitting shown exemplarily for (a) −0.5 V *vs.* Fc^+/Fc and (b) −1.5 V *vs.* Fc^+/Fc in N_2-purged 9:1 MeCN:H_2O (0.1 M $TBABF_4$) at room temperature. (c) Derived component fit spectra employed for fitting the recorded RR spectra of *meso*ITO|**CotpyP**. The component spectra are named after the assigned redox species, *i.e.* **CotpyP** in the oxidation states +1, +2, and +3, respectively. MeCN/$TBABF_4$ denotes the background.

Measurements recorded in CO_2-saturated conditions revealed the same spectral patterns as observed under N_2 (Fig. 4.6). Lowering E_{app} to the catalytic region of −1.6 V *vs.* Fc^+/Fc followed by stepping back to 0.5 V *vs.* Fc^+/Fc demonstrated full reversibility of the spectral features. Holding E_{app} at −1.4 V *vs.* Fc^+/Fc for 10 min resulted in no significant alteration of the $\mathbf{Co^{I}tpyP}$ spectrum. It is noted that catalytic intermediates are unlikely to be detectable in the experiment's timeframe due to their transient nature. These observations highlight the structural integrity of **CotpyP** even after catalytic turnover, which is consistent with the observations made from CVs (this chapter) as well as post-CPPE XPS and ATR-IR measurements (Chapter 3).

Nevertheless, a singular band at 1556 cm^{-1} that exhibits altered intensities at potentials more negative than −1.0 V *vs.* Fc^+/Fc under N_2 and CO_2 atmospheres was noted (Fig. 4.7). Component fit analysis showed that this band exhibits a different potential-dependence to that of $\mathbf{Co^{I}tpyP}$, suggesting that it involves a vibrational mode that is sensitive to a potential-coupled process other than mere reduction. Interestingly, this band was also found to be more pronounced

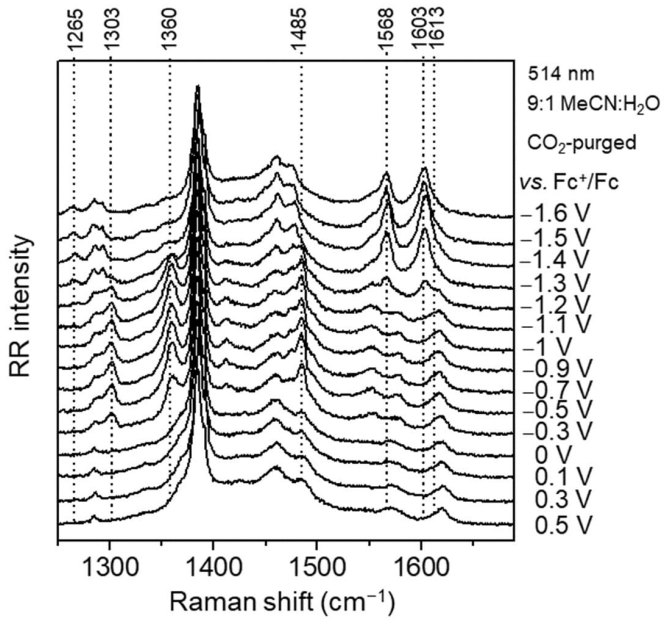

Fig. 4.6 Potential-dependent confocal RR spectra ($\lambda_{ex} = 514\,nm$) of *meso*ITO|**CotpyP** in CO_2-purged 9:1 MeCN:H_2O (0.1 M $TBABF_4$) solution at different applied potentials at room temperature.

in anhydrous MeCN electrolyte solution. We speculate that the terpyridine's normal mode that gives rise to this band contains large vibrational contributions from the deprotonated, unbound phosphonic acid group. As the introduction of water or CO_2 acidifies the solutions, protonation of this acid becomes likely at [Co^I]-affording potentials. This would therefore result in only a minor change in the catalyst's structure and conserve **CotpyP**'s molecular symmetry (a necessary prerequisite for resonance Raman enhancement to be maintained), which would explain the otherwise unchanged RR spectra at negative potentials. In this respect, step-wise lowering of the potential to very negative potentials could lead to a gradual positive shift of the phosphonic acid group's pK_a due to electrostatic considerations.[12,13] This would mean that the fraction of protonated **Co^ItpyP** increases with lowered potentials, leading to suppression of the band rising at $1556\,cm^{-1}$ and eventually affording its unique potential-dependence.

4.2.3 *In-Situ* Spectroelectrochemical Infrared Spectroscopy Studies

ATR-IR spectroelectrochemical measurements were also conducted under varying applied potentials, beginning at $E_{app} = -0.5\,V$ *vs.* Fc^+/Fc ([Co^{II}]-affording potential) and proceeding step-wise from $E_{app} = -1.0\,V$ through to $-1.5\,V$ *vs.* Fc^+/Fc

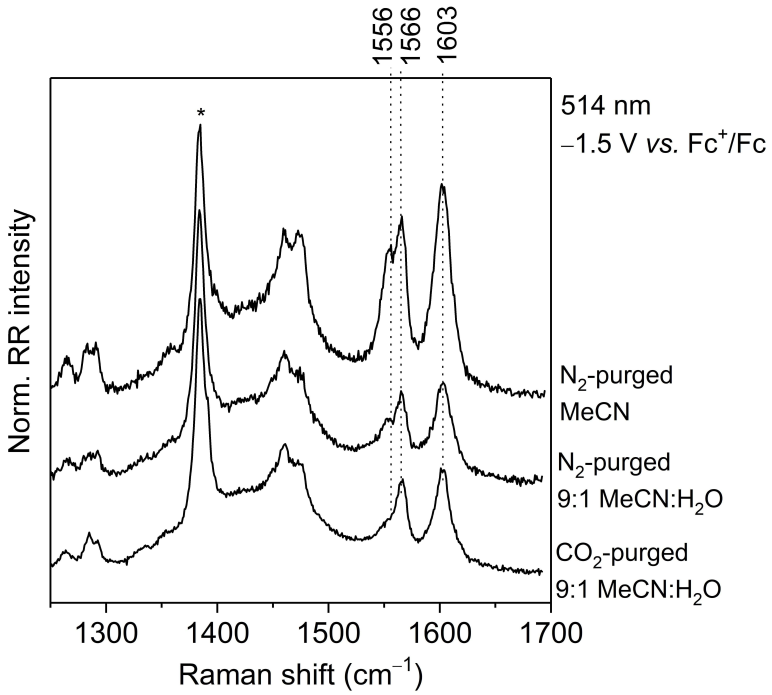

Fig. 4.7 Confocal RR spectra ($\lambda_{ex} = 514\,nm$) of *meso*ITO|**CotpyP** at $E_{app} = -1.5\,V$ *vs.* Fc^+/Fc in N_2- and CO_2-purged 9:1 MeCN:H_2O solution (0.1 M $TBABF_4$) at room temperature. For comparison, a RR spectrum at the same potential of H_2O-free MeCN solution (0.1 M $TBABF_4$) is also shown. Upon formation of $[\mathbf{CotpyP}]^+$, a decrease of the band at $1556\,cm^{-1}$ was noted in wet conditions, especially when purged with CO_2. * marks the background Raman rocking band of MeCN.

([Co^{I}]-affording potentials; Fig. 4.8). In agreement with the RR experiments, ATR-IR measurements in dry N_2, wet N_2 and wet CO_2 conditions likewise did not detect major changes in **CotpyP**'s primary coordination sphere. This is indicated by the similar spectral changes under both non-catalytic and catalytic conditions as observed in the difference and second derivative spectra in the terpyridine spectral region (blue regions of Fig. 4.9 and D.5, respectively), as (long-lasting) severe alterations to the metal coordination sphere would have otherwise led to more drastic changes in the spectra. Similarly, the reversibility of the spectra after exposure to catalytic conditions, as indicated by the fact that the difference spectrum in Fig. 4.9d (difference between pre-catalysis and catalysis spectra) provides entirely inverse spectral features to those of Fig. 4.9c (difference between post-catalysis and catalysis spectra), again confirmed the integrity of the catalyst after catalysis.

Spectroelectrochemical ATR-IR allowed us to probe media-dependent changes specifically in the phosphonate spectral region, affording a qualitative means to monitor their role *in situ* under applied potentials. As can be seen from the absorbance spectra, addition of H_2O (Fig. 4.8b) and, further, CO_2 (Fig. 4.8c) results in broadening of the band features in the phosphonate region – shown between 1250 and 900 cm^{-1}, corresponding to contributions from the acid's stretching frequencies[14] – indicating a reduction in symmetry at the phosphonate group that would be in line with protonation at this site, as previously reported in ATR-IR studies.[14,15]

Nevertheless, the broad band features of the phosphonate region are best deconvoluted into their discrete components by computing the second derivatives (Fig. 4.10) of the absorbance spectra. While no major changes in band intensities within this phosphonate region were observed upon reducing **Co^{II}tpyP** to **Co^{I}tpyP** under dry MeCN conditions (Fig. 4.10a), the addition of water in 9:1 MeCN:H_2O, N_2-purged electrolyte solution led to large spectral changes at [Co^{I}]-affording potentials across the entire phosphonate region (Fig. 4.10b).[14,15] Under CO_2, similar but significantly weaker changes to that found under wet, N_2-purged conditions were also observed when lowering E_{app} down to catalytic conditions (Fig. 4.10c). Overall, these observed trends are supportive of protonation of the phosphonate group upon addition of water under N_2, and a shift in the acid's protonation kinetic equilibrium during catalysis in presence of CO_2.

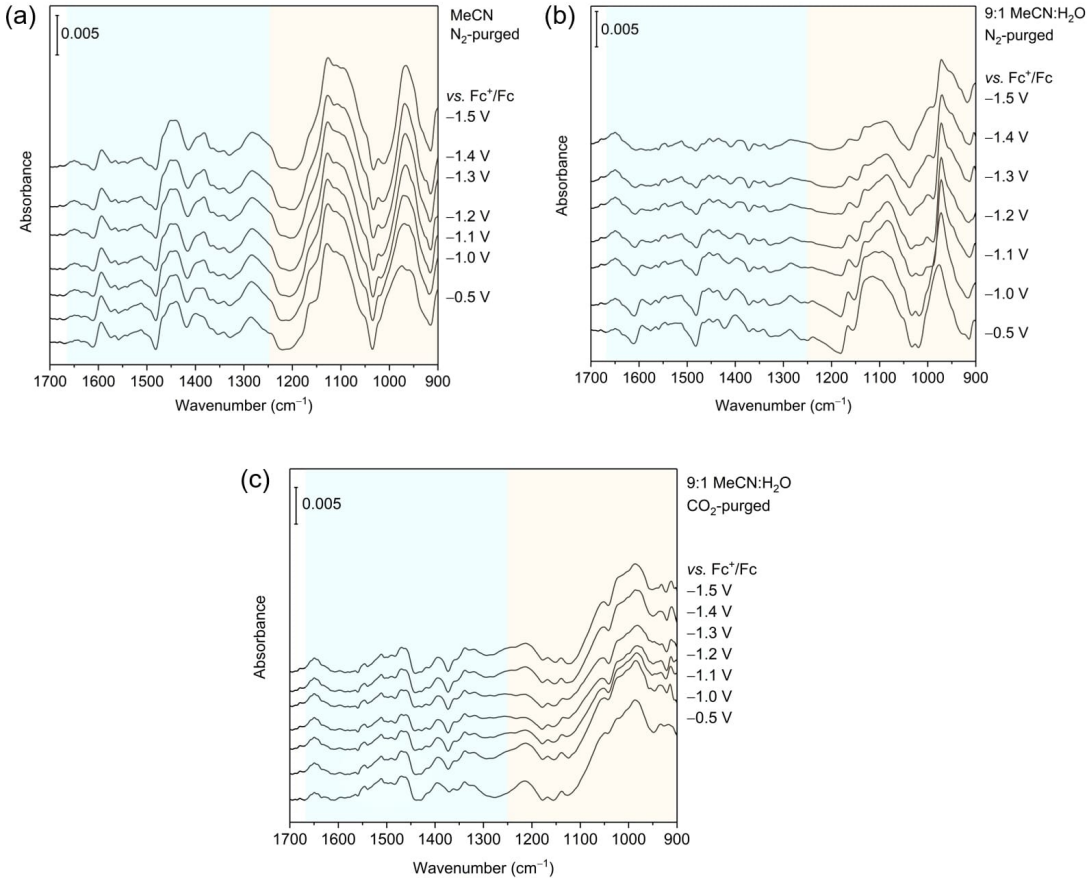

Fig. 4.8 ATR-IR absorbance spectra of *meso*ITO|**CotpyP** at different applied potentials in (a) N_2-purged MeCN, (b) N_2-purged 9:1 MeCN:H_2O and (c) CO_2-purged 9:1 MeCN:H_2O (0.1 M $TBABF_4$ in all cases) at room temperature. All spectra have been referenced to background spectra recorded from catalyst-free *meso*ITO for each of the above conditions. Blue and yellow regions indicate the terpyridine and phosphonate spectral regions, respectively.

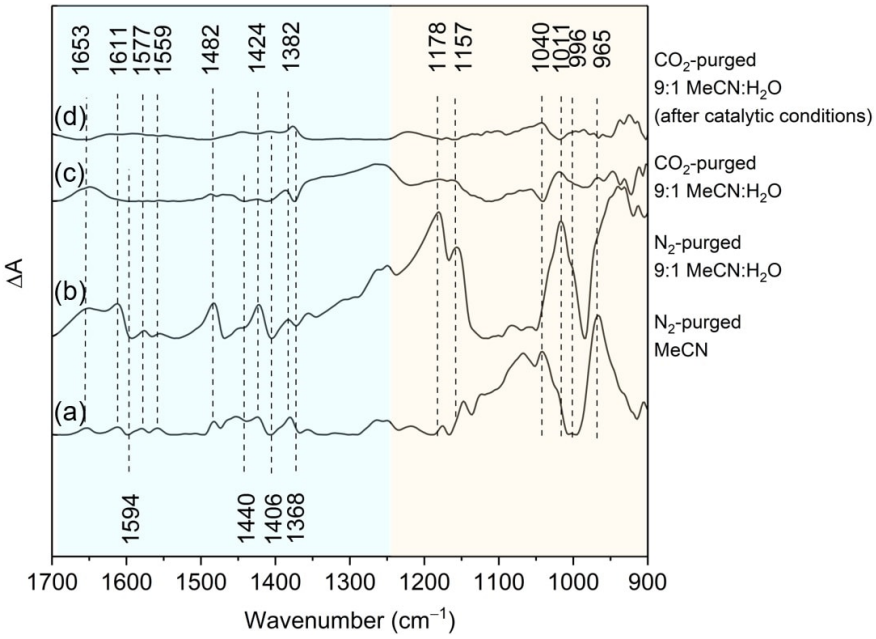

Fig. 4.9 (a-c) Difference spectra between ATR-IR absorbance spectra taken of *meso*ITO|**CotpyP** (Fig. 4.8) at $E_{\text{app}} = -1.5\,\text{V}$ *vs.* Fc^+/Fc and at $E_{\text{app}} = -0.5\,\text{V}$ *vs.* Fc^+/Fc, the latter *prior* to lowering to catalytic potentials, in (a) N_2-purged MeCN, (b) N_2-purged 9:1 MeCN:H_2O and (c) CO_2-purged 9:1 MeCN:H_2O (0.1 M $TBABF_4$ in all cases) at room temperature. (d) Difference spectrum between absorbance spectra taken at $E_{\text{app}} = -1.5\,\text{V}$ *vs.* Fc^+/Fc and at $E_{\text{app}} = -0.5\,\text{V}$ *vs.* Fc^+/Fc, the latter *after* lowering to catalytic potentials, in CO_2-purged 9:1 MeCN:H_2O (0.1 M $TBABF_4$), demonstrating reversibility of the band features after being under catalytic conditions. All spectra have been referenced to background spectra recorded from catalyst-free *meso*ITO for each of the above conditions. Blue and yellow regions indicate the terpyridine and phosphonate spectral regions, respectively. Positive and negative bands represent increasing and decreasing components, respectively.

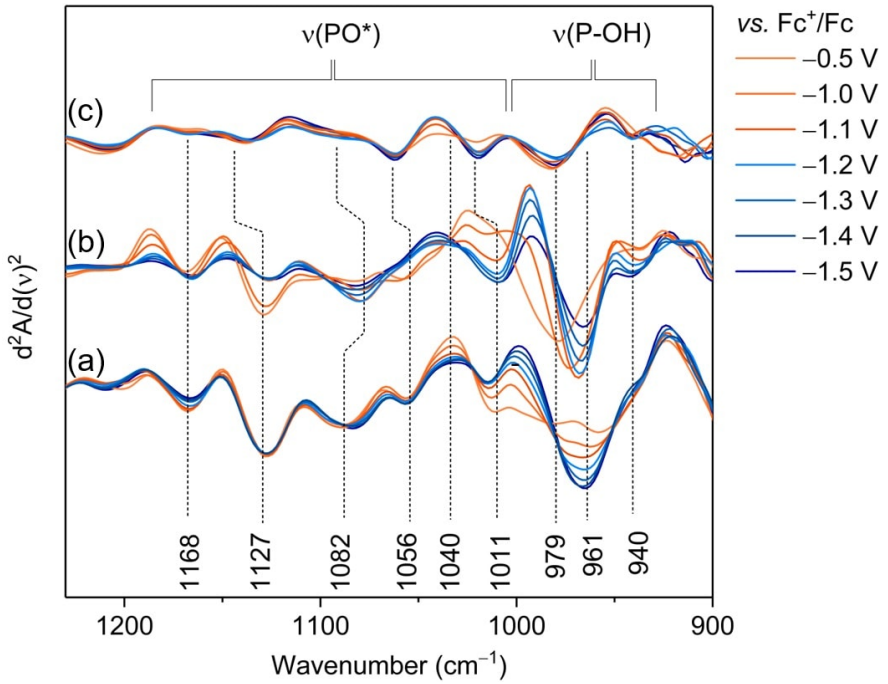

Fig. 4.10 Second derivatives of ATR-IR absorbance spectra in the phosphonate spectral region taken of *meso*ITO|**CotpyP** at different E_{app} (Fig. 4.8) in (a) N_2-purged MeCN, (b) N_2-purged 9:1 MeCN:H_2O and (c) CO_2-purged 9:1 MeCN:H_2O (0.1 M $TBABF_4$ in all cases) at room temperature. All spectra have been referenced to background spectra recorded from catalyst-free *meso*ITO for each of the above conditions. * indicates contributions from all possible P–O single bonds.

4.2.4 Mechanistic Interpretation

The spectroscopic and electrochemical evidence above strongly suggests that the complex's bis(terpyridine) ligation is preserved under (photo)electrocatalytic CO_2 reduction, and that catalysis does not involve irreversible structural alteration to the metal's first coordination sphere (Fig. 3.2, 3.4, 4.1a, 4.4a and 4.6). Considering that the immobilised **CotpyP** displays an onset for CO_2 reduction at a much more positive potential than that previously observed in solution, and that formate has previously been the only product from cobalt bis(terpyridine)-catalysed CO_2 reduction in water,[16] it is therefore proposed that the mechanism in our system proceeds differently to that commonly reported for metal bis(terpyridine) complexes.[1,2] Specifically, our catalytic mechanism involves retention of the bis-tpy ligation, whereas previous reports of homogeneous Co bis(terpyridine)s suggested that they always proceed *via* the irreversible loss of one terpyridine ligand to generate a Co(I) mono(terpyridine).[2] The contrasts between our proposed mechanism and that of commonly-reported literature precedence are outlined in Fig. 4.11.

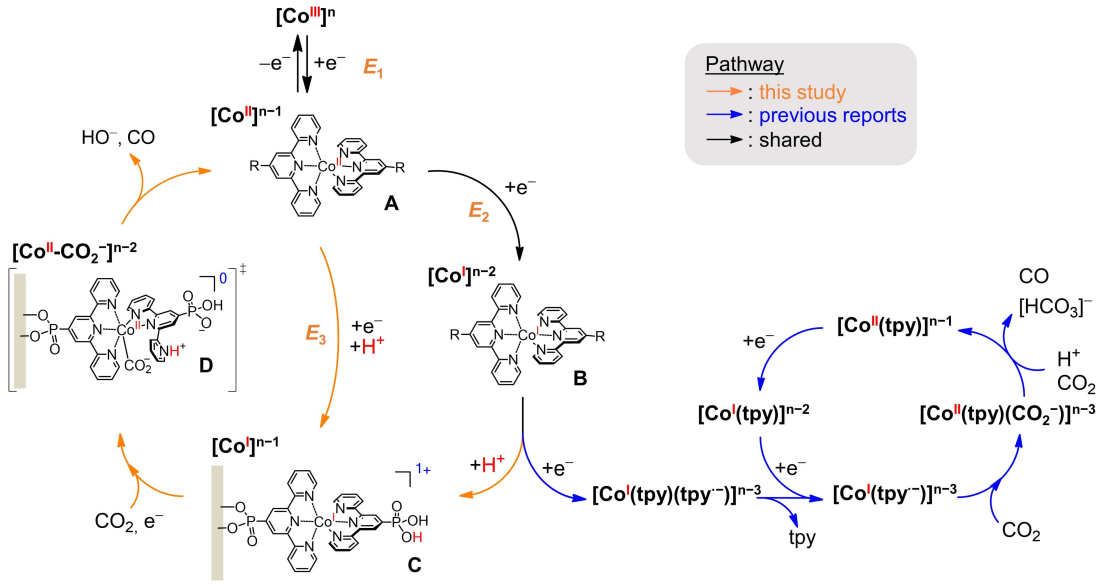

Fig. 4.11 Proposed catalytic mechanism and postulated intermediates for CO_2-to-CO reduction for immobilised **CotpyP** compared to the previously reported pathway for homogenous $[Co(tpy)_2]^{2+}$ (adapted from ref. [2]). $\boldsymbol{E_1}$-$\boldsymbol{E_3}$ refer to potentials recorded in 9:1 MeCN:H_2O solutions of the indicated redox couples in this study. R in **A** and **B** is respective to individual reports (this work and ref. [2].

The existence of a novel mechanism for immobilised **CotpyP** is also indicated by the emergence of waves at $\boldsymbol{E_3}$ during CV experiments, which has not been previously reported for cobalt bis(terpyridine)s. Moreover, the latter occurs at

a potential that matches the CO_2 reduction catalytic onset (Fig. 4.1 and 4.2), suggesting that the $\boldsymbol{E_3}$-related species is non-innocent towards CO_2 reduction. In light of the nature of the changes observed in the RR and ATR-IR spectra, it is probable that all chemical processes resulting from the redox steps at $\boldsymbol{E_1}$, $\boldsymbol{E_2}$ and $\boldsymbol{E_3}$ occur without major disruption of the Co coordination sphere, thereby ruling out ligand exchange possibilities. Rather, CV, RR and ATR-IR measurements suggest a proton-involving pathway that likely involves the unbound phosphonate group of the [Co^I] complex. From these observations, we propose that the species formed at $\boldsymbol{E_3}$ is a [Co^I] complex bearing a diprotonated phosphonic acid (Fig. 4.11, species **C**). This could be explained in two ways: (i) by the presumed increased basicity of the phosphonate group in the [Co^I] state as the π-symmetry of the filled Co d-orbital is suggested to allow the electronic density to spread on the π^* levels of the phosphonated terpyridine ligand, a relatively good π-acceptor, and (ii) by the phosphonic acid's increasing pK_a or decreasing local pH with negative polarisation of the electrode from the surface potential effect.[17] We deduce that species **C** can be generated either *via* a suspected concerted proton-coupled electron transfer process (PCET) from **A** or a chemical step from **B**, depending on the water content of the electrolyte solution. The former mechanism was observed at $\boldsymbol{E_3}$ in early CVs in water-rich solution, whereas **C** required several CV scans to become significantly apparent in water-deficient medium such as 9:1 MeCN:H_2O (Fig. 4.1b). We attributed this slow growth to a steady increase of the local proton concentration at the electrode-solution interface upon cycling (as previously observed for metal oxides), which would favour the PCET mechanism and further allow for the observed cycle-dependent behaviour in Fig. D.1.[18,19] This hypothesis is supported by the disappearance of wave $\boldsymbol{E_3}$ upon restoring the electrode to its initial state by allowing equilibration at open-circuit conditions (Fig. 4.1a, scan 8). As such, in such a water-poor medium, we attribute the origin of the oxidation wave of **C** seen in the first scan to the protonation of **B**, in a step-wise fashion.

On the other hand, the rapid formation of species **C** is promoted upon increasing the acidity of the medium (by increasing water content and/or purging with CO_2), with the catalytic potential towards CO_2 reduction matching the potential of the formation of species **C** (Fig. 4.1 and 4.2). These observations ultimately suggest that **C** is involved in the CO_2 reduction mechanism and we thus postulate that, upon reduction of the complex and coordination of CO_2, **D** is a plausible CO-releasing intermediate. Its formation would involve the de-coordination of one or two pyridines to create a vacant coordination site and, subsequently, the coordination of CO_2 (such a de-coordination has in fact been recently calculated

to be possible for Co bis(terpyridines) by density functional theory computational studies, albeit in a H_2-evolution catalysis context).[20] In fact, the d^8 configuration of [Co^I] species is likely to favour a square planar or tetrahedral geometry, as well as increase the lability of the ligand.[21,22] Moreover, the pyridine de-coordination is likely to be stabilised by protonation of its nitrogen atom from the diprotonated phosphonic acid due to the latter's lower pK_a value.[23] As a result, the deprotonated phosphonic acid could in effect act as a proton relay or H-bond source, utimately facilitating C-O bond cleavage during catalysis. However, at this stage, it is difficult to adjudicate whether the latter process would occur in **C** or only after further reduction of the catalyst. Thus, the suggested mechanistic pathway contrasts with previous reports and suggests exciting benefits of immobilising a metal complex (such as the opportunity to operate in an aqueous solution) that are not accessible in analogous homogeneous systems.[16,22,24,25]

4.3 Conclusion

In conclusion, intriguing insights into how the **CotpyP** catalyst is permitted to enter its reduced and pre-catalytic state were presented by in-depth cyclic voltammetry as well as *in situ* ATR-IR and RR spectroelectrochemical experiments, the latter being the first of their kind for spectroelectrochemical studies. The proposed formation of a key intermediate (species **C**) is revealed that creates an alternative and novel CO_2 reduction mechanism without requiring the loss of one terpyridine, which is in sharp contrast to the conventional understanding for metal bis(terpyridine) catalysts. Also key is the apparent protonation of a phosphonic acid group, which could facilitate eventual relay of this proton and the opening up of a coordination site at the Co metal centre.

This unexpected mechanistic pathway enabled **CotpyP** to perform CO_2 reduction on Si|*meso*TiO_2 (Chapter 3) thanks to a dramatically lower catalytic onset (almost 1 V), and consequently led to improved stabilities and a TON four times higher than previously reported for Co terpyridine complexes.[1] This unexpected performance enhancement was ultimately afforded by the synergy of having a phosphonic acid functional group alongside the possibility to operate the system under aqueous conditions – the latter having been conferred by first immobilising the catalyst. In addition to shedding insight on how our own complex behaves, these experiments also illustrate the power and precision offered by *in situ* vibrational spectroscopic techniques in the wider context of better understanding molecular catalyst-based solar fuel devices.

4.4 Experimental Section

4.4.1 Materials

Chemicals purchased for analytical measurements were of the highest available purity. FTO-coated glass sheets were purchased from Sigma Aldrich (SnO_2/F, 7 $\Omega\,sq^{-1}$ sheet resistance, 300 × 300 × 2 mm). ITO nanopowder (< 50 nm particle size; BET = 27 $m^2\,g^{-1}$; 90 % In_2O_3, 10 % SnO_2) was obtained from Sigma Aldrich. $KHCO_3$ and $Co(BF_4)_2{\cdot}6H_2O$ (96 %) were purchased from Alfa Aesar and 2,2':6',2"-terpyridine-4'phosphonic acid was purchased from HetCat, Switzerland (98 %). $TBABF_4$ was purchased from Sigma Aldrich (≥ 99.0 %, electrochemical grade). Methanol and acetonitrile were both distilled over calcium hydride before use. All aqueous experimental solutions were prepared with ultrapure Milli-Q® water (18.2 MΩ cm at 25 °C). Monoterpyridine [$CoCl_2$(tpy)] was prepared following a previously-reported procedure.[26]

The *meso*ITO|**CotpyP** electrodes used for the mechanistic studies described in this chapter were prepared according to the procedure outlined in Chapter 3 Experimental Section 3.4.4.

4.4.2 Cyclic Voltammetry Methods

All CV experiments were performed with an Ivium CompactStat potentiostat. A three-electrode configuration was employed in an airtight one-compartment cell, with $TBABF_4$ (0.1 M) as the electrolyte in a range of MeCN:H_2O solutions. The CE was a Pt mesh and the RE was a Ag/AgCl electrode in a solution with the same composition as the electrolyte (*i.e.* 0.1 M $TBABF_4$ in either 9:1 or 6:4 MeCN:H_2O) separated from the cell's electrolyte solution with a Vycor frit. The RE was regularly referenced against the ferrocene couple (Fc^+/Fc). Variations in the potential of the Fc^+/Fc couple in different solvent mixtures were taken into account.[27] The electrolyte solution was purged with N_2 or CO_2 prior to taking measurements to remove atmospheric O_2. All electrochemical measurements were performed at room temperature.

4.4.3 Spectroelectrochemical Resonance Raman Methods

Resonance Raman measurements of *meso*ITO|**CotpyP** were carried out in an airtight one-compartment quartz cell, with $TBABF_4$ (0.1 M) as the electrolyte

in 9:1 MeCN:H_2O solution (N_2- or CO_2-purged). The CE was a Pt wire and the RE was a $Ag/AgCl_{0.1\,M\ H_2SO_4}$ electrode (DriRef, WPI). A multi-channel MetrOhm MicroAutoLab potentiostat was used, alongside an xy-stage (OWISoft) on which the electrochemical cell was moved during measurements to avoid laser-induced sample degradation.

RR measurements were conducted using the 413 nm line of a Kr ion laser (Sabre), and the 458 nm and 514 nm lines of an Ar ion laser (Coherent Innova 300c). A Horiba LabRamII confocal Raman spectrometer equipped with a liquid N_2-cooled CCD detector (Symphony) was employed. The laser light was focused onto the sample using a 20 × objective (Nikon, 20 ×, NA 0.05).

Analysis of the spectra was performed using a home-made software (Qpipsi) and component fitting analyses were performed following published procedures.[8,28] To derive the component spectra, RR spectra of *meso*ITO|**CotpyP** obtained using 514 nm excitation and recorded at very positive (0.5 V *vs.* Fc^+/Fc), intermediate (−0.5 V *vs.* Fc^+/Fc) and very negative (−1.5 V *vs.* Fc^+/Fc) potentials were considered first. These spectra were each expected to be spectrally dominated by the **CotpyP** species in only one oxidation state ([Co^{III}], [Co^{II}] and [Co^{I}], respectively). The spectra were iteratively fitted using Lorentzian bands by varying their absolute intensities, half-widths and frequencies until a full reproduction of the spectra was achieved. The resulting bands were grouped to afford a component spectrum, *i.e.* three spectra were derived in total. RR spectra measured at all other potentials thereafter were fitted using the so-derived component spectra, allowing only a variation by a fitting parameter factor *GF*, *i.e.* by varying the spectral contribution of a respective component spectrum to the overall RR spectrum.

Group intensities were obtained by multiplying *GF* with a prominent, highly intense band found in the respective component spectrum to obtain the intensity of the respective component spectrum i, I_i. The relative intensity for a component spectrum i among a total of j component spectra, $I_{\mathrm{i,\,rel}}$, was calculated using the following equation:

$$I_{\mathrm{i,\,rel}} = \frac{I_\mathrm{i}}{\sum_{i=1}^{j} I_\mathrm{i}} \tag{4.1}$$

4.4.4 Spectroelectrochemical Infrared Spectroscopy Methods

Spectroelectrochemical ATR-IR measurements were carried out on *meso*ITO|-**CotpyP** prepared on a Si ATR prism as follows. An ITO suspension consisting of 10 wt % of ITO nanopowder in 5 M acetic acid in ethanol was prepared and sonicated well. This was spin-coated onto the flat surface of the Si ATR prism over the complete area of 3 cm^2, using a volume of 50 µL and a spin speed of 1000 rpm over 1 min. The solution was left to dry completely in air before annealing at 400 °C for 30 min (5 °C min^{-1}) under atmospheric conditions. **CotpyP** was adsorbed from 1 mL of the catalyst stock solution in MeOH (0.25 mM) for 45 min at room temperature. After the adsorption process was completed, the catalyst solution was removed from the ATR cell and the electrode rinsed several times with MeOH.

Spectroelectrochemical ATR-IR measurements were performed in a single-reflection PIKE ATR-IR setup and a customised ATR-IR spectroelectrochemical cell using an angle of incidence of 60 °. The electrochemical studies were carried out in a three-electrode system with the *meso*ITO|**CotpyP** film as WE, a Ag/AgCl electrode (in a solution with the same composition as the electrolyte) as RE, and a Pt wire as CE. Potentials were applied using an Ivium CompactStat potentiostat. The ATR-IR spectra were recorded in a spectral range from 4000 to 900 cm^{-1} (note that the range below 900 cm^{-1} was inaccessible due to strong absorption by the Si ATR prism) with a spectral resolution of 4 cm^{-1} on a Bruker Vertex 70 spectrometer equipped with a photovoltaic MCT detector. A total of 200 scans were co-added for one spectrum, requiring an accumulation time of 1.5 min. All measurements were carried out at room temperature, under either N_2 or CO_2 overpressure.

ATR-IR spectra were evaluated using the OPUS 5.5 software. Absorbance and difference spectra (A) were generated according to the Lambert-Beer equation:

$$A = -log\frac{I_{\text{sample}}}{I_{\text{reference}}} \tag{4.2}$$

where I_{sample} denotes the sample spectrum and $I_{\text{reference}}$ denotes the respective reference spectrum for either absorbance or difference spectra. Baseline corrections of the absorbance spectra and second derivative spectra were generated by means of the OPUS 5.5 software data analysis tools.

4.5 References

(1) Elgrishi, N.; Chambers, M. B.; Wang, X.; Fontecave, M. *Chem. Soc. Rev.* **2017**, *46*, 761–796.

(2) Elgrishi, N.; Chambers, M. B.; Artero, V.; Fontecave, M. *Phys. Chem. Chem. Phys.* **2014**, *16*, 13635–13644.

(3) Elgrishi, N.; Griveau, S.; Chambers, M. B.; Bedioui, F.; Fontecave, M. *Chem. Commun.* **2015**, *51*, 2995–2998.

(4) Kupfer, S.; Guthmuller, J.; Wächtler, M.; Losse, S.; Rau, S.; Dietzek, B.; Popp, J.; González, L. *Phys. Chem. Chem. Phys.* **2011**, *13*, 15580–15588.

(5) Šloufová, I.; Vlčková, B.; Procházka, M.; Svoboda, J.; Vohlídal, J. *J. Raman Spectrosc.* **2014**, *45*, 338–348.

(6) Keidel, A.; López, I.; Staffa, J.; Kuhlmann, U.; Bozoglian, F.; Gimbert-Suriñach, C.; Benet-Buchholz, J.; Hildebrandt, P.; Llobet, A. *ChemSusChem* **2017**, *10*, 551–561.

(7) Prusková, M.; Sutrová, V.; Šlouf, M.; Vlčková, B.; Vohlídal, J.; Šloufová, I. *Langmuir* **2017**, *33*, 4146–4156.

(8) Ly, H. K.; Wrzolek, P.; Heidary, N.; Götz, R.; Horch, M.; Kozuch, J.; Schwalbe, M.; Weidinger, I. M. *Chem. Sci.* **2015**, *6*, 6999–7007.

(9) Hugot-Le Goff, A.; Joiret, S.; Falaras, P. *J. Phys. Chem. B* **1999**, *103*, 9569–9575.

(10) Zhang, Y.; Kupfer, S.; Zedler, L.; Schindler, J.; Bocklitz, T.; Guthmuller, J.; Rau, S.; Dietzek, B. *Phys. Chem. Chem. Phys.* **2015**, *17*, 29637–29646.

(11) Quinet, O.; Champagne, B.; Rodriguez, V. *J. Chem. Phys.* **2006**, *124*, 244312.

(12) Rooth, M.; Shaw, A. M. *Phys. Chem. Chem. Phys.* **2006**, *8*, 4741–4743.

(13) White, H. S.; Peterson, J. D.; Cui, Q.; Stevenson, K. J. *J. Phys. Chem. B* **1998**, *102*, 2930–2934.

(14) Yaguchi, M.; Uchida, T.; Motobayashi, K.; Osawa, M. *J. Phys. Chem. Lett.* **2016**, *7*, 3097–3102.

(15) Arai, Y.; Sparks, D. L. *J. Colloid Interface Sci.* **2001**, *241*, 317–326.

(16) Yoshida, T.; Iida, T.; Shirasagi, T.; Lin, R.-J.; Kaneko, M. *J. Electroanal. Chem.* **1993**, *344*, 355–362.

(17) Potts, K. T.; Usifer, D. A.; Guadalupe, A.; Abruña, H. D. *J. Am. Chem. Soc.* **1987**, *109*, 3961–3967.

(18) He, T.; Wang, L.; Fabregat-Santiago, F.; Liu, G.; Li, Y.; Wang, C.; Guan, R. *J. Mater. Chem. A* **2017**, *5*, 6455–6464.

(19) Björneholm, O.; Hansen, M. H.; Hodgson, A.; Liu, L. M.; Limmer, D. T.; Michaelides, A.; Pedevilla, P.; Rossmeisl, J.; Shen, H.; Tocci, G.; Tyrode, E.; Walz, M. M.; Werner, J.; Bluhm, H. *Chem. Rev.* **2016**, *116*, 7698–7726.

(20) Aroua, S.; Todorova, T. K.; Mougel, V.; Hommes, P.; Reissig, H. U.; Fontecave, M. *ChemCatChem* **2017**, *9*, 2099–2105.

(21) Veldkamp, B. S.; Han, W. S.; Dyar, S. M.; Eaton, S. W.; Ratner, M. A.; Wasielewski, M. R. *Energy Environ. Sci.* **2013**, *6*, 1917–1928.

(22) Guadalupe, A. R.; Usifer, D. A.; Potts, K. T.; Hurrell, H. C.; Mogstad, A. E.; Abruña, H. D. *J. Am. Chem. Soc.* **1988**, *110*, 3462–3466.

(23) Nazeeruddin, M. K.; Zakeeruddin, S. M.; Humphry-Baker, R.; Kaden, T. A.; Grätzel, M. *Inorg. Chem.* **2000**, *39*, 4542–4547.

(24) Reuillard, B.; Ly, K. H.; Rosser, T. E.; Kuehnel, M. F.; Zebger, I.; Reisner, E. *J. Am. Chem. Soc.* **2017**, *139*, 14425–14435.

(25) Kuehnel, M. F.; Orchard, K. L.; Dalle, K. E.; Reisner, E. *J. Am. Chem. Soc.* **2017**, *139*, 7217–7223.

(26) Hogg, R.; Wilkins, R. G. *J. Chem. Soc.* **1962**, 341–350.

(27) Lanning, J. A.; Chambers, J. Q. *Anal. Chem.* **1973**, *45*, 1010–1016.

(28) Ly, H. K.; Utesch, T.; Díaz-Moreno, I.; García-Heredia, J. M.; De La Rosa, M. A.; Hildebrandt, P. *J. Phys. Chem. B* **2012**, *116*, 5694–5702.

Chapter 5

Rational Polymer Design Towards Tuneable Molecular CO_2 Reduction Catalysis

The contents of this chapter have been submitted for publication as a peer-reviewed article. Results presented were obtained solely by the author of this thesis, with contributions from others as outlined here: Julian Vigil synthesised the polymers and shared cyclic voltammetry experiments with the author. Julien Warnan shared ICP-OES measurements with the author and Julian Vigil. Esther Edwardes Moore prepared Ti/IO-TiO_2 electrodes. Andreas Wagner and Kenichi Nakanishi prepared the ALD-deposited TiO_2 layer on top of the Si wafers.

5.1 Introduction

Selective CO evolution and, more generally, energy-to-fuel conversion by electrocatalysts in water remains a major goal towards realising a sustainable and closed carbon cycle.[1] To this end, molecular catalysts have been developed taking inspiration from impressive natural archetypes, such as CO and formate dehydrogenase enzymes.[2,3] While still dominated by precious metal-based complexes, tremendous efforts have recently been focused towards designing Earth-abundant 3d transition metal-based (Co, Ni, Fe and Mn) catalysts, as has been described above in Chapter 1.[4,5] Often limited by their instability and/or insolubility, as well as the low solubility of CO_2 and competing H_2 evolution in water, the large majority of these latter complexes have been studied in organic solvents. Con-

sequently, examples of 3d metal-based complexes performing CO_2 reduction in aqueous environments remain scarce.

Since early reports of Ni cyclam and Lehn's Re catalysts, optimisation of molecular design towards improved product selectivity has been conducted primarily by tailoring the primary coordination sphere of the metal to promote interactions with CO_2. Alternative strategies have incorporated catalysts with electrodes such as carbon nanotubes or carbon cloth in order to provide a more hydrophobic environment conducive to CO_2 utilisation.[6,7] For CO_2 reduction in water, such molecular-based hybrid systems have almost exclusively been developed with carbon-based materials.[8–10] Considering their intrinsic semiconducting and water-stable properties, metal oxides represent an alternative class of promising cathode materials and have been successfully exploited both in colloidal schemes and as cathode substrates towards H_2 evolution, including in the works described above in Chapters 2-4.[8,9] However, their natural hydrophilicity and propensity towards hydrogen bonding generally promote H^+ reduction over CO_2 reduction.

In the previous two chapters, a system comprising a Co-based catalyst immobilised on a Si|*meso*TiO_2 scaffold to yield a photoelectrode capable of CO_2 reduction in aqueous conditions was described. Immobilisation of the molecular electrocatalyst onto the photoelectrode was an important first step in ensuring that aqueous operating solutions could be accessed by the water-insoluble catalyst. Moreover, the performance of this system was shown to be heavily influenced by changes in its external environment – namely, the proportion of MeCN and H_2O in the electrolyte solution, which was thought to bring about consequences such as CO_2 availability in the vicinity of the electrode as well as band-bending effects.

In this chapter, the development of the first rationally designed polymers towards selective CO evolution and their incorporation into porous TiO_2-based architectures to produce precious metal-free metal oxide cathodes for CO evolution are described. Building on the above-described utilisation of **CotpyP** as an electrocatalyst towards photoelectrochemical reduction of CO_2 in aqueous environments, we tailored coordination polymer scaffolds capable of immobilisation onto TiO_2 electrodes, tuneable crosslinking, and improved selectivity over the molecular counterparts. Although only a few reports on the use of coordination polymers in molecular CO_2 reduction catalysis are available,[11,12] we recently demonstrated that copolymers can provide several advantages over molecular species with complementary properties towards optimised H_2 evolution performance, as was discussed in Chapter 1 section 1.4.3.[13] By embedding a CO_2 reduction catalyst into a rationally designed copolymer, the work described in this chapter aims to demonstrate

that tuning the catalyst environment (outer coordination sphere) is a promising strategy in an attempt to emulate the environment that surrounds the metal centre in CO_2 reductases.

5.2 Results and Discussion

5.2.1 Polymer Synthesis

Based on the design principles outlined above, two low molecular weight copolymer scaffolds were synthesised with three monomers each: (i) a terpyridine (tpy) ligand for coordination to the metal centre; (ii) a phosphonic acid moiety for robust anchoring on metal oxide surfaces; and (iii) a functional group conducive to selective CO production.

The initial tpy-phosphonate ester copolymer (**5**, Fig. 5.1a) was obtained by free-radical polymerisation of the synthesised methacrylate-bearing tpy (**1**) and diethyl phosphonate (**2**) monomers in stoichiometric combination with a standard methyl methacrylate monomer (**3**). The phosphonate ester moieties in **5** were subsequently deprotected to yield the corresponding phosphonic acid groups in the final copolymer scaffold (**p1**, Fig. 5.1a). **p1** was then dissolved in MeOH and complexed with Co(II) by addition of $Co(BF_4)_2$ ($\mathbf{P1_x}$, where x represents the number of equivalents of Co per 2 equivalents of tpy in **p1**; Fig. 5.1a).

p2 was synthesised and isolated in a similar molecular weight according to the same procedure as for **p1**, but starting from monomer **4** rather than **3** (Fig. 5.1a). The polymer was subsequently coordinated with Co in bis(tpy) stoichiometry to yield $\mathbf{P2_1}$.

The Co-coordinated polymers are depicted schematically in Figure 5.1b, showing the functions of each monomer, the role of the polymer backbone near the active complexes, and an interplay between Co coordination and cross-linking of polymer chains. All synthetic procedures and characterisation (^{1}H, ^{13}C and ^{31}P NMR; elemental analysis, HRMS, ATR-FTIR; gel permeation chromatography (GPC)) of the monomers and polymers are provided in the Experimental Section 5.4.3.

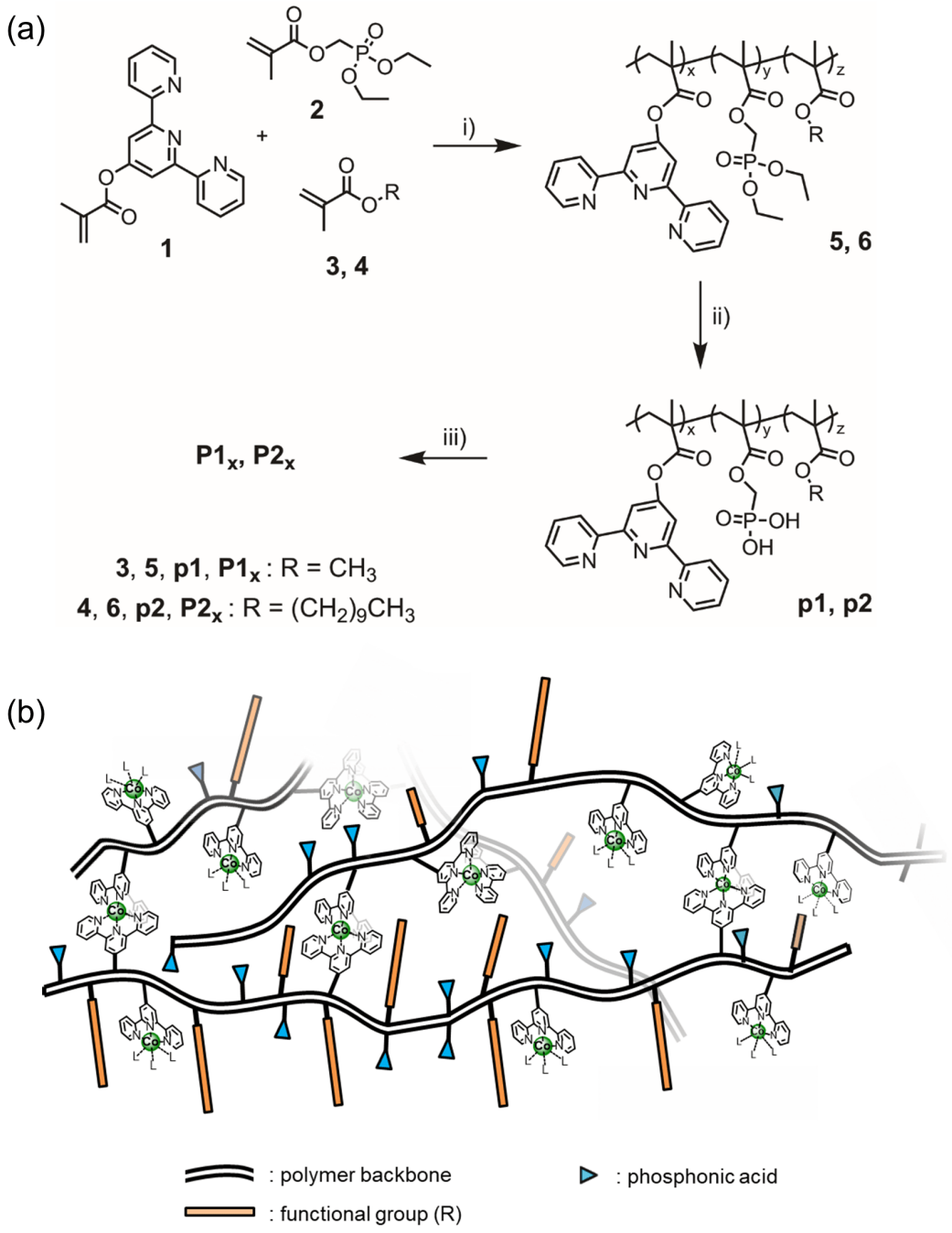

Fig. 5.1 (a) Synthetic route to the Co-coordinated polymers: i) 2,2'-azobis(2-methylpropionitrile) (AIBN), THF, 70 °C, 16 h; ii) (1) bromotrimethylsilane (TMS-Br), DCM, 0 °C, 16 h, (2) MeOH, 4 h; iii) $Co(BF_4)_2 \cdot 6H_2O$, MeOH, 16 h. Yields are provided in the Experimental Section. (b) Schematic representation of the $\mathbf{P1_x}$ and $\mathbf{P2_x}$ polymers with respective functional groups and phosphonic acid anchoring moieties.

5.2.2 Cross-Linkage Modulation in $P1_x$ Polymers

Physical and Electrochemical Characterisation

p1 was first coordinated with bis(tpy) stoichiometry (*i.e.* 1:2, Co:tpy) to yield $\mathbf{P1_1}$, which was isolated and purified for electroanalytical characterisation. Under inert N_2 atmosphere, the cyclic voltammogram of a 95:5 v:v DMF:H_2O solution of $\mathbf{P1_1}$ (0.5 mM Co) with 0.1 M $TBABF_4$ as electrolyte showed reversible electrochemical features between 0.0 and −2.0 V *vs.* Fc^+/Fc, and the onset of irreversible cathodic current at −2.2 V *vs.* Fc^+/Fc (Fig. 5.2a). Square wave voltammetry (SWV) was subsequently used to improve the ratio of Faradaic to capacitive current and elucidate the half-wave potentials ($E_{½}$) of electrochemical features observed using cyclic voltammetry. The most positive waves ($E_{½} = -0.46$, −0.56 V *vs.* Fc^+/Fc) are attributed to the $Co^{III/II}$ couple, followed by two waves also separated by ∼0.1 V ($E_{½} = -1.52$, −1.63 V *vs.* Fc^+/Fc) for the $Co^{II/I}$ couple (Fig. 5.2b).[14,15] We speculate that the origin of the two discrete features for both Co-based redox processes may be due to an environmental or solvent-dependent effect, as discussed below. Finally, two tpy-based ligand reductions were observed at −1.83 and −2.37 V *vs.* Fc^+/Fc. $E_{½}$ for the first ligand reduction corresponds well with the onset of current enhancement in the presence of CO_2 (Fig. 5.2a), confirming that the reduction of tpy triggers CO_2 reduction catalysis when in solution.[14]

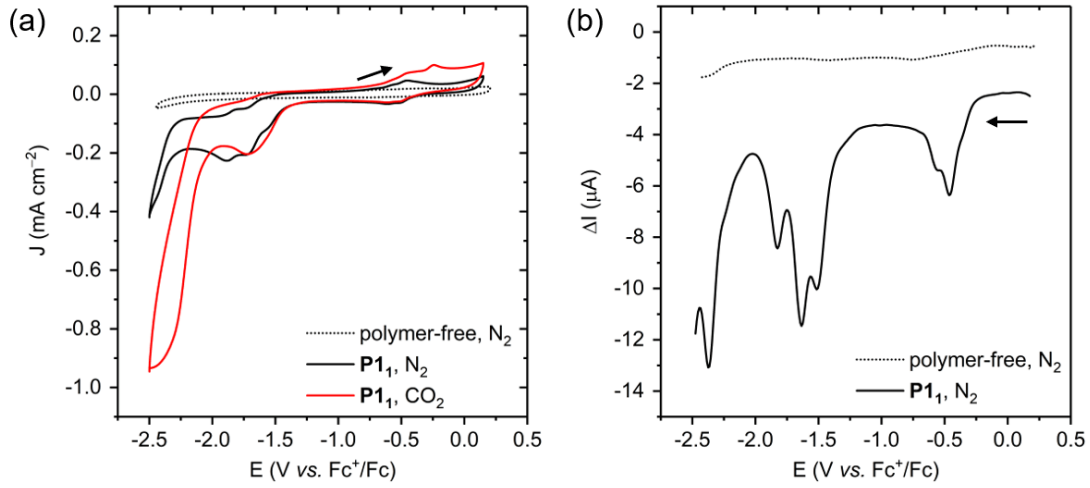

Fig. 5.2 (a) Cyclic voltammograms under N_2 and CO_2 atmosphere on a glassy carbon electrode in a 95:5 v:v DMF:H_2O (0.1 M $TBABF_4$) solution of $\mathbf{P1_1}$ (0.5 mM Co), 100 mV s^{-1}; (b) SW voltammogram under N_2 atmosphere and identical conditions to (a), cathodic scan beginning at 0.2 V *vs.* Fc^+/Fc. The response of a glassy carbon electrode in a polymer-free electrolyte solution under identical conditions is also shown. Arrows indicate scan starts.

Next, the interplay between Co loading, coordination equilibrium and crosslinking in the $\mathbf{P1_x}$ polymers was investigated using UV-vis spectroscopy. Spectra were collected for the uncoordinated **p1** polymer and a series of Co-coordinated $\mathbf{P1_x}$ polymers in MeOH, where x was varied from 0.6 to 5 (Fig. 5.3). Upon the addition of 0.6 eq Co to the **p1** polymer ($\mathbf{P1_{0.6}}$), three well-resolved absorption maxima were observed at 440, 505 and 550 nm, attributed to metal-to-ligand charge transfer (MLCT) transitions.[16] When the concentration of Co was increased to 1:2 (Co:tpy; $\mathbf{P1_1}$), the Co(II) bis(tpy) MLCT transitions were retained and the solution absorbs broadly at $\lambda < 600$ nm. At concentrations of Co corresponding to mono(tpy) stoichiometry ($\mathbf{P1_2}$) and a further excess of Co ($\mathbf{P1_5}$), the spectra showed a concomitant loss of the Co bis(tpy) MLCT transitions and the emergence of a broad absorption centred around 380 nm (Fig. 5.3, inset). Strong absorption in the UV at $\lambda < 400$ nm is characteristic of charge transfer from five-coordinate Co(II) mono(tpy) complexes.[17] These results indicate a dynamic coordination equilibrium within the polymeric matrix, with a transition from primarily bis(tpy) coordination in the $\mathbf{P1_{0.6}}$ and $\mathbf{P1_1}$ polymers to mono(tpy) coordination in the $\mathbf{P1_2}$ and $\mathbf{P1_5}$ polymers, likely accompanied by a reduction in the degree of cross-linking.

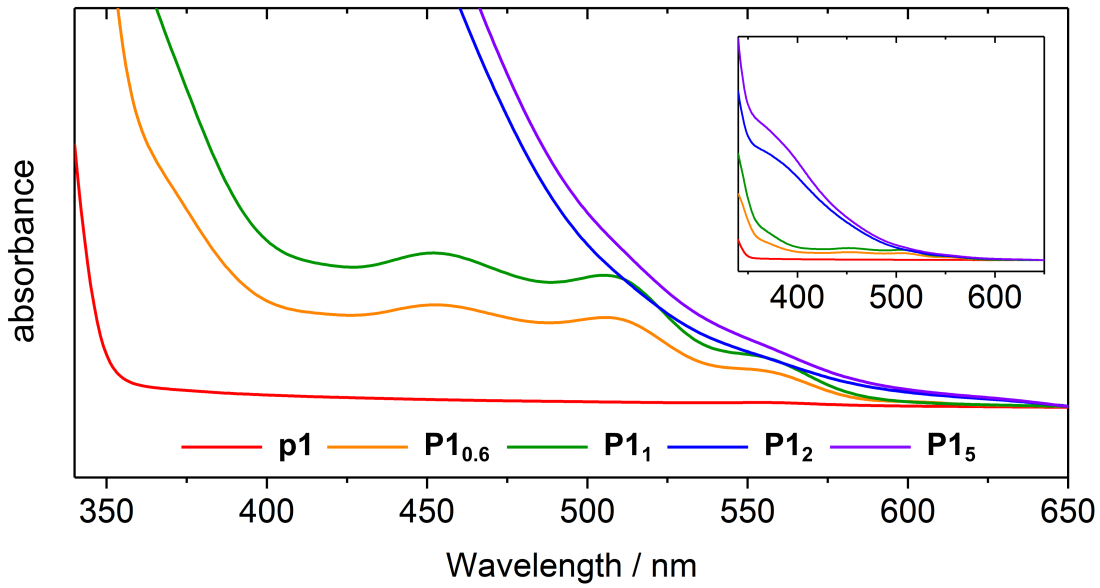

Fig. 5.3 UV-vis spectra of the uncoordinated **p1** (0.5 mM tpy) and Co-coordinated $\mathbf{P1_x}$ polymers in MeOH (0.25 mM Co); inset: reduced zoom view showing increased broad absorption at ∼380 nm with Co loading.

The $\mathbf{P1_x}$ polymers were immobilised on fluorine-doped tin oxide-supported inverse opal indium tin oxide electrodes (FTO|IO-ITO; 6 µm thick, ITO particle size < 50 nm) by immersion of the latter into solutions of the polymers. Such IO-ITO electrodes were originally optimised for the integration of large structures

(*e.g.* proteins)[18] and were used here to accommodate a high loading of the polymers in its 3D architecture, as the large pores of the inverse opal scaffold are size-compatible with the polymers.

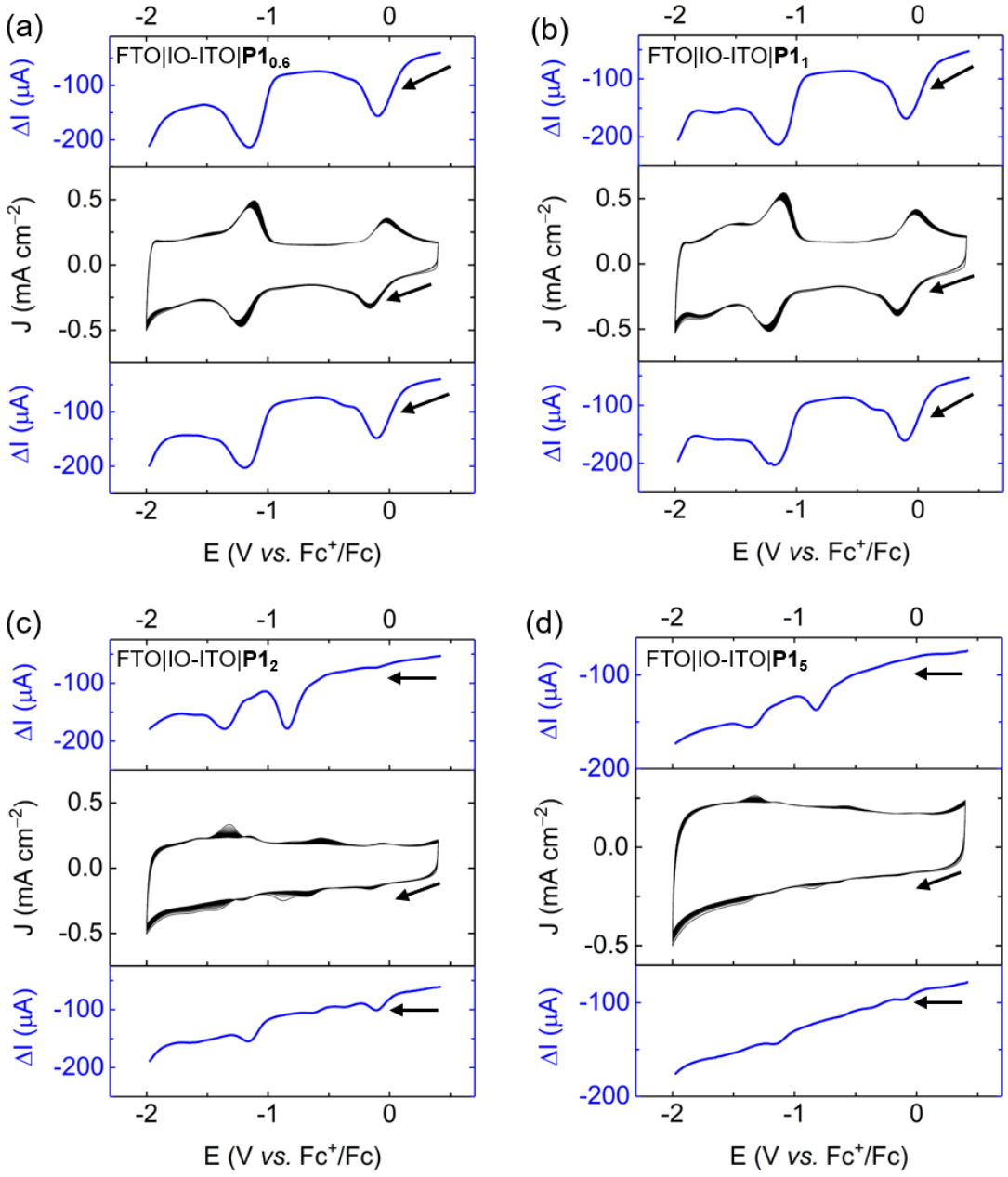

Fig. 5.4 Sequential electroanalytical characterisation of immobilised (a) $\mathbf{P1_{0.6}}$, (b) $\mathbf{P1_1}$, (c) $\mathbf{P1_2}$ and (d) $\mathbf{P1_5}$ polymers on FTO|IO-ITO electrodes: initial SW voltammogram (top), followed by 20 cyclic voltammetry cycles (middle) and a final SW voltammogram (bottom); anhydrous DMF (0.1 M $TBABF_4$), N_2-purged, 100 mV s^{-1}. Arrows indicate scan starts.

The immobilised $\mathbf{P1_x}$ polymers were characterised using CV and SWV in anhydrous DMF (Fig. 5.4) and 95:5 v:v DMF:H_2O (Fig. 5.5) electrolyte solutions.

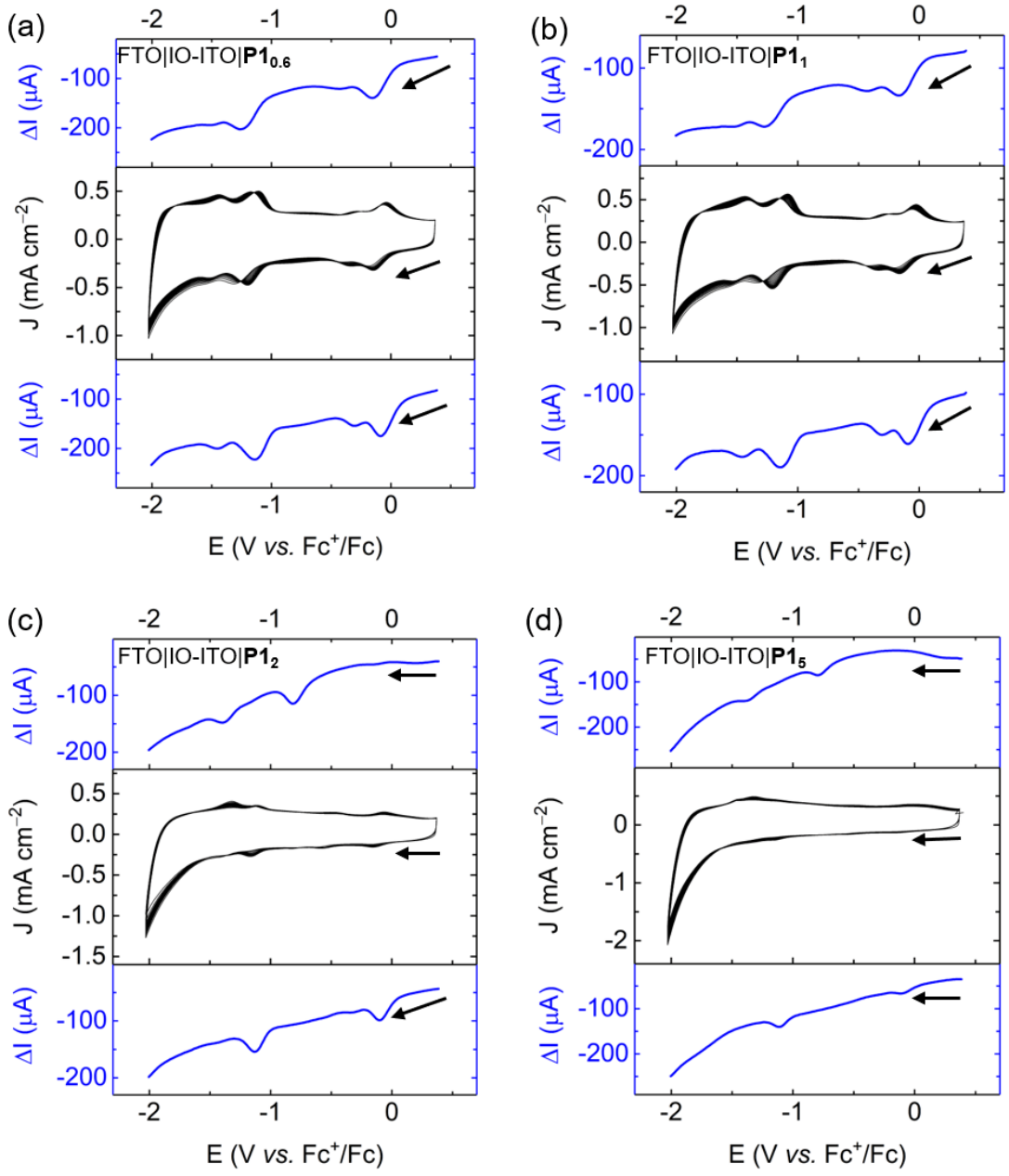

Fig. 5.5 Sequential electroanalytical characterisation of immobilised (a) $\mathbf{P1_{0.6}}$, (b) $\mathbf{P1_1}$, (c) $\mathbf{P1_2}$ and (d) $\mathbf{P1_5}$ polymers on FTO|IO-ITO electrodes: initial SW voltammogram (top), followed by 20 cyclic voltammetry cycles (middle) and a final SW voltammogram (bottom); 95:5 v:v DMF:H_2O electrolyte solution (0.1 M $TBABF_4$), N_2-purged, 100 mV s^{-1}. Arrows indicate scan starts.

Following an initial SW voltammogram, the electrode was cycled 20 times by CV to monitor changes in the coordination environment of Co in the immobilised polymer. In anhydrous DMF, the FTO|IO-ITO|$\mathbf{P1_1}$ electrode showed two stable reversible waves corresponding to the $Co^{III/II}$ and $Co^{II/I}$ couples ($E_{½} = -0.1$ and $-1.15\,V$ *vs.* Fc^+/Fc; Fig. 5.4b). By contrast, the initial SW voltammogram for the FTO|IO-ITO|$\mathbf{P1_2}$ electrode showed two primary features at -0.85 and $-1.35\,V$ *vs.* Fc^+/Fc, which subsequently decayed with cycling (Fig. 5.4c). A final SW voltammogram indicated a complete loss of these features and the corresponding emergence of redox couples at -0.1 and $-1.15\,V$ *vs.* Fc^+/Fc. The initial waves, particularly the shifted $Co^{II/I}$ wave at $-1.35\,V$ *vs.* Fc^+/Fc,[19,20] are indicative of Co mono(tpy) complexes and suggest that the more stable Co bis(tpy) complex is formed with cycling, accompanied by a loss of excess Co ions (confirmed by elemental analysis, as discussed below). The redox behaviour and stability of the immobilised $\mathbf{P1_{0.6}}$ and $\mathbf{P1_5}$ polymers were analogous to $\mathbf{P1_1}$ and $\mathbf{P1_2}$, respectively (Fig. 5.4a and d).

In the presence of H_2O, the immobilised $\mathbf{P1_{0.6}}$ and $\mathbf{P1_1}$ polymers demonstrated similar redox behaviour and stability (Fig. 5.5). Unlike in anhydrous DMF, however, two coupled features for both Co-based redox processes were observed (separated by 200-300 mV), analogous to the cyclic voltammograms of $\mathbf{P1_1}$ in solution (Fig. 5.2b). The immobilised $\mathbf{P1_2}$ and $\mathbf{P1_5}$ polymers again show a transition from mono(tpy) to bis(tpy) coordination with cycling (Fig. 5.5). The cathodic current for the FTO|IO-ITO|$\mathbf{P1_5}$ electrode at $-2.0\,V$ *vs.* Fc^+/Fc is also significantly enhanced relative to the other immobilised $\mathbf{P1_x}$ polymers, which suggests the large excess of Co ions results in Co-based or H^+ reduction at the electrode surface, independent of the polymeric matrix.

Electrocatalytic CO_2 Reduction

The $\mathbf{P1_x}$ polymers were subsequently immobilised on Ti foil-backed inverse opal TiO_2 electrodes (Ti|IO-TiO_2; 15 µm thick, TiO_2 particle size 10-30 nm; Fig. 5.6) for evaluation of their electrocatalytic CO_2 reduction performance. Ti foil was chosen over FTO as the supporting substrate owing to its greater stability under reducing conditions. The quantity of Co loaded per geometric surface area, measured by ICP-OES, was found to increase approximately proportionately to the Co:tpy ratio in the immobilised polymers (Table 5.1). ATR-FTIR measurements confirmed the preservation of the polymer's molecular integrity upon surface immobilisation (Fig. 5.7).

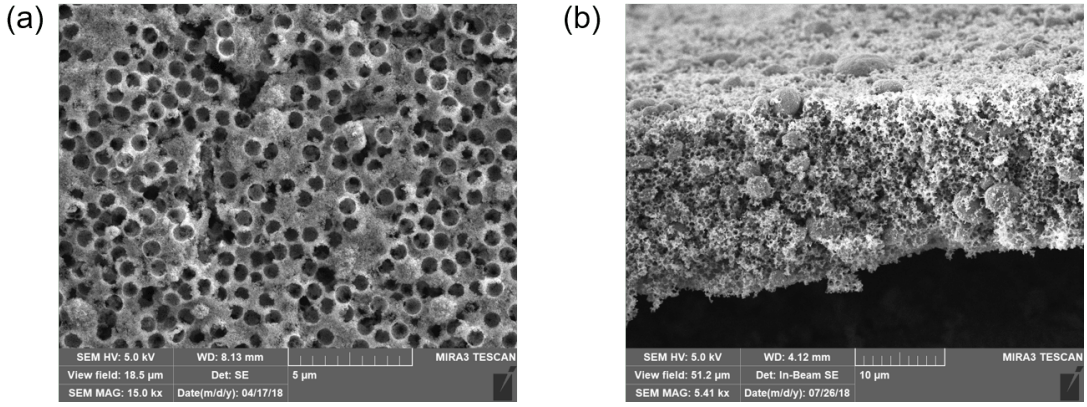

Fig. 5.6 SEM images of the Ti|IO-TiO_2 electrodes, as viewed (a) from the top surface and (b) in cross-section.

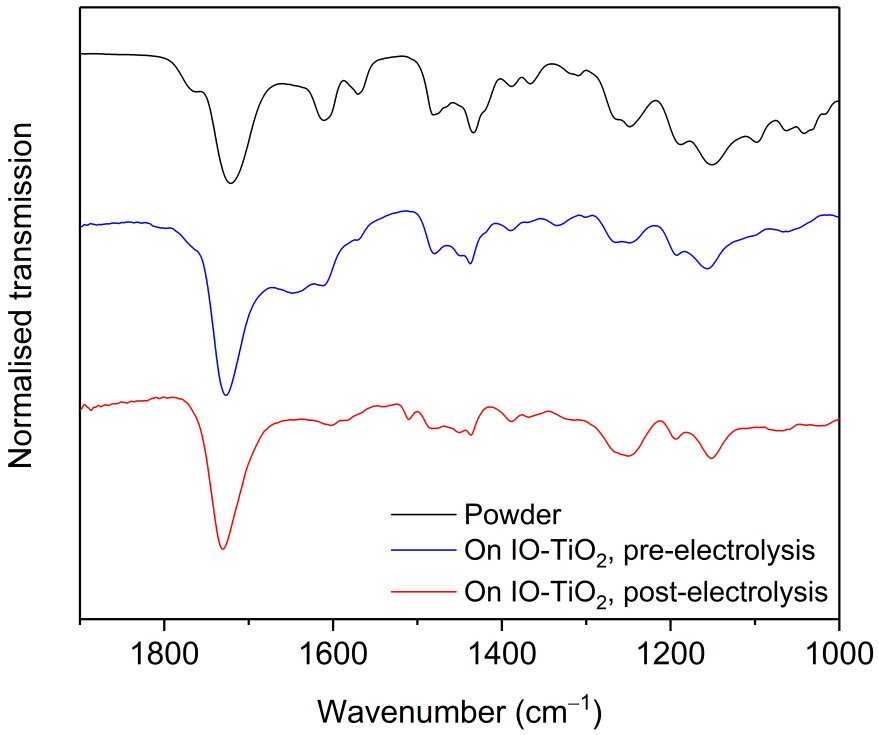

Fig. 5.7 ATR-FTIR spectra of $\mathbf{P1_1}$ as a powder (black trace), and after immobilisation on IO-TiO_2 before (blue trace) and after (red trace) 4 h CPE.

Table 5.1 Quantification of Co loaded onto surface of Ti|IO-TiO_2|$\mathbf{P1_x}$ and Ti|IO-TiO_2|$\mathbf{P2_x}$ electrodes as measured by ICP-OES. Loadings are given per geometric surface area.

Polymer	**x** ($\mathbf{P1_x}$ or $\mathbf{P2_x}$)	**Co loadings on Ti|IO-TiO_2** ($nmol\,cm^{-2}$)
P1	0.6	2.7 ± 0.0
	1	10.1 ± 1.0
	2	17.8 ± 2.8
	5	36.5 ± 0.6
P2	1	9.9 ± 0.0

The electrocatalytic CO_2 reduction activity of these electrodes was determined by controlled potential electrolysis (CPE) with an applied potential of $-1.3\,V$ *vs.* Fc^+/Fc in CO_2-saturated 6:4 v:v MeCN:H_2O electrolyte solution (0.1 M $TBABF_4$). These electrolyte solution conditions were previously found to be optimal for the analogous phosphonated molecular Co bis(tpy) catalyst **CotpyP** immobilised on TiO_2, as described in Chapter 3 section 3.2.2. In addition, current enhancement from the Ti|IO-TiO_2|$\mathbf{P1_1}$ electrode was observed to begin at potentials close to $-1.3\,V$ *vs.* Fc^+/Fc in the presence of CO_2 under such conditions (Fig. E.1). Gaseous products CO and H_2 were quantified by gas chromatography whereas formate was measured by ion chromatography, for which the latter was found to be below the detection limit in all cases.

While the stability of each electrode was found to be similar regardless of Co loading (Fig. 5.8), striking differences in activity and turnover numbers were observed (Fig. 5.9 and Table 5.2). After 4 h of CPE, the total amounts of product increased from a total of $0.34\,\mu mol\,cm^{-2}$ for Ti|IO-TiO_2|$\mathbf{P1_{0.6}}$ to $1.54\,\mu mol\,cm^{-2}$ for Ti|IO-TiO_2|$\mathbf{P1_2}$. Upon increasing the Co loading further (Ti|IO-TiO_2|$\mathbf{P1_5}$), activity decreased to only $0.56\,\mu mol\,cm^{-2}$ of product, resulting in a Gaussian relationship between absolute activity and Co loading. However, given that the Co loading on these electrodes varied widely (Table 5.1), the TONs present a vastly different picture of activity. The maximum TON (126, of which 78 is CO) was observed for the polymer with the lowest Co loading, Ti|IO-TiO_2|$\mathbf{P1_{0.6}}$, and the other polymers yielded progressively lower total TONs with a corresponding increase in Co loading.

Control CPE experiments were performed on the polymer-free Ti|IO-TiO_2 bare electrode (Fig. E.2) and metal-free Ti|IO-TiO_2|**p1** electrode (Fig. 5.8, black traces) under CO_2, and finally the Ti|IO-TiO_2|$\mathbf{P1_1}$ electrode under N_2 (Fig. E.3).

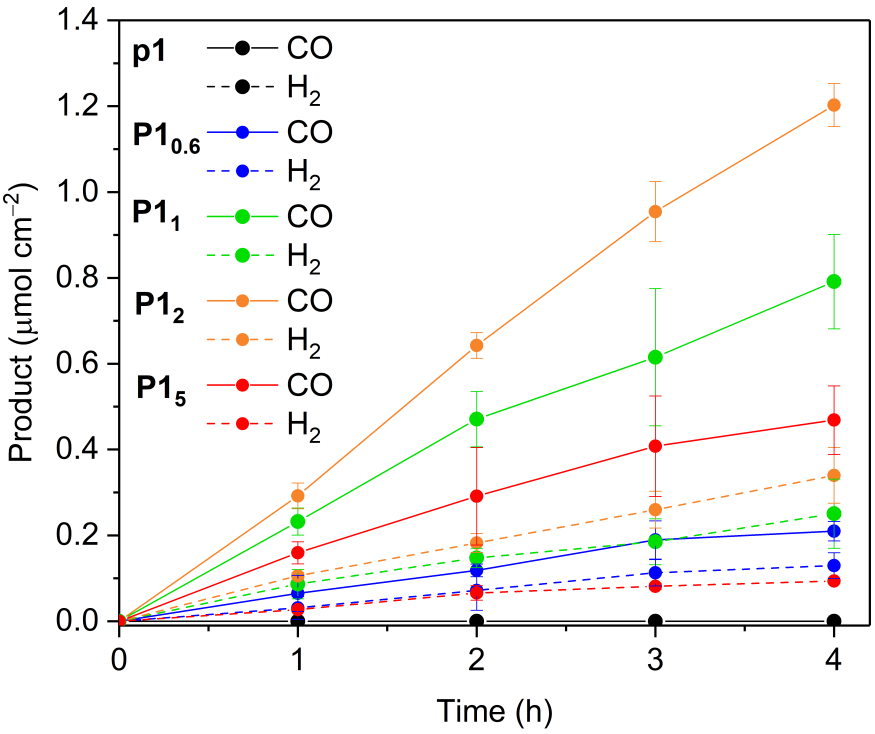

Fig. 5.8 Quantities of CO (solid lines) and H_2 (dashed lines) produced by Ti|IO-TiO_2|$\mathbf{P1_x}$, including Co-free **p1**. Conditions: 6:4 MeCN:H_2O (0.1 M $TBABF_4$), $E_{app} = -1.3$ V *vs.* Fc^+/Fc, CO_2-saturated conditions, room temperature.

These experiments produced no CO or H_2, confirming that both CO_2 and proton reduction must be carried out by the coordinated $\mathbf{P1_x}$ polymers (note that the lack of H_2 produced by Ti|IO-TiO_2|$\mathbf{P1_1}$ under N_2 can be explained by a higher pH of the electrolyte solution compared to that under CO_2, the latter of which would facilitate H^+ reduction). Isotopic labelling experiments conducted with a $^{13}CO_2$-saturated solution also confirmed CO_2 to be the source of the CO product (determined by gas-phase IR; Fig. E.4). Both the stable activity of these electrodes (Fig. 5.8) and ATR-FTIR measurements taken after CPE (Fig. 5.7) attest to the preservation of the molecular integrity of the coordinated $\mathbf{P1_x}$ polymers under catalytic conditions.

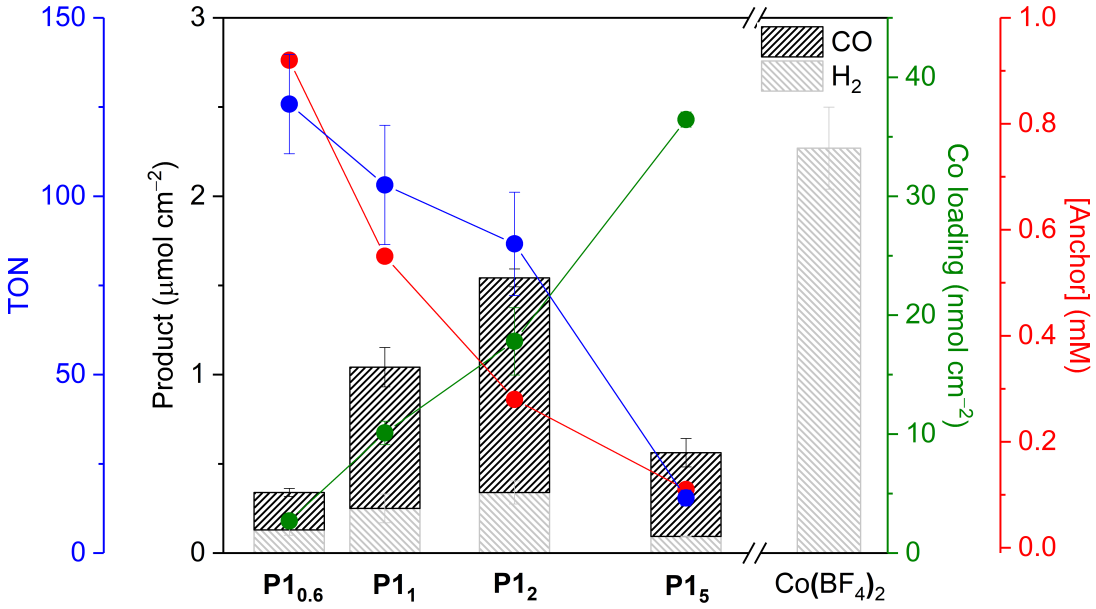

Fig. 5.9 Results from CPE of Ti|IO-TiO_2|$\mathbf{P1_x}$ electrodes after 4 h: product distribution (formate not detected in all cases), Co-based TONs (blue), Co surface loadings (as determined by ICP-OES, green) and anchor concentration (as determined by the known concentration of the phosphonic acid anchor in the $\mathbf{P1_x}$ immobilisation solution, red). The x-axis is presented on a $\log_{10}$ scale according to x ($\mathbf{P1_x}$). Product distribution from CPE of Ti|IO-TiO_2|$Co(BF_4)_2$ has been included for comparison. Conditions: 6:4 MeCN:H_2O (0.1 M $TBABF_4$), $E_{app} = -1.3$ V *vs.* Fc^+/Fc, CO_2-purged, room temperature.

Table 5.2 Summary of results obtained from 4 h of CPE of Ti|IO-TiO_2|$\mathbf{P1_x}$ with different Co loadings **x**: product quantities, Co-based TON, Faradaic efficiency cumulative over the 4 h period and product selectivity. CPE conditions: 6:4 MeCN:H_2O (0.1 M $TBABF_4$), $E_{app} = -1.3$ V *vs.* Fc^+/Fc, CO_2-purged, room temperature.

x ($\mathbf{P1_x}$)	**Product** (µmol cm^{-2})		**$\mathbf{TON_{Co}}$**		**FE** (%)	**Selectivity** (CO/H_2)
	CO	H_2	CO	H_2		
0.6	0.21 ± 0.02	0.13 ± 0.03	77.8 ± 8.4	48.1 ± 11.1	12.9 ± 3.3	1.6 ± 0.4
	Total = 0.34 ± 0.04		Total = 125.8 ± 13.9			
1	0.79 ± 0.11	0.25 ± 0.08	78.4 ± 13.3	24.8 ± 8.3	28.2 ± 6.3	3.2 ± 1.1
	Total = 1.04 ± 0.14		Total = 103.2 ± 16.7			
2	1.20 ± 0.05	0.34 ± 0.06	67.6 ± 11.1	19.1 ± 4.7	27.0 ± 4.0	3.5 ± 0.7
	Total = 1.54 ± 0.08		Total = 86.7 ± 14.5			
5	0.47 ± 0.08	0.094 ± 0.001	12.9 ± 2.2	2.57 ± 0.06	11.8 ± 0.7	5.0 ± 0.9
	Total = 0.56 ± 0.08		Total = 15.4 ± 2.2			

When considered together with the coordination equilibrium in the polymeric matrix shown using UV-vis and electroanalytical methods (see above), the CPE results suggest that the greatest Co-based activity (*i.e.* TON) can be achieved when Co centers are primarily in a bis(tpy) coordination environment (Fig. 5.9 and Table 5.2). As the population of mono(tpy) complexes increases with Co loading, TONs decrease, suggesting that Co mono(tpy) complexes in the polymeric matrix are less active towards CO_2 reduction under such conditions. Thus, in the case of Ti|IO-TiO_2|**P1$_1$** and Ti|IO-TiO_2|**P1$_2$**, a mixture of mono(tpy) and bis(tpy) environments results in a trade-off between absolute amount of product obtained [1.54 µmol cm^{-2} (Ti|IO-TiO_2|**P1$_2$**) > 1.04 µmol cm^{-2} (Ti|IO-TiO_2|**P1$_1$**)] or TON [103 (Ti|IO-TiO_2|**P1$_1$**) > 87 (Ti|IO-TiO_2|**P1$_2$**)] after 4 h. Notably, this observation that Co bis(tpy) complexes in the polymeric matrix are more active than mono(tpy) complexes at low overpotentials is in line with the previously discussed findings for immobilised Co bis(tpy) catalyst **CotpyP**.

Despite containing a greater Co loading, the Ti|IO-TiO_2|**P1$_5$** electrode produced far lower TONs than the other electrodes due to the predominantly mono(tpy) coordination. The low activity of this electrode is likely attributable to a minimal amount of Co bis(tpy) complexes that form after initial leaching of excess Co ions from the electrode. Such a transition was observed for FTO|IO-ITO|**P1$_2$** and FTO|IO-ITO|**P1$_5$** electrodes upon cycling in DMF-based electrolyte solutions, as discussed above. To quantify the loss of Co under relevant catalytic conditions, the Co loading was determined by ICP-OES for a FTO|IO-ITO|**P1$_5$** electrode before and after cycling to −1.3 V *vs.* Fc^+/Fc in 6:4 v:v MeCN:H_2O electrolyte solution. After 20 cycles, stable voltammograms were obtained and the Co loading on the cycled electrode decreased by 75 % relative to the pristine electrode (Table E.1). Finally, the inactivity of excess Co ions towards CO_2 reduction was confirmed by performing CPE with a bare TiO_2 electrode soaked in a $Co(BF_4)_2$ solution (Fig. 5.9). In this case, a large amount of H_2 and no CO was produced, confirming that the activity seen from Ti|IO-TiO_2|**P1$_5$** arose from only coordinated Co within the polymer matrix. Modest Faradaic efficiencies recorded for the Ti|IO-TiO_2|**P1$_x$** electrodes (Table 5.2) may be attributed to fundamental limitations of the Co bis(tpy) complex,[19] unproductive charge transfer pathways along the polymer backbone, as well as capacitive currents from TiO_2 charging and reduction of trapped O_2 within the mesoporous network.[21]

In summary, by modulating the Co loading and therefore the distribution of Co coordination environments within the polymeric matrix, the electrocatalytic activity towards CO_2 reduction could be tuned and optimised. In addition to

demonstrating the versatility of the polymer platform, these studies confirmed that predominantly Co bis(tpy) coordination favours catalysis, while highlighting the importance of striking the balance between total Co loading and active Co centres.

5.2.3 Tuneable Selectivity with Functional Co-Monomer

Electrochemical Characterisation and Electrocatalytic CO_2 Reduction

To take further advantage of this versatile platform for polymer synthesis, the methyl methacrylate monomer in **p1** was replaced with a long alkyl chain to yield the polymer **p2** (Fig. 5.1a). The n-decyl methacrylate monomer (**4**) was selected to provide a hydrophobic environment even more conducive towards selective CO_2 reduction over competing H^+ reduction (Fig. 5.1a).

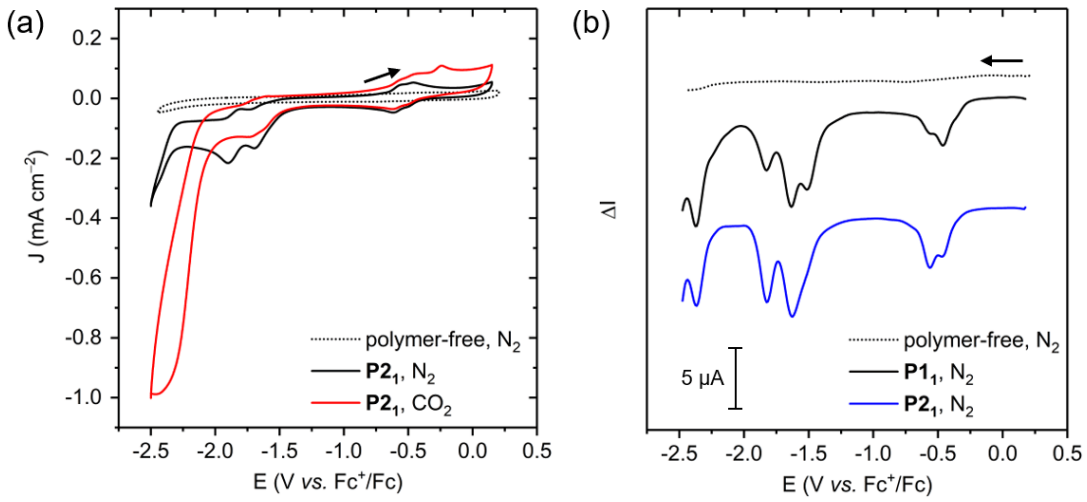

Fig. 5.10 (a) Cyclic voltammograms under N_2 and CO_2 atmosphere on a glassy carbon electrode in a 95:5 v:v DMF:H_2O (0.1 M $TBABF_4$) solution of $\mathbf{P2_1}$ (0.5 mM Co), 100 mV s^{-1}; (b) SW voltammogram under N_2 atmosphere and identical conditions to (a) for $\mathbf{P2_1}$ and $\mathbf{P1_1}$, cathodic scan beginning at 0.2 V *vs.* Fc^+/Fc. The response of a glassy carbon electrode in a polymer-free electrolyte solution under identical conditions is also shown. Arrows indicate scan starts.

The redox behaviour of the $\mathbf{P2_1}$ polymer is analogous to $\mathbf{P1_1}$, both in solution (Fig. 5.10) and immobilised on FTO|IO-ITO electrodes (Fig. 5.11). Cyclic and SW voltammograms of a 95:5 v:v DMF:H_2O solution of $\mathbf{P2_1}$ showed features for both Co-based redox processes (−0.3 to −0.7 V *vs.* Fc^+/Fc, $Co^{III/II}$; −1.4 to −1.7 V *vs.* Fc^+/Fc, $Co^{II/I}$), attributed to the Co bis(tpy) complex, and two ligand-based processes (−1.8 and −2.4 V *vs.* Fc^+/Fc), the first of which triggers catalysis

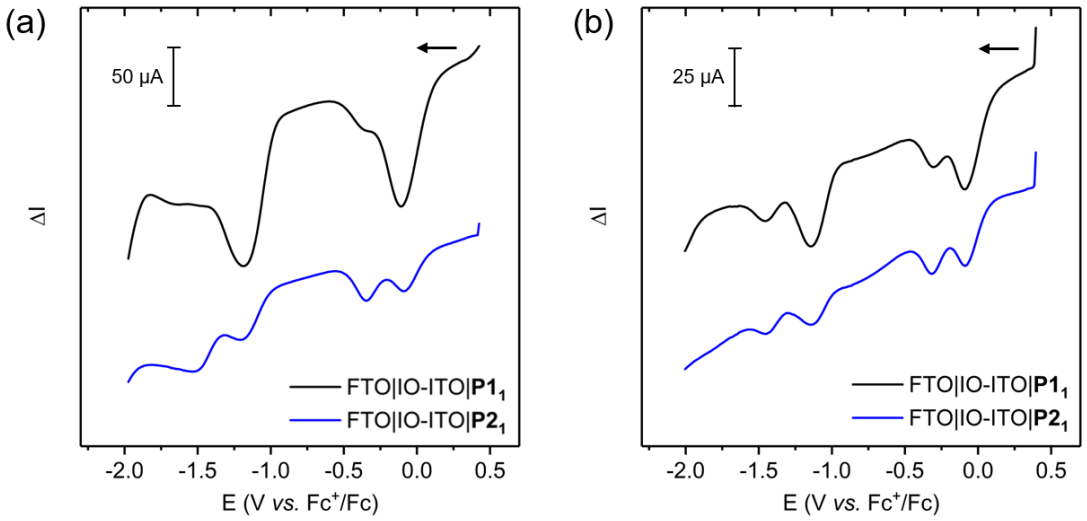

Fig. 5.11 SW voltammograms on the FTO|IO-ITO|**P1₁** and FTO|IO-ITO|**P2₁** electrodes in the cathodic direction at 100 mV s^{-1}, under N_2 atmosphere in (a) anhydrous DMF electrolyte solution (0.1 M $TBABF_4$), and (b) 95:5 v:v DMF:H_2O electrolyte solution (0.1 M $TBABF_4$). Arrows indicate scan starts.

in the presence of CO_2 (Fig. 5.10a). SW voltammograms of a FTO|IO-ITO|**P2₁** electrode in anhydrous DMF and 95:5 v:v DMF:H_2O electrolyte solutions also confirmed the bis(tpy) coordination on the electrode, with two waves associated with both $Co^{III/II}$ (0 to −0.5 V *vs.* Fc^+/Fc) and $Co^{II/I}$ (−1.1 to −1.6 V *vs.* Fc^+/Fc) couples (Fig. 5.11).

Upon immobilisation of **P2₁** onto Ti|IO-TiO_2 electrodes in the same manner as for the **P1ₓ** polymers, the CO_2 reduction activity of the resulting Ti|IO-TiO_2|**P2₁** cathodes indeed revealed a distinct difference in the product selectivity from **P2₁** compared to **P1₁** (Fig. E.5 and 5.12, Table 5.3). While the total product and TONs (the Co loading on Ti|IO-TiO_2|**P2₁**, as measured by ICP-OES, was within error to that of Ti|IO-TiO_2|**P1₁**; Table 5.1) were similar between the two polymers after 4 h of CPE, Ti|IO-TiO_2|**P2₁** produced significantly more CO and less H_2 than Ti|IO-TiO_2|**P1₁**, leading to a CO/H_2 ratio of 5.3 for the former compared to 3.2 for the latter. This difference is even greater at $t = 2$ h, when the selectivity ratio of Ti|IO-TiO_2|**P2₁** reaches 6.0, corresponding to a CO selectivity of 86 %. Once again, control experiments under N_2 produced no CO or H_2 (Fig. E.6) and isotopic labelling experiments confirmed CO_2 as the origin of CO (Fig. E.7). Furthermore, ATR-FTIR confirmed the preservation the molecular integrity of **P2₁**, both upon immobilisation and after CPE (Fig. 5.13).

The product selectivity achieved with **P2₁** is not only improved relative to that of **P1₁** but is also a stark improvement on the selectivity obtained with molecular

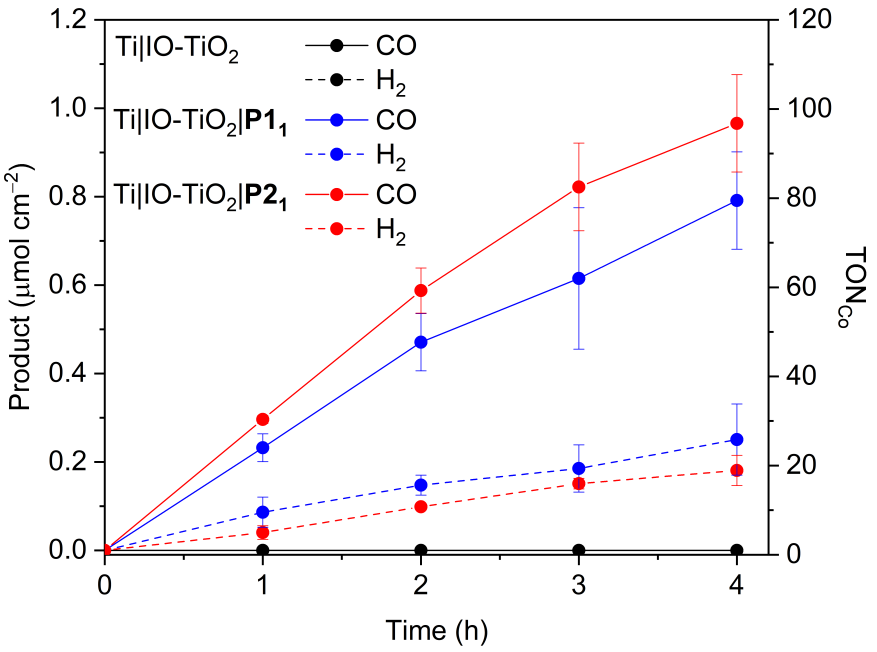

Fig. 5.12 Quantities and Co-based TONs of CO (solid lines) and H_2 (dashed lines) produced by Ti|IO-TiO_2, Ti|IO-TiO_2|**P1$_1$** and Ti|IO-TiO_2|**P2$_1$** under CPE. Conditions: 6:4 MeCN:H_2O (0.1 M $TBABF_4$), $E_{app} = -1.3$ V *vs.* Fc^+/Fc, CO_2-saturated conditions, room temperature.

Table 5.3 Controlled potential electrolysis results from Ti|IO-TiO_2|**P1$_1$** and TiO_2|**P2$_1$** electrodes after 4 h. CPE conditions: 6:4 MeCN:H_2O (0.1 M $TBABF_4$), $E_{app} = -1.3$ V *vs.* Fc^+/Fc, CO_2-purged, room temperature.

Polymer	**Product** (μmol cm^{-2})		**TON$_{Co}$**		**Selectivity** (CO/H_2)
	CO	H_2	CO	H_2	
P1$_1$	0.79 ± 0.11	0.25 ± 0.08	78 ± 13	25 ± 8	3.2 ± 1.1
	Total $= 1.04 \pm 0.14$		Total $= 103 \pm 17$		
P2$_1$	0.97 ± 0.11	0.18 ± 0.03	98 ± 11	18 ± 4	5.3 ± 1.2
	Total $= 1.15 \pm 0.12$		Total $= 116 \pm 12$		

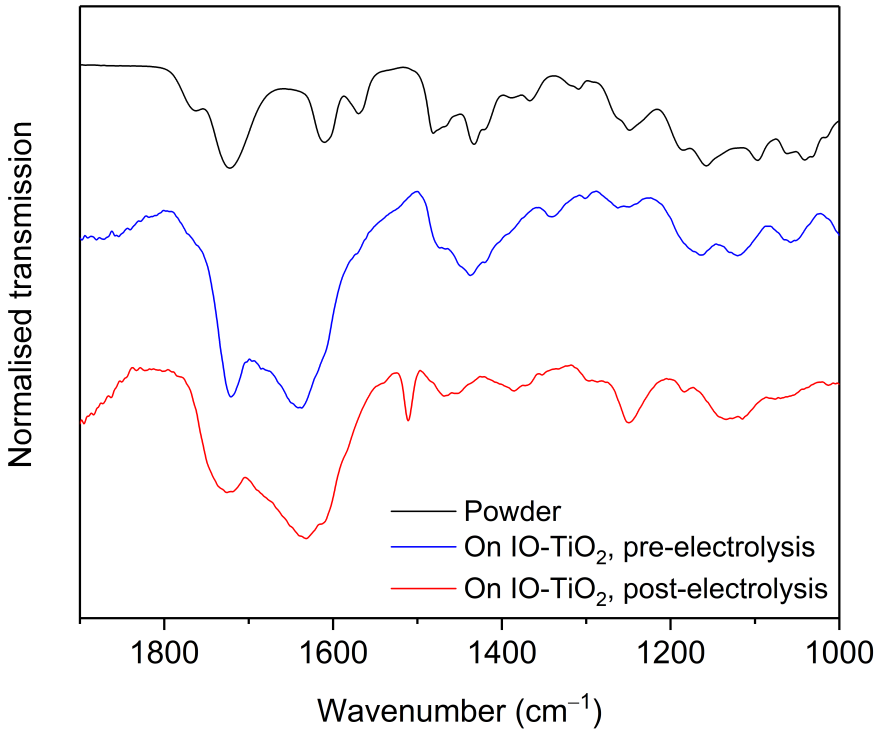

Fig. 5.13 ATR-FTIR spectra of **P2₁** as a powder (black trace), and after immobilisation on IO-TiO_2 before (blue trace) and after (red trace) 4 h CPE.

CotpyP, which produces CO at only 69 % selectivity ($CO/H_2 = 2.3$) on the same electrode (Fig. E.8). This is therefore a testament to the proof-of-principle that chemical modification in the outer coordination sphere of a molecular catalyst, by its incorporation into a rationally designed polymer matrix, is an effective strategy to improve performance without the need for severe synthetic modifications to the catalyst's primary ligand structure.[12,13] Moreover, in this case, product selectivity was gained, and not at the expense of other performance parameters like catalytic activity or stability.

Photoelectrocatalytic CO_2 Reduction on Si|IO-TiO_2

As **P2₁** was identified to be the most active polymer, a photocathode based on p-type silicon was fabricated with **P2₁** as the surface-immobilised catalyst to yield a CO_2-reducing hybrid photocathode. This was made possible by the previously-reported engineering of an inverse opal TiO_2 layer, which presents a high surface area for catalyst loading while interfacing with light-harvesting Si.[22] In order to protect the Si from surface passivation in the aqueous electrolyte solution, a ~4 nm thick TiO_2 layer was first deposited by ALD prior to deposition of IO-TiO_2.

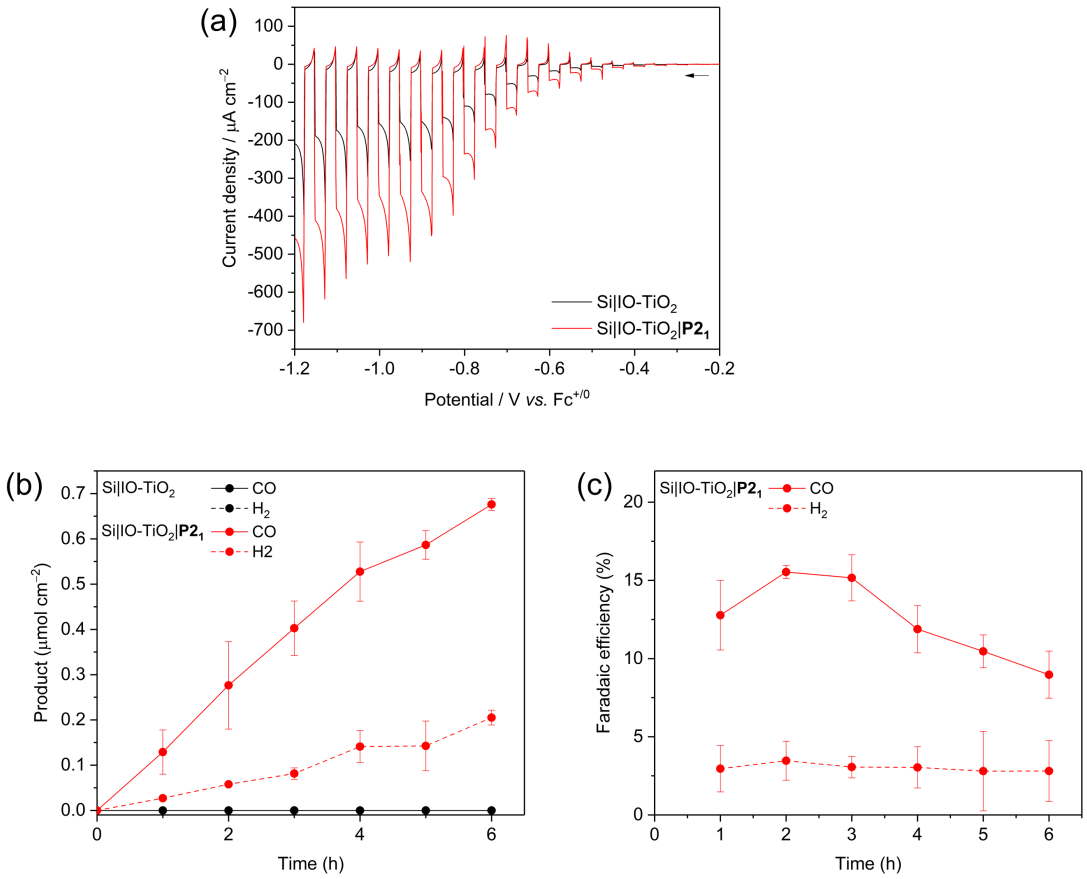

Fig. 5.14 (a) LSVs under chopped illumination of Si|IO-TiO_2 and Si|IO-TiO_2|**P2$_1$** photocathodes (arrow indicates scan start); (b) Product distribution and (c) Faradaic efficiency from CPPE of Si|IO-TiO_2 (product only) and Si|IO-TiO_2|**P2$_1$** at $E_{app} = -1.0\,V$ *vs.* Fc^+/Fc. Conditions: 1 Sun (AM1.5G, 100 mW cm^{-2}, $\lambda > 400$ nm), 6:4 MeCN:H_2O (0.1 M $TBABF_4$), CO_2-saturated conditions, room temperature.

Linear sweep voltammograms under chopped illumination were conducted on the resulting Si|IO-TiO_2|**P2$_1$** photocathode in the same electrolyte solution as that used for the Ti|IO-TiO_2|**P2$_1$** cathodes (CO_2-saturated 6:4 MeCN:H_2O, 0.1 M $TBABF_4$; Fig. 5.14a). A catalytic onset at -0.5 V *vs.* Fc^+/Fc and a photocurrent density of 450 µA cm^{-2} at -1.0 V *vs.* Fc^+/Fc were observed, the latter of which compares favourably to the 150 µA cm^{-2} achieved by a polymer-free Si|IO-TiO_2 control electrode.

Controlled potential photoelectrolysis at $E_{app} = -1.0$ V *vs.* Fc^+/Fc under simulated solar irradiation on Si|IO-TiO_2|**P2$_1$** produced CO at ∼80 % product selectivity with a low FE over 6 h (Fig. 5.14b-c). This low FE is coherent with the electrocatalysis results and highlights the need for a more inert or conductive polymer backbone and/or more efficient electron transfer between the surface and the polymer. The catalyst-free Si|IO-TiO_2 photoelectrode produced no CO or H_2, and neither did Si|IO-TiO_2|**P2$_1$** under a N_2 atmosphere.

5.3 Conclusion

In conclusion, rationally designed coordination polymers have been demonstrated as a versatile platform to achieve tuneable electrocatalytic CO_2 reduction in aqueous conditions. By first modulating the degree of crosslinking *via* Co loading in the polymer matrix, an equilibrium between mono(tpy) and bis(tpy) complexes was established that ultimately favours the more stable bis(tpy) complex and therefore electrocatalytic CO evolution. Second, the choice of the co-monomers was aimed towards the provision of an artificially engineered environment for the active Co bis(tpy) complex to improve CO_2 reduction selectivity. Selective CO production was ultimately demonstrated by the improvement of the H_2:CO product ratio from 1:2 (for the analogous molecular catalyst) to 1:6 for the polymer containing a hydrophobic alkyl chain conducive to CO_2 utilisation. The synergy of the polymer functionality with inverse opal electrode architectures was further demonstrated on Si|IO-TiO_2 photoelectrodes, where selective solar-driven CO_2 reduction was achieved. The strategy presented here calls for further development of catalyst-containing polymers with tailored functionality towards catalytic activity and selectivity, stability and charge transfer.

5.4 Experimental Section

5.4.1 Materials

All chemicals purchased from commercial suppliers were of the highest available purity and were used without further purification unless otherwise noted. FTO-coated glass sheets (SnO_2/F, 7 Ω sq^{-1} sheet resistance, 300 × 300 × 2 mm) were purchased from Sigma Aldrich, Ti foil (0.25 mM thick, 99.5 %) was purchased from Alfa Aesar, and *p*-type boron-doped silicon wafers (resistivity of 1-10 ohm cm; <100>; 500 µm thickness; single-side polished) were purchased from University Wafer. Polystyrene spheres (10 µm) were purchased from Polysciences Inc. and TiO_2 anatase nanoparticles (10-30 nm diameter, 99.5 %) were purchased from SkySpring Nanomaterials Inc. Methacryloyl chloride and $Co(BF_4)_2{\cdot}6H_2O$ were purchased from Alfa Aesar; 4'-hydroxy-2,2':6',2"-terpyridine was purchased from HetCat, Switzerland; bromotrimethylsilane, diethyl (hydroxymethyl) phosphonate, 2,2'-azobis(2-methylpropionitrile) (AIBN), methyl methacrylate (**3**) and n-decyl methacrylate (**4**) were purchased from Sigma Aldrich. $TBABF_4$ was purchased from Sigma Aldrich (≥ 99.0 %, electrochemical grade). All aqueous solutions were prepared with ultrapure Milli-Q® water (18.2 MΩ cm at 25 °C). $^{13}CO_2$ (> 99 atom % ^{13}C) was purchased from Sigma Aldrich. Dichloromethane (DCM), diethyl ether (Et_2O), tetrahydrofuran (THF), triethylamine (Et_3N), methanol (MeOH) and acetonitrile (MeCN) were distilled before use. Column chromatography was carried out over silica gel 60 (0.04-0.06 mm mesh, Material Harvest) or Sephadex™ LH-20 resin (18-111 µm, GE Healthcare). AIBN was recrystallised from MeOH prior to use and stored at −25 °C and in the absence of ambient light. Commercial methyl methacrylate (**3**) and n-decyl methacrylate (**4**) monomers were filtered over Al_2O_3 (90 standardised, Merck Millipore) prior to use to remove stabilisers.

5.4.2 Physical Characterisation

^1H, ^{13}C and ^{31}P NMR spectra were recorded on a Bruker 400 MHz or 500 MHz DCH cryoprobe spectrometer at room temperature. Chemical shifts for ^1H and ^{13}C NMR spectra are referenced to residual signals from the deuterated solvent. High-resolution mass spectra were recorded using a ThermoScientific Orbitrap Classic mass spectrometer. UV-vis spectra were collected using a Varian Cary 50 Bio UV-vis spectrometer with quartz cuvettes (Hellma, 1 cm path length). ATR-FTIR spectra were recorded on a Thermo Scientific Nicolet iS50 spectrometer. Elemental analysis was carried out by the Microanalysis Service of the Department

of Chemistry, University of Cambridge, using a Perkin-Elmer 240 Elemental Analyser. ICP-OES measurements were conducted by the Microanalysis Service of the Department of Chemistry, University of Cambridge, on a Thermo Scientific iCAP 7400 ICP-OES DUO spectrometer. The surface morphology of electrodes was analysed using a Tescan MIRA3 FEG-SEM. The weight-average molecular weight (M_w), number-average molecular weight (M_n) and polydispersity (PD) of the polymers were determined by gel permeation chromatography (GPC) in DMF (0.1 M LiBr, 2 mg mL^{-1} polymer), with a 0.7 mL min^{-1} flow rate and 100 µL injection volume, using a Shimadzu UFLC chromatograph at 65 °C with a SPD-M20A UV detector calibrated with polystyrene (PS) standards. Samples were filtered over 0.45 µm nylon filters prior to injection.

5.4.3 Synthesis and Characterisation of Monomers and Polymers

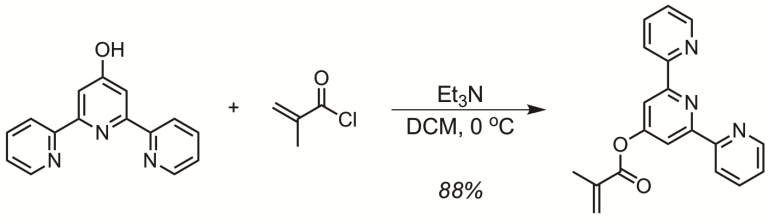

1

Compound 1. To a solution of 4'-hydroxy-2,2':6',2"-terpyridine (0.37 g, 1.5 mmol) and dry Et_3N (1.1 mL, 7.5 mmol) in 11 mL dry DCM at 0 °C under N_2 atmosphere, methacryloyl chloride (0.15 mL, 1.6 mmol) was added dropwise. The reaction mixture was stirred overnight and warmed from 0 °C to RT. The mixture was diluted with DCM and washed with 5 % $NaHCO_3$ (× 2), DI H_2O and saturated brine solution and dried over $MgSO_4$. The crude product was filtered and concentrated under reduced pressure. Purification by re-crystallisation and washing with cold ethyl acetate and hexane afforded the product as a white solid (0.419 g, 88 %) (m.p. 125 °C). ^{1}H NMR ($CDCl_3$, 400 MHz): δ/ppm = 8.69 (bm, 2H, py), 8.63 (bm, 2H, py), 8.30 (s, 2H, py), 7.87 (m, 2H, py), 7.34 (m, 2H, py), 6.41 (bm, 1H, CH_2), 5.82 (bm, 1H, CH_2), 2.09 (bm, 3H, CH_3). ^{13}C NMR ($CDCl_3$, 400 MHz): δ/ppm = 164.8, 160.2, 157.7, 155.5, 149.3, 137.1, 135.6, 128.3, 124.3, 121.5, 114.5, 18.5. HRMS (ESI, m/z) calculated for $C_{19}H_{15}O_2N_3$ $[M+H]^+$: 318.1237; found: 318.1234. EA (%) calculated for $C_{19}H_{15}O_2N_3$: C, 71.91; H, 4.76; N, 13.24; found: C, 71.63; H, 4.87; N, 12.99. ATR-FTIR σ/cm^{-1}: 1738 ($\nu_{C=O}$), 1637 ($\nu_{C=C}$), 1584 (ν_{py}), 1563 (ν_{py}).

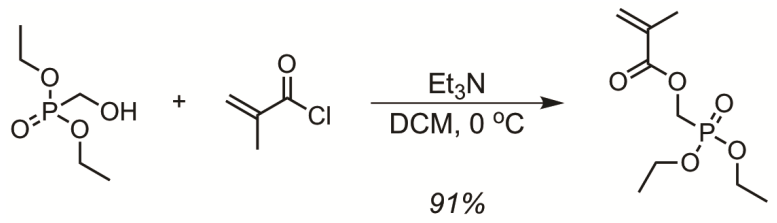

2

Compound 2. To a solution of diethyl (hydroxymethyl)phosphonate (1.61 mL, 10.9 mmol) and dry Et_3N (7.6 mL, 54.5 mmol) in 44 mL dry DCM at 0 °C under N_2 atmosphere, methacryloyl chloride (1.01 mL, 10.36 mmol) was added dropwise. The reaction mixture was stirred overnight and warmed from 0 °C to RT. The mixture was diluted with DCM and washed with 5 % $NaHCO_3$ (× 2), DI H_2O, and saturated brine solution and dried over $MgSO_4$. The product was filtered and concentrated under reduced pressure, affording a colourless oil (2.23 g, 91 %). The product was used without further purification. ^{1}H NMR ($CDCl_3$, 400 MHz): δ/ppm = 6.18 (bm, 1H), 5.64 (bm, 1H), 4.44 (d, J = 8.6 Hz, 2H), 4.18 (m, 4H), 1.97 (bm, 3H), 1.34 (t, J = 7.1 Hz, 6H). ^{13}C NMR ($CDCl_3$, 400 MHz): δ/ppm = 166.5, 135.4, 127.1, 62.9, 58.0, 56.4, 18.4, 16.6, 16.5. ^{31}P NMR (CD_2Cl_2, 400 MHz): δ/ppm = 18.6. HRMS (ESI, m/z) calculated for $C_9H_{17}O_5P$ $[M+H]^+$: 237.0886; found: 237.0879. EA (%) calculated for $C_9H_{17}O_5P$: C, 45.77; H, 7.25; found: C, 44.61; H, 7.40. ATR-FTIR σ/cm^{-1}: 1726 ($\nu_{C=O}$), 1638 ($\nu_{C=C}$), 1252 ($\nu_{P=O}$), 1018 (ν_{P-OR}).

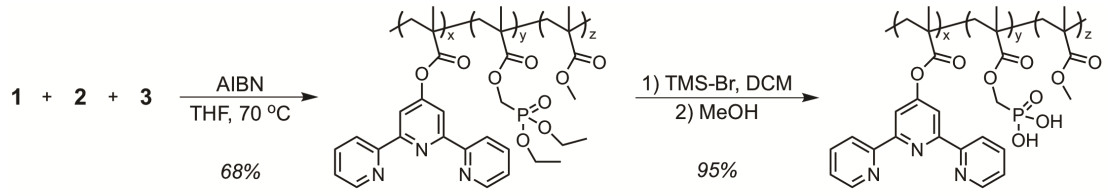

5 **p1**

Polymer 5. Compounds **1** (60 mg, 0.2 mmol), **2** (45 mg, 0.2 mmol) and AIBN (9 mg, 0.06 mmol) were transferred to a dry Schlenk flask under N_2 atmosphere. Dry THF (3.75 mL) was added to the flask with stirring, followed by **3** (20 µL, 0.2 mmol) dropwise; O_2 was finally removed from the mixture by three freeze-pump-thaw cycles. The flask warmed to RT and was transferred to a pre-heated oil bath at 70 °C with stirring overnight. After cooling to RT, the crude product in THF was concentrated to 1 mL and dropped into 50 mL hexane to precipitate the copolymer. The solid was filtered and washed with hexane and Et_2O to remove unreacted monomers. The product was isolated and dried under high vacuum,

affording a white solid (85 mg, 68 %). ^{1}H NMR ($CDCl_3$, 400 MHz): δ/ppm = 8.8-8.4 (bm, 4H), 8.4-8.2 (bs, 2H), 7.9-7.6 (bm, 2H), 7.4-7.1 (bm, 2H), 4.4-4.0 (bm, 7H), 3.7-3.5 (bm, 11H), 2.4-0.6 (bm, 36H). Molar monomer ratio (x:y:z) determined by integrating the ^{1}H NMR signals from aromatic tpy protons (8.8-7.1 ppm), **2** CH_2 protons (4.4-4.0 ppm) and **3** CH_3 protons (3.7-3.5 ppm): 1:1.1:3.6. ^{31}P NMR ($CDCl_3$, 400 MHz): δ/ppm = 18.8. EA (%) found: C, 60.88; H, 7.04; N, 4.89. ATR-FTIR σ/cm^{-1}: 1728, 1567,1403, 1246. GPC (PS standard, 2 mg mL^{-1} in DMF + 0.1 M LiBr): M_n = 2.11 kDa, PD = 3.98.

Polymer p1. To a solution of polymer **5** (40 mg) in 2 mL dry DCM at 0 °C under N_2 atmosphere, bromotrimethylsilane (16 µL, 0.1 mmol, 2.5 eq relative to the number of moles of phosphonate units in **5** using molar monomer ratios from ^{1}H NMR) was added dropwise. The reaction mixture was stirred overnight and warmed from 0 °C to RT. Dry MeOH (1 mL, 25 mmol) was then added directly to the reaction mixture at RT with stirring for 4 h. The crude product was concentrated and re-dissolved in a 1:1 v:v EtOH:DCM mixture and dropped into 50 mL hexane to precipitate the copolymer. The solid was filtered and washed with hexane. The product was isolated and dried under high vacuum, affording a light pink solid (38 mg, 95 %). ^{1}H NMR (CD_3OD, 400 MHz): δ/ppm = 9.2-7.8 (bm, 10H), 4.4-4.0 (bs, 2H), 3.9-3.5 (bm, 12H), 2.4-0.5 (bm, 40H). Molar monomer ratio (x:y:z) determined by integrating the ^{1}H NMR signals from aromatic tpy protons (9.2-7.8 ppm), phosphonic acid methylene CH_2 protons (4.4-4.0 ppm) and **3** CH_3 protons (3.9-3.5 ppm): 1:1:4. ^{31}P NMR (DMSO-d_6, 400 MHz): δ/ppm = 14.1. EA (%) found: C, 47.6; H, 5.77; N, 4.05. ATR-FTIR σ/cm^{-1}: 1722, 1593, 1429, 1266. GPC (PS standard, 2 mg mL^{-1} in DMF + 0.1 M LiBr): M_n = 3.3 kDa, PD = 1.60.

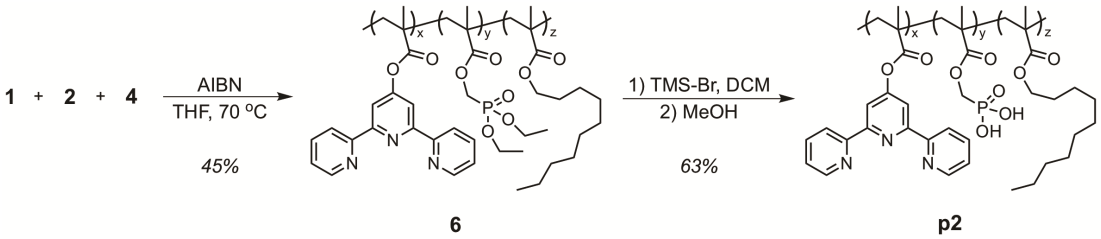

Polymer 6. Polymer **6** was synthesised according to the procedure for **5**, but with monomers **1** (45 mg, 0.1 mmol), **2** (34 mg, 0.1 mmol) and **4** (32 mg, 0.1 mmol) and AIBN (7 mg, 0.04 mmol). After cooling to RT, the crude product in THF was concentrated to ∼1 mL and dropped into 50 mL hexane to precipitate the copolymer. The solid was filtered and washed with hexane to remove unreacted monomers. The product was isolated and dried under high vacuum, affording a

white solid (50 mg, 45 %). ^{1}H NMR ($CDCl_3$, 400 MHz): δ/ppm = 8.8-8.1 (bm, 6H), 7.9-7.6 (bm, 2H), 7.4-7.0 (bm, 2H), 4.5-3.9 (bm, 8H), 2.5-0.5 (bm, 43H). Molar monomer ratio (x:y:z) determined by integrating the ^{1}H NMR signals from aromatic tpy protons (8.8-7.0 ppm), the 4.5-3.9 ppm region (6H per **2**, 2H per **4**) and the 2.5-0.5 ppm region (5H per **1**, 11H per **2**, 24H per **4**): 1:1:1.2. ^{31}P NMR ($CDCl_3$, 400 MHz): δ/ppm = 18.7. EA (%) found: C, 63.70; H, 7.11; N, 5.82. ATR-FTIR σ/cm^{-1}: 2922, 1728, 1565, 1402, 1251. GPC (PS standard, 2 mg mL^{-1} in DMF + 0.1 M LiBr): M_n = 2.1 kDa, PD = 2.19.

Polymer p2. The polymer **p2** was synthesised according to the procedure for **p1**, but with polymer **6** (40 mg) and 15 µL bromotrimethylsilane (0.1 mmol). The copolymer was precipitated upon the addition of excess MeOH, filtered, and washed with MeOH. The product was isolated and dried under high vacuum, affording a light pink solid (25 mg, 63 %). ^{1}H NMR (CD_2Cl_2/CD_3OD, 400 MHz): δ/ppm = 9.5-7.3 (bm, 10H), 4.5-3.9 (bm, 2H), 2.5-0.5 (bm, 38H). Molar monomer ratio (x:y:z) determined by integrating the ^{1}H NMR signals from aromatic tpy protons (9.5-7.3 ppm), the 4.5-3.9 ppm region (2H per **4**) and the 2.5-0.5 ppm region (5H per **1**, 5H per phosphonic acid, 24H per **4**): 1:1:1.2. ^{31}P NMR (DMSO-d_6, 400 MHz): δ/ppm = 13.8. EA (%) found: C, 50.0; H, 5.50; N, 5.14. ATR-FTIR σ/cm^{-1}: 2925, 1725, 1597, 1428, 1251. GPC (PS standard, 2 mg mL^{-1} in DMF + 0.1 M LiBr): M_n = 3.1 kDa, PD = 1.36.

Coordination of the polymers p1 and p2 with Co(II). The coordinated $\mathbf{P1_x}$ and $\mathbf{P2_1}$ copolymers were prepared by the addition of 1-2 mL dry MeOH to a flask, under N_2 atmosphere, containing a stoichiometric combination of the corresponding dry **p1** or **p2** copolymer scaffold and $Co(BF_4)_2{\cdot}6H_2O$, and stirred overnight. A portion of the reaction volume was removed and added to dry MeOH to give a final Co(II) concentration of 0.25 mM for immobilisation. This immobilisation solution was stored in the dark at RT. In the case of $\mathbf{P1_1}$ and $\mathbf{P21_1}$, the remaining reaction volume was dropped into an excess of Et_2O to precipitate the coordinated copolymer. The solid was filtered, washed with Et_2O, and dried under high vacuum to yield the coordinated copolymer as a red-brown powder.

CotpyP. CotpyP was synthesised according to the procedure described in Chapter 3 section 3.4.3.

5.4.4 Assembly of Electrodes

Fabrication of FTO|IO-ITO Electrodes

FTO|IO-ITO electrodes were fabricated according to a previously-reported procedure.[18]

Fabrication of Ti|IO-TiO_2 Electrodes

A mixed dispersion of TiO_2 anatase nanoparticles (10-30 nm diameter) and polystyrene beads (750 nm diameter, 2.54 % w/v suspension in water) was prepared as follows: TiO_2 anatase nanoparticles (36 mg) were dispersed by sonication in a water/MeOH mixture (4:1 v:v) (346 µL) for 2 h using a Bandelin Sonorex Digiplus sonicator. The dispersion of polystyrene spheres (1000 µL) was centrifuged, the supernatant removed, and the polystyrene pellet re-dispersed in MeOH (1000 µL). The polystyrene dispersion was centrifuged again, the supernatant removed, and the dispersion of TiO_2 nanoparticles added to the polystyrene pellet. The mixture was further diluted by the addition of the water/MeOH mixture (4:1 v:v) (346 µL) and then vortexed and sonicated for 5 min in ice-cold water ($< 5\,^{\circ}C$) to give the polystyrene–TiO_2 dispersion, which was used immediately. The Ti foil (7 × 12 × 0.25 mm) was sonicated sequentially in isopropanol and ethanol for 30 min. A parafilm ring was placed onto the substrate to define the geometrical surface area for the IO-TiO_2 films, and the polystyrene–TiO_2 dispersion was drop-cast onto this pre-defined area. An amount of 5 µL of the described polystyrene–TiO_2 dispersion on a 0.28 cm^2 geometrical surface area corresponds to a 15 µm thick IO-TiO_2 structure. The electrode was allowed to dry for at least 4 h before the parafilm was removed. The electrodes were heated in a Carbolite furnace at a rate of $1\,^{\circ}C\,min^{-1}$ from room temperature to 500 °C and annealed at this temperature for 20 min before slowing cooling down to room temperature.

Fabrication of Si|IO-TiO_2 Electrodes

The Si|IO-TiO_2 photoelectrodes were prepared in two steps - atomic layer deposition of a thin TiO_2 layer followed by deposition of an inverse opal TiO_2 layer – according to previously-described procedures.[22]

First, the Si wafer were cleaned in isopropanol, dried under a N_2 airflow, etched for 2 min in buffered oxide etch (6:1 v:v of 40 % NH_4F in water and 49 % HF), rinsed in water and dried under N_2. The wafer was loaded at 60 °C into the

ALD chamber (Cambridge Nanotech Savannah S100 G1), which was immediately evacuated to prevent oxide formation, before being ramped to 200 °C. TiO_2 was deposited in a multi-pulse mode at 200 °C as described in detail previously.[23] Titanium(IV) isopropoxide (TTIP), volatilised at 90 °C, was used as the precursor and DI H_2O vapour as the oxidant. Both TTIP and H_2O doses were set equally at 1.45-1.65 Torr·s. The precursor and oxidant were delivered sequentially to the reaction chamber separated by 15 s of purging with 20 sccm of N_2 to prevent a CVD-like reaction. TTIP was pulsed first in the sequence to minimise any initial oxidation. The total number of cycles was set to 115 to achieve an atomic layer deposition of approximately 4 nm thick TiO_2 layers.

The IO-TiO_2 layer was assembled on top of the Si|ALD-TiO_2 surface (1 cm × 2 cm) following a previously reported co-assembly procedure for hierarchical indium tin oxide.[18] Briefly, TiO_2 nanoparticles (P25, 36 mg) were dispersed by sonication in a 4:1 v:v MeOH:H_2O mixture (360 µL) for 3 h. A dispersion of polystyrene beads (1.2 mL; 2.54 % w/v suspension in water; 750 nm bead diameter) was centrifuged to remove the supernatant. The P25 nanoparticle solution was added to the polystyrene pellet, and sonicated for 5 min in ice-cold water (< 5 °C) to give the polystyrene-P25 dispersion. This dispersion (5 µL) was drop-cast onto the Si|TiO_2 surface (0.178 cm^2 geometrical surface area) to fabricate a 10 µm thick IO-TiO_2 layer. The electrodes were sintered at 450 °C for 2 h under an Ar atmosphere (ramping rate 1 °C min^{-1} from room temperature).

Assembly of FTO|IO-ITO|-, Ti|IO-TiO_2|- and Si|IO-TiO_2|polymer electrodes

Immobilisation of all polymers on all types of electrodes was carried out by soaking the electrodes in a methanolic solution of the respective polymer (prepared by the dropwise addition of a MeOH solution of either **p1** or **p2** to a MeOH solution of $Co(BF_4)_2{\cdot}6H_2O$ to give a final Co concentration of 0.25 mM) for 16 h. In the case of the metal-free control experiment, a MeOH solution of the polymer in the absence of the Co salt (with the polymer in the same concentration as was used for the metal-complexed solution) was used to sensitise the electrodes instead. In the case of Ti|IO-TiO_2- and Si|IO-TiO_2-based electrodes, the (photo)cathodes were subsequently back-contacted and insulated by an epoxy adhesive prior to further use. Sand paper was used to abrade the surface of the electrode's back side before application of a conductive silver paint (RS® Components 186-3593), after which an electrical wire was connected to the dry silver using the same conductive silver paint. Upon drying, an off-white opaque epoxy adhesive (Loctite® EA 9466)

was applied on both sides of the electrodes, leaving only the photoactive surface ($S \approx 0.1$-$0.2\,\mathrm{cm}^2$) exposed. The cells were allowed to dry thoroughly for 40 h in air before use.

Quantification of Catalyst Loading

The quantification of the amount of immobilised polymer (mole Co per geometrical area) on the electrodes was evaluated in triplicate by ICP-OES after digestion of the electrodes ($\approx 0.56\,\mathrm{cm}^2$ film area for Ti|IO-TiO_2 and $0.28\,\mathrm{cm}^2$ film area for FTO|IO-ITO) in aqueous HNO_3 (70 %) overnight and dilution to 2 % v/v with Milli-Q® water.

5.4.5 Electrochemical Methods

General Methodology

Electrolysis experiments were performed on an Ivium CompactStat potentiostat and CV and SWV experiments were performed on a BioLogic VSP potentiostat. A three-electrode configuration was employed in an airtight cell, with a Pt mesh CE and a Ag/AgCl RE in an electrolyte solution of the same composition as that used for all dry DMF and mixed DMF:H_2O and MeCN:H_2O experiments. The potential of the RE was referenced daily against the ferrocene/ferrocenium couple (Fc^+/Fc) in the corresponding electrolyte solution. The supporting electrolyte was $TBABF_4$ (0.1 M) in all electrolyte solutions. All electrochemical measurements were performed at room temperature.

Dark Electrochemical Characterisation

Cyclic and square wave voltammetry experiments were performed in the cell described above with either a glassy carbon WE, or a polymer-free (blank) or polymer-modified FTO|IO-ITO WE. The electrolyte solution was purged with either N_2 or CO_2 for 20 min to remove atmospheric O_2 and saturate the solution. For SWV, scans proceeded in the cathodic direction from the positive potential limit after a 30 s equilibration time. For CV, scans began as indicated in each figure, either (i) at the open circuit potential and initially proceeded in the anodic direction to the positive potential limit, or (ii) at the positive potential limit and in the cathodic direction during sequential SWV-CV studies. For solution-based experiments, the isolated $\mathbf{P1_1}$ and $\mathbf{P2_1}$ copolymers were re-dispersed in a mixture

of DMF and DI H_2O (95:5 v:v DMF:H_2O), with 0.1 M $TBABF_4$, at 0.5 mM Co(II) concentration.

(Photo)Electrocatalytic Studies

Controlled potential electrolysis was performed on Ti|IO-TiO_2-based electrodes as the working electrodes in the dark, while LSVs and controlled potential photoelectrolysis under simulated solar irradiation were performed on Si|IO-TiO_2-based electrodes as the working electrodes. Custom-made airtight two-compartment electrochemical cells with a glass frit to separate the compartments were employed for all experiments. A Newport Oriel Xenon 150 W solar light simulator (100 mW cm^{-2}, AM1.5G containing IR water and UV ($\lambda > 400$ nm) filters) was used as the light source for photoelectrocatalytic studies on Si|IO-TiO_2-based electrodes. LSVs were conducted at a scan rate of 5 mV s^{-1} with chopped light alternating between dark and light every 5 s. The catalytic onset potential is defined as the potential at which a photocurrent density of $|J| = 5$ µA cm^{-2} was achieved by the respective electrode. The applied potential during CP(P)E was -1.3 V *vs.* Fc^+/Fc or -1.0 V *vs.* Fc^+/Fc for Ti|IO-TiO_2- or Si|IO-TiO_2-based electrodes, respectively. For CPPE, continuous illumination was maintained, apart from hourly dark chops lasting for 2 min each.

Product Quantification

Prior to all (photo)electrochemical experiments, the electrolyte solution in both compartments of the photoelectrochemical cell was purged with CO_2 containing 2 % CH_4 as an internal standard for gas chromatography (GC) measurements; the only exception was in the case of N_2 atmosphere control experiments, where the solution was purged with N_2 containing 2 % CH_4. The amount of gaseous CO and H_2 produced was analysed by headspace gas analysis using a Shimadzu Tracera GC-2010 Plus with a barrier discharge ionisation detector (BID). The GC was equipped with a ShinCarbon micro ST column (0.53 mm diameter) kept at 40 °C using helium carrier gas. Aliquots (50 µL) of the headspace gas were removed for GC analysis at regular time intervals. Formic acid was analysed by ion chromatography using a Metrohm 882 compact IC plus ion chromatography system but any amount produced was found to be below the detection limit. The Faradaic efficiency of the cathodes was calculated by comparing the expected amount of total product as indicated by the total charge passed through the electrode and the actual amount produced. Analytical measurements were performed in triplicate

and the standard deviation of each data point is given in the tables and denoted by error bars in the graphs.

Isotopic Labelling Studies

CP(P)E of Ti|IO-TiO_2|$\mathbf{P1_1}$ and Ti|IO-TiO_2|$\mathbf{P2_1}$ electrodes were performed with $^{13}CO_2$ as the headspace gas. After 4 h, the electrochemical cell headspace was transferred to an evacuated gas IR cell (SpecAc, 10 cm path length, equipped with KBr windows) and a high-resolution transmission spectrum was collected on a Thermo Scientific Nicolet iS50 FT-IR spectrometer.

5.5 References

(1) Herron, J. A.; Kim, J.; Upadhye, A. A.; Huber, G. W.; Maravelias, C. T. *Energy Environ. Sci.* **2015**, *8*, 126–157.

(2) Can, M.; Armstrong, F. A.; Ragsdale, S. W. *Chem. Rev.* **2014**, *114*, 4149–4174.

(3) Armstrong, F. A.; Hirst, J. *Proc. Natl. Acad. Sci.* **2011**, *108*, 14049–14054.

(4) Takeda, H.; Cometto, C.; Ishitani, O.; Robert, M. *ACS Catal.* **2017**, *7*, 70–88.

(5) Francke, R.; Schille, B.; Roemelt, M. *Chem. Rev.* **2018**, *118*, 4631–4701.

(6) Reuillard, B.; Ly, K. H.; Rosser, T. E.; Kuehnel, M. F.; Zebger, I.; Reisner, E. *J. Am. Chem. Soc.* **2017**, *139*, 14425–14435.

(7) Wang, M.; Chen, L.; Lau, T. C.; Robert, M. *Angew. Chem. Int. Ed.* **2018**, *57*, 7769–7773.

(8) Tian, H. *ChemSusChem* **2015**, *8*, 3746–3759.

(9) Willkomm, J.; Orchard, K. L.; Reynal, A.; Pastor, E.; Durrant, J. R.; Reisner, E. *Chem. Soc. Rev.* **2016**, *45*, 9–23.

(10) Rosser, T. E.; Reisner, E. *ACS Catal.* **2017**, *7*, 3131–3141.

(11) Sahu, S.; Cheung, P. L.; Machan, C. W.; Chabolla, S. A.; Kubiak, C. P.; Gianneschi, N. C. *Chem. Eur. J.* **2017**, *23*, 8619–8622.

(12) Kramer, W. W.; McCrory, C. C. *Chem. Sci.* **2016**, *7*, 2506–2515.

(13) Reuillard, B.; Warnan, J.; Leung, J. J.; Wakerley, D. W.; Reisner, E. *Angew. Chem. Int. Ed.* **2016**, *55*, 3952–3957.

(14) Elgrishi, N.; Chambers, M. B.; Artero, V.; Fontecave, M. *Phys. Chem. Chem. Phys.* **2014**, *16*, 13635–13644.

(15) Elgrishi, N.; Chambers, M. B.; Wang, X.; Fontecave, M. *Chem. Soc. Rev.* **2017**, *46*, 761–796.

(16) Enachescu, C.; Krivokapic, I.; Zerara, M.; Real, J. A.; Amstutz, N.; Hauser, A. *Inorg. Chim. Acta* **2007**, *360*, 3945–3950.

(17) Judge, J. S.; Baker, W. A. J. *Inorg. Chim. Acta* **1967**, *1*, 239–244.

(18) Mersch, D.; Lee, C. Y.; Zhang, J. Z.; Brinkert, K.; Fontecilla-Camps, J. C.; Rutherford, A. W.; Reisner, E. *J. Am. Chem. Soc.* **2015**, *137*, 8541–8549.

(19) Elgrishi, N.; Chambers, M. B.; Fontecave, M. *Chem. Sci.* **2015**, *6*, 2522–2531.

(20) Elgrishi, N.; Griveau, S.; Chambers, M. B.; Bedioui, F.; Fontecave, M. *Chem. Commun.* **2015**, *51*, 2995–2998.

(21) Leung, J. J.; Warnan, J.; Nam, D. H.; Zhang, J. Z.; Willkomm, J.; Reisner, E. *Chem. Sci.* **2017**, *8*, 5172–5180.

(22) Nam, D. H.; Zhang, J. Z.; Andrei, V.; Kornienko, N.; Heidary, N.; Wagner, A.; Nakanishi, K.; Sokol, K. P.; Slater, B.; Zebger, I.; Hofmann, S.; Fontecilla-Camps, J. C.; Park, C. B.; Reisner, E. *Angew. Chem. Int. Ed.* **2018**, *57*, 10595–10599.

(23) Aria, A. I.; Nakanishi, K.; Xiao, L.; Braeuninger-Weimer, P.; Sagade, A. A.; Alexander-Webber, J. A.; Hofmann, S. *ACS Appl. Mater. Interfaces* **2016**, *8*, 30564–30575.

Chapter 6

Conclusions

6.1 Summary

The aim of this thesis was to develop molecular photocathodes towards solar fuel synthesis in aqueous conditions using only Earth-abundant components, both as a means towards low-cost photoelectrochemical devices and also as a platform from which to demonstrate and explore the benefits of molecular catalyst surface immobilisation.

First, the fabrication of a functional, versatile *p*-silicon|mesoporous titania (Si|*meso*TiO_2) photoelectrode was established. The function of the mesoporous TiO_2 is multi-fold: (i) to stabilise Si against severe SiO_x formation in the presence of air and water, which would have otherwise eventually rendered the photoelectrode inactive, (ii) to provide a high-surface-area scaffold capable of simultaneously loading a large amount of molecular catalyst, and (iii) to act as an electron-selective conduit between the underlying light harvester and the surface-immobilised catalyst. The Si|*meso*TiO_2 electrode was prepared using a simple doctor-blading method immediately following HF-etching of the Si wafer, followed finally by a multi-step sintering process under air. Despite the lack of more complex deposition methods and exposure to air during annealing, this method proved effective at maintaining a stable connection between the Si and TiO_2, as evidenced by the photoelectrode's constant photovoltage of $+0.4\,V$ *vs.* RHE and an analogous TiO_2-free Si electrode being inactive after treatment under similar conditions.

The metal oxide nature of TiO_2 lends itself well to anchoring by functional groups such as acids. In our case, phosphonic acid-functionalised molecular catalysts featured throughout this thesis as a consequence of both readily available

coordination complexes as well as the superior stability that phosphonates afford under slightly acidic operating conditions over carboxylates. Beginning with H_2 evolution, a DuBois-type catalyst, **NiP**, and a cobalt diimine-dioxime catalyst, **CoP³** – both of which bear phosphonic acid moieties – were immobilised on Si|*meso*TiO_2 to yield the corresponding photoelectrodes. Both molecular photocathodes performed in pH 4.5 aqueous conditions to the same (if not slightly better) degrees as their solution-based counterparts in the literature, and represent the first reports of molecular-based proton-reducing photocathodes on Si operating in water. Moreover, Si|*meso*TiO_2|**NiP** was found to be active for over 24 h, yielding a turnover number of ∼1000 and a Faradaic efficiency nearing 90 %, setting a new benchmark for molecular H_2 evolution photocathodes and making it the best-performing system for an immobilised DuBois-type catalyst in terms of photocurrents and TONs. The biocompatibility of TiO_2 as a material and the versatility of the photoelectrode scaffold was further demonstrated by incorporation of a naturally-occurring [NiFeSe]-hydrogenase enzyme onto Si|*meso*TiO_2. This photocathode also displayed high photocurrents and Faradaic efficiencies but was ultimately limited by the mismatch in size between the enzyme and the electrode's pores, which led to enzyme desorption and therefore unsustainable activity beyond a couple of hours.

An interesting, unforeseen phenomenon that was observed with the Si|*meso*TiO_2 motif was a charging up behaviour, whereby it appears that photogenerated electrons can remain relatively long-lived (on the order of several minutes) in the conduction band of TiO_2 when in the absence of an efficient catalyst at the surface. The charging up and discharging of the TiO_2 CB was studied by multiple electrochemical techniques, including a comparison between catalyst-free and catalyst-modified electrodes, and the deliberate addition of an electron acceptor into solution in order to observe a forced discharge of the TiO_2 CB. These experiments demonstrated that the well-known ability of *meso*TiO_2 to trap electrons can be exploited in our Si|*meso*TiO_2 architecture, representing the first application of this phenomenon *via* the fabrication of a device capable of storing visible light-generated electrons on an electrode. The realisation of these long-lived electrons following photoexcitation of the Si|*meso*TiO_2 electrode could allow one to envision devices that are capable of temporal decoupling between the photo-production of the electric charge and its utilisation in the form of electricity or chemical synthesis.

Having demonstrated the robustness and versatility of the Si|*meso*TiO_2 architecture, we took this platform further and developed a CO_2 reduction pho-

tocathode using a previously-unreported, phosphonic acid-modified cobalt(II) bis(terpyridine) electrocatalyst, **CotpyP**. **CotpyP** can be synthesised in a simple one-step self-assembly process combining a Co(II) salt and the phosphonate-containing terpyridine ligand, the resulting solution of which can be used to directly modify an immersed electrode. Si|*meso*TiO_2|**CotpyP** represents the first molecular photocathode free of precious metal components in any conditions (organic and aqueous alike). This photocathode was found to perform CO_2 reduction in MeCN:H_2O mixtures of varying ratios with selectivity primarily for CO_2 reduction products (CO and formate), where a 6:4 v:v MeCN:H_2O ratio was found to yield the optimum performance (TON = 381, FE = 77 %, lasting for > 24 h), setting a new benchmark for molecular CO_2 photocathodes. Several explanations were given to rationalise why such an optimum at median water concentrations was observed; these include a shifting thermodynamic landscape where $E^{\circ\prime}(CO_2/CO)$ changes with MeCN:H_2O ratios, CO_2 solubility and hence availability in MeCN *vs.* in H_2O, and effects at the TiO_2|electrolyte interface (band-bending, H^+ concentration *etc.*). These reasons go further to explain why the observed activity and product selectivity worsened upon switching to purely aqueous conditions. Nevertheless, despite improvements in performance being possible, the achievement of CO_2 reduction in 100 % water with a precious metal-free photocathode is in itself a significant milestone.

An in-depth mechanistic investigation was thereafter launched in response to two observations: (i) the apparent energy mismatch between the photovoltage deliverable by the Si|*meso*TiO_2 electrode and the catalytic overpotential required of solution-based cobalt bis(terpyridine)s reported in the literature, and (ii) the molecular integrity of **CotpyP** on our photoelectrode even after long-term photoelectrocatalysis. These findings are at odds with literature precedence, which suggests the need to lose an entire equivalent of terpyridine to form the mono(terpyridine) species that thereafter catalyses CO_2 reduction at potentials negative enough to reduce the ligand. A mixture of (spectro)electrochemical techniques were employed on surface-immobilised **CotpyP** to investigate this discrepancy. All results confirmed the retention of the metal complex's bis(terpyridine) ligation even after being subject to catalytic conditions. Crucially, evidence pointed towards a small change in the structure of the catalyst that both maintained this bis(terpyridine) symmetry and also responded to changes in the water content of the solution. Direct evidence that this change is located at the phosphonic acid moiety of the catalyst was given by spectroelectrochemical IR, ultimately leading to a proposed mechanism that is in sharp contrast to that for reported Co bis(terpyridine)s in solution (homogeneous conditions). Namely, in our case, the

loss of a terpyridine is apparently unnecessary, as protonation of the phosphonic acid results in an internal proton source that yields a pyridinium capable of stabilising an open coordination site at the Co metal centre for the approach of CO_2. This mechanism is seemingly possible as a result of both having the in-built acid in close proximity to the Co centre, as well as immobilising the catalyst in the first place in order to access a sufficient concentration of protons in water-rich solutions. Ultimately, this led to the aforementioned earlier catalytic onset and better electrocatalytic performances, while enabling aqueous CO_2 reduction with our hybrid photocathode.

Finally, with the aim of demonstrating that catalyst performance can be influenced without directly modifying its primary coordination sphere, we took this work with **CotpyP** further by rationally designing polymers that incorporate three elements in their co-monomers: (i) the cobalt bis(terpyridine) motif as the CO_2 reduction catalytic centre, (ii) a phosphonic acid moiety to anchor onto metal oxide surfaces, and (iii) an additional functional group to induce variations in the catalyst's outer coordination sphere environment. These polymers were immobilised on inverse opal-type electrodes designed specifically to accommodate large molecules. First, the ability to modulate cross-linkage of the polymer scaffold with varying populations of mono(terpyridine) and bis(terpyridine) populations and subsequently tune its electrocatalytic performance was demonstrated. Second, the rational design of the polymer's functional group was also aimed towards the provision of an artificial environment for the active complex that would influence product selectivity, which was ultimately demonstrated by the improvement of a H_2:CO product ratio of 1:2 (molecule) to 1:6 (polymer). The best performing polymer was also immobilised on a Si|inverse-opal TiO_2 scaffold and was demonstrated to be able to achieve solar-driven, selective CO_2 reduction.

In conclusion, we set out to demonstrate that molecular photocathodes that are stable and efficient in aqueous conditions towards reductive solar fuel synthesis can be achieved in a straightforward manner. In addition to achieving this milestone and setting new literature benchmarks for photocathode performance along the way, intriguing insights were also made with respect to influences on mechanistic pathways that might have only come about as a consequence of surface-immobilising these catalysts. The scope for further improvement in device performance by means of influencing its external environment rather than the catalytic core itself was also demonstrated.

6.2 Outlook

There continues to be great scope for the continued development of precious metal-free molecular photocathodes towards solar fuel synthesis. Going forward, we can envision several areas of improvement that would benefit overall performance.

While p-type silicon has proven to be a profitable choice as an Earth-abundant light-harvesting material in the work described in this thesis, one of its primary limitations arises from one of its strengths: its relatively small energy band gap enables its utilisation of long-wavelength photons – even in the infrared – but ultimately results in a relatively positive conduction band potential and therefore a small photovoltage. The low-cost method by which we chose to deposit the TiO_2 interlayer under aerobic conditions also likely contributed to the low photovoltage of the resulting photoelectrode. Although this sufficed for the molecular catalysts that were employed in this thesis, it will limit the scope of catalysts that can be used with the Si|TiO_2 scaffold, especially for CO_2 reduction, where some of the most recently published state-of-the-art molecular catalysts require overpotentials that our electrode would be unable to deliver. We could therefore envision a similarly simple approach towards utilising semiconductors with larger band gaps (*e.g.* Cu_2O), where surface stabilisation against aqueous conditions and the presentation of a high surface area scaffold may also be achieved in one step as they were in this work.

Another key area of improvement would be the CO_2 reduction performances of these devices in pure water – in terms of both absolute activity and product selectivity. The reasons suspected to explain the less-than-optimal performance of Si|*meso*TiO_2|**CotpyP** in pure water have already been discussed, and may serve as launching points from which to design better systems. One way in which we tried to do this was to use a polymer matrix that both embedded the catalyst as well as provided a hydrophobic environment for it, which led to improved product selectivity for CO_2 reduction products. This strategy presents endless possibilities for future work, where one might envision the incorporation of several other functionalities in the system simply by assigning a co-monomer to impart each of these desired properties. Options include proton relays to help both proton reduction mechanisms and proton-dependent CO_2 reduction mechanisms; light-absorbing molecules (*e.g.* a dye) to yield an "in-house" light harvester in the polymer; and other moieties like amines that would serve to entrap CO_2 directly in the vicinity of the catalyst. However, in order to realise the full potential that catalyst-embedding polymers can offer, the electrode-polymer interface needs to

be improved. The low Faradaic efficiencies we observed in our CO_2-reducing metal oxide-polymer cathodes were the most significant bottleneck towards achieving higher performances. Therefore, working towards understanding and addressing this would be an obvious first step towards more elegant, optimised systems.

Appendix A

General Data Analysis Methods

The methods used to treat and analyse data throughout this thesis are outlined in this Appendix.

A.1 Data Treatment

Throughout this thesis, analytical measurements have been performed in triplicate, most notably when quantifying the amount of product obtained from (photo)electrocatalysis. The data were treated as follows to give the mean and standard deviation for each data point.

For a sample of j observations x_{i} (where typically $j = 3$), the unweighted mean value, x_0, was calculated using the equation

$$x_0 = \sum_{i=1}^{j} \frac{x_{\mathrm{i}}}{j} \tag{A.1}$$

and the standard deviation, σ, was calculated using the equation:

$$\sigma = \sqrt{\sum_{i=1}^{j} \frac{(x_{\mathrm{i}} - x_0)^2}{(j-1)}} \tag{A.2}$$

A.2 Gas Product Quantification

Throughout this thesis, GC was used to quantify the amount of gaseous product (H_2 and/or CO) produced. The GC trace gives peaks for the product(s) produced, alongside peaks for N_2 or CO_2 (depending on which was the purging gas used) and the internal standard, CH_4. The amount of product produced was quantified by comparison to the CH_4 internal standard using the calculation below.

The molar quantity of the produced gas (n_x, where $x = H_2$ or CO) can be calculated using the relative integration areas of the product gas (A_x) and the internal standard (A_{CH_4}), the fixed molar quantity of the internal standard purged into the photoelectrochemical vessel prior to the experiment (n_{CH_4}), and the GC instrument's calibrated response factor of the product gas relative to the internal standard (RF_x):

$$n_x = \frac{A_x}{A_{CH_4}} \cdot \frac{1}{RF_x} \cdot n_{CH_4} \tag{A.3}$$

The molar quantity of the CH_4 internal standard (present always in the vessel at 2 % as a result of the gas cylinders used for purging), n_{CH_4}, can be estimated using the ideal gas law and knowledge of the electrochemical vessel's gas headspace volume, $V_{headspace}$, as follows:

$$n_{CH_4} = \frac{2pV_{headspace}}{100RT} \tag{A.4}$$

where p is pressure, T is absolute temperature, and R is the gas constant; the former two take values for standard room temperature and pressure.

Using H_2 as an example as the product of interest, substitution of A.4 into A.3 would lead to

$$n_{H_2} = \frac{A_{H_2}}{A_{CH_4}} \cdot \frac{1}{RF_{H_2}} \cdot \frac{2pV_{headspace}}{100RT} \tag{A.5}$$

Faradaic efficiency, FE, is calculated by comparing the expected amount of product, $n_{expected}$, to the actual amount produced, n_x.

$$n_{expected} = \frac{n_{e^-}F}{Q} \tag{A.6}$$

where F is the Faraday constant, Q is the amount of charge passed through the electrode, and n_{e^-} corresponds to the number of moles of electrons needed to yield one mole of product, which is 2 in our case according to the following equations:

$$2H^+ + 2e^- \longrightarrow H_2 \qquad\qquad CO_2 + 2H^+ + 2e^- \longrightarrow CO + H_2O$$

Therefore,

$$FE = \frac{n_x Q}{2F} \tag{A.7}$$

Turnover numbers and turnover frequencies are expressed in units of $mol_x \cdot mol_{catalyst}{}^{-1}$ and $mol_x \cdot mol_{catalyst}{}^{-1} \cdot h^{-1}$, respectively, where x is once again the product in question.

Appendix B

Appendix to Chapter 2

B.1 Supplementary Figures

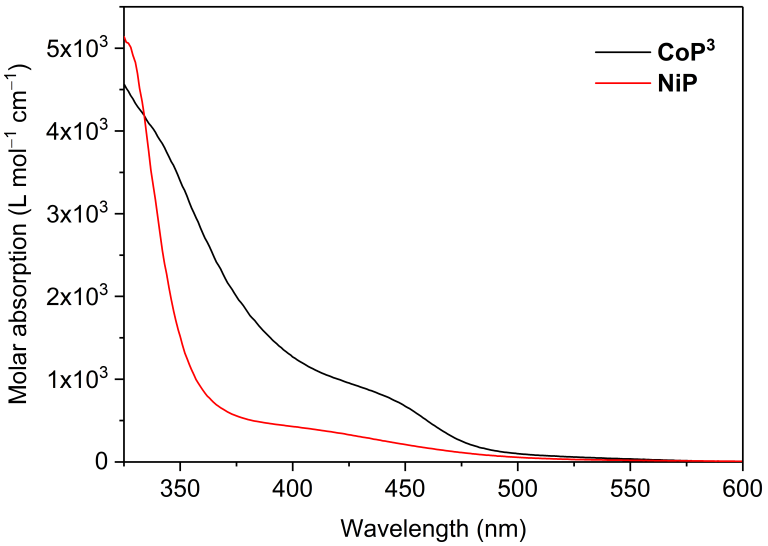

Fig. B.1 UV-visible spectra of **CoP^3** (black) and **NiP** (red) solubilised in methanol in the presence of tetrabutylammonium hydroxide (0.1 M), measured at room temperature.

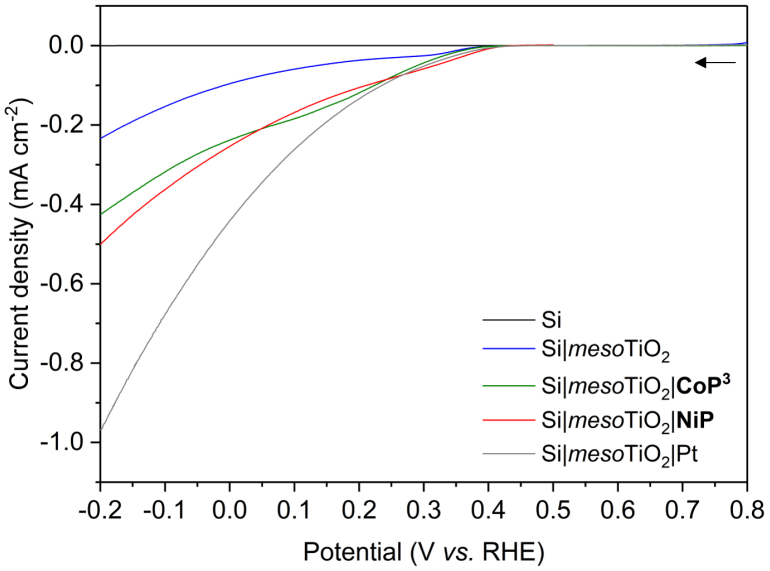

Fig. B.2 LSVs of Si (black), Si|*meso*TiO_2 (blue), Si|*meso*TiO_2|**CoP³** (green), Si|*meso*TiO_2|**NiP** (red) and Si|*meso*TiO_2|Pt (grey) electrodes under continuous illumination. Arrow indicates scan start and direction. Conditions: aqueous acetic acid solution (0.1 M, pH 4.5), UV-filtered simulated solar light irradiation (AM1.5G, 100 mW cm^{-2}, $\lambda > 400$ nm), N_2 atmosphere, room temperature, $\nu = 5$ mV s^{-1}.

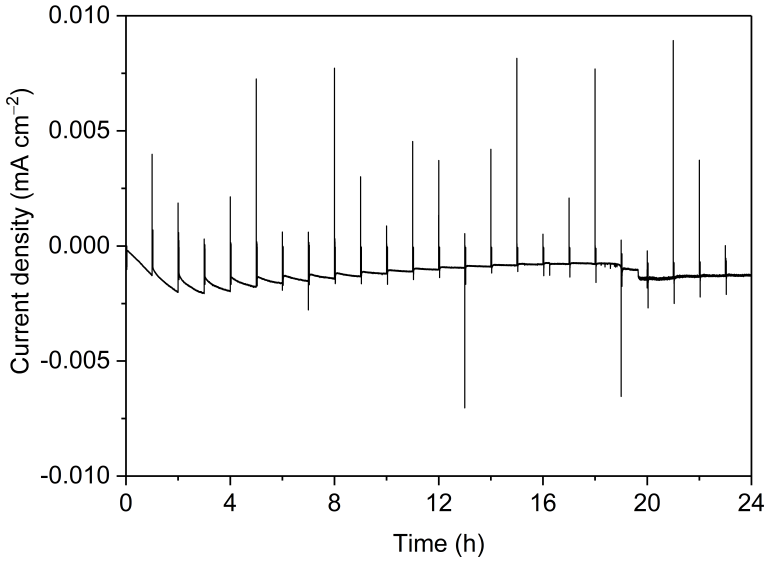

Fig. B.3 CPPE trace for bare Si electrode at $E_{app} = 0.0$ V *vs.* RHE under continuous illumination with an hourly dark chop lasting for two min each. Conditions: aqueous acetic acid solution (0.1 M, pH 4.5), UV-filtered simulated solar light irradiation (AM1.5G, 100 mW cm^{-2}, $\lambda > 400$ nm), N_2 atmosphere, room temperature.

Appendix C

Appendix to Chapter 3

C.1 Supplementary Figures

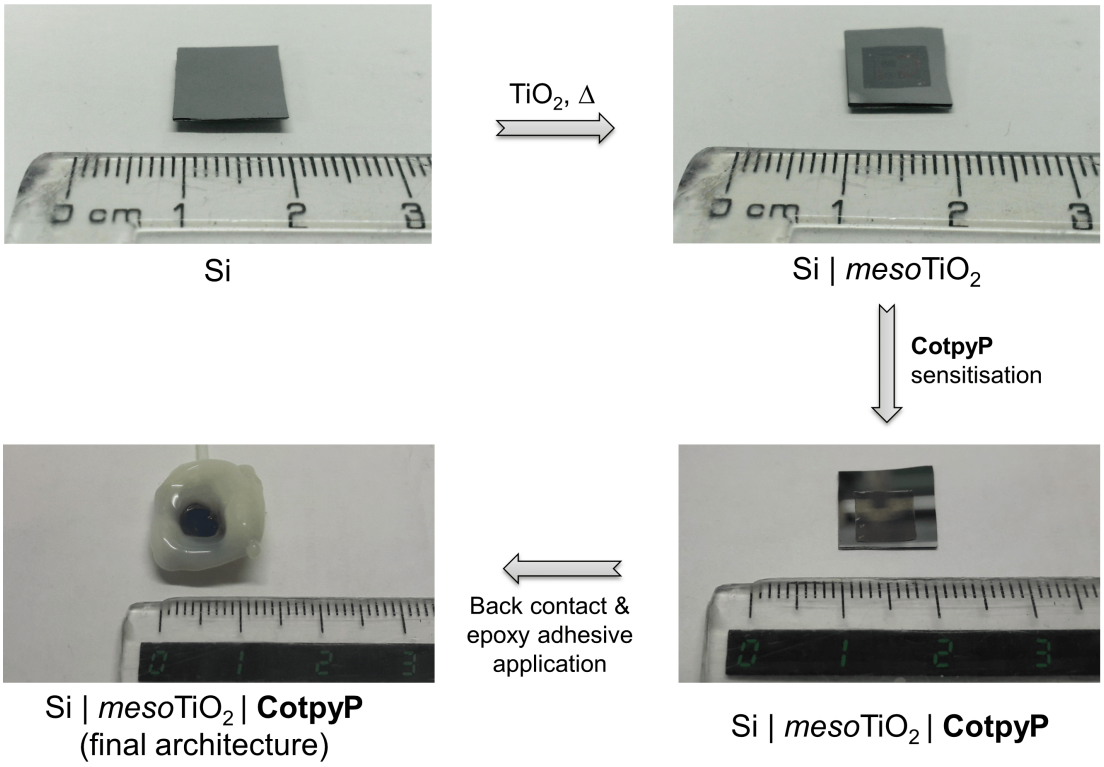

Fig. C.1 Photographs of typical electrodes at various stages of preparation towards the final Si|*meso*TiO_2|**CotpyP** photocathode. In brief, the Si wafer is etched with HF acid, followed by immediate deposition and sintering of a *meso*TiO_2 film. **CotpyP** sensitisation is carried out by immersion of the Si|*meso*TiO_2 electrode into a solution of the catalyst. Finally, back contact preparation and epoxy insulation of inactive areas yield the final photocathode.

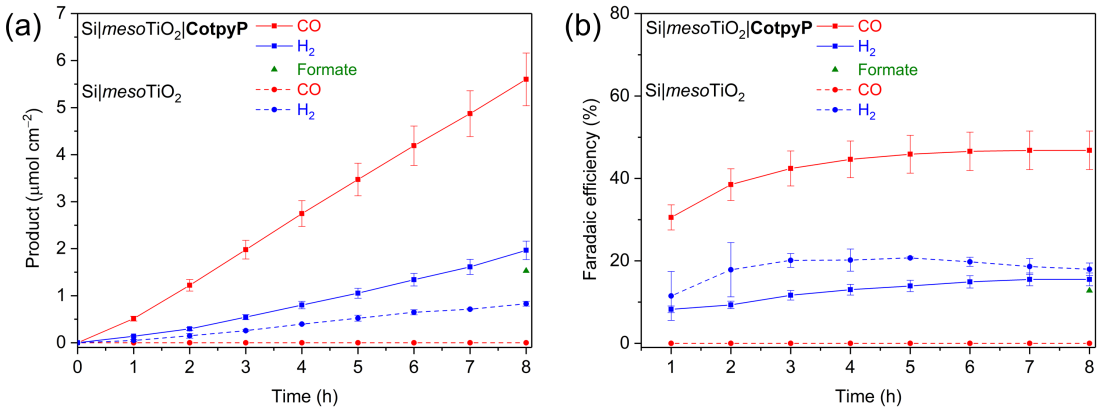

Fig. C.2 Control experiments comparing the photoelectrocatalytic behaviour of Si|*meso*TiO_2 with Si|*meso*TiO_2|**CotpyP** photocathodes: (a) quantities of CO, formate and H_2 formed during CPPE, and (b) FEs (cumulative over the duration of the CPPE) for the three different products. Note that the corresponding *J*-*t* traces are given in Fig. 3.7a. Conditions: 6:4 MeCN:H_2O (0.1 M $TBABF_4$); $E_{app} = -1.0$ V *vs.* Fc^+/Fc ; 1 Sun (AM1.5G, 100 mW cm^{-2}, $\lambda > 400$ nm); CO_2-saturated conditions; room temperature.

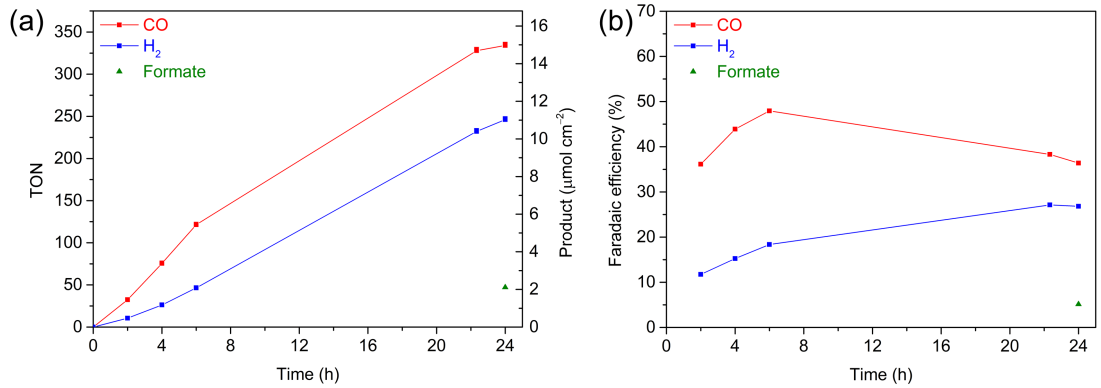

Fig. C.3 (a) TON and product quantities and (b) FE (cumulative over duration of CPPE) for CO, formate and H_2 production by Si|*meso*TiO_2|**CotpyP** photocathode for 24 h of CPPE. Conditions: 6:4 MeCN:H_2O (0.1 M $TBABF_4$); $E_{app} = -1.0$ V *vs.* Fc^+/Fc ; 1 Sun (AM1.5G, 100 mW cm^{-2}, $\lambda > 400$ nm); CO_2-saturated conditions; room temperature.

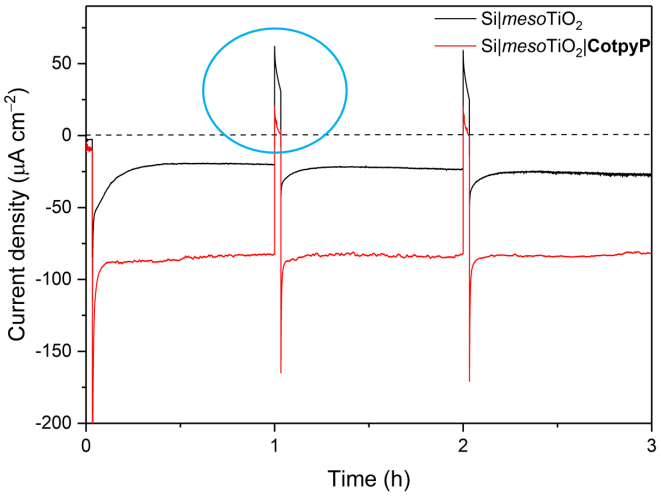

Fig. C.4 Close-up of J-t traces from first 3 h of CPPE with Si|*meso*TiO_2 (black trace) and Si|*meso*TiO_2|**CotpyP** (red trace) photocathodes under continuous illumination and an hourly 2 min dark chop. Following "charging up" in the light, evidence of anodic discharging in the dark of the bare Si|*meso*TiO_2 electrode appears (blue circle), as we have previously reported with this scaffold and as discussed in Chapter 2 section 2.2.7. Full J-t trace for 8 h CPPE is given in Fig. 3.7a. Conditions: 6:4 MeCN:H_2O (0.1 M $TBABF_4$); $E_{app} = -1.0$ V *vs.* Fc^+/Fc ; 1 Sun (AM1.5G, 100 mW cm^{-2}, $\lambda > 400$ nm); CO_2-saturated conditions; room temperature.

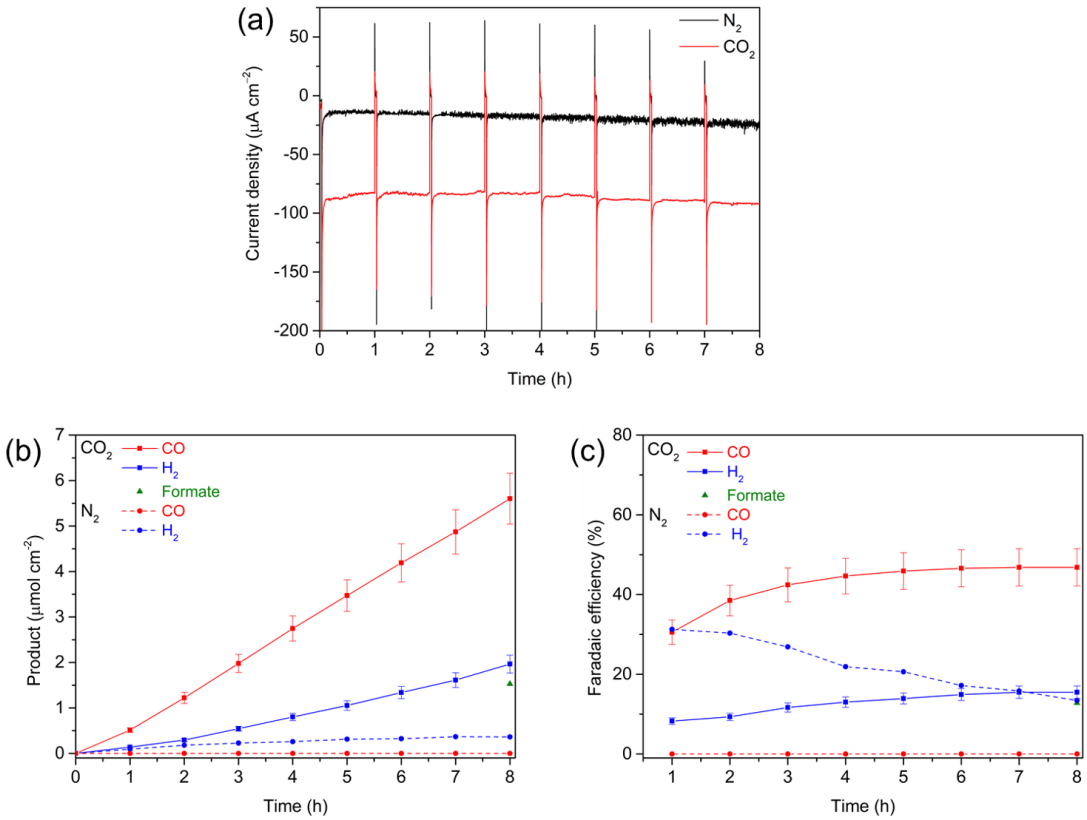

Fig. C.5 Control experiments comparing the photoelectrocatalytic behaviour of Si|*meso*TiO_2|**CotpyP** under N_2 and CO_2 atmospheres: (a) *J*-*t* traces under continuous light illumination with an hourly 2 min dark chop, (b) quantities of CO, formate and H_2 formed during CPPE, and (c) FEs (cumulative over the duration of the CPPE) for the three different products. Conditions: 6:4 MeCN:H_2O (0.1 M $TBABF_4$); $E_{app} = -1.0$ V *vs.* Fc^+/Fc ; 1 Sun (AM1.5G, 100 mW cm^{-2}, $\lambda > 400$ nm); room temperature.

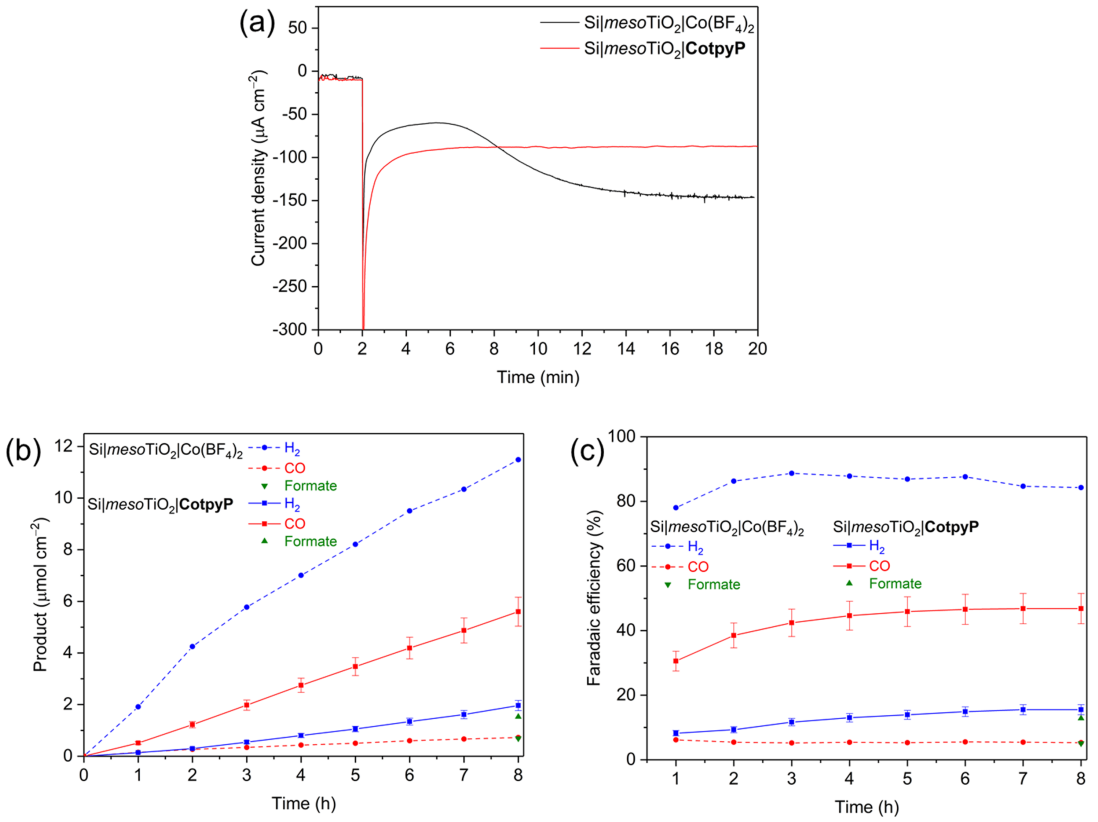

Fig. C.6 Control experiments comparing the photoelectrocatalytic behaviour of Si|*meso*TiO_2|$Co(BF_4)_2$ and Si|*meso*TiO_2|**CotpyP**: (a) *J*-*t* traces shown for the first 20 min, highlighting the initial period of growth suggestive of deposition from $Co(BF_4)_2$ and therefore catalysis performed by a heterogeneous catalyst, (b) quantities of H_2, CO and formate formed across 8 h, and (c) FEs (cumulative over the duration of the CPPE) for the three different products across 8 h of CPPE. Conditions: 6:4 MeCN:H_2O (0.1 M $TBABF_4$); $E_{app} = -1.0$ V *vs.* Fc^+/Fc ; 1 Sun (AM1.5G, 100 mW cm^{-2}, $\lambda > 400$ nm); CO_2-saturated conditions; room temperature.

Appendix D

Appendix to Chapter 4

D.1 Supplementary Tables

Table D.1 Frequencies ($\tilde{\nu}$, cm^{-1}) of prominent RR bands of **CotpyP** adsorbed on *meso*ITO electrodes in comparison to those obtained for powders of [$\mathbf{Co^{II}tpyP}$] and [$Co^{II}Cl_2$(tpy)].

$\mathbf{Co^{II}tpyP}$ on *meso*ITO electrode	$\mathbf{Co^{II}tpyP}$ powder	$Co^{II}Cl_2$(tpy) powder
1355	1355	1339
1483	1483	1470
1493	1493	-
1554	1554	1570
1579	1579	1581
1609	1613	1602

Table D.2 Frequencies ($\tilde{\nu}$, cm^{-1}) of prominent RR bands of**CotpyP** adsorbed on *meso*ITO electrodes at different E_{app} in N_2-purged 9:1 MeCN:H_2O (0.1 M $TBABF_4$). Lowering the electrode potential E_{app} from positive to negative values afforded a redox transition of the complex from Co^{III} to Co^{II} to Co^{I} with unique marker frequencies as derived from component fitting analysis. Note that the table columns have no relation to one another across their rows.

$\mathbf{Co^{III}tpyP}$	$\mathbf{Co^{II}tpyP}$	$\mathbf{Co^{I}tpyP}$
1571	1358	1476
1621	1485	1566
	1552	1603
	1610	

D.2 Supplementary Figures

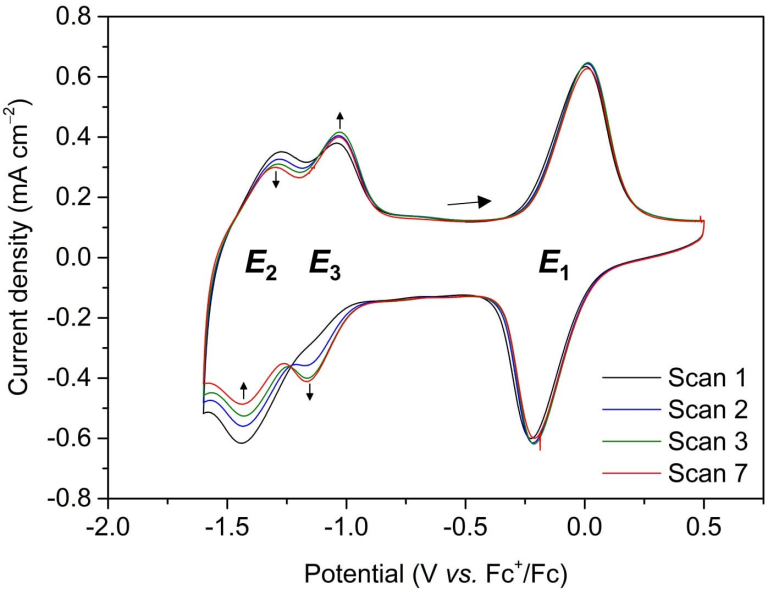

Fig. D.1 Consecutive CVs of *meso*ITO|**CotpyP** in 9:1 MeCN:H_2O (0.1 M $TBABF_4$) with the arrow indicating the scan start. Small black arrows indicate changing peak intensities. Conditions: $\nu = 50\,\mathrm{mV\,s^{-1}}$; N_2 atmosphere; room temperature.

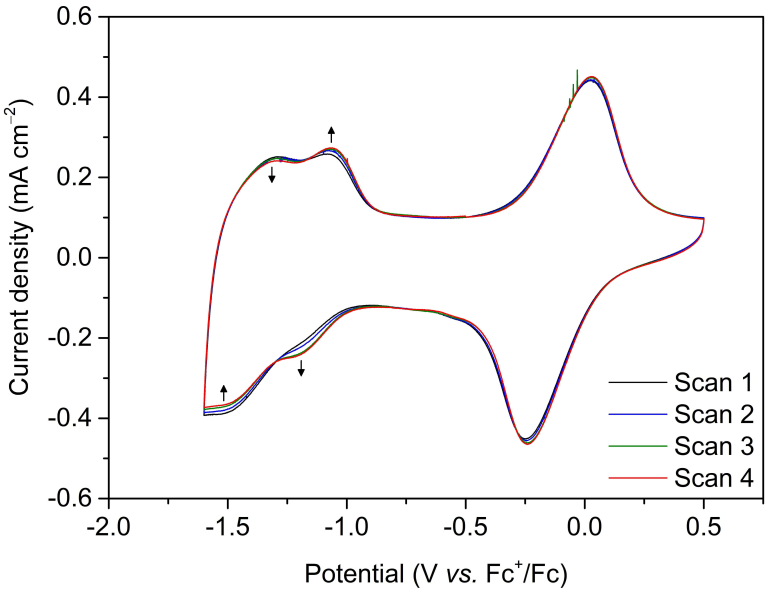

Fig. D.2 Consecutive CVs of *meso*ITO|**CotpyP** in 9:1 DMF:H_2O (0.1 M $TBABF_4$) with the arrow indicating the scan start. Small black arrows indicate changing peak intensities. Conditions: $\nu = 50\,\mathrm{mV\,s^{-1}}$; N_2 atmosphere; room temperature.

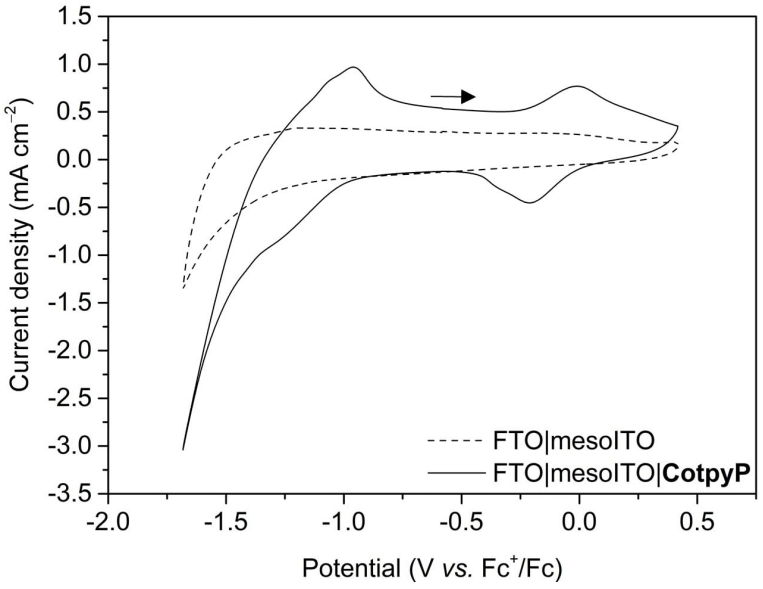

Fig. D.3 CV of *meso*ITO|**CotpyP** in comparison to mesoITO as a control in 6:4 MeCN:H_2O (0.1 M $TBABF_4$) in CO_2-saturated conditions. Arrow indicates scan start. Conditions: $\nu = 50\,\mathrm{mV\,s^{-1}}$; room temperature.

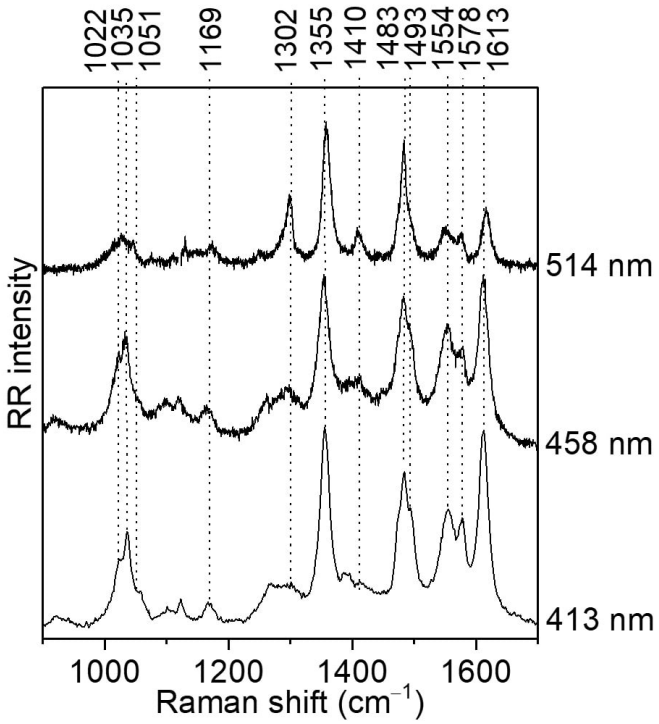

Fig. D.4 Confocal RR spectra of dry *meso*ITO and *meso*ITO|**CotpyP** (in absence of solution) recorded at three different excitation wavelengths $\lambda_{ex} = 413$, 458 and 514 nm.

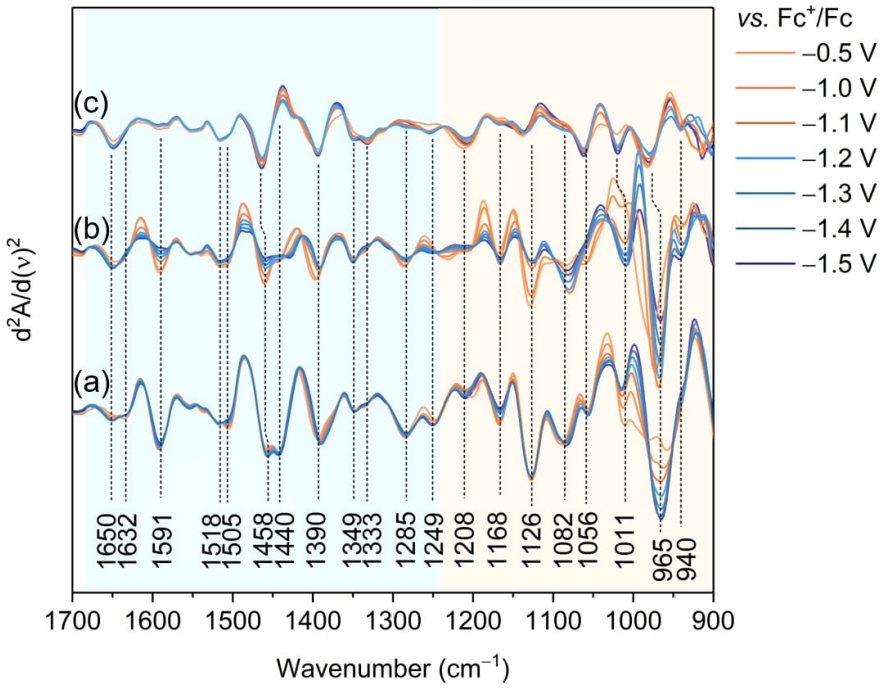

Fig. D.5 Second derivatives of ATR-IR spectra (full regions of Fig. 4.10) taken of *meso*ITO|**CotpyP** at different E_{app} (Fig. 4.8) in (a) N_2-purged MeCN, (b) N_2-purged 9:1 MeCN:H_2O and (c) CO_2-purged 9:1 MeCN:H_2O (0.1 M $TBABF_4$ in all cases) at room temperature. All spectra have been referenced to background spectra recorded from catalyst-free *meso*ITO for each of the above conditions. Negative bands represent band components and their intensities. Blue and yellow regions indicate the terpyridine and phosphonate spectral regions, respectively.

Appendix E

Appendix to Chapter 5

E.1 Supplementary Tables

Table E.1 Quantification of Co loaded on surface of FTO|IO-ITO|$\mathbf{P1_5}$ electrodes (thickness $\approx 6\,\mu m$) before and after CV cycling in 6:4 MeCN:H_2O (0.1 M $TBABF_4$), as measured by ICP-OES. Loadings are given per geometric surface area.

	Co loading on FTO|IO-ITO|$\mathbf{P1_5}$ ($nmol\,cm^{-2}$)
Before cycling	17 ± 2
After cycling	4.3 ± 0.3

E.2 Supplementary Figures

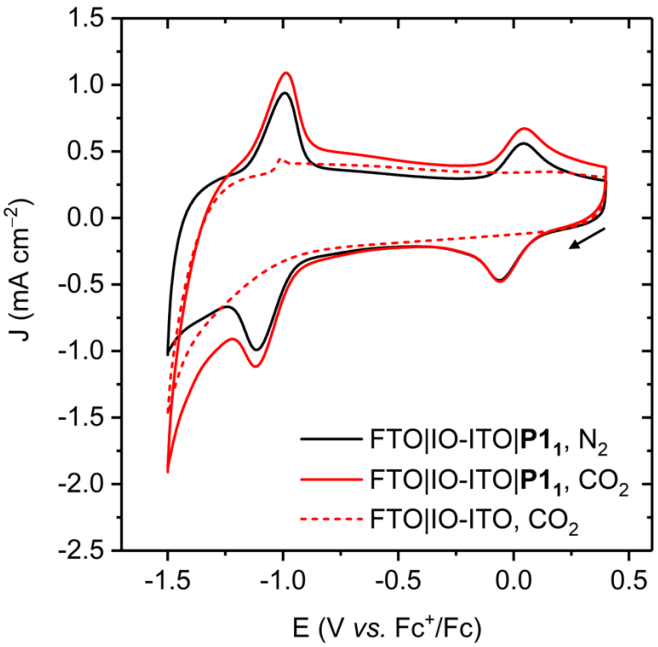

Fig. E.1 Cyclic voltammograms on the FTO|IO-ITO|**P1$_1$** electrode under N_2 and CO_2 atmosphere in 6:4 v:v MeCN:H_2O electrolyte solution (0.1 M $TBABF_4$), 100 mV s^{-1}. The response of a polymer-free FTO|IO-ITO electrode under CO_2 atmosphere and otherwise identical conditions is also shown. Arrow indicates scan start.

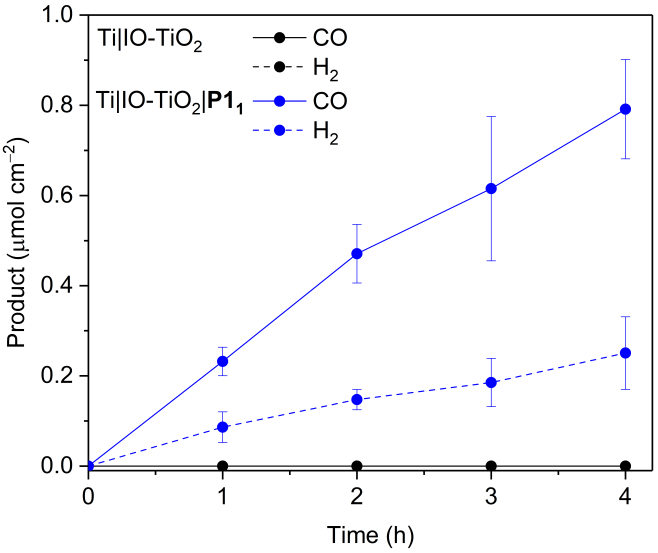

Fig. E.2 Control experiment comparing the quantities of CO (solid lines) and H_2 (dashed lines) produced by polymer-free Ti|IO-TiO_2 and Ti|IO-TiO_2|**P1$_1$** cathodes. Conditions: 6:4 MeCN:H_2O (0.1 M $TBABF_4$), $E_{app} = -1.3$ V *vs.* Fc^+/Fc, CO_2-saturated conditions, room temperature.

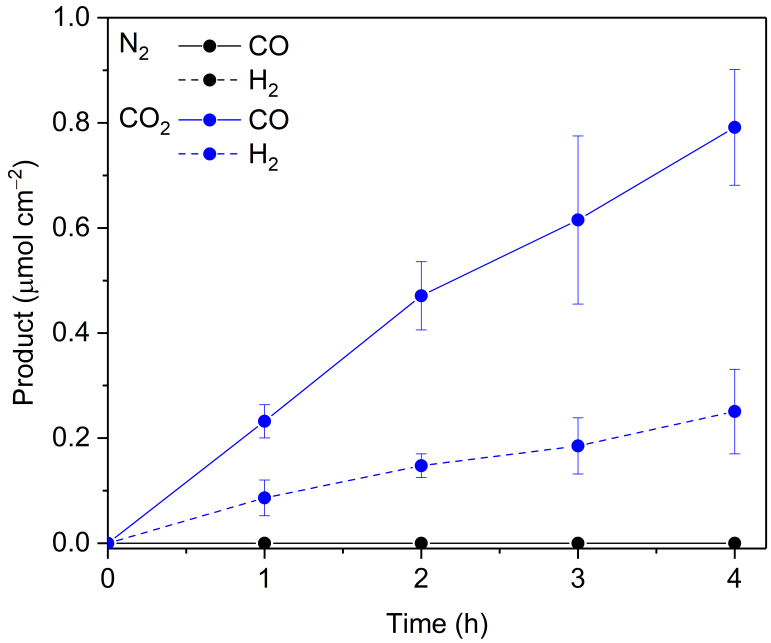

Fig. E.3 Control experiment comparing the quantities of CO (solid lines) and H_2 (dashed lines) produced by Ti|IO-TiO_2|**P1$_1$** cathodes under N_2 and CO_2 atmospheres. Conditions: 6:4 MeCN:H_2O (0.1 M $TBABF_4$), $E_{app} = -1.3$ V *vs.* Fc^+/Fc, room temperature.

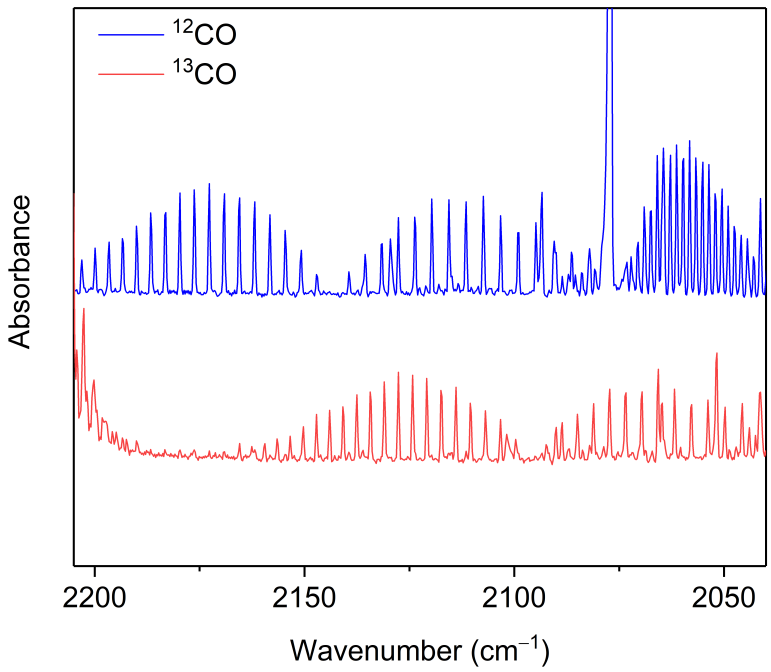

Fig. E.4 Isotopic labelling control experiment: IR spectra of samples of the gaseous products taken after 4 h of CPE of Ti|IO-TiO_2|**P1$_1$** under a $^{12}CO_2$ and a $^{13}CO_2$ environment. Conditions: 6:4 MeCN:H_2O (0.1 M $TBABF_4$), $E_{app} = -1.3$ V *vs.* Fc^+/Fc, room temperature.

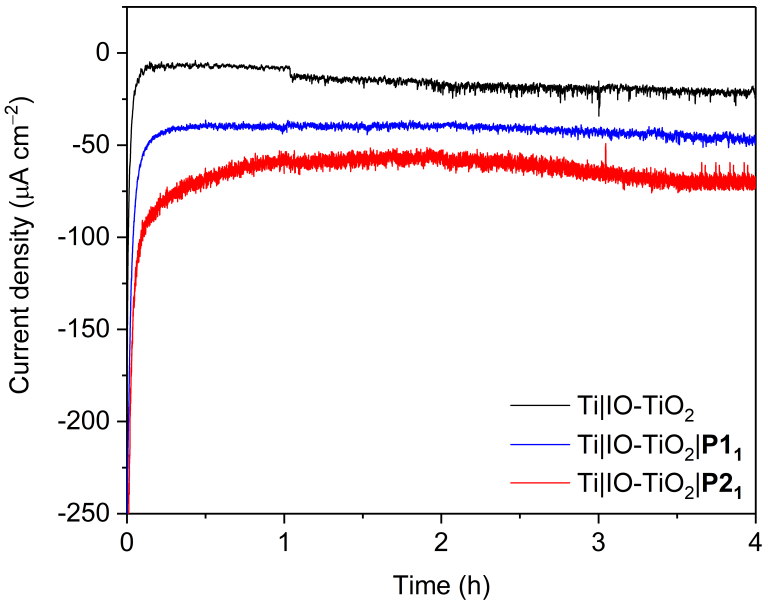

Fig. E.5 J-t traces of CPE performed on by Ti|IO-TiO_2, Ti|IO-TiO_2|**P1$_1$** and Ti|IO-TiO_2|**P2$_1$**. Conditions: 6:4 MeCN:H_2O (0.1 M $TBABF_4$), $E_{app} = -1.3$ V *vs.* Fc^+/Fc, CO_2-saturated conditions, room temperature.

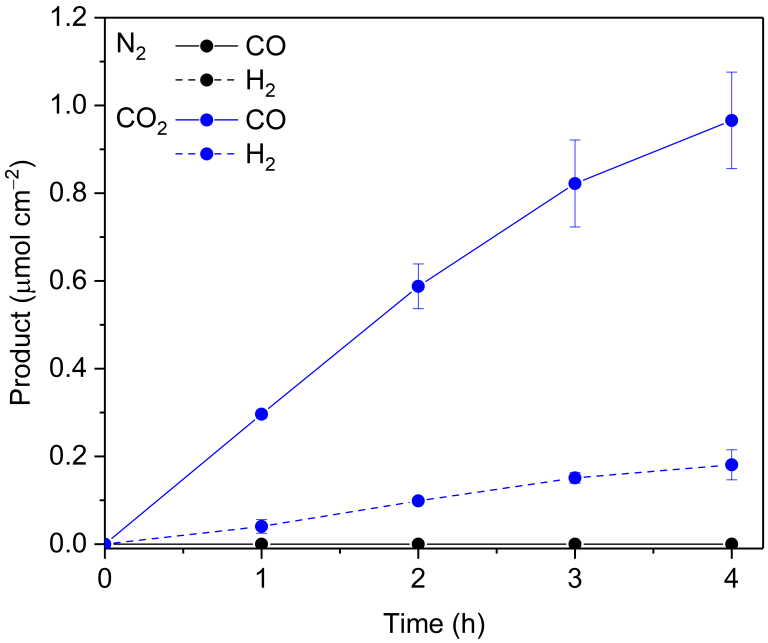

Fig. E.6 Control experiment comparing the quantities of CO (solid lines) and H_2 (dashed lines) produced by Ti|IO-TiO_2|**P2$_1$** cathodes under N_2 and CO_2 atmospheres. Conditions: 6:4 MeCN:H_2O (0.1 M $TBABF_4$), $E_{app} = -1.3$ V *vs.* Fc^+/Fc, room temperature.

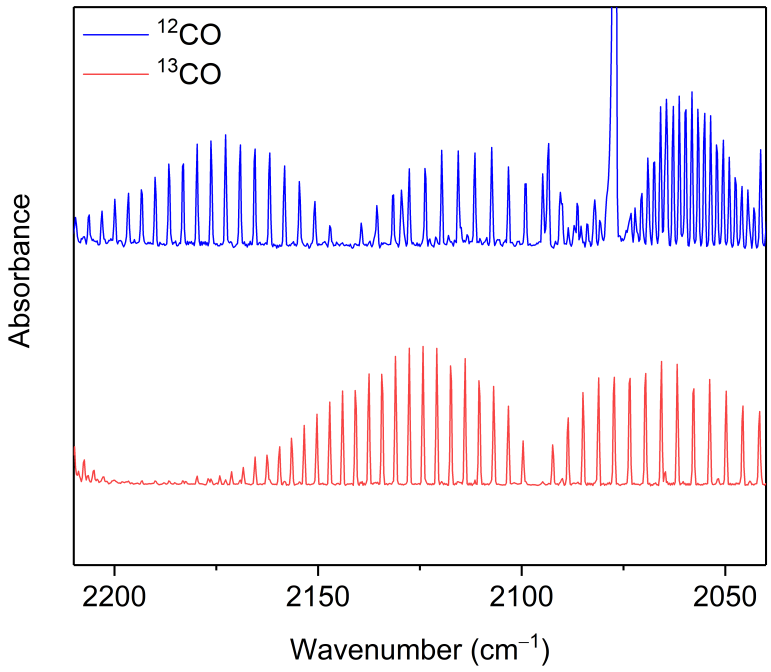

Fig. E.7 Isotopic labelling control experiment: IR spectra of samples of the gaseous products taken after 4 h of CPE of Ti|IO-TiO_2|**P2$_1$** under a $^{12}CO_2$ and a $^{13}CO_2$ environment. Conditions: 6:4 MeCN:H_2O (0.1 M $TBABF_4$), $E_{app} = -1.3$ V *vs.* Fc^+/Fc, room temperature.

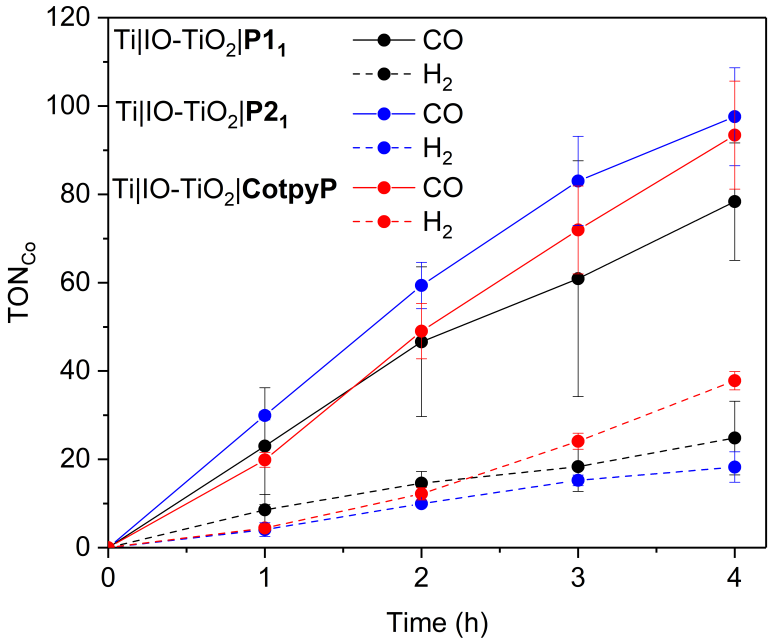

Fig. E.8 Co-based TONs of CO (solid lines) and H_2 (dashed lines) produced by Ti|IO-TiO_2|**P1$_1$**, Ti|IO-TiO_2|**P2$_1$** and Ti|IO-TiO_2|**CotpyP** under CPE. Note that Co loading on Ti|IO-TiO_2|**CotpyP** electrodes was measured by ICP-OES to be 26.1 ± 0.9 nmol cm^{-2}. Conditions: 6:4 MeCN:H_2O (0.1 M $TBABF_4$), $E_{app} = -1.3$ V *vs.* Fc^+/Fc, CO_2-saturated conditions, room temperature.